**UNIVERSIDAD DE CHILE**
**FACULTAD DE CIENCIAS FÍSICAS Y MATEMÁTICAS**
**DEPARTAMENTO DE INGENIERÍA CIVIL**

# ESTUDIO NUMÉRICO DE EFECTOS DE ESCALA EN LA RESISTENCIA AL CORTE DE DIACLASAS BIDIMENSIONALES EN ENSAYOS DE CORTE DIRECTO

MEMORIA PARA OPTAR AL TÍTULO DE INGENIERO CIVIL

MAURICIO IGNACIO CÁRCAMO MEDEL

PROFESOR GUÍA:
CÉSAR PASTÉN PUCHI

MIEMBROS DE LA COMISIÓN:
SHENG DAI
SERGIO SEPÚLVEDA VALENZUELA

SANTIAGO DE CHILE
2018

**RESUMEN DE MEMORIA PARA OPTAR AL**
**TÍTULO DE:** Ingeniera Civil con mención en
Estructuras, Construcción y Geotecnia
**POR:** Mauricio Ignacio Cárcamo Medel
**FECHA:** 07/05/2018
**PROFESOR GUÍA:** César R. Pastén Puchi

# ESTUDIO NUMÉRICO DE EFECTOS DE ESCALA EN LA RESISTENCIA AL CORTE DE DIACLASAS BIDIMENSIONALES EN ENSAYOS DE CORTE DIRECTO

Barton (1973) caracterizó la resistencia al corte de diaclasas en escala de laboratorio (~100 mm), desarrollando un criterio de resistencia al corte que considera la influencia de la rugosidad de la junta mediante el *Joint Roughness Coefficient* (JRC). A pesar de que inicialmente se desarrolló como un parámetro de ajuste, el JRC de diaclasas in-situ, cuyo largo varía en varios ordenes de magnitud, es determinado empíricamente mediante comparación visual con un set de perfiles representativos de pequeña escala elaborado por Barton & Choubey (1977). El objetivo de este trabajo es estudiar numéricamente el efecto de escala y el intervalo de muestreo espacial del perfil en la resistencia al corte de diaclasas bidimensionales sometidas a cargas normal constante. Se utilizaron simulaciones numéricas de elementos finitos de ensayos de corte directo para perfiles de pequeña y gran escala (~100 y ~1000 mm respectivamente), generados mediante el escalamiento de los perfiles standard de Barton & Choubey (1977), considerando además distintos intervalos de muestreo espacial y rugosidades. La elaboración de la geometría de los modelos y sus mallados, la ejecución de las simulaciones y el procesamiento de los resultados fueron automatizados para facilitar los cientos de simulaciones requeridas para el estudio. Los modelos fueron calibrados mediante análisis de sensibilidad, teniendo en consideración la precisión, convergencia y tiempo de cómputo de las simulaciones. Los resultados obtenidos muestran una buena relación con los resultados experimentales y confirman que el intervalo de muestreo en la caracterización de la rugosidad de las diaclasas afecta sus curvas tensión de corte desplazamiento. Las simulaciones de diaclasas de distinta escala, que sólo difieren en su largo y altura de asperezas manteniendo el resto de las propiedades constantes (i.e. propiedades del material, geometría del perfil, condiciones de borde), no muestran diferencias en la resistencia al corte máxima movilizada.

**RESUMEN DE MEMORIA PARA OPTAR AL**
**TÍTULO DE:** Ingeniera Civil con mención en
Estructuras, Construcción y Geotecnia
**POR:** Mauricio Ignacio Cárcamo Medel
**FECHA:** 07/05/2018
**PROFESOR GUÍA:** César R. Pastén Puchi

# NUMERICAL STUDY OF SCALE EFFECTS IN THE SHEAR STRENGTH OF FRESH ROCK JOINT PROFILES UNDER 2D DIRECT SHEAR LOADING

Barton (1973) characterized the small-scale shear strength of joints (~100 mm), developing a nonlinear shear strength criterion which considers the influence of roughness on the shear strength using the Joint Roughness Coefficient (JRC). Although initially developed as a curve fitting parameter, the JRC of in-situ joints, whose length varies in several orders of magnitude, is empirically determined through visual comparison with a representative set of standard small-scale profiles, elaborated by Barton & Choubey (1977). The objective of this work is to study the effects of scale and spatial sampling of the profile in determining the shear strength of two-dimensional fresh rock joints under constant normal load. FEM numerical simulations of direct shear tests models were used, for profiles of small and large scale (~100 and ~1000 mm respectively), generated by enlarging the Barton & Choubey (1977) standard profiles, for varying sampling intervals and roughness. The development of the model's geometry and its mesh, the execution of the tests simulations, and the processing of the results where automated to facilitate the hundreds of tests required for the study. The models were calibrated by sensitivity analyses for key parameters with the consideration of the model's accuracy, convergence, and computing time. The obtained results show a good relationship with the experimental results found in literature and confirm that the sampling interval in the roughness characterization influence the joint shear stress – displacement curve. The simulations of two-dimensional profiles performed under various scales, whose only differ on its length and asperity height, with the rest of the properties (i.e. material properties, profile geometry, boundary conditions) kept constant, don't show differences in the mobilized peak shear strength.

*Cuidado con esa inteligencia excesiva, samana.*

# Acknowledgements

Este trabajo no hubiese sido posible sin el apoyo de todos aquellos que me rodean, sin duda hicieron de este proceso mucho más “fácil” (si se le pudiera llamar así), ya sea con palabras de aliento, consejos o simplemente risas. Si bien no puedo mencionarlos a todos aquí, sepan que su apoyo, en cualquiera de sus formas ha sido invaluable!

Quiero comenzar agradeciendo a mi pequeña familia, comenzando por mi mamá, sin duda el pilar más importante en lo que va de mi existencia; la vida no te la hizo fácil y aún así te las arreglaste para sacar fuerzas para darnos todo, no solo económico sino también tu sabiduría, apoyo, y una fuente infinita de amor. Estoy muy orgulloso del ejemplo que has sido para nosotros tus hijos, y estoy seguro de que el papá lo estaría también. Jani, si bien nuestra relación es bastante particular, te agradezco por todas las risas (sería difícil encontrar tu humor en otro lado) y consejos, aun estando muy ocupados siempre hay tiempo para una conversación sobre cualquier cosa! Me aliviano mucho cuando el estrés y el cansancio se acumulaban. A pesar de que soy poco demostrativo, tengan claro que a ambas las quiero mucho!

Si bien mi familia cercana es pequeña ¡Esto se compenso con primos que parecen hermanos! Les doy las gracias a todos por su apoyo y constante preocupación en lo que ha sido todo este proceso ¡no podría pedir mejores personas cerca! Quiero darles especiales gracias al Sebastián (Tatán), quien fue quien inició mis gustos por la ciencia y la ingeniería, y quien sin duda ha sido un modelo a seguir. Muchas gracias también a mi tío Rodrigo, quien pese a las circunstancias se ha preocupado por mi desarrollo personal y profesional, incentivando a que desarrolle y aproveche mis capacidades. También quiero agradecer a alguien que, si bien apareció hace poco, ha sido muy importante en este tramo final, Muchas gracias Belén por todo! Me diste fuerza para seguir adelante en los momentos más difíciles, te quiero mucho negrita!

Es claro que el camino recorrido hasta ahora no comenzó hace 6 años, sino mucho antes en el colegio, tuve la suerte de conocer a mis mejores amigos ahí, le agradezco a todos por su amistad, apoyo y cariño!, Agradecimientos especiales a los Kbros (Mauri, Juaco, Bruno y Benja) son un grupo de gente la raja y estoy muy feliz de haberlos conocidos, cuantas risas, pizzas y buenos momentos hemos tenido! Por otro lado, muchas gracias Isa y Manu, esas juntas donde el manu hasta las 7 AM, discutiendo, gritando y especialmente tomando son de las cosas que siempre necesitaré, les tengo mucho cariño cabros.

Pensar que este proceso en la universidad ya esta acabando hace dar cuenta de toda la gente grandiosa que he conocido, todos aportaron de alguna forma u otro a la persona que soy actualmente. Saludos especiales a los cabros de la sección, Goza y Martín B, a los civiles Charlie, Gonzo, Pablo, Pato, Peter, Gustavo y Jaime, ha sido un periodo la raja y he aprendido mucho de ustedes! Espero que el contacto se mantenga y les deseo mucho éxito en lo que se les venga. Ya al final de mi vida universitaria, sin esperarlo, tuve la suerte de conocer un muy buen grupo de personas, Los Ignacios (Meili, Alo, Diego y Ele) y la gente de la Geopecera (Javi, Salomón, Emi, José F., Negro, Magda y Suso), a pesar de que muchas veces eran más risas que trabajo, no pude haber pedido mejores grupos de amigos para concluir este proceso! no hay dudas de su calidad como persona y profesionales. Saludos especiales a Salomón y la Javi por encargarse de que perdiera el tiempo en lugar de terminar la memoria, fue necesario el ocio!

Finalmente, quiero agradecer a mi profesor guía, César Pastén, por introducirme a la geotecnia y el mundo académico, exigirme lo que creía debía rendir y darme la oportunidad de conocer cómo se trabaja afuera e ir un poco más allá. Muchas gracias también a Sheng por su consejo y buena disposición, fue muy importante en esta etapa final de mi carrera. Gracias profesor Sepúlveda por sus comentarios y correcciones, la opinión de un experto en el tema fue invaluable para poder terminar el trabajo de forma correcta.

## Contents

# Figures

# Tables

# 1 Introduction

## 1.1 Background

Rock mechanics is an applied science concerning the response of rock and rock masses to the force fields exerted on their physical environment (Brady & Brown, 1971).The discipline of rock mechanics is especially visible in countries where the ground surface is predominantly composed of rock, for example, Chile, Finland, Scotland and Spain (Hudson & Harrison, 1997).

One of the main characteristics of a rock mass is the presence of discontinuities. The word ‘discontinuity’ denotes any separation in the rock continuum having effectively zero tensile strength and is used without any genetic connotation (Hudson & Harrison, 1997). Rock mass mechanical properties and behavior are hugely influenced by the discontinuities properties, which means an effective design of underground excavations and rock slopes requires a good understanding of the mechanical behavior of rock joints (Bahaaddini et al., 2014).

Rock masses can be treated as a pseudo-continuum, in terms of their mechanical properties, by using empirical criteria that apply a reduction factor to the intact rock strength, as a simplification of the intact rock plus the joint sets behavior. This method is usually used in tunnel design and underground mining in general, where the geomechanical engineering project scale is larger than the rock block, as seen in the mine pillar displayed in Figure 1.1 (Brady & Brown, 1971).

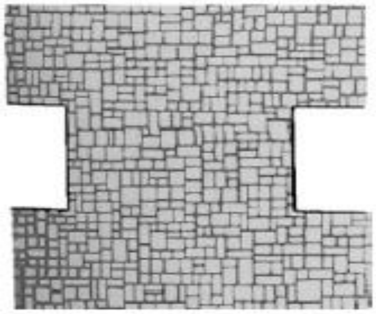

Figure 1.1. Mine pillar operating as a pseudo-continuum (Brady & Brown, 1971).

In open-pit mining and roads and highways cuts, rock slope stability is one of the main factors considered in the design (Wyllie & Mah, 2004). Rock slope stability is controlled by the potential mode of failure, given by joint geometry and orientation (Barton, 1973), and the shear resistance of the rock mass, which depends heavily on the irregularities of the joints along the failure surface, as noted by Newland and Alley (1957) and Withers (1964)**.** Therefore, it is important to characterize the discontinuities of the rock mass, as they are essential in the stability assessment.

Several names are used, in literature and practice, to refer to discontinuities. In general, the adopted name depends on the length of the analyzed discontinuity, as seen in Figure 1.2. The term joint is defined as “a discontinuity plane of natural origin along which there has been no visible displacement (ISRM, 1975)”, which means that discontinuities from the seismic origin are not considered, as there is relative motion between both joint surfaces.

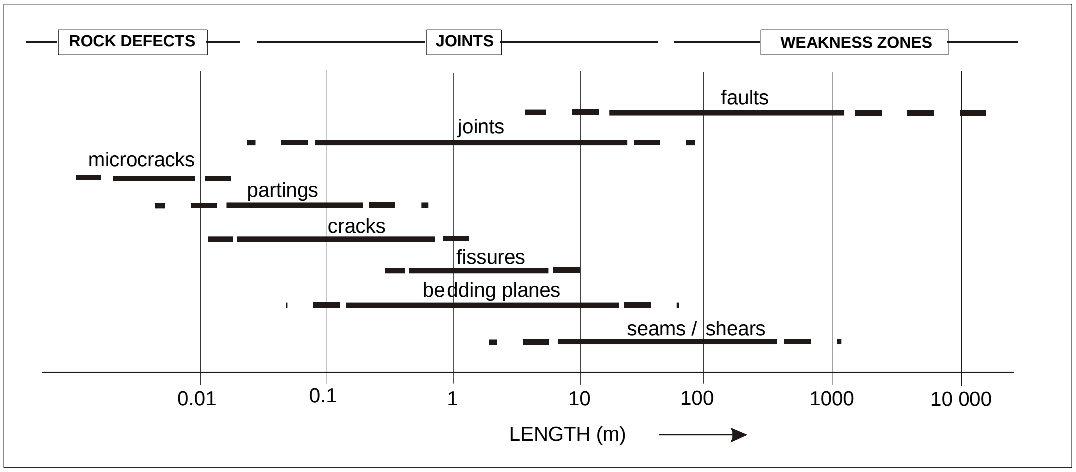

Figure 1.2. Discontinuities classification according to their length (Palmström, 2001).

With the progressing climate change, seasonal weather is expected to shift to more extremes patterns. This change implicates that rock joints are subjected to more intense cyclic loads of thermal, hydro-mechanical or freeze-thaw cycles. The cyclic loading is associated with a fatiguing factor in the resistance of the joints, as indicated by Zangerl (2010), Gischig (2011) and Preisig (2016). Natural rock slopes or man-made rock cuts that were once stable, may not be in future, thus a reassessment of their stability is required. The failure of many of these slopes and rock cuts may result in economic losses and in worse cases, the loss of lives (Wyllie & Mah, 2004)

Rock slopes in Chile, located in the Pacific ring of fire, are subjected to high seismic loading. The associated seismic loading occurring during an earthquake may act as a triggering factor in a joint sliding, in the short term, and as a preparatory factor in the long term (induced fatigue due to the shaking), as seen in Figure 1.3.

In the last decades, several methods to quantitatively characterize the roughness of a joint or surface have been developed, using newly introduced technology in engineering geology, such as laser photogrammetry and interferometry (ISRM, 1978; Sturzenegger & Stead, 2009). These methods become cheaper and more accessible every day, allowing a complete topographic characterization of the exposed surface of joints.

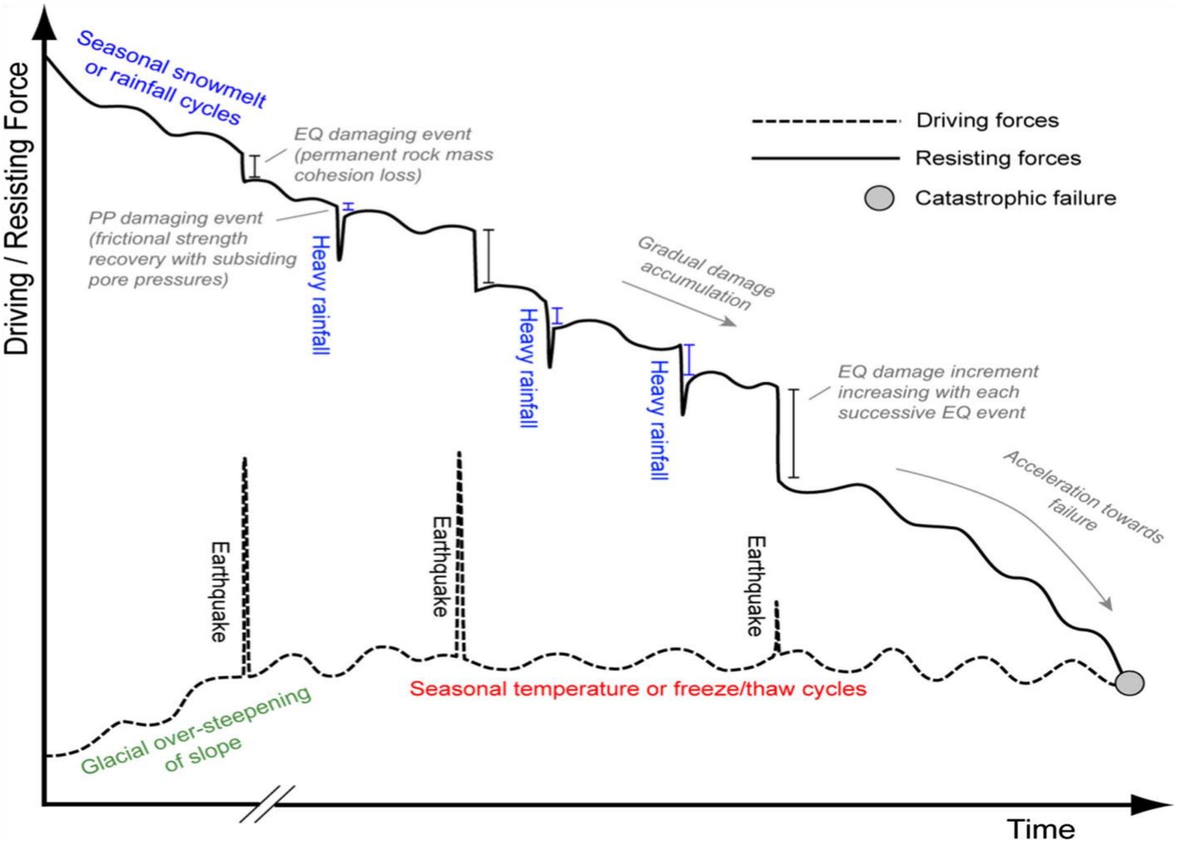

Figure 1.3. Driving and resistance forces in rock slope stability (Gischig et al., 2016)

The roughness of a joint has been recognized as a key parameter in the characterization of its shear strength, as concluded by Patton (1966) and Barton (1973). Several authors have developed shear strength criteria using laboratory data that considering the roughness of the joints. In section 2.5, the most relevant criteria are presented. Although an important number of criterions have been developed, the Barton – Bandis criterion (Barton & Bandis, 1990) is still the most widely used criterion to model the shear strength of discontinuities (Hoek, 2006), which considers the roughness effect on the shear strength with the Joint Roughness Coefficient (JRC) parameter.

Scale effects in the shear strength of joints have been observed empirically by several authors when comparing big size in-situ shear tests with the results of the shear tests of smaller specimens in the laboratory. It is important to note that, there is a geometrical scale effect due to the nature of discontinuities geometry and a scale affect associated to a reduction in the material resistance, being both phenomena important in the scaling of the shear strength (Tatone & Grasselli, 2013).

This effect was first studied by Bandis (1980) who concluded that there is a reduction in the shear strength of rock joints with an increment in the joint size. Based on Bandis' results, charts and equations were derived to scale the strength predicted by the Barton – Bandis criterion (Barton & Bandis, 1990). The methodology followed by Barton to study the scale effects has been questioned, because of outdated measurement systems used on his study and an ignorance of the results scatter due to the use of mean measurements (Leal Gomes, 2003; Papaliangas et al., 1994). In section 2.6, Bandis and other studies of joints scale effects are detailed.

## 1.2 Motivation

Understanding the behavior of rock joints, when subjected to shear stresses, is key to characterize a rock mass. A good degree of empiricism still prevails when characterizing rock mass roughness used in constitutive models for rock joints. There is often uncertainty about scaling experimental results to field conditions. Empirical methods, whose effectiveness is proved for specifics sets of conditions, are still widely used to scale results from small-scale experiments to large-scale properties of the rock mass and fracture systems. There is a need for a deeper understanding of rock joint geometry and of more powerful and precise techniques for rock joint characterization (Lanaro, 2000). The qualitative characterization of the joints and the use of empirical relationships had been enough to characterize rock masses and design safe geo-structures, but as projects get bigger and more ambitious, an accurate quantitative characterization of joints should be encouraged.

Although several models of varying complexity successfully characterize rock joints mechanical behavior at the laboratory scale (around ~100 mm), it is still not known how these models should be adjusted to consider scale effects on the shear strength of the joint.

A numerical approach to study the scale effect in rock discontinuities is proposed in this study, based on the simulation of shear tests of the joints, making use of the advantage of numerical simulations in terms of the possibility of scripting, repeatability of the tests and relative easiness of post-processing. Ideally, the proposed adjustment should be as simple as possible, considering all the key properties, but still being a viable solution for practical problems.

## 1.3 Objectives

### 1.3.1 Main Objective

Study the scale effect of fresh rock joints shear strength through numerical simulations of direct shear tests under varying loads, profile geometries and lengths, using the finite element method for analysis, considering a Mohr-Coulomb plasticity model for the intact rock and a Barton – Bandis shear strength criterion for the joint.

### 1.3.2 Specific Objectives

- With a profile geometry as input, automate the shear box drawing process, mesh generation and shear test numerical simulation process through computational scripts in Matlab.

- Using numerical simulations of direct shear tests, considering a Mohr-Coulomb plasticity model and Barton-Bandis shear criterion for the joint, Characterize the shear strength effect of the sampling interval of the joint and the scale, for profiles of varying lengths and roughness, through a back analysis of the JRC Parameter.

- Generate charts that describe the influence of the sampling of the joint length, on the roughness in the shear strength of the joints, based on the back-calculation of the JRC parameter.

# 2 Literature Review

Although the studies of interfaces mechanical behavior are numerous, the literature review will focus on the rock mass discontinuities under the following conditions:

- The joints are free of any filling material and clean.
- Joints are well mated, free of alteration and weathering on the joint walls.
- Constant normal load boundary condition may be assumed.

The review has five main points:

- Give a summary of the direct shear test procedures, under constant normal load, and its uses to characterize joints shear strength.
- Describe Roughness importance in rock joints and its shear strength.
- Describe the main surface roughness measurement methods.
- Introduce the models used to characterize rock joint surface roughness through empirical, statistical or fractal formulations.
- Present the most relevant model used to estimate the shear strength of joints under constant load boundary condition.
- Summarize the current complex issues that exist to this day, for the characterization of rock joint shear strength, with a focus on scale effects.

These points follow the order in which they are described above, as a basic understanding of the precursor points is required to understand the next one.

## 2.1 Direct Shear Test

Assessing the shear strength of rock joints is usually performed using direct shear apparatuses (Figure 2.1). (Muralha et al., 2014).

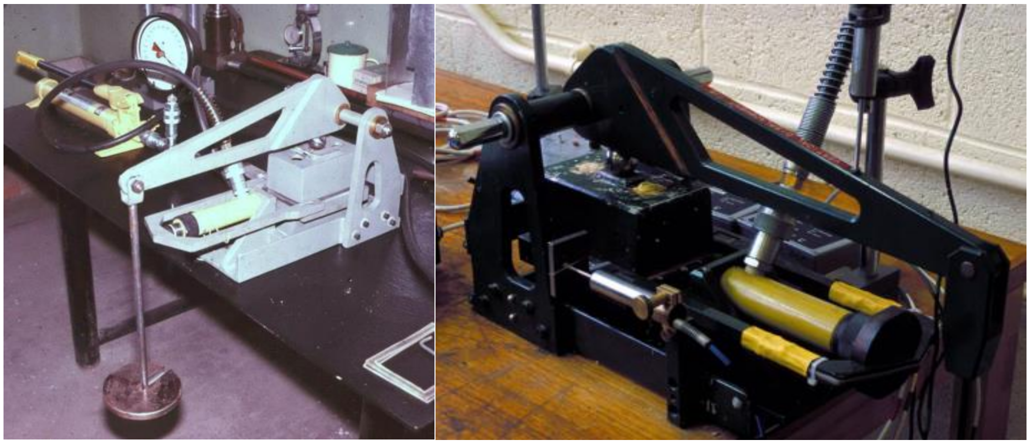

Figure 2.1. Shear Test Apparatus (Hencher and Richardson,1982, and Hencher et al, 2015).

The guidelines to the correct test execution are given in the ASTM standard "Standard Test Method for Performing Laboratory Direct Shear Strength Tests of Rock Specimens Under Constant Normal Force (Last modification Dec 1, 2016)". It is important to have in mind that the following guidelines only apply for constant normal load (CNL) boundary condition (Figure 2.2a), which may not necessarily represent in-situ conditions, as the shearing may be dilatancy controlled, as is the case of the Constant Normal Stiffness (CNS) condition (Figure 2.2b). Controlled-displacement tests are considered for this review.

.

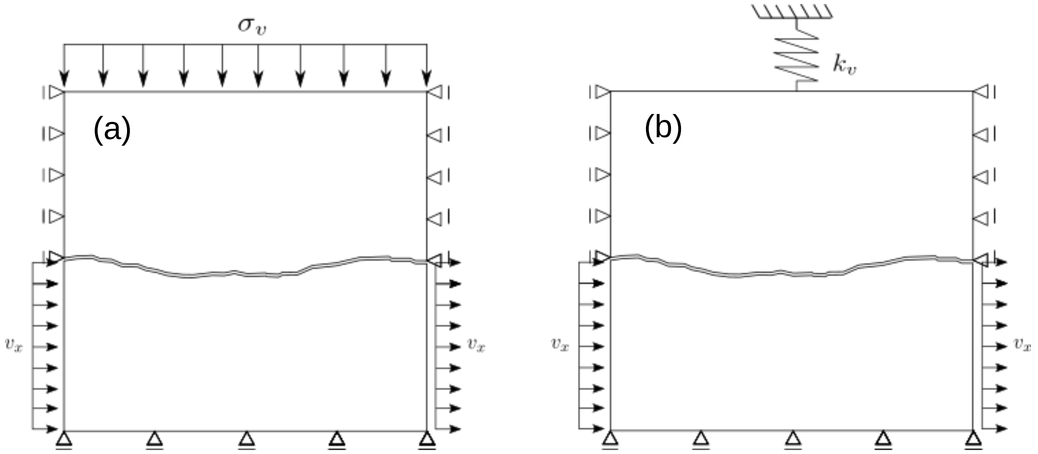

Figure 2.2. (a) CNL conditions (b) CNS conditions.

General guidelines of the test are described below, more detailed information may be found in the ASTM standard mentioned above.

### 2.1.1 Test Objective

While maintaining a constant force normal to the nominal shear plane of the specimen, an increasing external shear force is applied along the designated shear plane to cause shear displacement. The applied normal and shear forces and the corresponding normal and shear displacements are measured and recorded (Astm, 2008).

### 2.1.2 Required Equipment

- Testing Machine – Loading device that applies and registers normal and shear forces on the specimen. With the testing machine, load monitoring, pressure maintaining and displacement measuring devices must be included, in the case of the last one, displacement in both normal and tangential direction must be included.
- Specimen Holding Rings – Steel holdings with enough internal space to accommodate mounted specimens (Figure 2.3).
- Encapsulating Compound – Material used to fill the Holding Rings void space, to hold the specimen in place (Figure 2.3).

- Split Spacer Plates – Plastic plates used for isolating a fresh specimen’s shear zone from the encapsulating compound (Figure 2.3).
- Data Acquisition Equipment – A computer is recommended to be used to control the test, acquire data and plot the results. Ideally, acquisition rates must be nearly continuous (sampling frequency larger than 1 Hz).

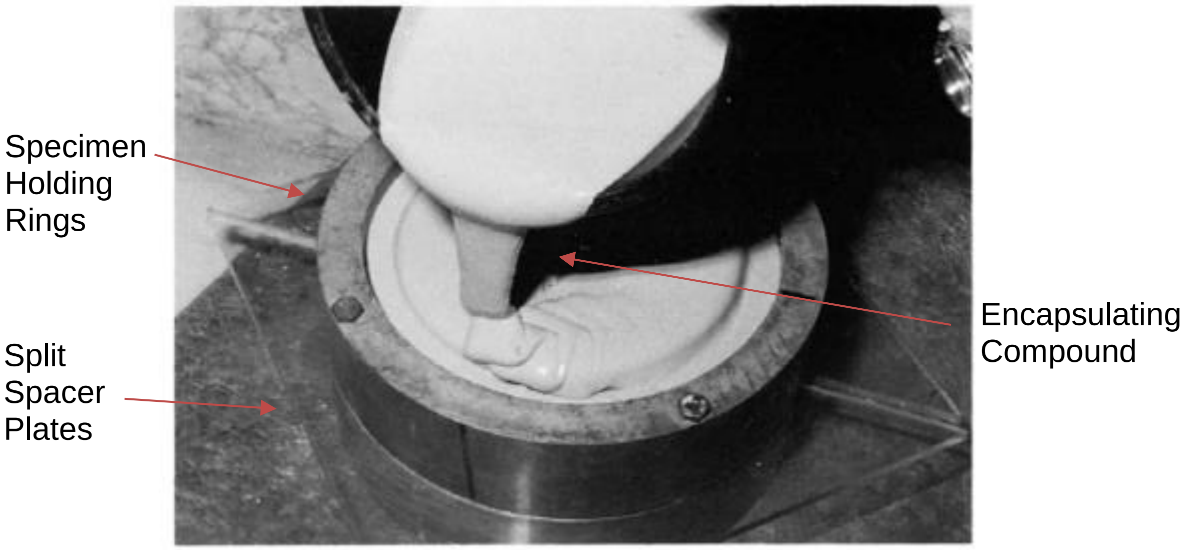

Figure 2.3. Pouring of encapsulating compound around the specimen (Astm, 2008).

### 2.1.3 Test Procedure and Results

First, the specimen geometry must be characterized completely, measuring dimensions, nominal area and joint roughness in the shear direction. Taking a photograph of both surfaces before and after the test is recommended. The next step is to encapsulate the specimen, in case a porous rock is tested, a sealer must be used as a coating, to prevent absorption of water from the encapsulating compound. The encapsulating compound must be allowed to cure without disturbance. When this process is finished, the spacer plate is removed, exposing the test zone for shear testing.

Once the specimen is ready, it must be mounted on the shear box together with displacement measuring devices, making sure that there are enough contact and room to measure the displacements and that these are fixed to start at zero displacement value; the recording must begin before the application of loads.

Finally, the load must be applied; the test starts with a small seating normal load applied (around 450 to 900 N), depending on the specimen size. Once the system is stabilized and the loads are measured, normal load is increased at a constant rate until the required load is achieved. Once the vertical load has been stabilized the shear displacement is applied at rates between (0.1 to 0.2 mm/min), readings must continue after the peak shear strength is reached, until a residual strength is established.

The test must be executed under 4 different vertical loads at least, which may be using the same specimen, with increasing vertical loads and reallocation of the joint, or with 4 different specimens, extracted from the same joint and representative of the joint surface. The obtained results must be plotted in 3 different spaces:

- Shear strength v/s shear displacement (Figure 2.4a).
- Normal displacement v/s shear displacement (Figure 2.4b).
- Shear strength v/s nominal normal stress, for peak and residual shear strength (Figure 2.5).

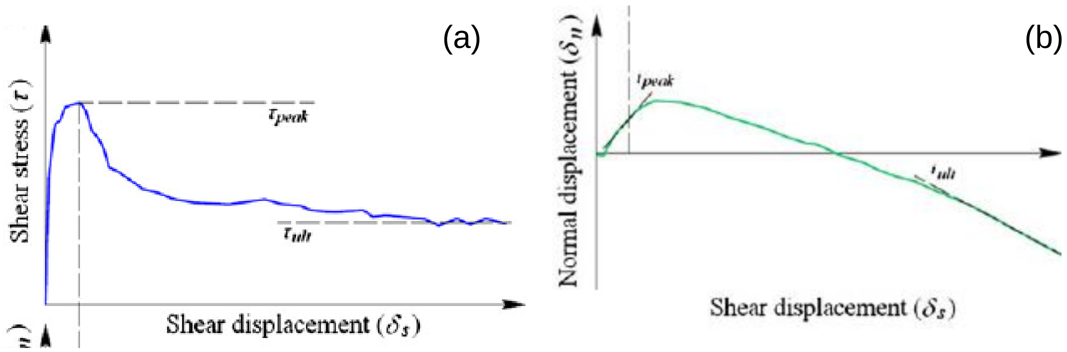

Figure 2.4. (a) Shear strength v/s shear displacement (b) Normal displacement v/s shear displacement (Modified from Muralha et al., 2014).

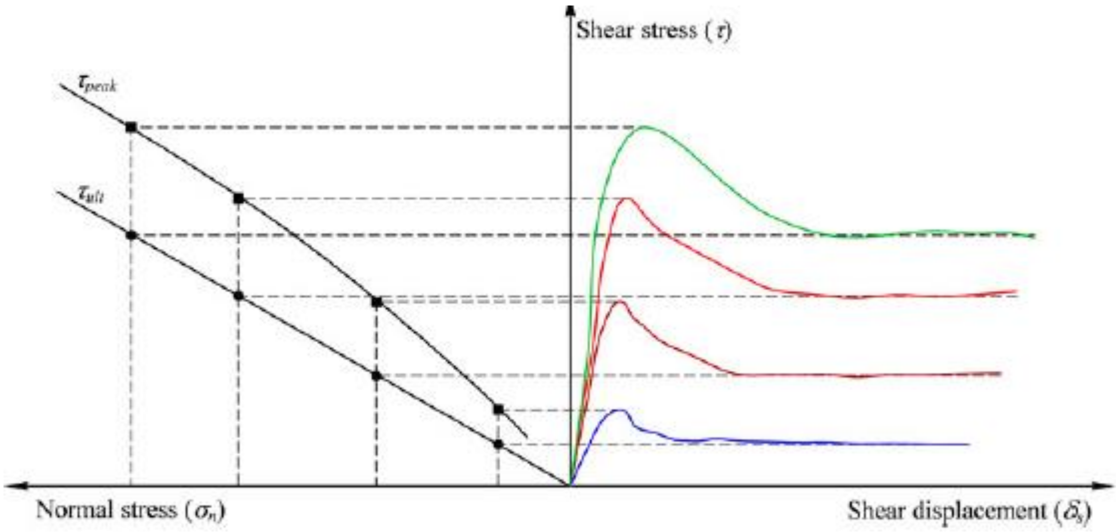

Figure 2.5. Shear strength v/s nominal normal stress, for peak and residual shear strength (Modified from Muralha et al., 2014).

These results are used to estimate the joint shear strength. The Mohr-Coulomb failure criterion is recommended in case of a planar joint, and a nonlinear criterion is recommended for rough joints, being the Barton – Bandis (Barton & Bandis, 1990) the most common one, as suggested by the ISRM (Muralha et al., 2014). The existing shear strength models are described in section 2.5.

## 2.2 Surface Roughness Definitions

There are several factors that influence friction during sliding contact conditions. The surface topography is one of the key factors that affect the coefficient of friction μ (Menezes & Kailas, 2016). In the rock mechanics context, surface topography is the most important parameter, at low stresses, in the shear strength of clean rock joints (Barton, 1973).

Although having a complete topographic measure of joints wall surfaces may be desirable in certain cases, such as academic studies of joint shear behavior, in practice the time and resources required to do so are out of reach in an engineering project. Also, in most cases, joints wall surfaces are not reachable at all. A practical alternative is to characterize the surface roughness in a qualitative or quantitative way of a representative specimen, associating its roughness value to a certain shear strength factor and assuming it may be extrapolated to the rest of the joint.

### 2.2.1 Definition of Roughness and Waviness

Surfaces in nature are composed of irregularities of multiple wavelengths (Figure 2.6), from atomic to the macro scale. Tribology is the science that studies how these irregularities behave across scales and their influence in frictional behavior, a big field of study in physics, with application in multiple other fields. In Rock mechanics, as a simplification, the number of studied irregularities wavelengths has been reduced to two, first order large-scale irregularities (waviness or planarity) and second order small-scale irregularities (roughness or unevenness). It is appropriate to divide the roughness into these two different features (Figure 2.7), as it is often easier to characterize them separately in the joint survey (Palmström, 2001).

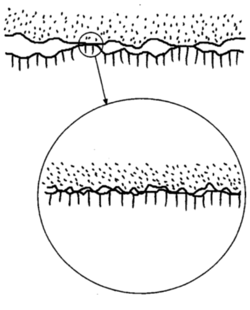

Figure 2.6. Irregularities across multiple scales and wavelengths (Persson et al., 2002)

In general, waviness affects the initial direction of shear displacement relative to the mean discontinuity plane, while unevenness affects the shear strength that would normally be sampled in a laboratory or medium scale in situ direct shear test (ISRM, 1978), but how these features affect depends on the geostructure conditions, joint weathering degree or cumulative displacement due to repetitive earthquake induced loading. In these cases, the joints tend to suffer a failure of their smaller asperities, If the damage is big enough, the waviness will control dilation and the shear strength of the joint. In pit slopes, these phenomena do not affect the joint walls and the roughness of the joint has the main influence on the stability of these slopes (Patton, 1971).

## Waviness

According to Palmström (2001), waviness is defined by the equation:

$$\mathrm{U} = \frac{\mathrm{a_{max}}}{\mathrm{L_j}} \tag{2.1}$$

Where $\mathrm{a_{max}}$ [mm] is the maximum amplitude from planarity and $\mathrm{L_j}$ [m] is the length of the joint. In practice, waviness is easily measured using a straight edge placed on the joint surface and a measuring the maximum amplitude $\mathrm{a_{max}}$, as seen in Figure 2.8a). Waviness wavelength is measured in meters and its amplitude in millimeters (Figure 2.7a), this means that it may only be measured in-situ and not in laboratory conditions. In practice, waviness is measured by sight by an experienced professional.

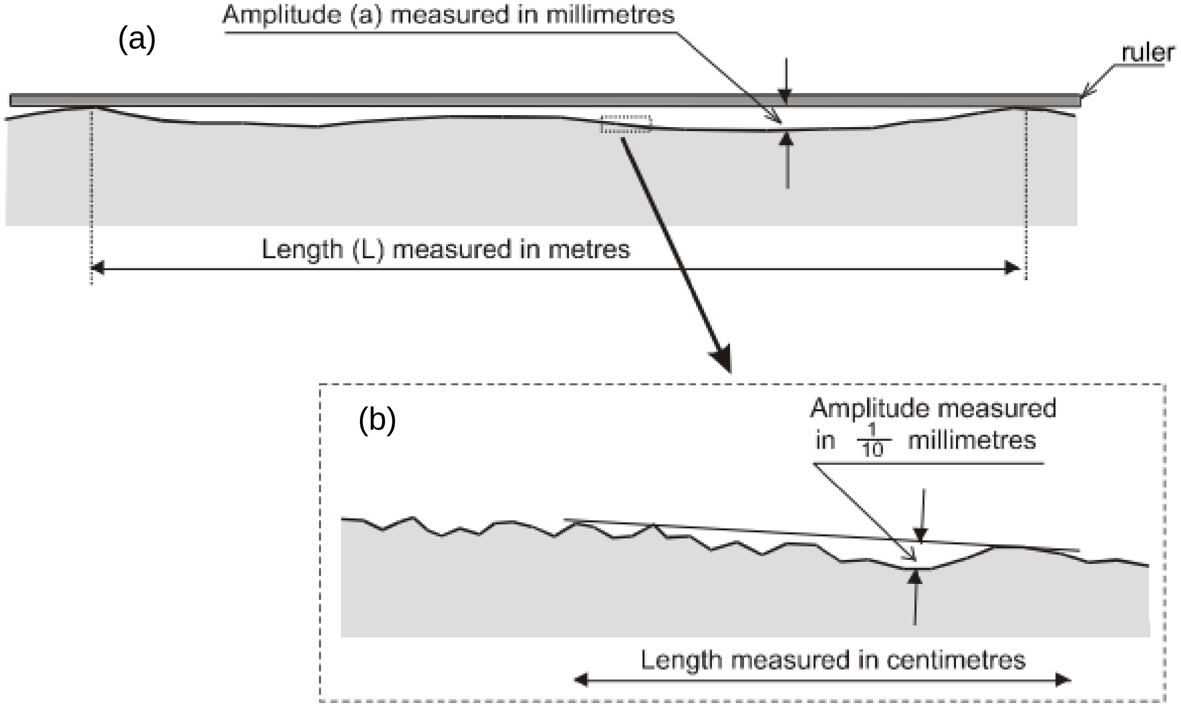

Figure 2.7. (a) Waviness and (b) roughness of a rock surface (Palmström, 2001).

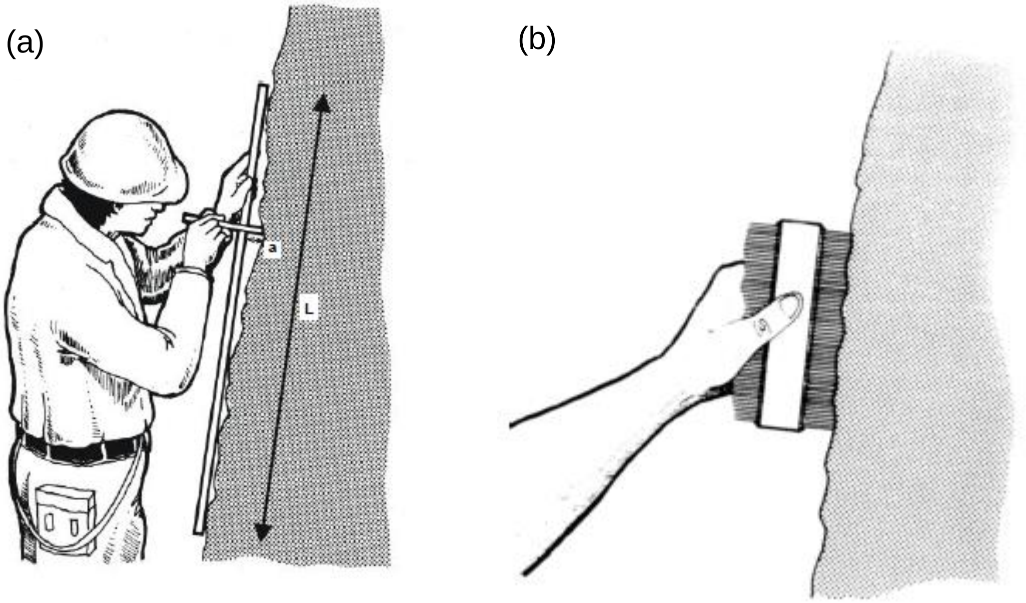

Figure 2.8. (a) Measurement of waviness U (b) Measurement of roughness with a comb (Palmström, 2001).

## Roughness

Surface roughness or unevenness is the nature of the asperities in the joint surface which can be felt by touch. This is an important parameter contributing to the condition of joints. Asperities that occur on the two matching joint surfaces interlock if they are clean and closed, and inhibit shear movement along joint surfaces (Palmström, 2001). Roughness wavelength is measured in centimeters and its amplitude in 1/10 millimeters to millimeters (Figure 2.7b). This means that it may be measured both in-situ and in laboratory conditions.

All the methods described in section 2.3 may be used to characterize roughness, including the comb (Figure 2.8b), method indicated by Palmström (2001) and the ISRM (1978) as the most accurate yet practical. In practice, roughness is measured by touch by an experienced professional, who then assign a smoothness factor (Js). This methodology is prone to errors and is severely subjective and as such, shouldn't be used when joints mechanical behavior is key to the geostructure stability (slopes or tunnels for example). Quantitative methods to characterize roughness as those described below should be encouraged as technology gets cheaper and more accessible.

## 2.3 Discontinuity Roughness Measurement

Over the years, several methods had been developed to characterize the roughness of discontinuities in situ or in a laboratory setup. These methods can be divided into two categories (Tatone, 2009):

1. Contact Methods: The instrument requires contact with the analyzed surface, mainly used to describe two-dimensional profiles.
2. Non-Contact Methods: Contact with the analyzed surface is not required, usually use for full three-dimensional characterization of the surface.

Even if this work focuses on discontinuity profiles, methods to characterize both 2D profile and 3D surface exist, this review will cover both, understanding that profiles can be obtained directly from complete surfaces measurements. The most used method are included in Appendix A. Although non-contact methods for two-dimensional profiles exist (Figure 2.9), these methods are usually reserved for measurement of the whole surface topography, as a complete characterization would be preferred if the equipment is available.

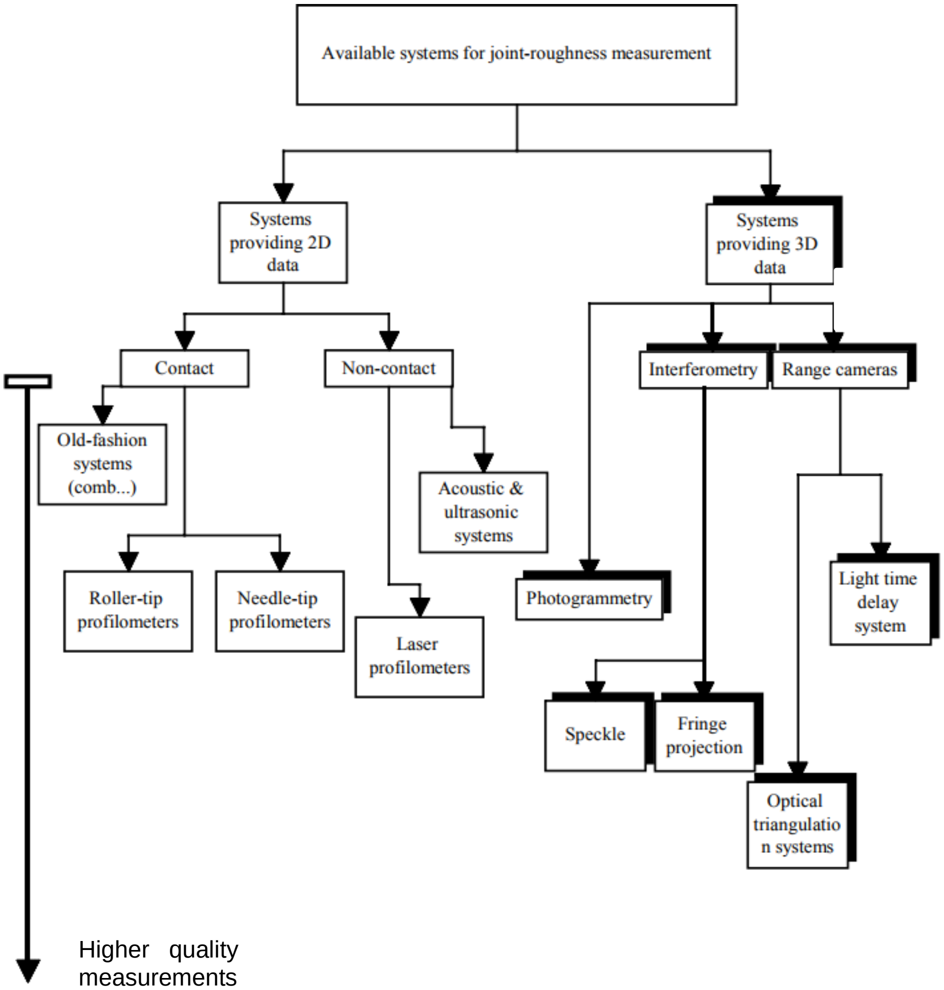

Figure 2.9. Available system for joint-roughness measurements (Modified from Grasselli, 2001).

## 2.4 Surface Roughness Characterization Models

### 2.4.1 Classical Methods

Since Barton's work (1973), rock joint roughness has been mostly characterizing by the Joint Roughness Coefficient (JRC), a parameter that considers roughness influence in the shear strength estimated by the Barton – Bandis model (Barton & Bandis, 1990), detailed in section 2.5.3. Originally, the JRC was an empirical coefficient, obtained by back analysis of direct shear test under varying vertical loads of the tested joints. Due to the difficulties to perform accurate shear tests, representative of in-situ condition of the studied rock joints, Barton and Choubey (1977) presented an optional method to estimate the JRC, which required to visually compare the joint of interest with a set of predefined profiles (Figure 2.10), then the JRC value of the most similar profile was assigned to the studied rock joint.

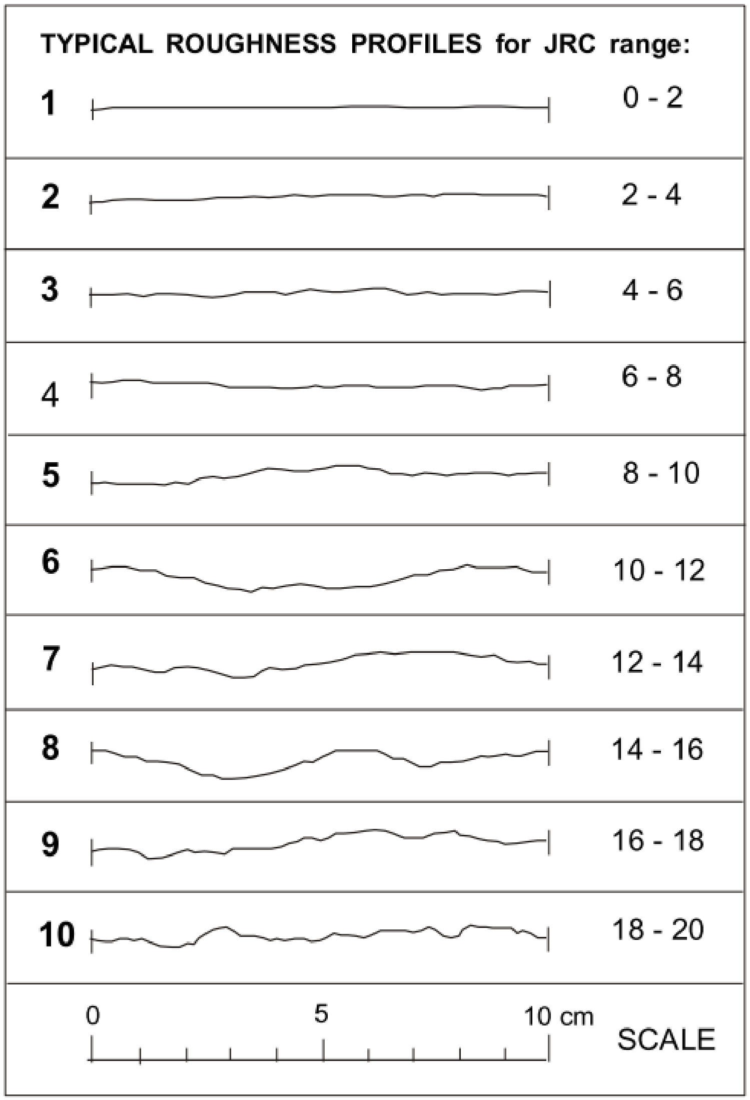

Figure 2.10. Set of predefined profiles of increasing roughness (Barton & Choubey, 1977).

Although the measure of the profile could be precise, this method still requires a subjective comparison to be made by the specialist. While the method is still widely used and recommended**,** it has been recognizing as unreliable due to large differences between the estimated JRC by different rock mechanics experts (Maerz, 1990; Tatone & Grasselli, 2010).A survey was carried by Beer (2002) to measure the existant deviation in the estimation of the JRC, by different professionals, of a profile. It was found that profiles that don't display any resemblance to Barton's predefined profiles, as the one shown in Figure 2.11, lack any accuracy in the JRC obtained by visual estimation,  With the estimated JRC varying from 6 to 20, in this case.

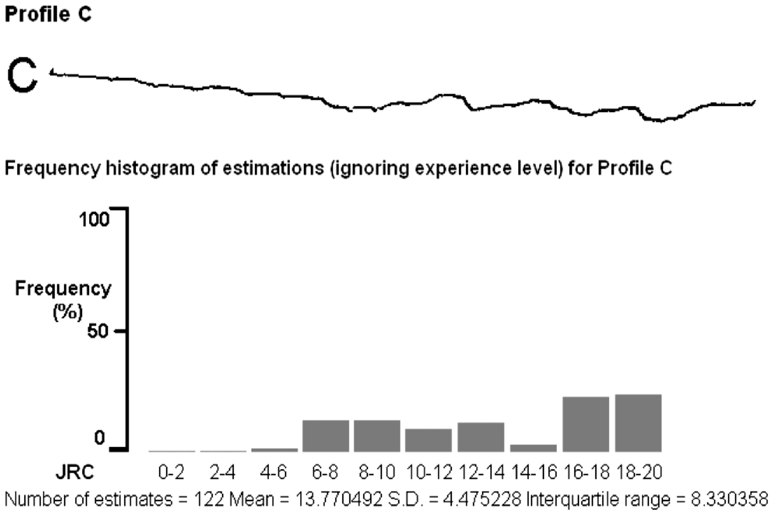

Figure 2.11. The frequency of JRC estimation for profile C (Modified from Beer et al., 2002).

The most relevant statistical and fractal methods used for rock joint roughness characterization are described in Appendix B.

### 2.4.2 Sampling Interval and Scale Effects on Surface Roughness Characterization

A sampling window is defined as the geometrical area used to characterize the topography of the analyzed joint surface; sampling windows of varying sizes are displayed in Figure 2.12. Sampling window dimensions and sampling interval have been identified as important sources of result differences in surface topography characterization, with sampling interval being the key parameter (Fardin, 2008; Kulatilake, 1995). In the study made by Tatone & Grasselli (2013) the estimated roughness of joints of tensile failure origin, using the maximum apparent dip angle (section 0), varied by up to 88 % over the range of measurement resolutions considered (0.44 – 1 mm), with higher roughness obtained for the smaller sampling interval, this implies that variation of the sampling interval across various windows size would induce an underestimation of the surface roughness for larger sampling intervals (usually associated with bigger sampling window lengths),a common error found in literature (Tatone & Grasselli, 2013). Based on these results, it is expected that models calibrated using the same profiles and techniques, but different sampling intervals will give different calibration results.

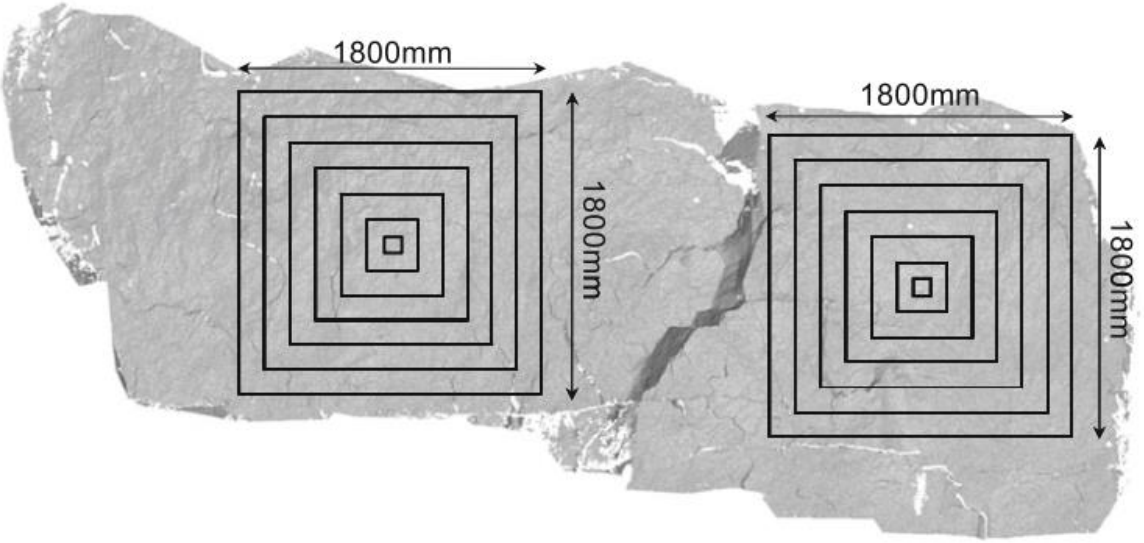

Figure 2.12. The square window of varying size (Tatone & Grasselli, 2013).

Jang et al. (2014) studied the correlation between different statistical parameters used to characterize the roughness of a profile and the JRC. They digitized Barton's profiles and calculated the value of the statistical parameters of interest for each profile, using various sampling intervals [0.1 – 0.5 – 1 – 2 mm]. From their results, they derived power law relationships ($\mathrm{JRC} = \mathrm{a} * \mathrm{P}^{\mathrm{b}} + \mathrm{c}$) between the JRC and the most used parameters to characterize roughness in the literature ($\mathrm{Z}_2, SF, \frac{\theta_{\max}}{C+1}$,D) for each sampling interval, and compared their results to the JRC back-calculated by Barton and Choubey (1977) of the profiles and other relationships derived by several authors (Figure 2.13). The most important results of the study are:

- There is good agreement between the derived relationships and the JRC value of the profiles (all fall in the ± 5% error range, except in the case of the Barton profile n° 4, JRC 6-8)
- The Roughness Parameters are not independent of the sampling interval. Different sampling intervals give different coefficients for the adopted power law relationship used.
- The relationships between the JRC and Statistical Parameters derived by Maerz (1990) and Tse and Cruden (1979) don't correlate well with the true JRC values. Sampling errors are the probable reason.

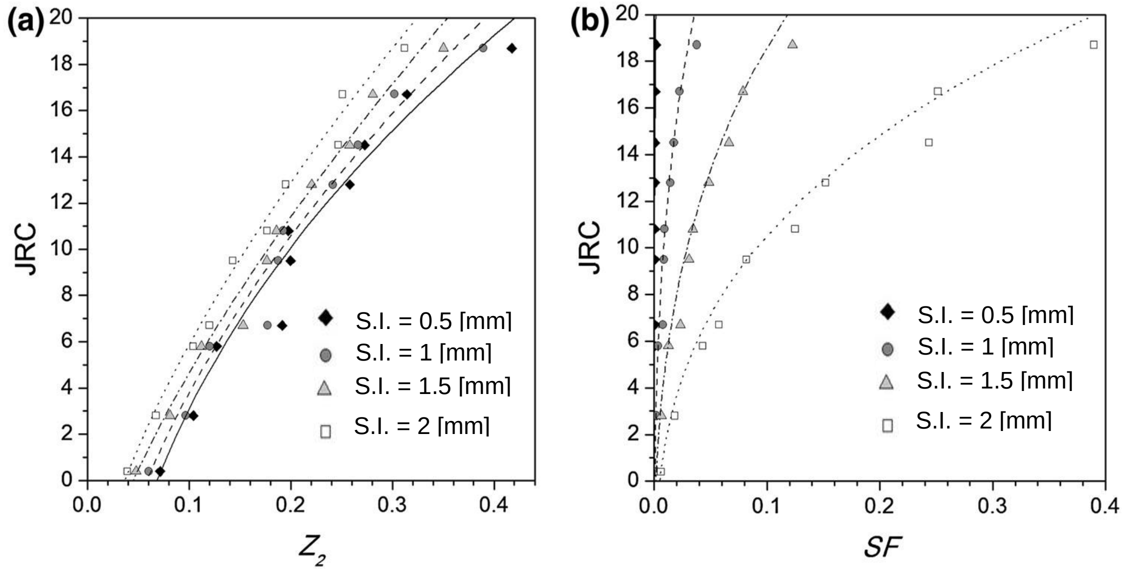

Figure 2.13. (a) Correlation between the JRC and the Z2 parameter, (b) Correlation between the JRC and the SF parameter (Jang et al., 2014).

## 2.5 Rock Joints Shear Strength Models

Failure of discontinuities in the brittle material is usually of shear failure origin, as tensile and torsion strength are negligible, and compression is controlled by the rock intact properties. All rock masses contain discontinuities such as bedding planes, joints, shear zones, and faults. At shallow depth, where stresses are low, failure of the intact rock material is minimal and the behavior of the rock mass is controlled by sliding on the discontinuities (Hoek, 2006). The main shear strength models used for rock joints are described below.

### 2.5.1 Mohr-Coulomb model

The Mohr-Coulomb model is based on Coulomb's fracture failure formulation and Mohr's maximum shear stress model (Figure 2.14), which assumes the limiting shear stress in a plane to be a function of the normal stress in the same section at an element point.

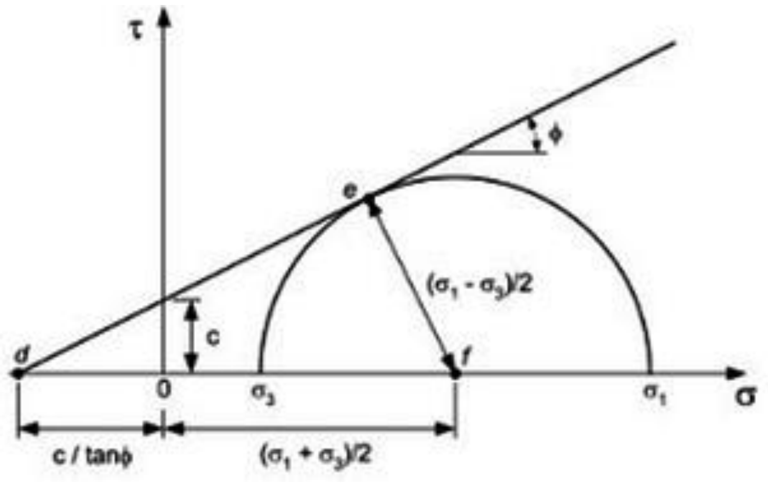

Figure 2.14. Mohr-Coulomb shear strength criterion (Sorensen, 2012)

In the case of discontinuities, as indicated in section 2.1, the shear strength of joints is estimated using direct shear tests, under constant normal load or normal stiffness conditions. If a cemented planar joint ($\sigma_t \neq 0$) is sheared under normal load and controlled displacement conditions as described in section 2.1.3, the shear stress will increase until the peak shear strength is achieved, then it will decrease asymptotically to the residual shear strength (Figure 2.5) Both values of shear strength may be plotted against the applied normal stress. if this process is repeated for the same joint under varying normal stress, the peak shear strength as a function of normal stress is characterized by the Mohr-Coulomb model, which is defined by the equation (Hoek, 2006):

$$\tau_p = c + \sigma_v \tan\phi \tag{2.2}$$

Where, $\tau_p$ is the shear strength of the joint, $\sigma_v$ the normal stress to the joint, $\phi$ is the angle of friction and $c$ is the cohesive strength of the surface. Is important to note that the residual strength characterizes the pure frictional component of the joint shear strength, which means that the cohesive component decreases progressively until it completely disappears, under high shear displacements.

### 2.5.2 Patton model

Although the Mohr-Coulomb model was developed for a perfectly smooth plane of failure, its use in engineering practices has been extended to rough surfaces, where an apparent cohesion c is used to characterize the peak shear strength of the joint. While this formulation may be acceptable for joints under high normal stresses, it overestimates the strength of the joint for low stresses, as the criterion fails to model the purely frictional, surface roughness dependent behavior.

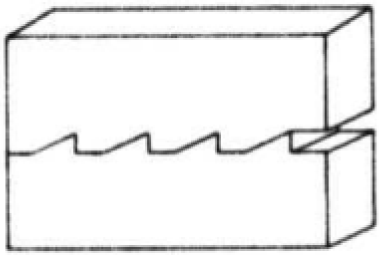

Figure 2.15. Sawtooth specimens used by Patton, the inclination angle of 25° (Modified from Patton, 1966)

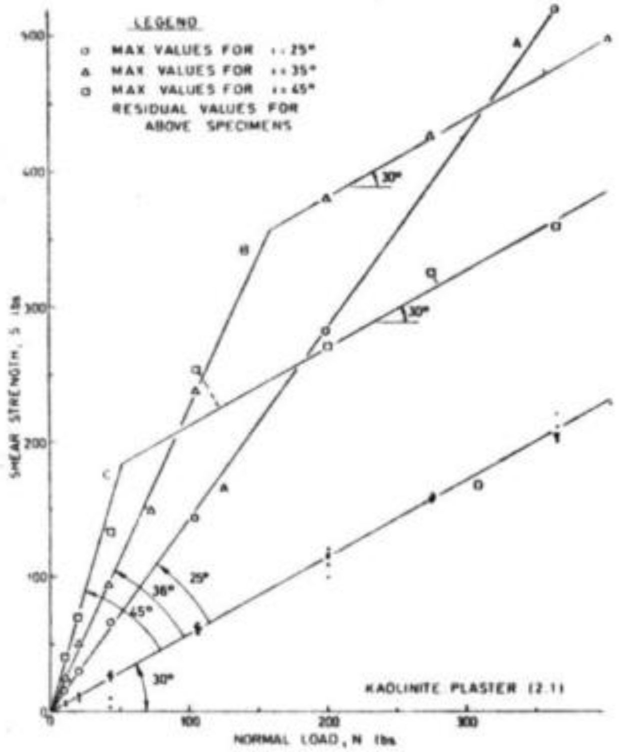

Figure 2.16. Sawtooth shear test results (Patton,1966).

Patton (1966) studied the joints strength dependence on roughness through lab testing of sawtooth-shaped specimens (Figure 2.15.). On his experience, the failure envelopes are curved, with a change in the slope of the curve representing a change in the mode of failure of the joint, as a function of the joint normal stress. Patton's experimental results could be accurately modeled using a bilinear criterion (Figure 2.16), defined by equations:

$$\tau_p = \sigma_v \tan(\phi_\mu + i) \tag{2.3}$$

$$\tau_p = \sigma_v \tan(\phi_r) \tag{2.4}$$

Where $\mathrm{i}$ is the angle of inclination of the sawtooth asperities, $\phi_\mu$ is the angle of frictional resistance of an intact smooth wall and $\phi_r$ is the angle of friction of residual shearing resistance. It is important to note that, while the definition of $\phi_\mu$ and $\phi_r$ are different, $\phi_r$ is used for post-peak shear strength measures at high levels of deformation, in Patton results in the variation between $\phi_\mu$ and $\phi_r$ was negligible, making both terms interchangeable in the equations (2.3) and (2.4). The criterion represents the shift of shear behavior from asperity-controlled shear strength, under low normal stresses, to purely residual strength, govern by the material friction, due to the asperities shearing at higher loads.

### 2.5.3 Barton – Bandis model

While Patton characterization of joint failure envelopes was important as a first approach in describing rock joint shear strength as a pure frictional problem, and not as the sum of a cohesive and a frictional component, as the use of a Mohr-Coulomb model may suggest, a bigger effort was required, as said by Patton (1966): “For some engineering design purposes straight-line failure envelopes are adequate. But to facilitate an understanding of the failure mechanisms, curved failure envelopes reflecting the multiple modes of shear failure appear to be a necessity”.

The Barton – Bandis model (Barton & Bandis, 1990) is one of the most used shear strength criteria in rock mechanics until this day. Its formulation considers the change in the mode of failure by assuming that at low stresses, the shear strength of the joint is controlled by the asperities in the surface of the discontinuity, but, at higher stresses, the asperities are crushed or sheared, due to restraint of the dilation (Astm, 2008) which implies that the asperities influence in the shear strength decreases. The Barton nonlinear criterion is defined as:

$$\tau_p = \sigma_v \tan\left(\phi_b + \mathrm{JRC} * \log_{10}\left(\frac{\mathrm{JCS}}{\sigma_v}\right)\right) \tag{2.5}$$

Where JRC is the Joint Roughness Coefficient and JCS is the Joint Wall Compressive Strength, the first parameter takes into account the roughness of the joint and the second one accounts for the compressive strength of the wall of the discontinuity, is usually related to the uniaxial compressive strength of the rock mass (UCS). This formulation is a straightforward way to consider dilation and its variation at higher loads. The effect on the shear strength of both parameters is seen in Figure 2.17. Clearly, the JRC has a bigger impact on the shear strength. It is important to note that Barton (1973) noted that the ratio of the JCS to normal stress must be between 1 and 100; for higher values, the friction angle should be fixed at 70° (Woo et al., 2010).

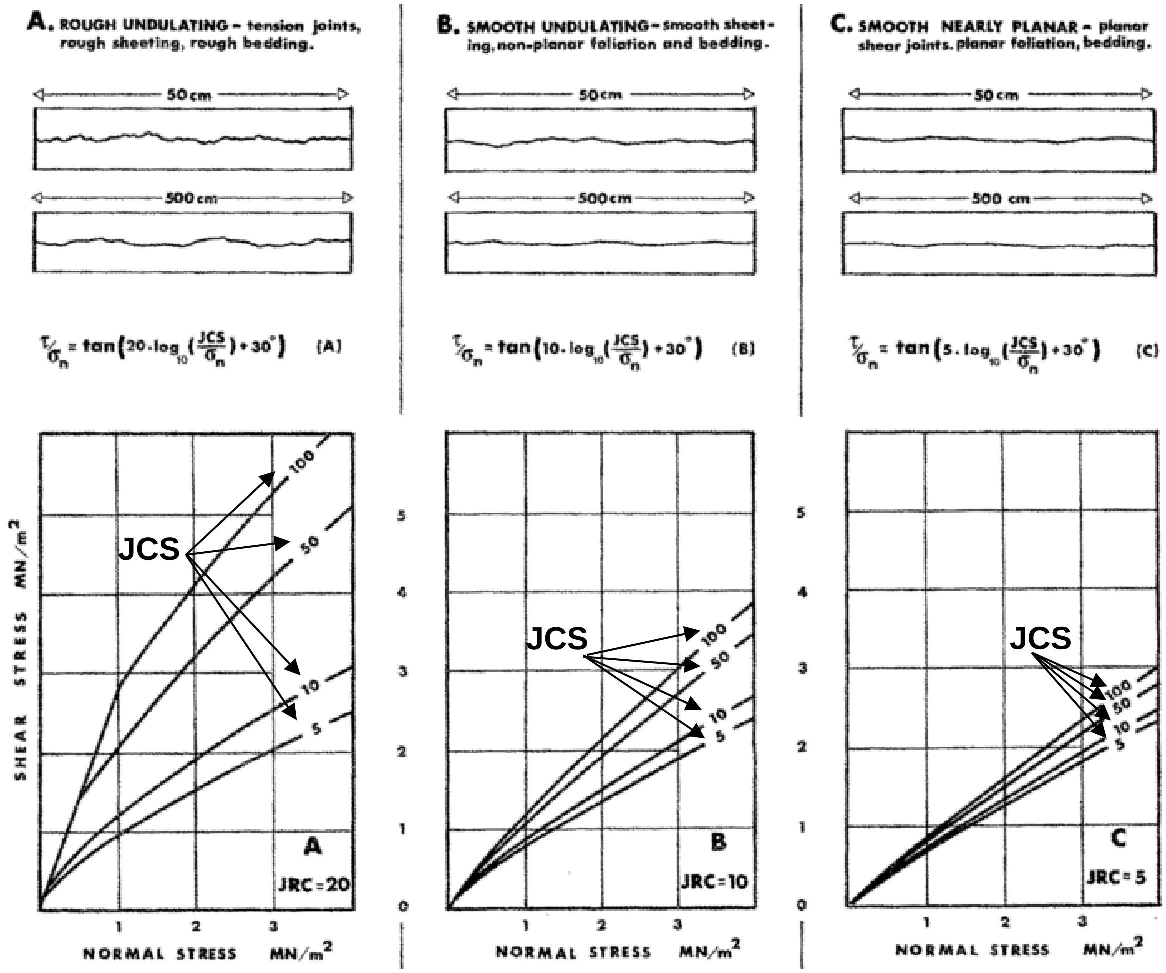

Figure 2.17. JRC and JCS influence in peak shear strength (Modified from Barton & Choubey, 1977).

The Barton – Bandis model was developed empirically through statistical fitting of the results of joints sheared in laboratory conditions. While observations indicated that the JRC was related to the roughness of the joint and the JCS to the intact compressive strength of the rock, only the latter could be directly related to the UCS of the rock, while the former had to be retro calculated, doing direct shear tests of multiple samples taken from the joint of study, in a lab setup (Barton, 1973), using the equation:

$$\mathrm{JRC} = \frac{\left(\mathrm{atan}\left(\frac{\tau_p}{\sigma_v}\right) - \phi_b\right)}{\log_{10}\left(\frac{\mathrm{JCS}}{\sigma_v}\right)} \tag{2.6}$$

A correct sampling of the joints specimens and laboratory test executions deemed to be too hard in practice for rock mass joint characterization, so methods for estimation of these parameters (JRC and JCS) in-situ were introduced, which are described in appendix B.

## JCS In-situ Estimation

An alternative method to estimate the JCS in-situ is using the Schmidt hammer rebound test, considering the correlation between the UCS and Schmidt Hardness (Deere & Miller, 1966), the diagram presented in Figure 2.18 may be used to back-calculate the Uniaxial Compressive Strength of the rock based on the number of Schmidt hammer strikes required to fracture it, the hammer orientation used in the test and the measured unit weight of the rock $\gamma$ [kN/m$^3$]. The diagram is used following the dashed line, starting at the bot and ending at the left.

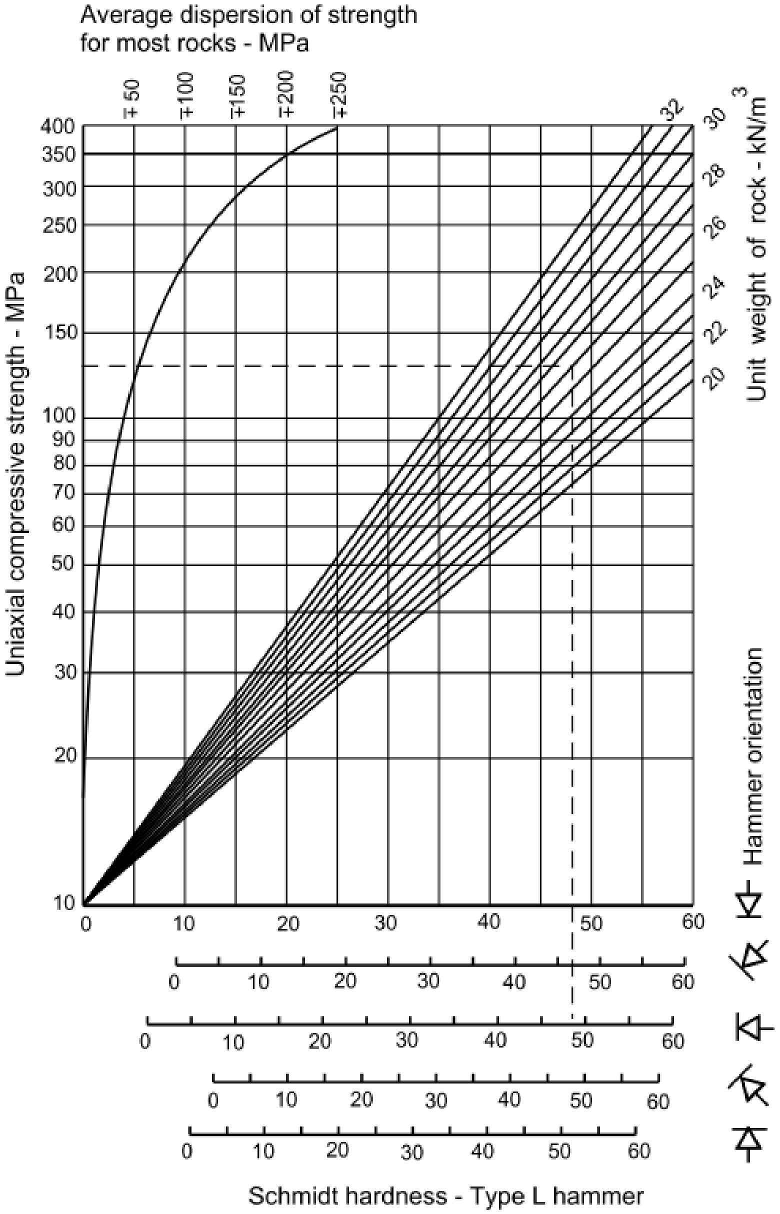

Figure 2.18. Correlation between UCS and Schmidt hardness (Modified from Hoek, 2006)

It is important to note that the thin layers adjacent to joint walls are weathered more severely than the interior of the rock. The joint wall can become weathered gradually by chemical and physical weathering processes, which can lead to poor contact between joint walls (Woo et al., 2010). If this is the case, the UCS of the intact rock is not a good an estimation of the JCS, and then a Schmidt rebound test directly on the walls of the joint is suggested.

### JRC In-situ Estimation

For in-situ estimation of the JRC parameter, Barton & Choubey (1977) suggest the use of the tilt test (Figure 2.19), in which a representative sample of the joint is cut and tested. The test consists of a gradual clockwise rotation of the joint until sliding of the top side is achieved, the angle α of failure is measured, and used to estimate the joint JRC, using the equation:

$$\mathrm{JRC} = \frac{(\alpha - \phi_r)}{\log\left(\frac{\mathrm{JCS}}{\sigma_n}\right)} \tag{2.7}$$

The use of tilt test for joints with JRC values greater than about 10 is generally impossible and an alternative must be used (Barton & Bandis, 1990). A cheaper alternative is the characterization of the joint through profile measurements and characterizations, methods detailed in section 2.2.

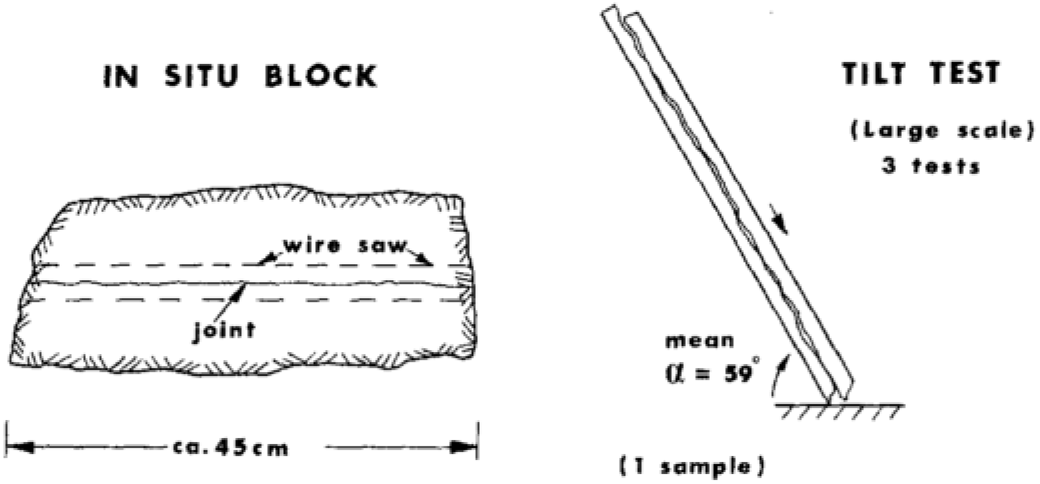

Figure 2.19. Tilt test (Modified from Barton & Choubey, 1977)

### 2.5.4 Other Models

With better surface topography characterization methods developed over time, more complex models have been created. With the key models being already detailed, there is still a vast number of shear strength models to list, developed by several authors. While describing all of them is out of this work scope, there are two models that are important to point out, as they represent the advances in the understanding of the joint shear phenomenon.

### Kulatilake's Model

The shear strength of rock joints is strongly anisotropic, which means that the shear strength of the joint depends on the shear direction (Huang & Doong, 1990). This phenomenon is not captured by a single two-dimensional roughness characterization of the joint, nor a shear strength criterion derived from one. Kulatilake (1995) developed a shear strength criterion based on the fractal characterization of the surface roughness (Appendix B.2.2 – Variogram Method), which was defined by the following equation:

$$\tau_{\mathrm{p}} = \sigma_{\mathrm{v}} \tan\left(\phi_{\mathrm{b}} + \mathrm{a}(\mathrm{SRP})^{\mathrm{c}} * \left(\log_{10}\left(\frac{\sigma_{\mathrm{J}}}{\sigma_{\mathrm{v}}}\right)\right)^{\mathrm{d}} + \mathrm{I}\right) \tag{2.8}$$

The term $\mathrm{a}(\mathrm{SRP})^{\mathrm{c}}$ is defined as the stationary roughness parameter may be represented by the following expressions

$$\mathrm{a}(\mathrm{SRP})^{\mathrm{c}} = \begin{cases} \mathrm{a}Z_2'^{\mathrm{c}} \\ \mathrm{a}K_{\mathrm{d}}^{\mathrm{b}}D^{\mathrm{c}} \\ \mathrm{a}K_{\mathrm{s}}^{\mathrm{b}}D^{\mathrm{c}} \\ \mathrm{a}K_{\mathrm{v}}^{\mathrm{b}}D^{\mathrm{c}} \end{cases} \tag{2.9}$$

Where $\sigma_{\mathrm{J}}$ is a joint compressive strength, $Z_2$ is the derivative of the RMS, I represent the angle of the large-scale undulations, $K_{\mathrm{d}}, K_{\mathrm{s}}, K_{\mathrm{v}}$ are the intercept constant of the log-log plot used to estimate the fractal dimension D (Appendix B.2), obtained through a least squares analysis. a, b, c and d are coefficients calibrated through a regression analysis. $K_{\mathrm{d}}$ corresponds to the constant obtained when the divider method is used (Appendix B.2.1 – Divider Method), $K_{\mathrm{s}}$ is the constant obtained using the power law – spectral method. (references to this method may be found in Brown & Scholz, 1985) and $K_{\mathrm{v}}$ is the constant obtained using the variogram method ( Appendix B.2.2 – Variogram Method).

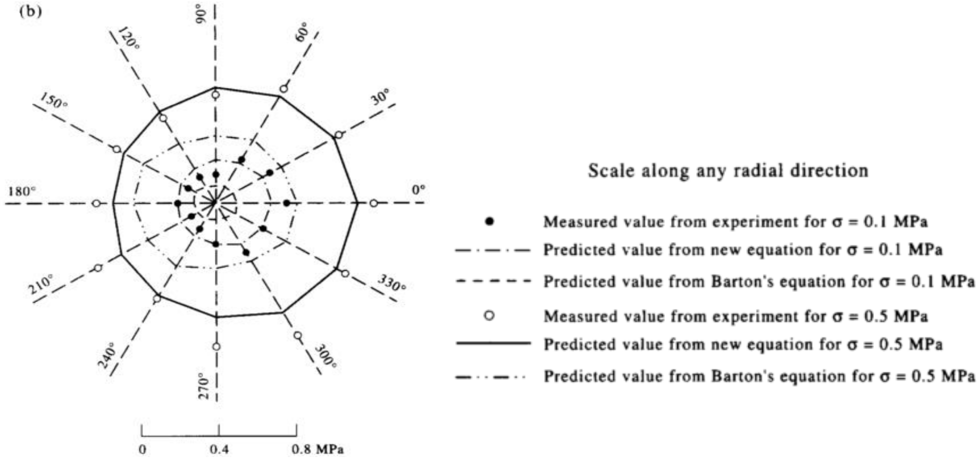

Figure 2.20. Comparison between measured peak shear strength from tests predicted values by Barton's equation and by Kulatilake shear strength criterion (Modified from Kulatilake, 1995).

In Figure 2.20, results of shear tests performed on replicas of the profile, measured from the same rock joint surface, for 12 different radial directions, are presented in a polar form (shear strength increase as the point move away from the origin). It is shown that the Kulatilake's model estimates the shear strength of the rock surface more accurately than Barton's one, which heavily underestimates the shear strength of the profiles for both 0.1 and 0.5 MPa normal stresses and doesn't capture the anisotropic behavior of the surface either.

### Grasselli's Model

While Kulatilake's work is an improvement in terms of characterizing the rock anisotropy, it's still not able to capture the difference in strength in terms of the shear direction. This problem is overcome using the Graselli's model (Grasselli et al., 2002), which is based on the Maximum Apparent Dip angle method (0 - Maximum Apparent Dip Angle). The model shear strength criterion is defined by the equation:

$$\tau_p = \sigma_n \tan(\phi_r^*) \, [1 + e^{-\frac{(\theta_{max}^* \sigma_n)}{9A_0 \, C \, \sigma_t}}] \qquad (2.10)$$

This method considers shear direction because $\theta_{max}^*$, $A_0$ and C depends on the direction selected, as described in section (0).

## 2.6 Scale Effects in Rock Joints Shear Strength

Although the shear strength of rock joints in laboratory conditions is understood, it is still not clear how the shear strength measured at the laboratory should be scaled to in-situ conditions, where the joints tend to be several times bigger than the scale analyzed in a laboratory setup. Originally, it was believed that the shear strength of joints had a negative scale effect, which means that at bigger scales a reduction in the shear strength of the joints existed, compared to laboratory specimens (Bandis, 1980; Barton & Choubey, 1977). Later some researchers questioned this idea, based on laboratory experiment results and theoretical formulations (Leal Gomes, 2003; Papaliangas et al., 1994; Ueng et al., 2010).

### 2.6.1 Bandis Scale Effects Study

Bandis' (1980) investigation constitutes the first comprehensive work about scale effects on rock joint shear strength and dilation, his methodology has set the standard for the following scale effects studies, although the methodology has been questioned (Hencher & Richards, 2015; Papaliangas et al., 1994) and his results are used to this day.

Bandis (1980) studied the effect of scale on rock shear strength by doing direct shear box tests on various sized portions of replicas of joint surfaces. A rubber hot melt molding compound of high resolution was used to take precise impressions of the roughness from a variety of natural joint surfaces in various rock types (Figure 2.21). Joints lengths used were between 36 and 40 cm, and molds were prepared from both sides of the joint. A multicomponent brittle material was used to cast several model replicas of identical interlocking specimens from each pair of molds.

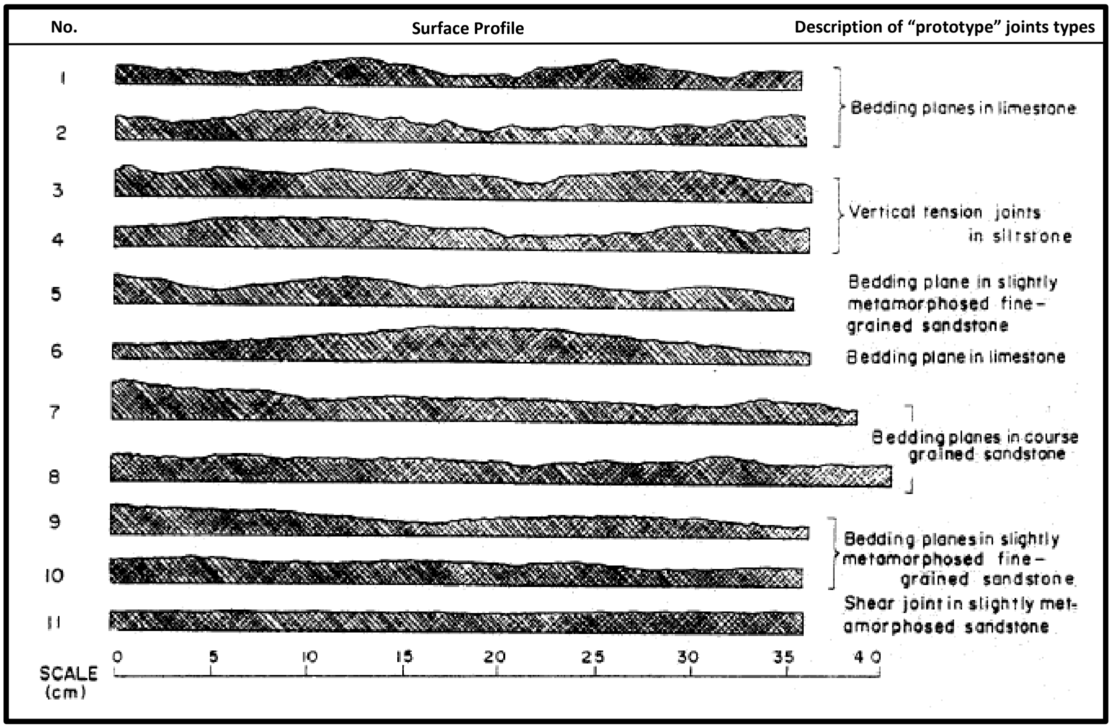

Figure 2.21. Profiles of the joints surface used (Modified from Bandis, 1980).

A total of eleven natural joint samples were selected by Bandis for the scale effect investigation. Surfaces ranged from rough undulating to almost smooth and planar. Replicas of varying size were made for each profile: 5-6 cm,10-12 cm,18-20 cm and 36-40 cm. Using the model theory, each replica had an associated prototype dimension of 1.5-1.8 m, 3.0-3.6 m. 5.4-6.0 m and 10.8-12.0 m, respectively.

Bandis analyzed the scale effect on the following properties:

- Size and distribution of contact areas (as seen in Figure 2.22 a and Figure 2.23 a)
- Peak shear strength and ultimate shear strength (as seen in Figure 2.22 b and Figure 2.23 b)
- JRC and JCS.

The results are summarized in Table 2.1.

Table 2.1. Summary of Bandis (1980) results and conclusions

| Analyzed Property | Increased Block Size leads to: |
|---|---|
| **Effect of scale on peak strength and ultimate shear strength** | Gradual Increase in the peak shear displacement (Figure 2.22a) |
| | The transition from brittle to plastic mode of failure (Figure 2.22b and Figure 2.23b) |
| | Insignificant scale effects in the case of smooth joint types (Figure 2.23b) |
| **Effect of scale on size and distribution of post-test contact areas** | There is a transition from a high number of small contact areas on small samples, to individual, larger, contact areas on larger samples (Figure 2.22a and Figure 2.23a). |
| | This effect is more apparent in rougher joints, in planar joints the scale effect is reduced (Figure 2.22b and Figure 2.23b). |

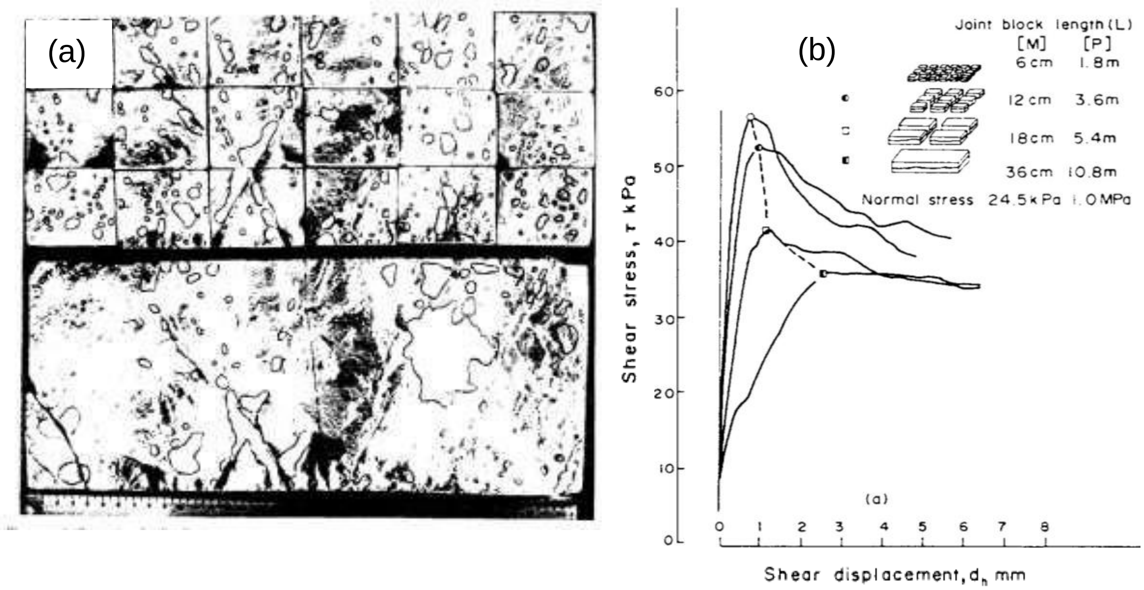

Figure 2.22. (a) Effect of scale on size and distribution of contact areas (b) shear stress v/ shear displacement, for model 1 (rougher joint) (Modified from Bandis, 1980).

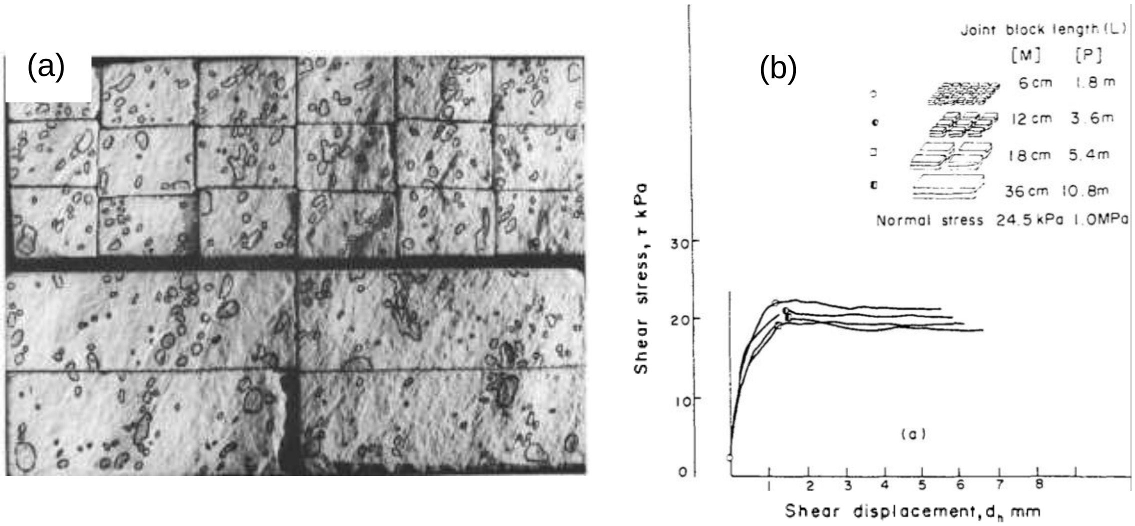

Figure 2.23. a) Effect of scale on size and distribution of contact areas (b) shear stress v/ shear displacement, for model 10 (smoother joint) (Modified from Bandis, 1980).

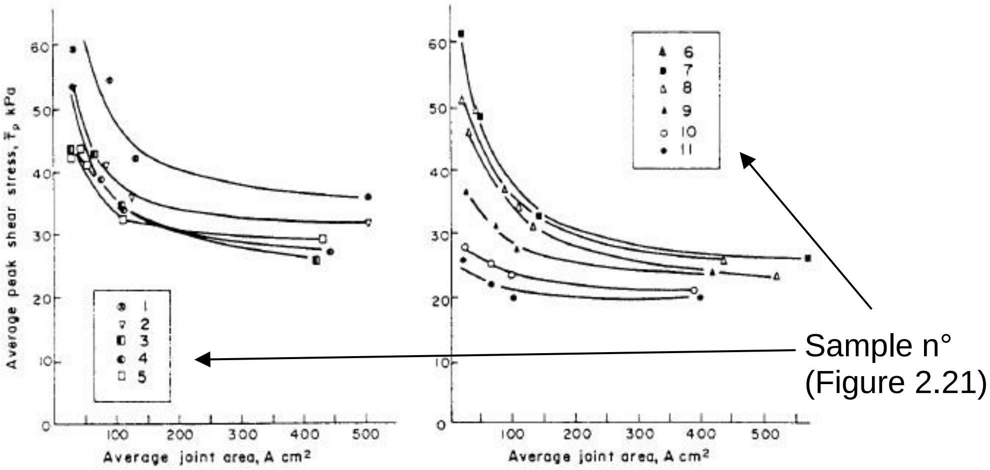

Sample n°
(Figure 2.21)

Figure 2.24. Variation of joint peak shear stress with the joint area (Modified from Bandis, 1980)

Bandis back-calculated the mean JCR-Joint Length relation using the Barton empirical equation for peak shear strength equation (2.6) and the average peak shear strength for each block size (Figure 2.24).Then, the JRC value as a function of the joint length has negative scale effect as seen in Figure 2.25.

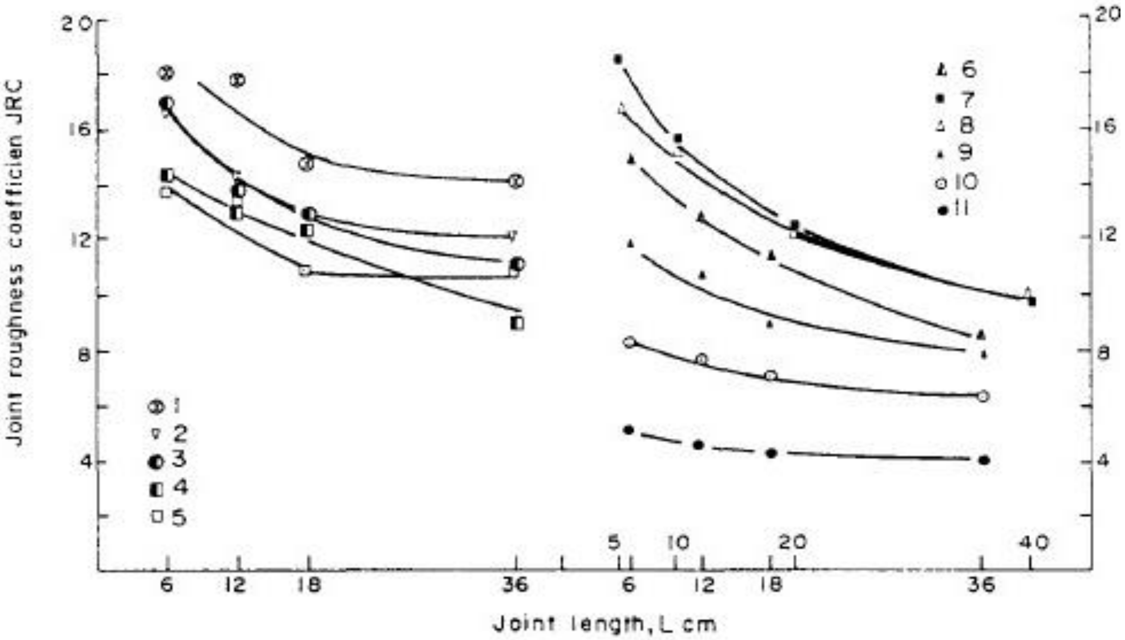

Figure 2.25. Scale effect on the JRC for models of varying roughness (Bandis, 1980).

Later, Barton & Bandis (1982) derived the following expressions for the JRC/JCS variation, using the curve that was the best fit to the results obtained by Bandis:

$$\mathrm{JRC_n} \approx \mathrm{JRC_0}\left(\frac{\mathrm{L_n}}{\mathrm{L_0}}\right)^{-0.03\,\mathrm{JRC_0}} \tag{2.11}$$

$$\mathrm{JCS_n} \approx \mathrm{JCS_0}\left(\frac{\mathrm{L_n}}{\mathrm{L_0}}\right)^{-0.03\,\mathrm{JRC_0}} \tag{2.12}$$

Where, Subscripts (0) and (n) refer to lab scale (100 mm) and in situ block sizes, respectively.

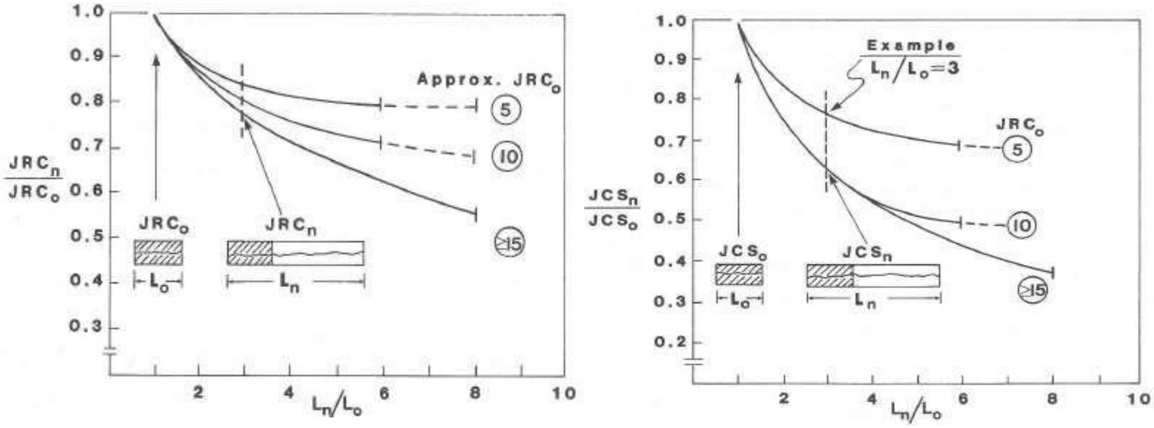

Figure 2.26. Scale effect in JRC and JCS (Barton & Bandis, 1990).

### 2.6.2 Other Studies

Table 2.2 summarizes some of the scale effects studies made by several authors.

Table 2.2. Summary of rock joint scale effects studies found on literature

| Author | Year | Type of Study | Result | Description of the Study |
|---|---|---|---|---|
| **Krsmanovic and Popovic** | 1966 | In-situ and Laboratory Tests | Negative Scale Effect | In situ direct shear tests were performed on limestones and compared to laboratory tests performed on smaller samples. |
| **Barton & Choubey** | 1977 | Laboratory Tests | Negative Scale Effect | Tilt tests were performed on larger granite specimens and smaller ones, obtained by dividing the larger samples. |
| **Leichnitz and Natau** | 1979 | Laboratory Tests | Negative Scale Effect | Shear box tests were performed on large plaster replicas of sandstone specimens, which were compared with test undertook on subdivided specimens. |
| **Yoshinaka et al.** | 1991 | Laboratory Tests | Negative Scale Effect | Shear box tests were performed on specimens of the different surface area, obtained from fresh granite. |
| **Papaliangas & Hencher** | 1994 | Laboratory Tests | No Scale Effect | Bandis experiment was repeated using the same material, molds and shear box tests, but with improved measurement tools. According to the authors, Bandis results were obtained by a faulty methodology. |
| **Fardin et al.** | 2001, 2004, 2008 | Laboratory Tests | 2001 and 2004, Negative Scale Effects. 2008 Positive scale effects | Fardin measured the roughness of rock surfaces using laser scanners (2001) and LIDAR (2004). The objective was to study the differences in the fractal parameters obtained by using different window sizes and zones of the same joint surface. Also, shear tests of the analyzed joints were performed (2008). |
| **Leal & Gomes** | 2003 | Laboratory Tests | Positive Scale Effect | He investigated scale dependency of joint roughness on replicas of porphyritic granite using the pull test, described by Barton & Choubey (1977). |
| **Kveldsvik et al.** | 2007 | Field Tests & Numerical Simulations | Negative Scale Effect | In-situ measurement of roughness was performed on the Åknes rock slope in Norway, for 0.25 m and 1 m length sizes, JRC was estimated using roughness amplitude/ joint length Barton (1981) chart, a negative scale effect was found on the JRCs obtained. Numerical simulations of the rock slide were performed, where through a back analysis it was found that the JRCs obtained from the 1 m samples were closer to the maximal possible JRC that allows the failure of the slope. |

| | | | | |
|---|---|---|---|---|
| **Ueng et al.** | 2010 | Laboratory Tests | No Scale Effect | They investigated the effect of scale on the peak shear strength of artificial enlarged rock joints of standard JRC profiles, a natural joint profile of sandstone and saw-tooth joints using plaster replicas, no apparent scale effect was found. |
| **Oppikofer et al.** | 2001 | Field Measurements & Numerical Simulations | Positive Scale Effect | Joint surfaces geometry in the Åknes rockslide was measured, using laser scanning (TLS and ALS), to study the slope stability through a digital elevation method (DEM). The JRC of the surfaces was estimated separating the surfaces in sets of 10 profiles, using the asperity amplitude method (Barton, 1982). The profiles length varied between 1 and 350 meters. Oppikofer found that the JRC values obtained by their analysis were considerably higher than those gotten from Kveldsvik (2007) measures of smaller profiles (0.25 – 1m). |
| **Tatone & Grasselli** | 2012 | Numerical Simulation | No Scale Effect | Combined FEM/DEM simulations of shear box tests, considering asperity failure, were performed on a profile of known roughness and subdivided copies of the same profile. |
| **Bahaaddini et al.** | 2014 | Numerical Simulation | Negative Scale Effect | Numerical Simulations of shear box tests, considering asperity failure, were performed using PFC (DEM) on a profile of known roughness and subdivided copies of the same profile. |
| **Johansson** | 2016 | Laboratory Tests | Scale Effect Depends on the Degree of Matedness | Shear box tests were performed on rock joints of varying scale and horizontal displacement, to study the effect of matedness on shear strength, for varying scales. |

# 3 Numerical Simulation of Direct Shear Tests

Although performing laboratory tests for the study would be desirable, numerical simulations were selected for the research, because ,provided that the geometry of the discontinuities is known, it is possible to perform numerical direct shear tests of a large number of discontinuities, at a wide range of scales, in an automated way, as an alternative to physical testing, which would be a much more time consuming, expensive, and difficult (Tatone & Grasselli, 2012).
A variety of numerical simulations methods have been used to model rock joints in previous works, in mining and civil engineering, where 4 methods stand out:

- Finite Differences Method (FDM).
- Finite Elements Method (FEM).
- Discrete Element Method (DEM).
- Finite/Discrete Element Method (FEM/DEM)

In the last years, the rock joint modelling has been mainly made in Discrete Element Method and Finite/Discrete Element Method, due to the possibility to model the brittle behavior of rocks in an accurate way (Bahaaddini et al., 2014, 2013; Mahabadi et al., 2012; Tatone & Grasselli, 2012), but these methods have two big disadvantages, the learning curve is quite steep to use them properly and the processing power required to do the simulations in a relatively brief time, is not yet available. On the contrary, Finite Elements Method has difficulties modeling brittle behavior and discontinuities in general (Selvadurai & Yu, 2005), but the computing time is quite low in contrast with the discrete based models. Details of the DEM and FEM/DEM applications may be found on the works of (Bahaaddini, 2016; Bahaaddini et al., 2014, 2013; Giacomini et al., 2008; Mahabadi et al., 2012; Tatone & Grasselli, 2012). Although less popular, where FEM is used in some studies as a base for the simulation of shear tests rock joints (Giacomini et al., 2008; Selvadurai & Yu, 2005)

With the conditions described above, FEM was chosen as the base method for the simulation, Abaqus® was used for this work because of the extensive bibliography and support available and the possibility to be used in conjunction with other software, which is required for the automation of the simulations process. Finite elements theory is the base of the method, but it won’t be described here, as the formulation is extensive and widely available elsewhere.

## 3.1 Model Setup

The direct shear test conditions had been described in section 2.1, which are the one that is tried to be replicated. Tatone’s (2012) and Bahaaddini’s (2013) work (Figure 3.1a and Figure 3.1b respectively) were chosen as a guideline for the model setup, to replicate a direct shear test in a computer simulation. Although, the shear of a rough surface is a three-dimensional problem, all of the shear test simulations models used in this work will be two dimensional, under a plane strain condition, as this facilitates automatization and follows the line of most of the literature found.

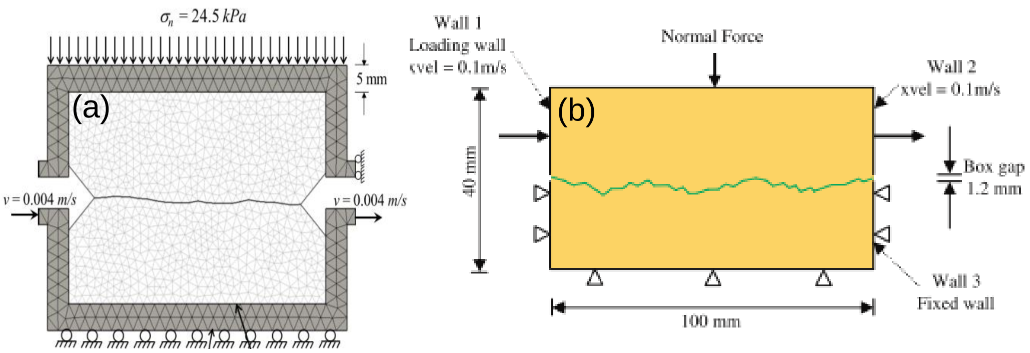

Figure 3.1. (a) Shear box model developed by Tatone & Grasselli (2012) and (b) Bahaaddini et al. (2014).

For the following sections, Barton profiles are used in the numerical simulations calibrations, using the number included in Figure 2.10 to refer them when it is necessary.

### 3.1.1 System of Units

Abaqus has no units built into it except for rotation and angle measures. Therefore, the units chosen must be self-consistent, which means that derived units of the chosen system can be expressed in terms of the fundamental units without conversion factors (Dassault Systèmes Simulia Corp., 2013a). The selected system units correspond to the millimeter version of the international system of units one (Column n° 2 in Table 3.1).

Table 3.1. The available self-consistent system of units

| **Quantity** | **SI** | **SI (mm)** | **US UNIT (ft)** | **US UNIT (inch)** |
|---|---|---|---|---|
| Length | m | mm | ft | in |
| Force | N | N | lbf | lbf |
| Mass | kg | tonne ($10^3$ kg) | slug | lbf $s^2$/in |
| Time | s | s | slug | s |
| Stress | Pa (N/$m^2$) | MPa (N/$mm^2$) | lbf/$ft^2$ | psi (lbf/$in^2$) |
| Energy | J | mJ ($10^3$ J) | ft lbf | in lbf |

### 3.1.2 Mesh element properties

To select the mesh element properties appropriately, the following point must be kept in mind:

- The family of the element and it uses.
- Number of nodes and order of interpolation.
- Compatibility with meshing software.

The solid (or continuum) elements in Abaqus can be used for linear analysis and for complex nonlinear analyses involving contact, plasticity, and large deformation (Dassault Systèmes Simulia Corp., 2013a). To achieve the objectives of this work, an automatic meshing generator software is needed. Triangular elements are easily generated by these kinds of software and should be used if they satisfy the model needs.

Second order of interpolation is preferred (6 node elements instead of 3), as it provides higher accuracy and avoids classical linear element problems with stress analysis problems: over stiff elements and slow convergence with mesh refinement. Abaqus offers a modified 6-node element that's recommended for contact problems that involve a hard contact formulation, because they provide uniform contact pressures in situations with the default "hard" contact relationship, exhibit minimal shear and volumetric locking (details of these phenomena may be found in the Abaqus Analysis manual, 2013a), and are robust during finite deformation (Dassault Systèmes Simulia Corp., 2013a). Finally, the mesh elements used in this study are "plane strain 6-node modified (CPE6M)" elements (Figure 3.2).

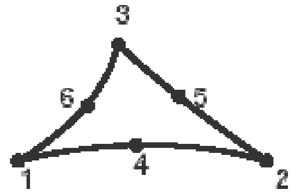

Figure 3.2. 6-node modified element (Dassault Systèmes Simulia Corp., 2013a).

### 3.1.3 Boundary conditions

The general boundary conditions for the models, for displacement-controlled and load controlled models, are summarized below.

**Displacement-Controlled Model**

The model has the following boundary conditions (Figure 3.3):

1. Rolling support on the base to avoid vertical translation of the base
2. Pinned support in the sides of the top side box, to avoid lateral translation.
3. Uniform vertical stress on the top of the box surface $\sigma_v$.
4. Uniform lateral velocity imposed in the nodes on the sides of the bottom of the box $v_x$.

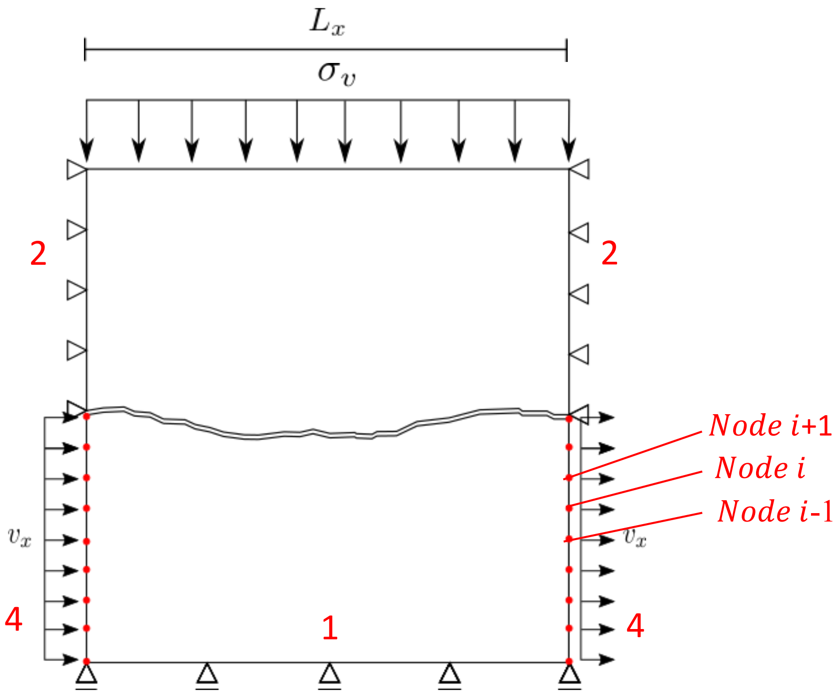

Figure 3.3. Displacement-controlled model boundary conditions.

The horizontal reaction force and horizontal displacement were measured in the external nodes of the bottom of the box, for each increment, the vertical dilation of the joint was measured in each node of the lateral faces of the top side of the box (Figure 3.3)
. The shear strength was calculated as:

$$\tau_s = \sum_{i=1}^{n} \frac{RF_i}{L_x} \tag{3.1}$$

Where $\tau_s$ is the shear strength of the joint in each increment, $RF_i$ is the force in the Node i. $L_x$ the length of the profile and n the total number of nodes. Then, the peak shear stress $\tau_p$ is calculated as:

$$\tau_p = MAX\,(\,\tau_s) \tag{3.2}$$

The secant dilation angle $d_s$ was calculated as:

$$d_s = \operatorname{atan}\left(\frac{\delta_v}{\delta_h}\right) \tag{3.3}$$

Where $\delta_v$ is the vertical displacement of the top side of the box and $\delta_h$ is the horizontal displacement.

As described in section 2.1, to characterize a joint the test simulations were performed for a set of at least 4 different normal stresses.

**Load-Controlled Model**

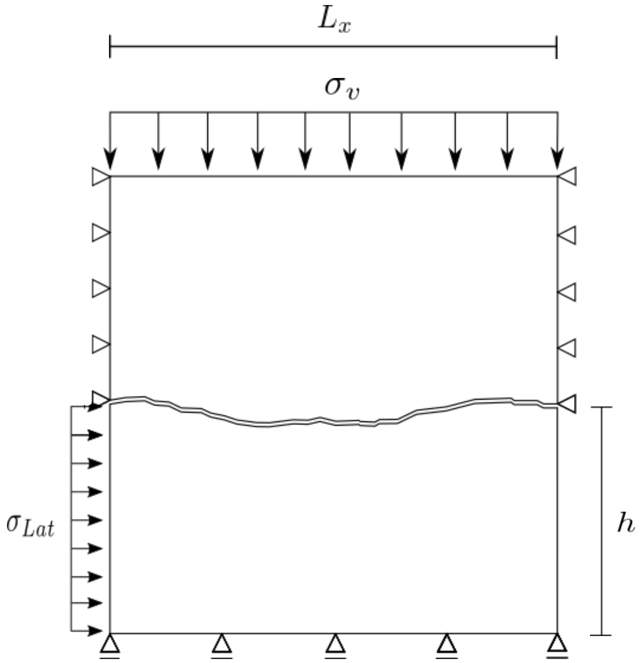

Figure 3.4. Load-controlled model boundary conditions.

In the load-controlled tests, boundary conditions 1,2 and 3 of the displacement-controlled model are keep the same, the only difference is condition n° 4, where the uniform lateral velocity applied at both sides is changed for a uniform unilateral stress applied on the left side of the model as seen in Figure 3.4. The effective shear stress on the joint is calculated using equation:

$$\tau_s = \frac{\sigma_{Lat}}{L_x} * h \tag{3.4}$$

Where h is the height of the bottom side of the box. Since there is no way stop the test once the joint reach its peak shear strength, the measured shear stress increases continuously. To determine the peak shear stress of the joint a displacement related criterion must be used. Based on literature and the results obtained on the displacement-controlled tests simulations, peak shear strength usually is completely mobilized at around 2 mm of shear displacement, for a ~100 mm specimen. Although the results are consistent, it is still only a reference, and values will be obtained graphically.

It is important to note that, most direct shear test simulation models (Bahaaddini et al., 2014; Tatone & Grasselli, 2012) use a 1-1.5 mm wide gap between the upper and lower joint surfaces, to better represent the direct shear tests performed on a laboratory (as described in section 2.1), this gap was included initially on the model, but was later discarded due to issues with automatization  of the shear box generation process, No difference in the results between models with and without the gap were found.

## 3.2 Constitutive Law and Material Properties

Hawkesbury Sandstone, properties were used as input for the model, because the material is well described and mechanically characterized (Pells, 2004; Roshan et al., 2017; Sharrock & Akram, 2009; Standard, 1964) and has been successfully used for joint direct shear tests numerical modelling (Bahaaddini et al., 2014, 2013; Sharrock & Akram, 2009).

The selected material constitutive model for the simulations is a Mohr-Coulomb plasticity model, which requires elastic properties, the Young's Modulus E and Poisson's ratio $\nu$, and plasticity properties cohesion c, friction angle $\phi$ and dilation angle $\psi$. Cohesion degradation with plastic strain was not considered as there is not experimental data to calibrate the values

A plastic constitutive model will not represent the brittle like the behavior of rock under low confining stresses, nor how this impact the joint behavior (asperities degradation). Although Abaqus, as a FEM based software, has difficulties with brittle behavior modeling, it offers options to consider cracking and fracture of the elements, such as:

- xFEM (Enriched Finite elements model formulation)
- Deletion of elements that fail under tension and/or shear conditions.
- Cracking model for concrete.

All of these methods increase the computation time drastically, require several more parameters to calibrate, and have difficulties with the contact interaction used. However, a more accurate representation of the reality is not guaranteed using these models, as may be seen in the results obtained by Giacomini (2008), where element deletion was used to consider the degradation of the asperities. When observing Figure 3.5, the result does not reflect the real behavior (the only contact in the joint is the pile of remaining elements).

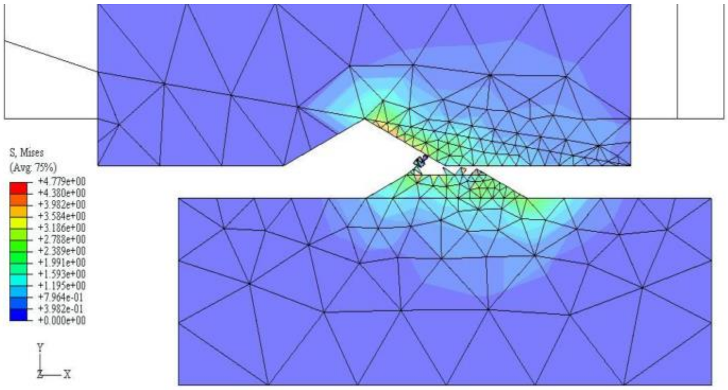

Figure 3.5. Shear test simulation of a single asperity using element deletion to consider degradation (Giacomini et al., 2008).

The material properties values used (Table 3.2) correspond to the mean values obtained experimentally by Sharrock & Akram (2009). Using Barton-Bandis criterion, the input parameters are the JRC, friction angle of a planar joint $\phi_b$ and the JCS, which is considered as the Uniaxial Compressive Strength (UCS) in a fresh rock. Because the UCS is not an input in the M-C plasticity model, a band of the Barton-Bandis shear strength criterion, given by equation (2.5), predicted results are considered, which will be made using the mean ± the standard deviation of the UCS value. The dilation angle was assigned after a sensitivity analysis, included in section 3.6.

Table 3.2. Material Properties (Sharrock & Akram, 2009)

| **Material Properties** | |
|---|---|
| UCS [MPa] | 27.4 ± 9.8 |
| c [MPa] | 4.9 |
| $\phi$ [°] | 50.7 |
| E [GPa] | 4.2 |
| $\nu$ [-] | 0.2 |

## 3.3 Joint Contact Model

### 3.3.1 Contact Definition

Contact is the physical interaction between bodies. In terms of the simulation of rock joints shear test, contact can be divided into two parts:

- Contact pressure, which resists penetration.
- Frictional stress, which resists sliding.

## Contact Pressure and Overclosure

The adopted contact formulation in this work is the “Hard Contact”, which considers the transfer of compressive stresses between two surfaces, only when the surfaces are in contact, which is modeled as:

$$\begin{gathered} \mathrm{p} = 0 \text{ for } \mathrm{o_c} < 0 \\ \mathrm{o_c} = 0 \text{ for } \mathrm{p} > 0 \end{gathered} \tag{3.5}$$

Where p is the pressure at a detection point i in the contact surface and $\mathrm{o_c}$ is the overclosure or clearance of the surface at the same point (interpenetration of the surfaces), as seen in Figure 3.6. Theoretically, the contact constraint is enforced with a Lagrange multiplier representing the contact pressure in a mixed formulation. The virtual work contribution is (Dassault Systèmes Simulia Corp., 2013b):

$$\delta\Pi = \delta \mathrm{p} \mathrm{o_c} + \mathrm{p} \delta \mathrm{o_c} \tag{3.6}$$

And the linearized form of the contribution is:

$$\mathrm{d}\delta\Pi = \delta \mathrm{p} \mathrm{d} \mathrm{o_c} + \mathrm{d}\mathrm{p} \delta \mathrm{o_c} \tag{3.7}$$

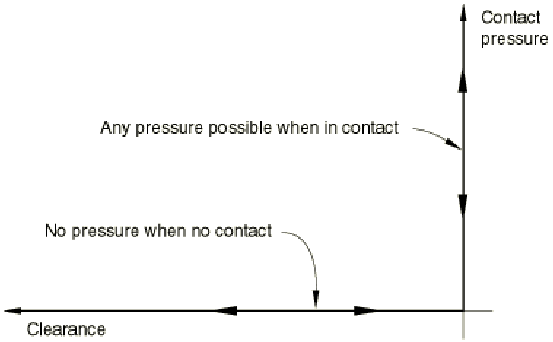

Figure 3.6. Overclosure relationship (Dassault Systèmes Simulia Corp., 2013a).

In practice, the contact constraint must be enforced with a mathematical formulation. The two basics one in FEM packages are:

- Penalty Method
- Augmented Lagrange

The penalty method is a simple method that considers the introduction of a force in the contact detection points, where there is a penetration in the surface, given by:

$$\mathrm{F_c} = \mathrm{k_c} \mathrm{D_p} \tag{3.8}$$

Where $\mathrm{F_c}$ is the force introduced, $\mathrm{D_p}$ is the interpenetration of the surfaces and $\mathrm{k_c}$ the contact normal stiffness. If there is no penetration, the force is null.

For a constant $\mathrm{k_c}$, a higher penetration of the surfaces equals a bigger force required to bounce it back. The issues with this method are:

- Neither the penetration nor the force required to bounce the penetrating surface back is known beforehand.
- Arbitrarily big forces can't be used to avoid excessive penetration, as the surface may be sent flying away.
- A higher assigned $\mathrm{k_c}$ would result in smaller overall penetration on the surfaces but will incur in higher computation times.

With the first two points in mind, a degree of penetration between the surfaces will always exist, generally, the penetration incurred in the models using the penalty formulation doesn't affect the results, only in special cases like the displacement-controlled test with coarse meshes (Dassault Systèmes Simulia Corp., 2013a). This topic will be discussed in more detail in section 3.6.

The Augmented Lagrange method is based on the penalty method but includes an internally calculated extra term I in the force estimation, that is used to decrease surface penetration. In this method, the force is given by:

$$\mathrm{F_c = k_c D_p + I} \tag{3.9}$$

The iterative process followed in this method is:

1. Perform step calculation using penalty method.
2. Compute factor I
3. Compare the obtained penetration with the accepted penetration range.
4. If the obtained penetration is within the range of the accepted values, proceed to the next step, if not then perform points 2-4 again.

Although this method ensures that there is going to be less penetration of the surfaces, when compared to a model that uses the penalty stiffness method, it increases computation time and may induce a lack in convergence. For this work a penalty method was deemed enough to perform the simulations, a topic discussed further in section 3.6.

### Shear Stress

Peak shear stress $\tau_{\mathrm{peak}}$ on surfaces in contact is estimated using basic Coulomb friction relationship for non-cohesive surfaces:

$$\tau_{\mathrm{peak}} = \sigma * \mu \tag{3.10}$$

Where $\sigma$ is the stress normal to surface and $\mu$ its friction coefficient. To compute the mobilized stress in the model, a penalty method is used in this work, as in most cases (Dassault Systèmes Simulia Corp., 2013a). The frictional stress $\tau$ is given by:

$$\tau = \mathrm{k_s} * \gamma \tag{3.11}$$

Where $\mathrm{k_s}$ is the contact frictional stiffness and $\gamma$ is the elastic slip of the interacting surfaces. It is important to note that there is some slip, as seen in Figure 3.7, before the whole shear strength is mobilized, contrary to the idea of Coulomb's model, where perfectly planar surfaces in contact, under a constant normal load, will stick together until the friction resistance is overcome.

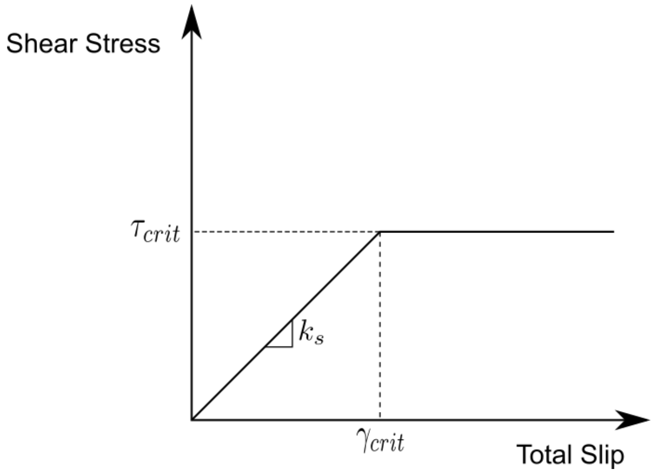

Figure 3.7. Shear Stress / Slip Relationship.

The penalty friction model is then governed by at least 2 parameters $\mu$ and the critical elastic slip $\gamma_{\mathrm{crit}}$ or $\mu$ and $\mathrm{k_s}$, with the normal load $\sigma$ as va ariable. Although $\gamma_{\mathrm{crit}}$ or $\mathrm{k_s}$ should only influence the total slip accumulated before the surface slide on the shear strength, as noted by Selvadurai et al. (2005), as seen in Figure 3.8.

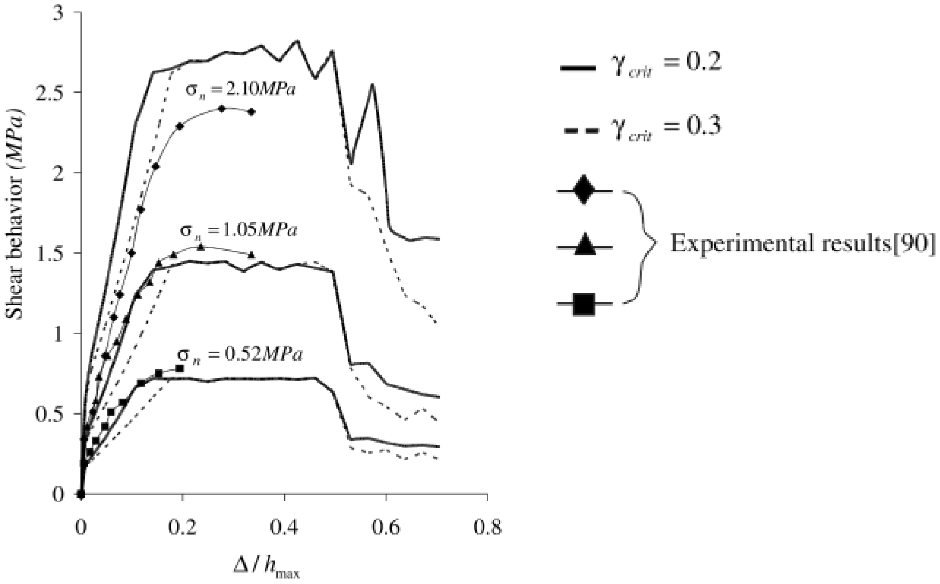

Figure 3.8. Shear stress v/s shear displacement (normalized by max. asperity height) for several $\gamma_{\text{crit}}$ (Selvadurai & Yu, 2005).

In this work, it was found that the $\gamma_{\text{crit}}$ and $k_s$ may have an incidence on the peak shear strength, if their value gets large enough (the peak shear strength is not mobilized), this topic will be further discussed in section 3.6.

### 3.3.2 Contact Model

To build a contact model, a contact surface discretization method must be used and its corresponding sliding algorithm has to be assigned (King & Richards, 2013). Currently, the two most used methods to assign the contact interaction are the node to surface and surface to the surface method. In both methods, a master and a slave surface must be assigned, with methods differing in how the slave surface behave. The node to surface method discretize the slave surface as a conjunct of nodes, with each single slave node on one side of a contact interface interacting with a point of projection on the "master" surface on the opposite side of the contact (Figure 3.9), the interaction of the surfaces occurs in each pair of nodes in contact. The surface to surface formulation enforces contact conditions in an average sense over regions nearby slave nodes, rather than only at individual slave nodes, thus the interaction will occur in each pair of nodes in contact but considering adjacent slaves nodes.

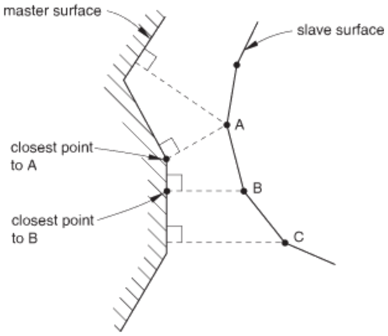

Figure 3.9. Node to Surface contact discretization (Dassault Systèmes Simulia Corp., 2013a).

Since in the case of node to surface, the interaction between surfaces only occurs in the slave nodes, penetration of master nodes with no slave nodes nearby is likely (Figure 3.10a). Surface to surface was developed as an overall improved method over the node to surface one, as there is less penetration in the interface due to the averaging of contact conditions (Figure 3.10b), the deformation of the surfaces is more realistic and the convergence of the simulation is more likely (King & Richards, 2013).

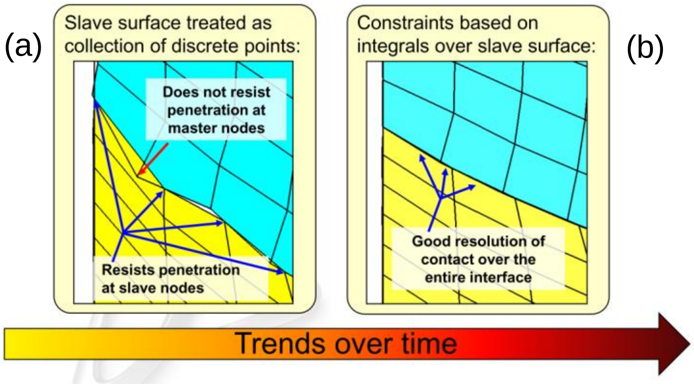

Figure 3.10. (a) Node to the surface and (b) Surface to surface discretization methods (King & Richards, 2013).

In this work, only the joint surfaces interact, with the master surface being the one in the top side of the model and the slave surface the one in the bottom.

For the sliding formulation, a finite sliding algorithm was assigned for the contact formulation, an overall better algorithm in almost every way over the small sliding formulation, detail of both formulations may be found on Abaqus Analysis User Manual (Dassault Systèmes Simulia Corp., 2013a). For both the overclosure constraint and the frictional model, a penalty method was employed, described in section 3.3.1. The properties values assigned on the interface will be resumed in section 3.8.2.

### 3.3.3 Model Steps

To perform the numerical simulation of the shear test, 2 steps were included in the model, in the first, the vertical stress is applied slowly on the top surface of the box (Figure 3.11a) until the desired stress is reached. In step 2, for the displacement-controlled test, a constant velocity is applied on both sides of the bottom half of the box (Figure 3.11b). In the load-controlled test, a homogenous lateral stress is applied on the left side, which is increase slowly with simulation time until the desired amplitude is reached (Figure 3.11c)

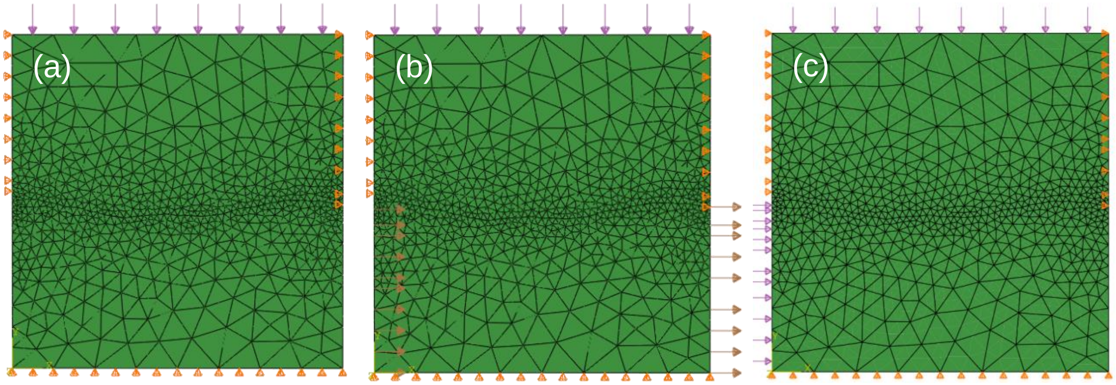

Figure 3.11. (a) Vertical stress applied on the top half of the box (b) Lateral velocity applied on both sides of the bottom half of the box (c) Lateral stress applied on the left side of the bottom half of the box.

## 3.4 Automatization of the Simulation Process

Due to the need of executing direct shear test simulations of several profiles, under different loads, sampling intervals and scales, an automated process of preprocessing of the input files used on the simulation and postprocessing of the simulation results was required. A diagram of the automatized process is shown in Figure 3.12, each step will be described below, including the software and resources used in each one. All of the processes is controlled and executed using scripts on MATLAB, which are able to call the rest of the used software (GMSH and Abaqus) when it is necessary.

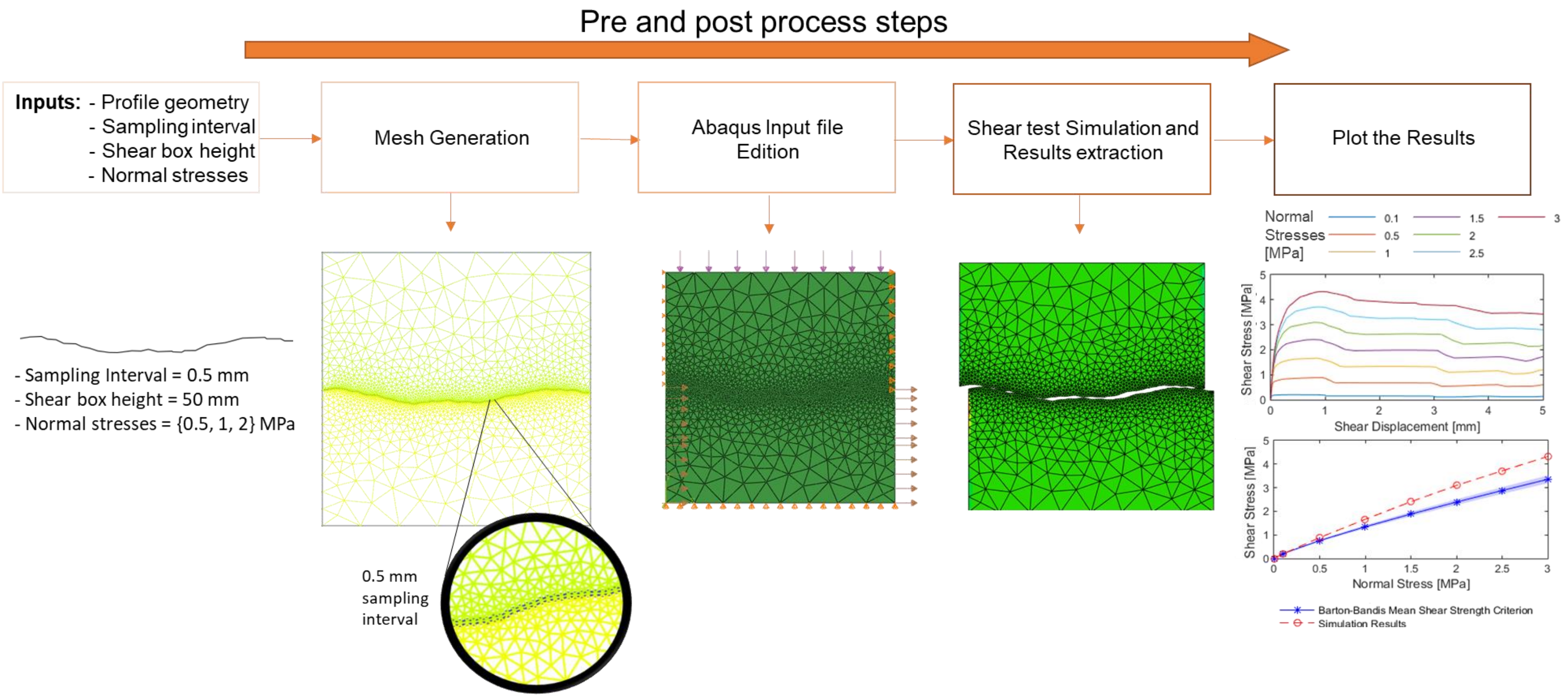

Figure 3.12. Automatized simulations process diagram.

### 3.4.1 Model Input

To create the shear box model, the following inputs are required:

- The profile geometry
- The sampling interval of the joint length
- The height of the shear box
- The normal stress

The profile sampling process is shown in Figure 3.13, for Barton's profile n°8 and a sampling interval of 5 mm, the profile length is around 100 mm. The height of the shear box h should be large enough as to not disturb the joint contact stresses, a box height equal to half the profile length has been deemed as enough. The normal stress is defined by the user, in this work low values of normal stress are used (3 MPa at maximum), as big normal stresses are associated to CNS boundary conditions, which escapes the scope of this work.

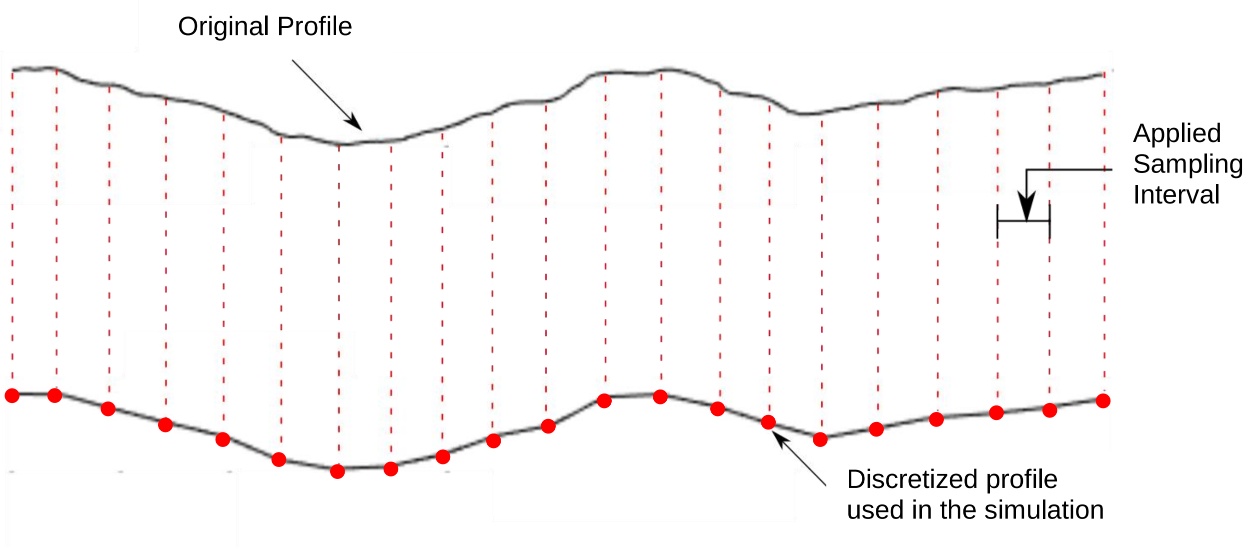

Figure 3.13. Profile sampling process (Barton's profile n° 8).

### 3.4.2 Model Drawing and Mesh Generation

To draw the shear box model and generate the corresponding mesh, the software GMSH is used. Although several free access meshing software exists, GMSH has the advantage of easiness of use, the possibility of execution by command and compatibility with the Abaqus file format (.inp). GMSH input files (.geo) can be made with scripts, when the geometry is not complex, as in the case of this work. Figure 3.14 illustrates the shear box drawing made with a MATLAB script, before and after generating the mesh.

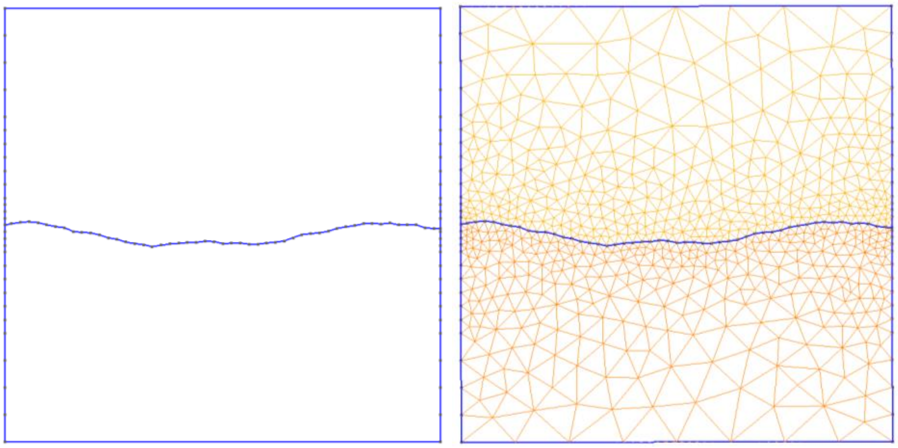

Figure 3.14. GMSH model input, before and after generating the mesh (Barton profile N°6, Sampling Interval = 2 mm).

The Delaunay algorithm was used to create the meshes, details of the algorithm may be found in the GMSH Guide (Geuzaine & Remacle, 2017). GMSH allow to export the mesh directly to the Abaqus .inp format, the exported file includes the geometry, the mesh, and the node sets created.

### 3.4.3 Abaqus Input File Edition

The input file must be edited to include applied loads, boundary conditions, surface assignments, interactions, material properties and steps definitions. All these properties were described above in section 3.3. After this step, the simulation is ready to be executed and the model should look like in Figure 3.11b.

### 3.4.4 Shear Test Simulations and Result Extraction

Once the simulation has finished, the results are extracted into MATLAB, for implicit analyses (Abaqus/Standard), the results are obtained from the .dat files created in the simulation execution. For explicit analyses (Abaqus/Explicit), results are gotten directly from the .odb file (Abaqus simulation database) using a free external MATLAB App, Abaqus2Matlab (Papazafeiropoulos et al., 2017) (Figure 3.15).

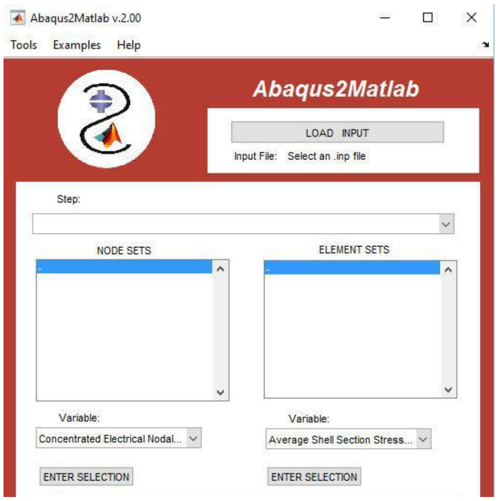

Input File: Select an .inp file

Variable: Concentrated Electrical Nodal...

Variable: Average Shell Section Stress...

Figure 3.15. Abaqus2Matlab Interface.

For the results analysis, in the displacement-controlled test, the reaction forces in the external nodes and the lateral displacement are extracted. In the load-controlled test case, the displacements and time of the simulation are extracted. Finally, the results are plotted for the subsequent analysis (Figure 3.16).

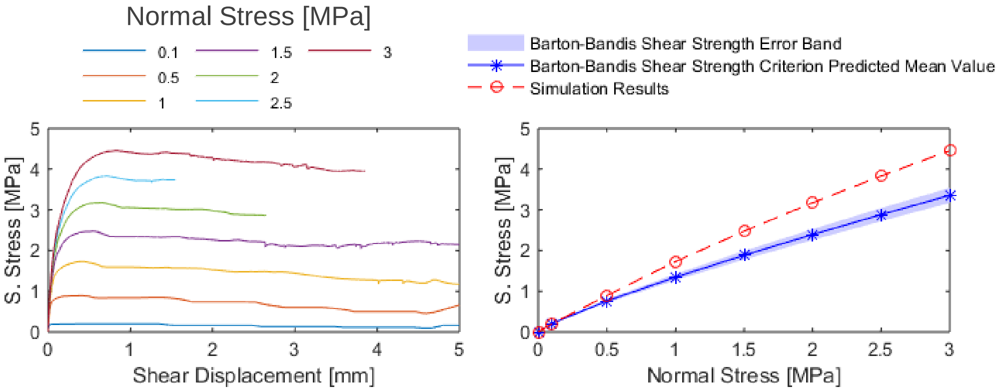

Figure 3.16. Shear Stress v/s Shear Displacement and Shear Stress v/s Normal Stress Results.

For the load-controlled analysis, the reaction force is not possible to measure and the required stress to overcome the joint resistance isn’t know beforehand, to overcome this, the Barton-Bandis predicted shear strength is used as a reference load and an amplitude factor is applied, to ensure that the joint slides. The lateral applied stress $\sigma_{\mathrm{Lat}}$ is given by the equation:

$$\sigma_{\mathrm{Lat}} = \tau_{B-B} * A(t) \tag{3.12}$$

Where $\tau_{B-B}$ is the predicted Barton-Bandis shear strength for profile nominal JRC, A(t) is the amplitude as a function of simulation time t. Since the amplitude is related to the simulation time (Figure 3.17), the applied lateral stress can be back-calculated from the simulation time. Similarly, the shear stress is calculated using equation (3.4). Finally, results are plotted in a similar fashion to displacement-controlled models results. Figure 3.18 illustrates how the results of both analyses compare.

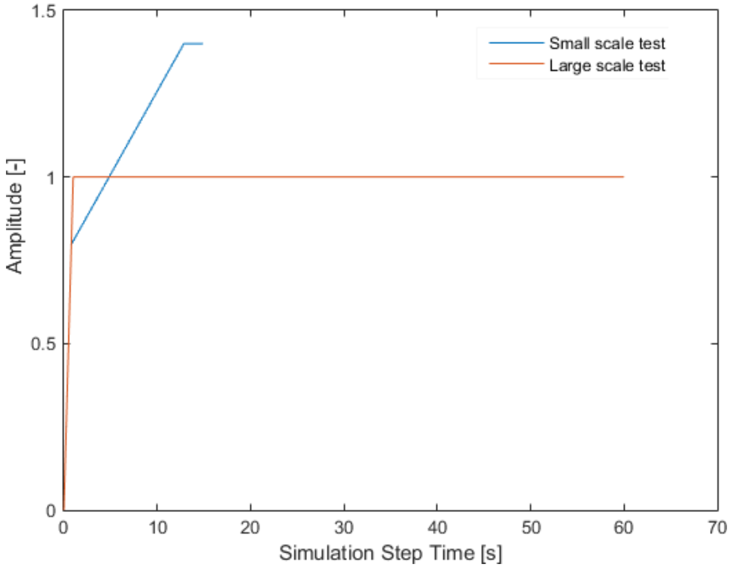

Figure 3.17. Amplitude relationship with simulation time.

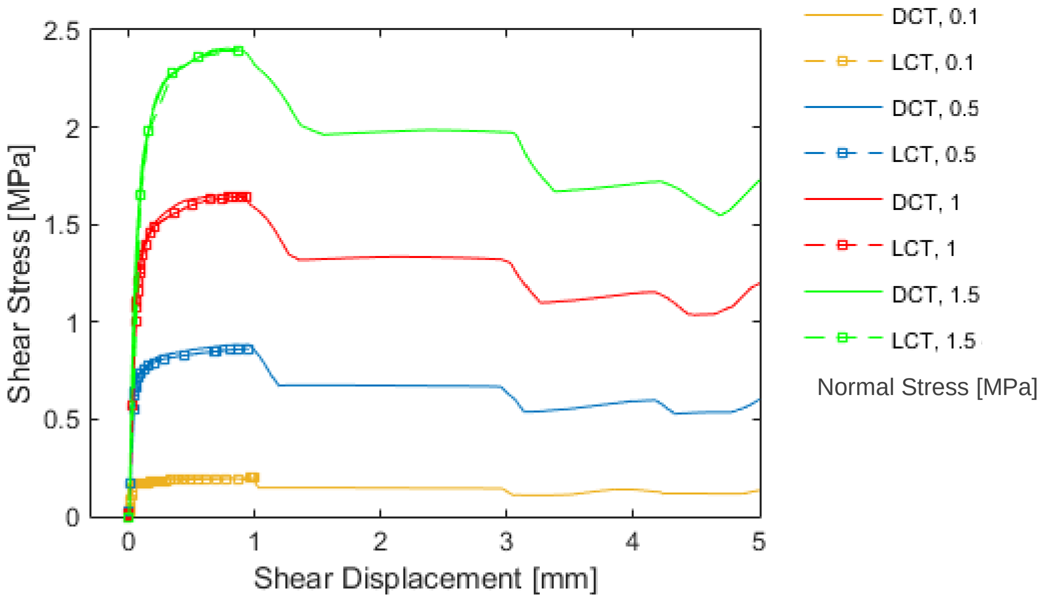

Figure 3.18. Load-Controlled (LCT) and Displacement-Controlled (DCT) tests.

## 3.5 Implicit and Explicit Analysis

FEM analysis solves non-linear problems by using incremental steps (load or displacement). These increments may induce geometry changes (displacements, velocities and/or accelerations) or material changes (yield or degradation), these changes need to be considered by updating the stiffness matrix.

In an explicit analysis (Abaqus/Explicit) the FEM problem is solved by doing the increment in load (or displacement) and then applying the geometry changes and updating the stiffness matrix, if necessary. To ensure that the solution is correct, small increments must be used, if this is not done, the solution may diverge from the correct one. Abaqus ensures that the increment is small enough by estimating the required increment based on the mesh size (small element sizes requires smaller increments), always being on the safe side. However, for quasi-static analysis (the inertial forces must be near 0) the process may be hurried, without incurring a lack of accuracy in the solution. Simulation solved by the explicit method will always be completed, but the obtained solution must be treated carefully, as a divergence from the real solution may occur. Due to the transient nature of the explicit analysis, obtained results include high-frequency oscillations added to analysis results, these high-frequency oscillations must be removed in post-processing, to get the quasi-static analysis response, the post-processing process and the parameters used may be found in section Appendix C – Results processing in Abaqus/Explicit.

In an implicit analysis (Abaqus/Standard), the model solution is obtained by applying the increments of load or displacement and updating the geometry and/or stiffness matrix, with the addition that the equilibrium of the external and internal forces of the model is check, using the Newton-Raphson algorithm after each increment, which means that an implicit analysis is unconditionally stable, However, complex problems require a large number of iterations, turning large problems in computationally expensive ones, also over constraint or highly non-linear problems may require increments smaller than the minimal accepted value, which may cause an abortion of the simulation.

In addition, there are differences between the capabilities of both analyses related to the Abaqus software development, which is summarized in Table 3.3.

Table 3.3. Difference in capabilities between Abaqus/Standard and Abaqus/Explicit ((Dassault Systèmes Simulia Corp., 2013a)

| Quantity | Abaqus/Standard | Abaqus/Explicit |
|---|---|---|
| Element library | Offers an extensive element library. | Offers an extensive library of elements well suited for explicit analyses. The elements available are a subset of those available in Abaqus/Standard. |
| Analysis procedures | General and linear perturbation procedures are available. | General procedures are available. |
| Material models | Offers a wide range of material models. | Similar to those available in Abaqus/Standard; a notable difference is that failure material models are allowed. |
| Contact formulation | Has a robust capability for solving contact problems. | Has a robust contact functionality that readily solves even the most complex contact simulations. |
| Solution technique | Uses a stiffness-based solution technique that is unconditionally stable. | Uses an explicit integration solution technique that is conditionally stable. |
| Disk space and memory | Due to the large numbers of iterations possible in an increment, disk space, and memory usage can be large. | Disk space and memory usage are typically much smaller than that for Abaqus/Standard. |

### 3.5.1 Inertial Forces and Mass Scaling

In the Explicit quasit-static analysis, the main source of error is the appearance of non-negligible inertial forces, which induce an acceleration in the system and therefore a lack of equilibrium, this occurs when the increments used are bigger than the acceptable. Even though using Abaqus suggested increments would certainly avoid this issue, the required computation time increases significantly, making this type of analysis useless for this work, as several models need to be performed in succession. This issue may be avoided applying a mass scaling, a tool used in explicit Analysis procedures where the time scale of the problem is not important, as it’s the case in the quasi-static analysis.

In explicit solved models, the runtime is not only a function of the model size but also the smaller element size, due to the Courant condition, given by:

$$\Delta \mathrm{t} \leq \mathrm{f} * \left(\frac{d}{\mathrm{c}}\right)_{min} \tag{3.13}$$

Where Δt is the stable time step, d is the smallest dimension of the model, f is a stability factor (usually around 0.9) and c is the wave speed. The condition limits the time step so that the stress wave, which transmits the stresses in the model, cannot travel more than the smallest dimension in a single step, since mesh size can't be easily altered without affecting the model resolution, the wave velocity is modified to increase time step.

the wave velocity is defined as:

$$\mathrm{c} = \sqrt{\frac{E}{\rho}} \tag{3.14}$$

The principle behind mass scaling is to artificially augment the mass of the model to induce an increment in the density of the system (geometry is kept the same), and thus reducing the wave velocity. In this work, the mass scaling is applied by selecting the desired time step, that balance computation time with model accuracy, which is related to the inertial forces generated in the model. As a rule of thumb, the total kinetic energy must be less than 10% of the internal energy of the model to assure that inertial forces are kept low.

## 3.6 Calibration of Model Parameters

To ensure that the models behave well and represent the reality, calibration of some key parameters is required. Although some parameters are calibrated because there is no information about them (Dilation), most of them are just numerical parameters that have no physical meaning and must be calibrated for every model.

In general, most of the analyses were done for one or few Barton's profiles (Figure 2.10), whether it was judged as representative for the rest of the profiles, or the most critical, in terms of model convergence (usually the roughest and with lower sampling intervals had the biggest issues with convergence).

In the following sections, the calibration made for the Abaqus/Standard based models is presented. The Abaqus/Explicit calibration work is included in Appendix C. Since Abaqus Standard is the most used Abaqus analysis, various analysis related parameters are given by default by the software, still, it was checked if the default values were appropriated to run the models.

### Material Dilation

The material dilation is a parameter that must be obtained from experimental results. Abaqus requires inputting a dilation angle different than 0 to use the Mohr-Coulomb plasticity model. Since all of the parameters used for Hawkesbury Sandstone have been obtained from bibliography (section 3.2) and there was no information found about the material dilation angle, a sensitivity analysis was performed to study the dilation angle influence on the joint shear behavior.

The analysis was made for one constant vertical stress (1 MPa) and sampling interval (1 mm). A rough profile was preferred over a perfectly smooth surface, as the dilation effect on the shear strength would be meaningful when the material suffers plastic strains; Barton profile N° 6 was used (Figure 2.10). Thirteen different dilation angles values were used, whose angles in degrees are included in the legend of the left plot, with all numbers being in degree units.

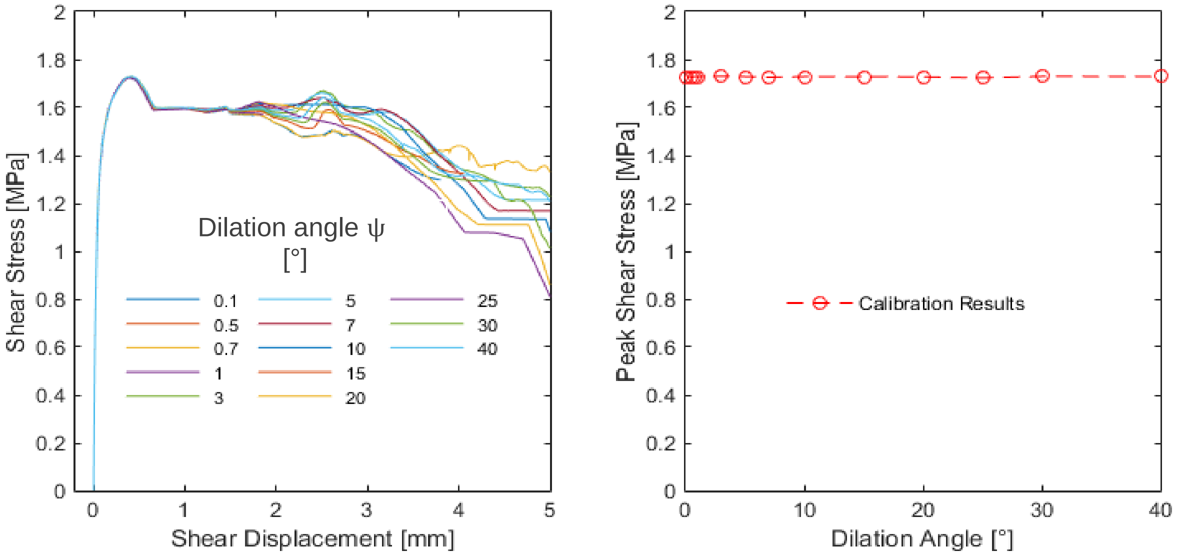

Figure 3.19. Sensitivity analysis for Dilation Angle.

Since no apparent influence of the dilation angle on the peak shear strength was found, the dilation angle ψ was adopted as 0.1 ° and constant for all the executed models.

Differences were found in the post-peak behavior of the results with a “second peak” found for higher values of dilation angle (30 or more). This may be explained since big dilation angles induce an increment in the required override of the joint. This dilation effect is more apparent under high plastic strains.

### Critical Displacement $\gamma_{\text{crit}}$

A sensitivity analysis was performed to study the critical displacement effect on the shear strength, as noted in section 3.3. In theory, $\gamma_{\text{crit}}$ should only influence the shear displacement required to mobilize the shear strength.

The simulations were made for one constant vertical stress (1 MPa) and 4 different sampling intervals (0.5, 1, 2 and 5 mm. Again, a rough profile was preferred over a perfectly smooth surface, as a smooth surface mobilizes its shear strength with almost no displacement; Barton profile N° 6 was used (Figure 2.10).

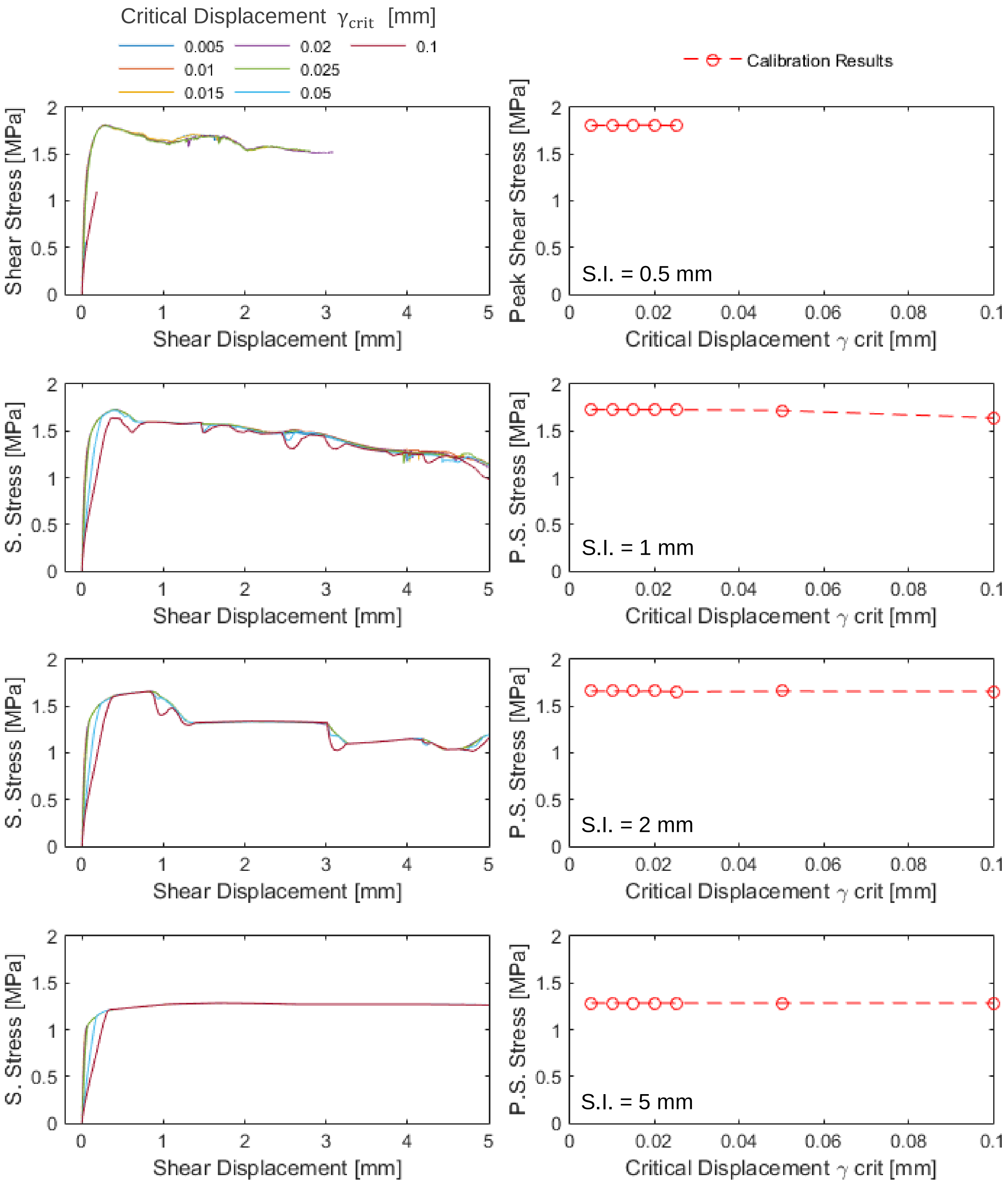

Figure 3.20. Sensitivity analysis for critical displacement $\gamma_{crit}$.

In Figure 3.20, a reduction in the peak shear strength is shown for the model with sampling interval equal to 1 mm, the test wasn't able to finish for sampling interval 0.5 mm but it is expected to show the same behavior, on the higher sampling intervals only a delay, in terms of displacement, on the shear strength mobilization is observed, but the magnitude stays the same. In general, it was noted that high values of $\gamma_{crit}$ do have an impact on the peak shear strength of the models. The differences in the peaks, on shear/displacement curves, are related to the sampling interval of each model and not to the $\gamma_{\text{crit}}$ variation. The $\gamma_{\text{crit}}$ do have an impact on how much shear displacement takes to degrade the peak shear strength to lower values. As a cautious measure, $\gamma_{\text{crit}}$ will be equal to 0.025 mm on all models, to avoid any possible peak shear strength reduction.

## Normal Stiffness

Abaqus considers a default Normal Stiffness value, assigned as ten times the value of the underlying elements in the interface, which corresponds to the assigned Young Modulus of the models, equal to 4.2 GPa (Table 3.2). On the Abaqus manual, it is established that the default stiffness included in the software is usually enough to avoid issues with the contact, with the exception of displacement-controlled test with coarse meshes. To verify that the penetration of surfaces is not excessive, the rougher models, Barton's profiles N° 9 and 10 were analyzed (Figure 2.10), under the larger sampling intervals (S.I = 2 and 5 mm) and the higher stresses (3 MPa) applied.

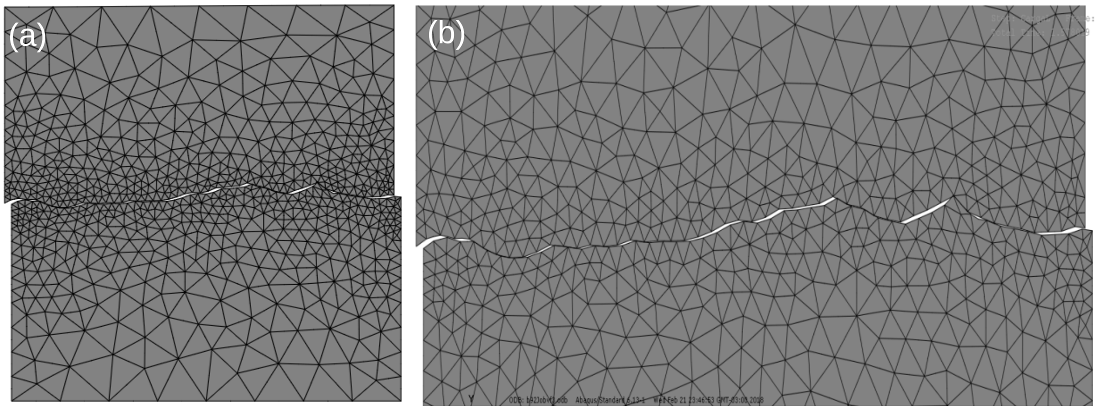

Figure 3.21. Sheared profile N°9, Sampling Interval = 2 mm, Vertical Stress = 3 MPa (a) whole model (b) Zoomed (vertical dimension exaggerated).

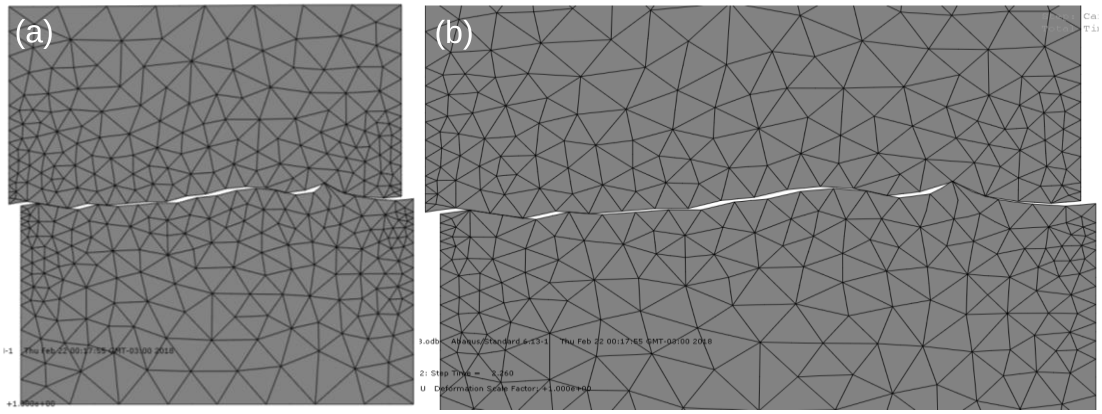

Figure 3.22. Sheared profile N°9, Sampling Interval = 5 mm, Vertical Stress = 3 MPa (a) whole model (b) Zoomed (vertical dimension exaggerated).

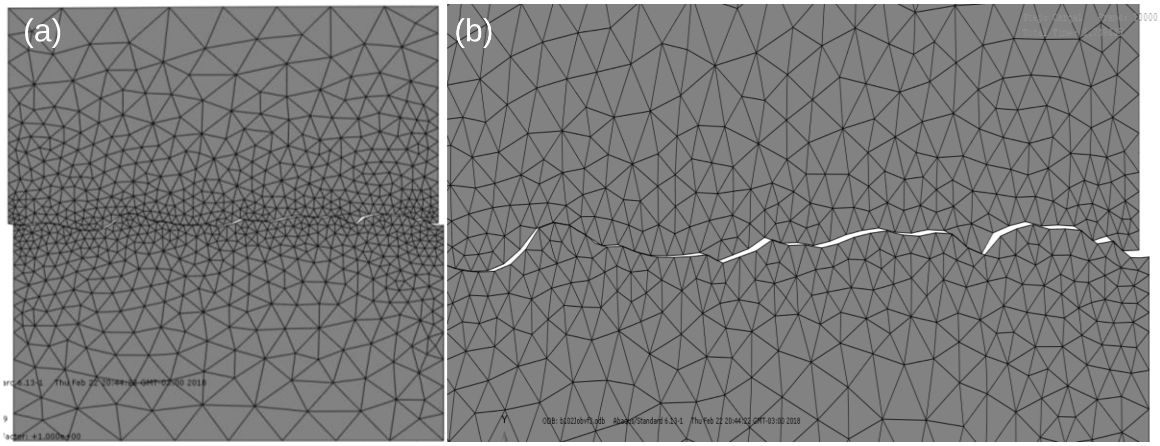

Figure 3.23. Sheared profile N°10, Sampling Interval = 2 mm, Vertical Stress = 3 MPa (a) whole model (b) Zoomed (vertical dimension exaggerated).

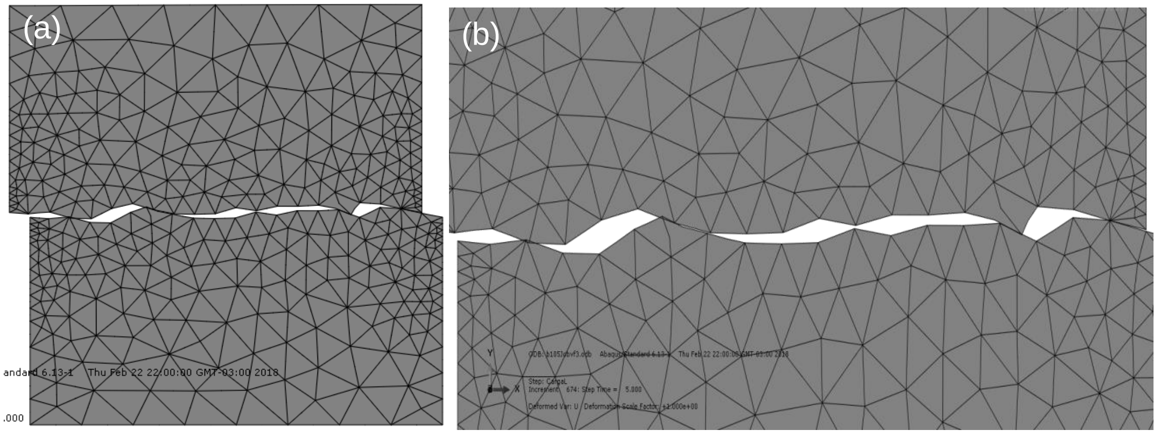

Figure 3.24. Sheared profile N°10, Sampling Interval = 5 mm, Vertical Stress = 3 MPa (a) whole model (b) Zoomed (vertical dimension exaggerated).

Overall, the observed penetrations in Figure 3.21, Figure 3.22, Figure 3.23 and Figure 3.24 are acceptable and do not influence the peak shear strength. Moreover, the peak shear strength is achieved at around 0.5 mm of shear displacement, while the Figures display the models under 2-3 mm of shear displacement, the point at which the penetration is negligible. Higher values of normal stiffness were applied, and the same degree of penetration and negligible peak shear strength differences were found for the models, as seen in Figure 3.25 and Figure 3.26.

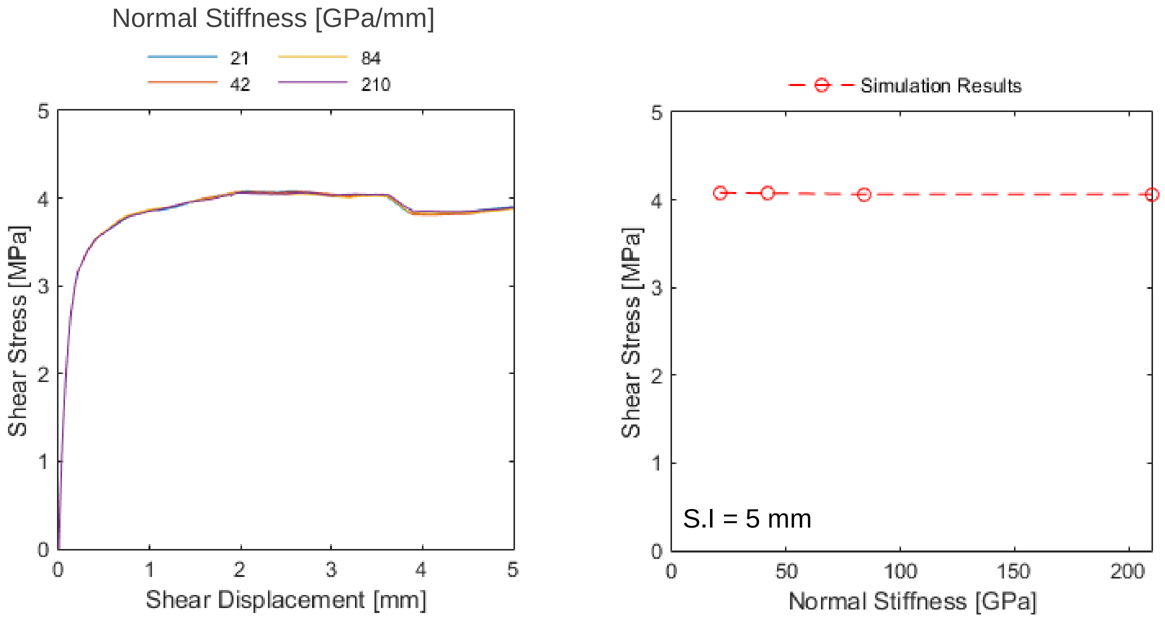

Figure 3.25. Sensitivity Analysis for Normal Stiffness, Barton profile 9, normal stress = 3 MPa and S.I.= 5 mm.

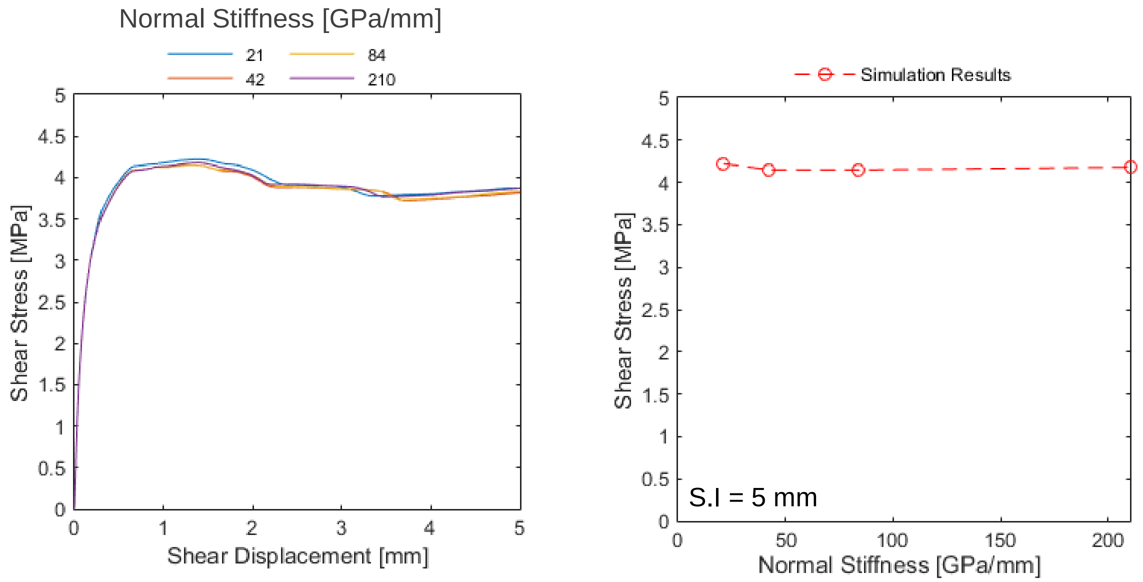

Figure 3.26. Sensitivity Analysis for Normal Stiffness, Barton profile 10, normal stress = 3 MPa and S.I.= 5 mm.

## 3.7 Scale effects Related Issues and Solutions

Initially, displacement-controlled simulated tests would be the only ones to be used for the study, because they give a stress-displacement curve that has a clear peak shear stress and its post-peak behavior, also it is easier to configure and post-process its results. However, issues with enlarged profiles were found when the displacement-controlled methods were used. As may be seen in Figure 3.27, the peak shear strength increases considerably when the model has enlarged from 100 mm (Figure 3.27b) to 1000 mm (Figure 3.27a) approximately. This increase may be modeled as the sum of the small-scale behavior plus an “apparent cohesion”, which was present in every enlarged shear test simulation.

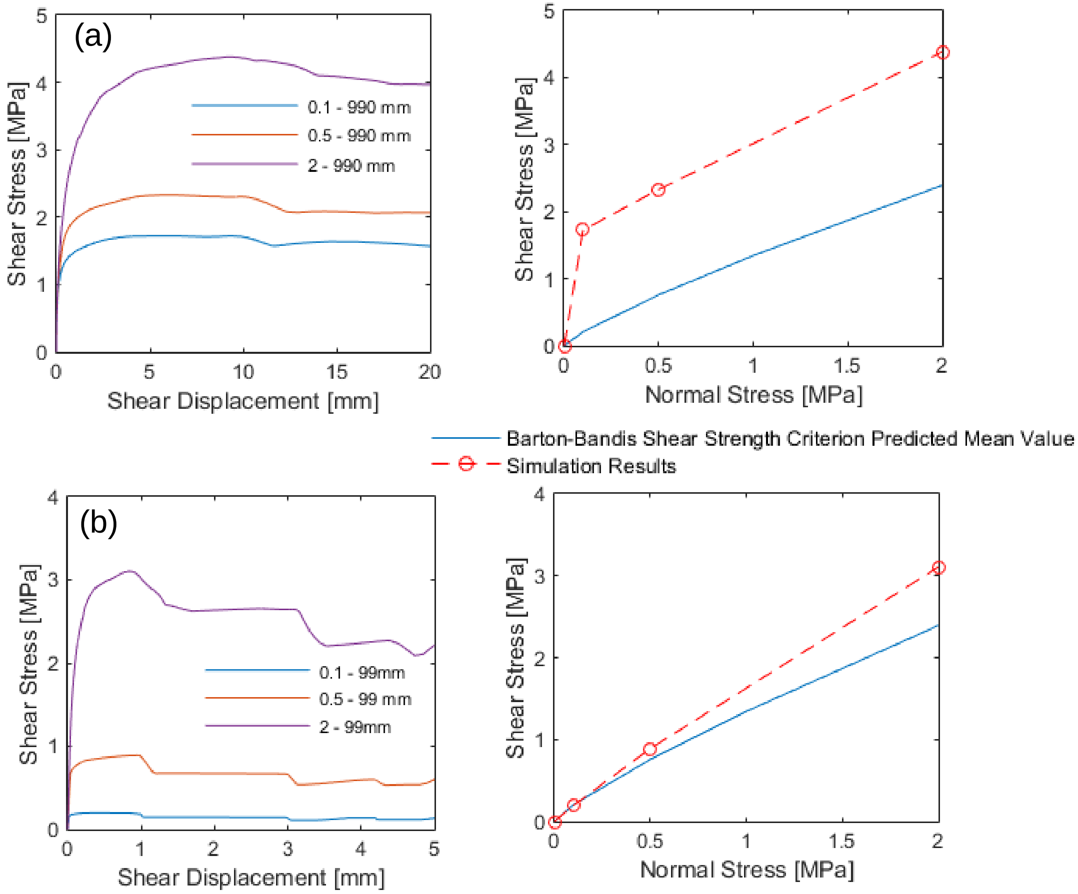

Figure 3.27.(a) Results for large scale profile (~1000 mm) and (b) Results for small scale profile (~100 mm).

To test this apparent cohesion, shear tests of perfectly smooth surfaces were performed, with low friction coefficient value (μ = 0.01), three different model of equal box height (h = 100 mm) and varying total length (Lx = 100, 500 and 1000 mm), for four different normal stress were used.

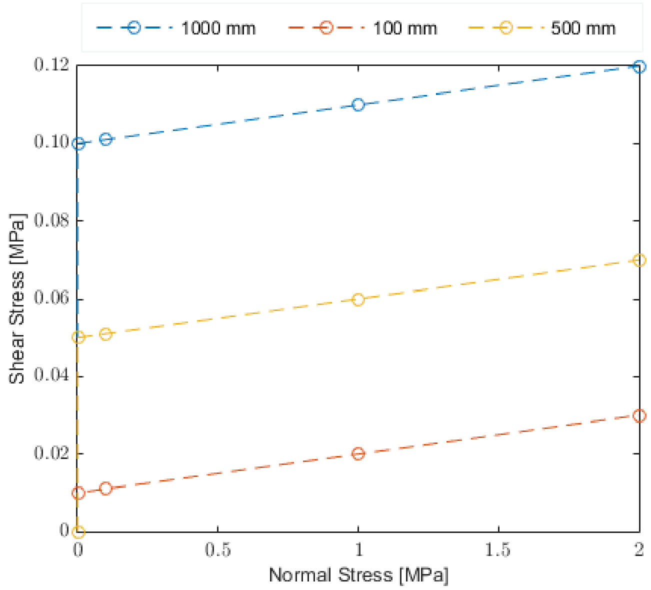

Figure 3.28. Scale studies results, Shear Stress v/s Normal Stress for joint lengths equal to 100, 500 and 1000 mm.

It was found that the apparent cohesion was intrinsically associated to the displacement-controlled test and is a function of the size of the model, which can be modeled by the equation:

$$\mathrm{AC} = \frac{\mathrm{A_{model}}}{1\left[\frac{m}{MPa}\right]}, \tag{3.15}$$

where AC is the apparent cohesion in MPa and A is the area of the model in meters. On the other side, load-controlled tests did not show this behavior with changes in scale, as shown in Figure 3.29. The nomenclature used in the legend for these analyses is resumed in Table 3.4, the XX number refers to the applied vertical stress in MPa, a set of examples is included in Table 3.5 to show how the nomenclature is used.

Table 3.4. Legend nomenclature for scale analyses

| Boundary Condition | Model Scale | Legend abbreviation |
|---|---|---|
| Displacement-Controlled | Small Scale | DCT, XX - SM |
| Load-Controlled | | LCT, XX - SM |
| Load-Controlled | Large Scale | LCT, XX - LM |

Table 3.5. Nomenclature examples

| Example | Boundary Condition | Model Scale | Normal stress [MPa] | Nomenclature |
|---|---|---|---|---|
| Ex 1. | Displacement-Controlled | Small Scale | 0.5 | DCT, 0.5 - SM |
| Ex 2. | Load-Controlled | | 1 | LCT, 1 - SM |
| Ex 3. | Load-Controlled | Large Scale | 2 | LCT, 1.5 - LM |

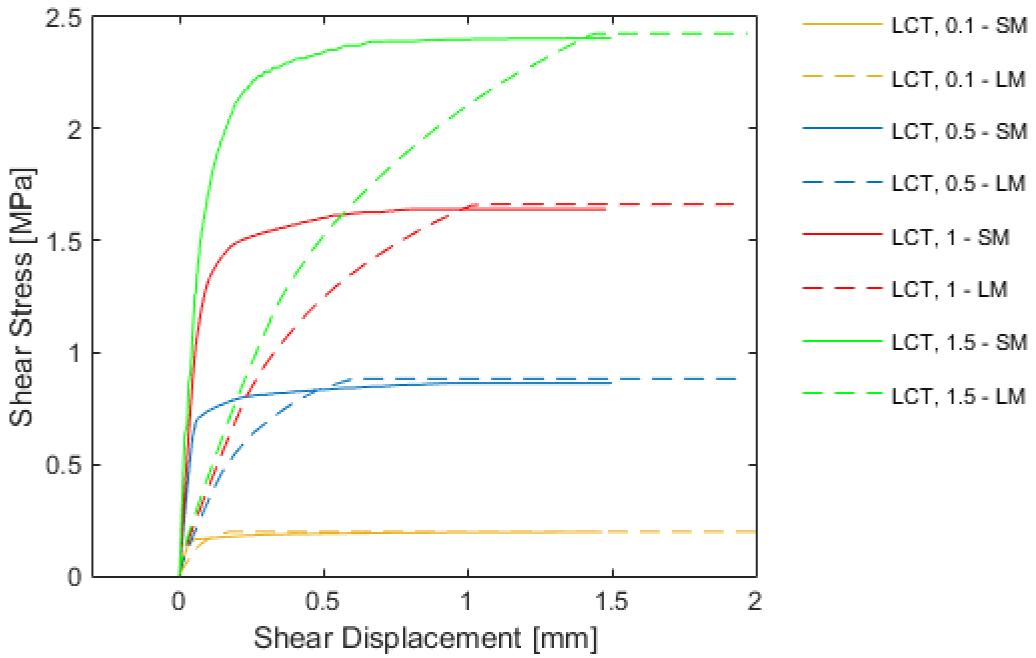

Figure 3.29. Load-controlled tests (LCT), shear stress v/s shear displacement results for small models (SM) and large models (LM), Barton profile N° 6 results, nominal JRC = 10.8.

Large-scale L-C tests does not show the same behavior because these were executed with the exact expected shear strength applied as max possible stress (Figure 3.17), obtained from the small-scale results, the reason for this is because large-scale models take more simulation time to stabilize and would not show a clear shear strength peak unless plenty of time is given to the model for the stabilization. It is important to note that these issues are particular to the version of the software used and is not a result that has any relevance besides numerical simulation on this set of conditions.

## 3.8 Summary

Finally, a summary of the methods and properties used for this work, based on the analysis made in this chapter, is presented.

### 3.8.1 Analysis Conditions

Table summarizes which types of analysis will be used in each study. A more detailed explanation of the type analysis selection is presented in sections 4 and 5.

Table 3.6. The method used for each study

| | |
|---|---|
| **Type of Analysis Used in All Studies** | Implicit Analysis (Abaqus/Standard) |
| **Sampling Interval Influence on Shear Strength** | Displacement-Controlled Tests |
| **Scale Effects on Shear Strength** | Load-Controlled Tests |

### 3.8.2 Model Properties

Table 3.7 summarizes the model main conditions, material properties are summarized in Table 3.2 and Table 3.8 summarizes the joint interaction. The basic friction angle used is based on direct shear tests of smooth surfaces performed by Bahaaddini (2013), for the Hawkesbury Sandstone.

Table 3.7. Model General Properties

| | |
|---|---|
| **Constitutive Law** | Mohr-Coulomb Plasticity. |
| **Interaction Properties** | Finite Sliding |
| **Overclosure Relation** | Abaqus Default Penalty |

Table 3.8. Interaction Properties

| | |
|---|---|
| **Friction Angle [°]** | 37.8 |
| **Joint Normal Stiffness [GPa]** | 42 (default) |
| **Critical Displacement [mm]** | 0.025 |

# 4 Results of Sampling Interval and Scale Effects

Barton's profiles were selected for this work (Figure 2.10) because they were used to calibrate the Barton-Bandis Model and their geometry are well documented. Table 4.1 summarizes the nominal JRC of the profile, back calculated by Barton & Choubey (1977) from their laboratory tests and its length (Barton & Choubey, 1977; Tatone, 2009). Simulation results of four profiles (from now on selected profiles), selected as representative of smooth (N°1 and N°2), moderately rough (N°6) and rough profiles (N°9), are presented in this chapter and analyzed in Chapter 5. The rest of the results may be found on the Appendix D.

Table 4.1. Nominal JRC and profile length, the profiles selected are highlighted in bold (N° 1, 2,6 and 9)

| Profile N° | Nominal JRC | Length [mm] |
|---|---|---|
| **1** | **0.4** | **97.5** |
| **2** | **2.8** | **100.5** |
| 3 | 5.8 | 100 |
| 4 | 6.7 | 99 |
| 5 | 9.5 | 98.5 |
| **6** | **10.8** | **99** |
| 7 | 12.8 | 96 |
| 8 | 14.5 | 100.5 |
| **9** | **16.7** | **99** |
| 10 | 18.7 | 99.5 |

The description of each study and the main results are given below, the analysis of the results is included in Chapter 5.

## 4.1 Sampling Interval effects on Shear Strength

Sampling interval influence in shear strength was studied performing numerical simulations of each Barton's profile, for a fixed set of constant vertical stresses. The sampling intervals and vertical stress used are presented in Table 4.2. The parameters used for the back-calculation of the JRC are included in Table 4.3.

Table 4.2. Sampling intervals and Normal stresses used for the Sampling Interval analysis

| | | | | | | | | |
|---|---|---|---|---|---|---|---|---|
| **Normal Stresses [MPa]** | 0.5 | 0.1 | 0.5 | 1 | 1.5 | 2 | 2.5 | 3 |
| **Sampling Intervals [mm]** | 0.5 | 1 | 2 | 5 | | | | |

Table 4.3. Parameters used for the JRC back-calculation

| $\phi_b$ [°] | JCS [MPa] |
|---|---|
| 37.8 | 27.4 |

### 4.1.1 Shear Test Simulation Results

#### Shear Stress

The results in Figure 4.1 show the effect of the sampling interval on the stress/displacement curves on the simulations performed for a normal stress of 1 MPa.

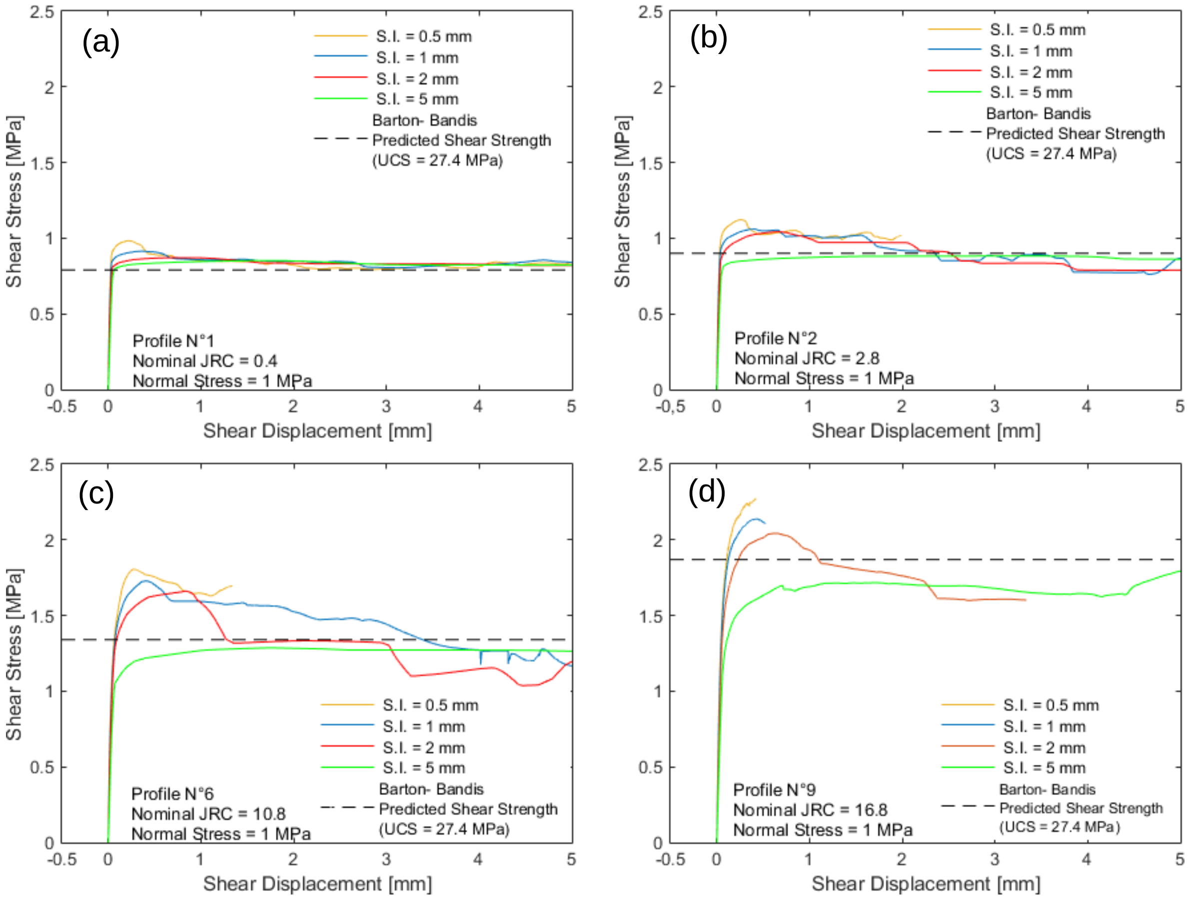

Figure 4.1. Sampling interval effect on the shear stress/displacement curve, normal stress = 1 MPa. (a) Profile N°1, nominal JRC = 0.8 (b) Profile N°2, nominal JRC = 2.8 (a) Profile N°6, nominal JRC = 10.8 (a) Profile N°9, nominal JRC = 16.7.

A summary of the effect of the sampling interval on peak shear strength, as a function of the normal stress, achieved by each of the selected profiles on the numerical tests is presented in Figure 4.2.

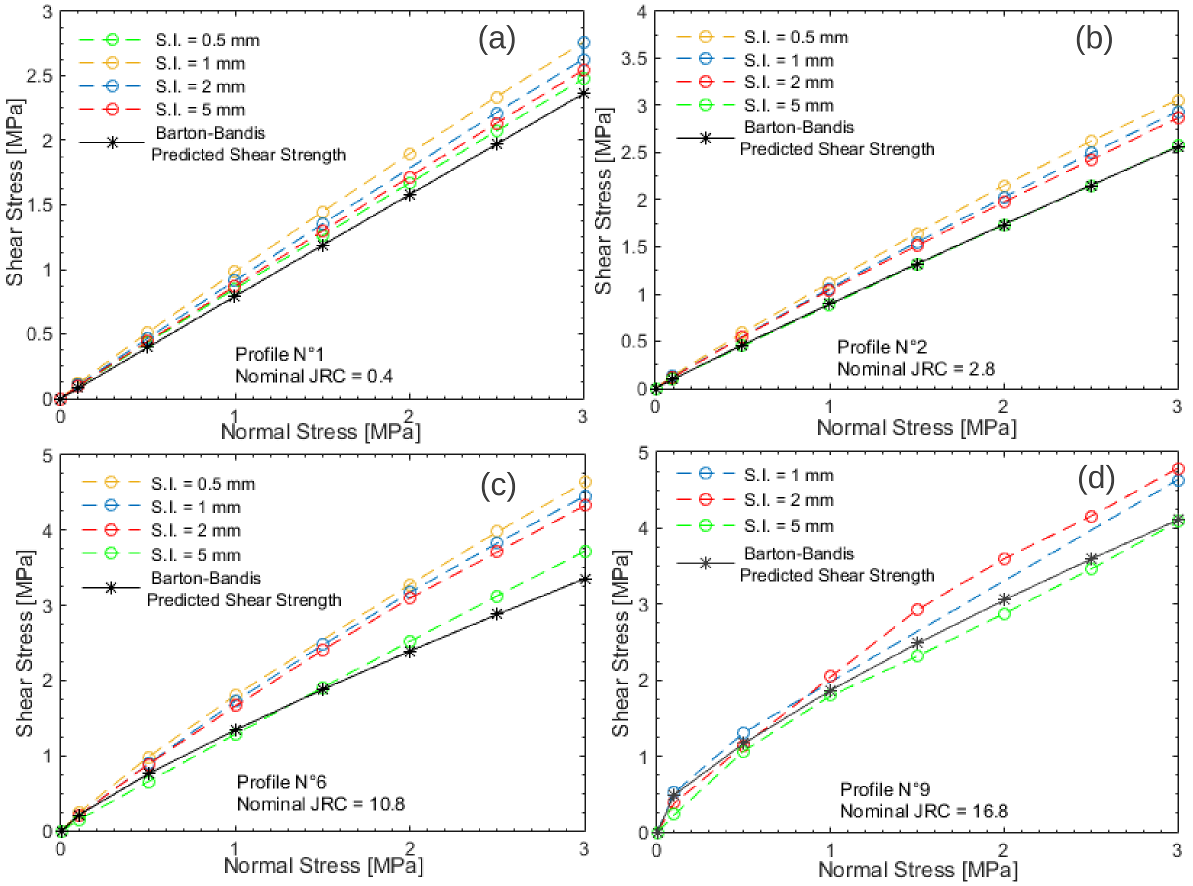

Figure 4.2. Sampling interval effect on the peak shear strength. (a) Profile N°1, nominal JRC = 0.8 (b) Profile N°2, nominal JRC = 2.8 (c) Profile N°6, nominal JRC = 10.8 (d) Profile N°9, nominal JRC = 16.7.

Figure 4.3 summarizes the shear stress – displacement curves for every test performed on the left side, and the peak shear strength of each test as a function of the normal stress, with Barton-Bandis predicted shear strength for comparison, on the right side, for each tested sampling interval of Barton profile n°6. Because the UCS is not an input in the Mohr-Coulomb plasticity model, a scatter band of the Barton-Bandis shear strength criterion predicted results is plotted, which is elaborated using the mean ± the standard deviation of the UCS value. The results of the rest of the profiles are included in Appendix D.

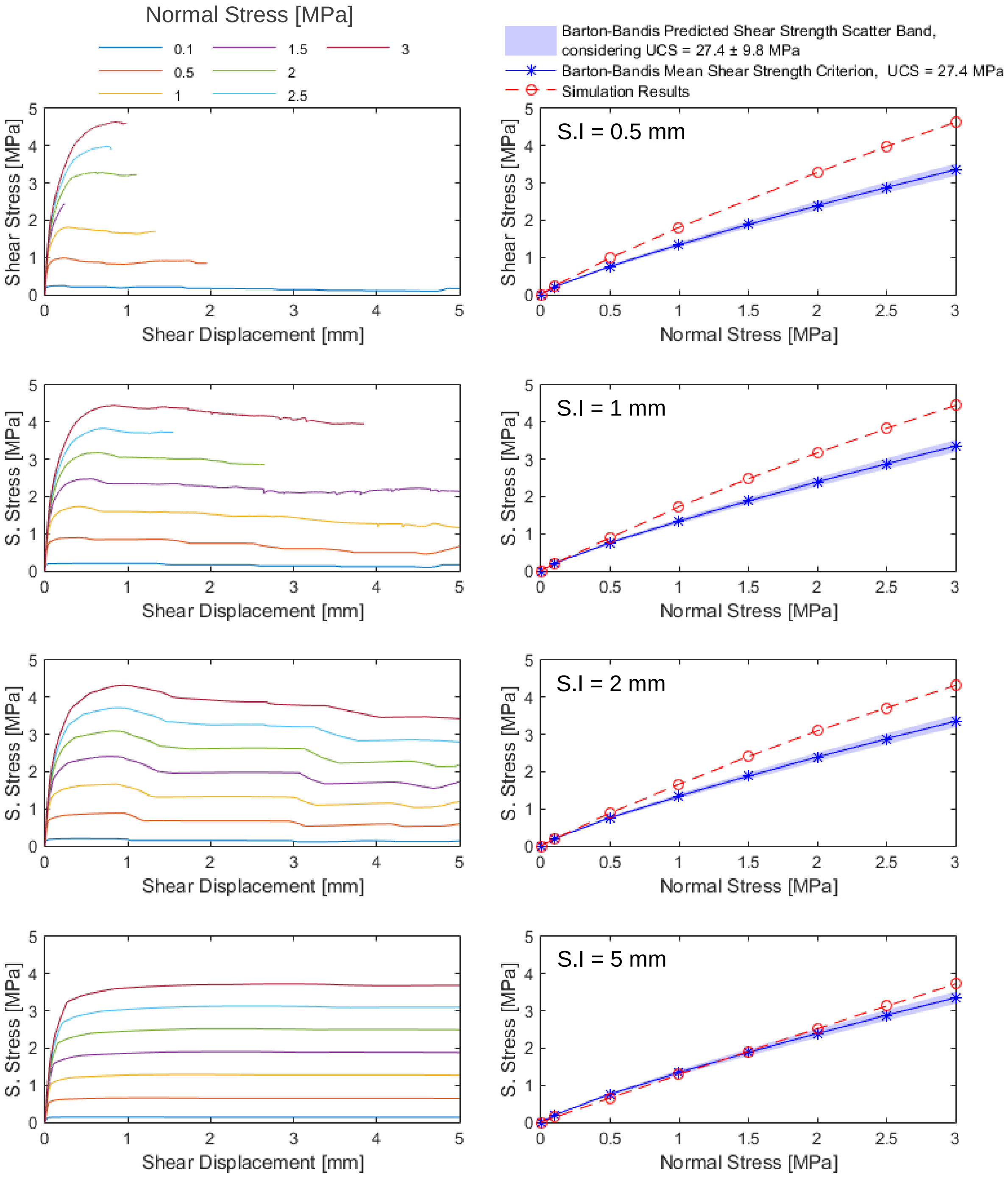

Figure 4.3. Stress-displacement curve and peak shear strength as a function of the normal stress, Barton profile N°6, Profile Length = 99 mm, nominal JRC = 10.8.

Figure 4.4 presents the variation of Barton profile n°6 under different sampling intervals and summarizes the peak shear stress achieved by each modified profile for the applied normal stresses.

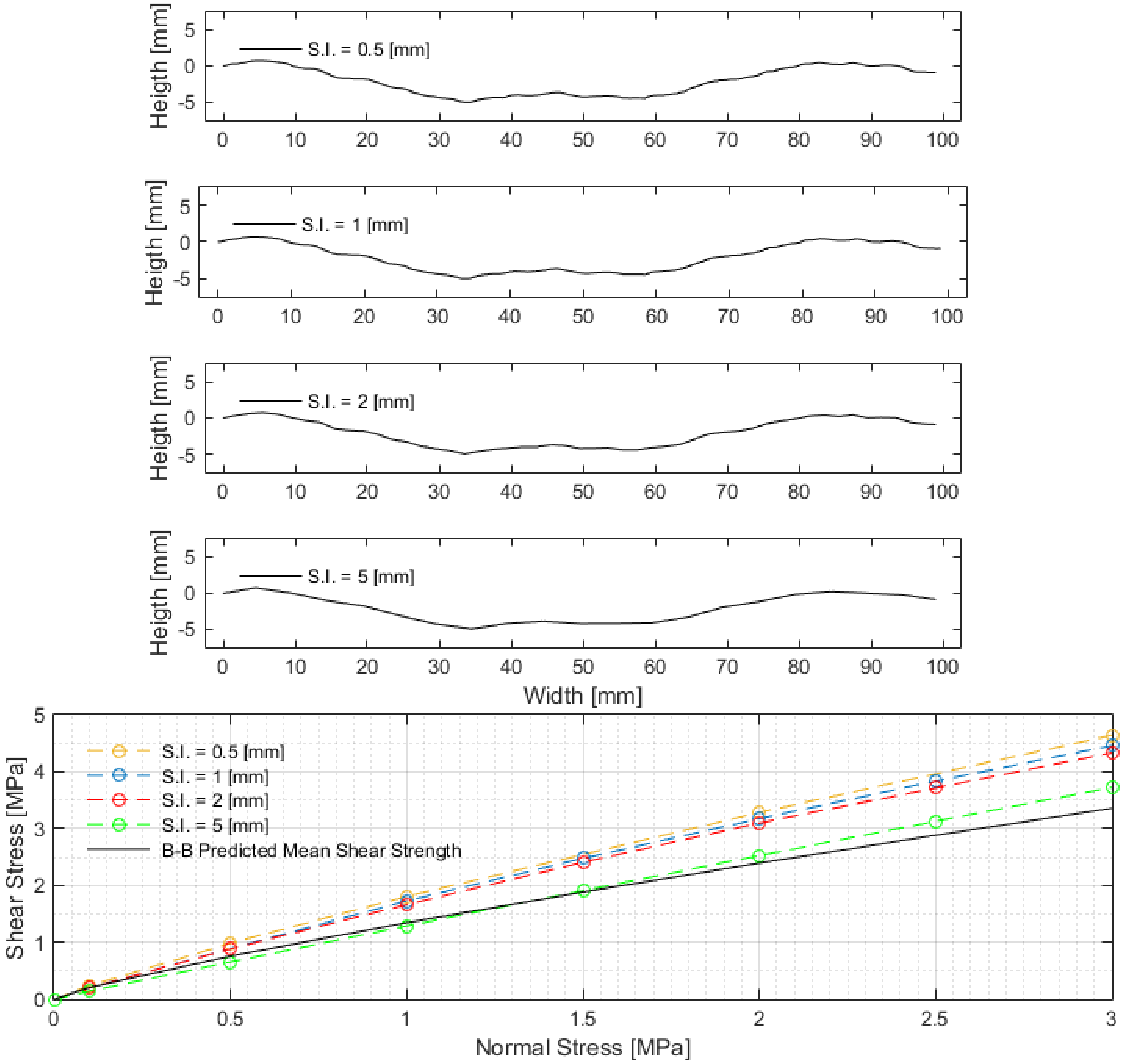

Figure 4.4. Barton's profile n°6, sampled under different interval values and a summary of the simulation results for each sampling interval considered, nominal JRC = 10.8.

Figure 4.5 summarizes the peak shear strength found for the selected profiles, as a function of the used sampling interval, for each normal stress.

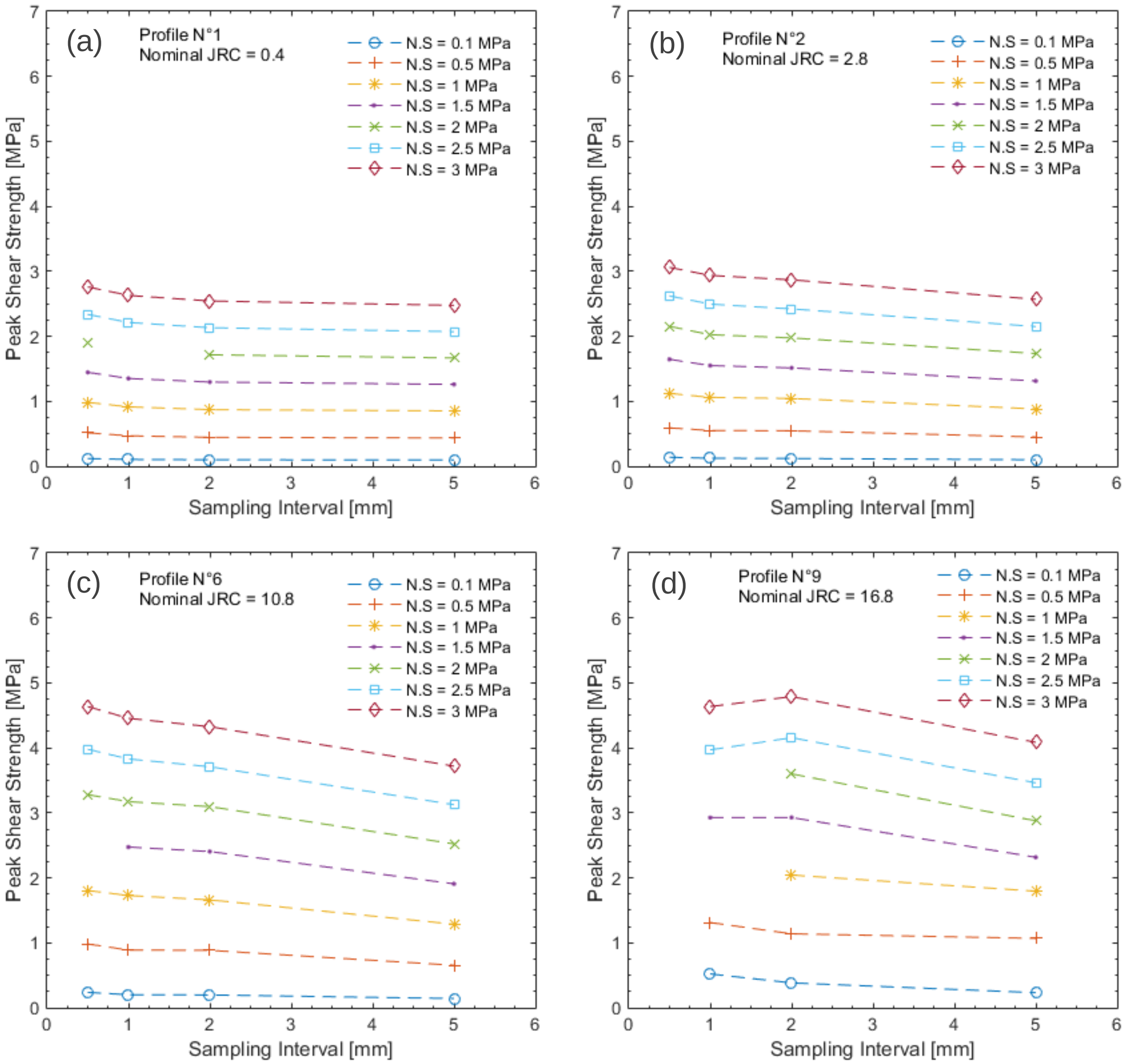

Figure 4.5. Peak Shear Strength as a function of sampling interval, estimated for each normal stress (N.S). (a) Results for profile N° 1 (b) Results for profile N° 2 (c) Results for profile N° 6 (d) Results for profile N° 9.

### Dilation

Figure 4.6 shows the vertical displacement of the joint as a function of the shear displacement, the secant dilation angle(3.3) and different sampling intervals, for each of the selected profiles and a normal stress of 1 MPa.

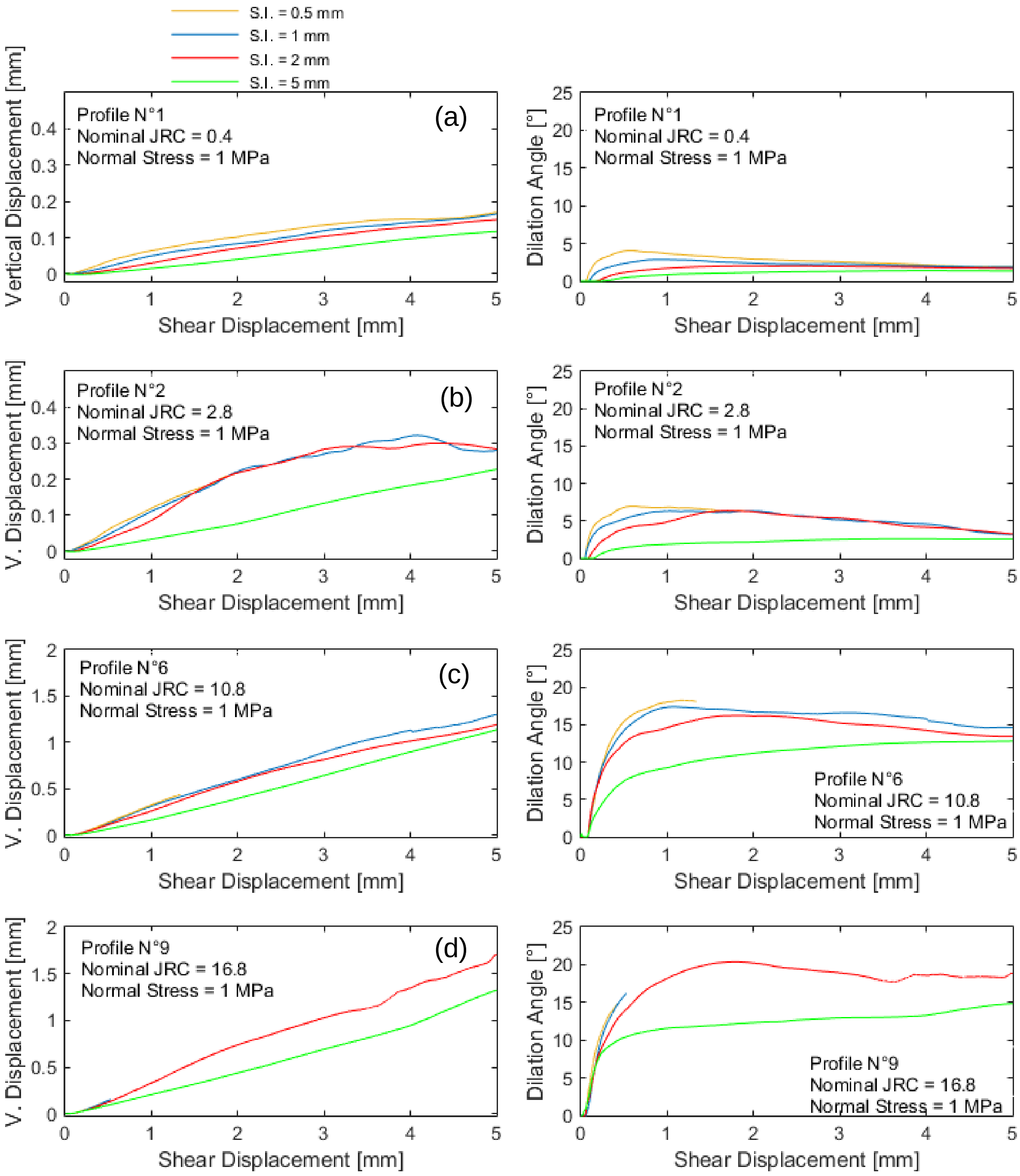

Figure 4.6. Vertical displacement and secant dilation angle (3.3) as a function of shear displacement, for varying sampling intervals (a) Profile N° 1, nominal JRC = 0.4 (b) Profile N° 2, nominal JRC = 2.8 (c) Profile N° 6, nominal JRC = 10.8 (d) Profile N° 9, nominal JRC = 16.7.

Figure 4.7 summarizes the vertical displacement – shear displacement curves for every test performed at different normal stresses on the left side, separated by sampling interval, and the secant dilation angle of each test, for Barton profile n°6. The results of the rest of the profiles are included in Appendix D.

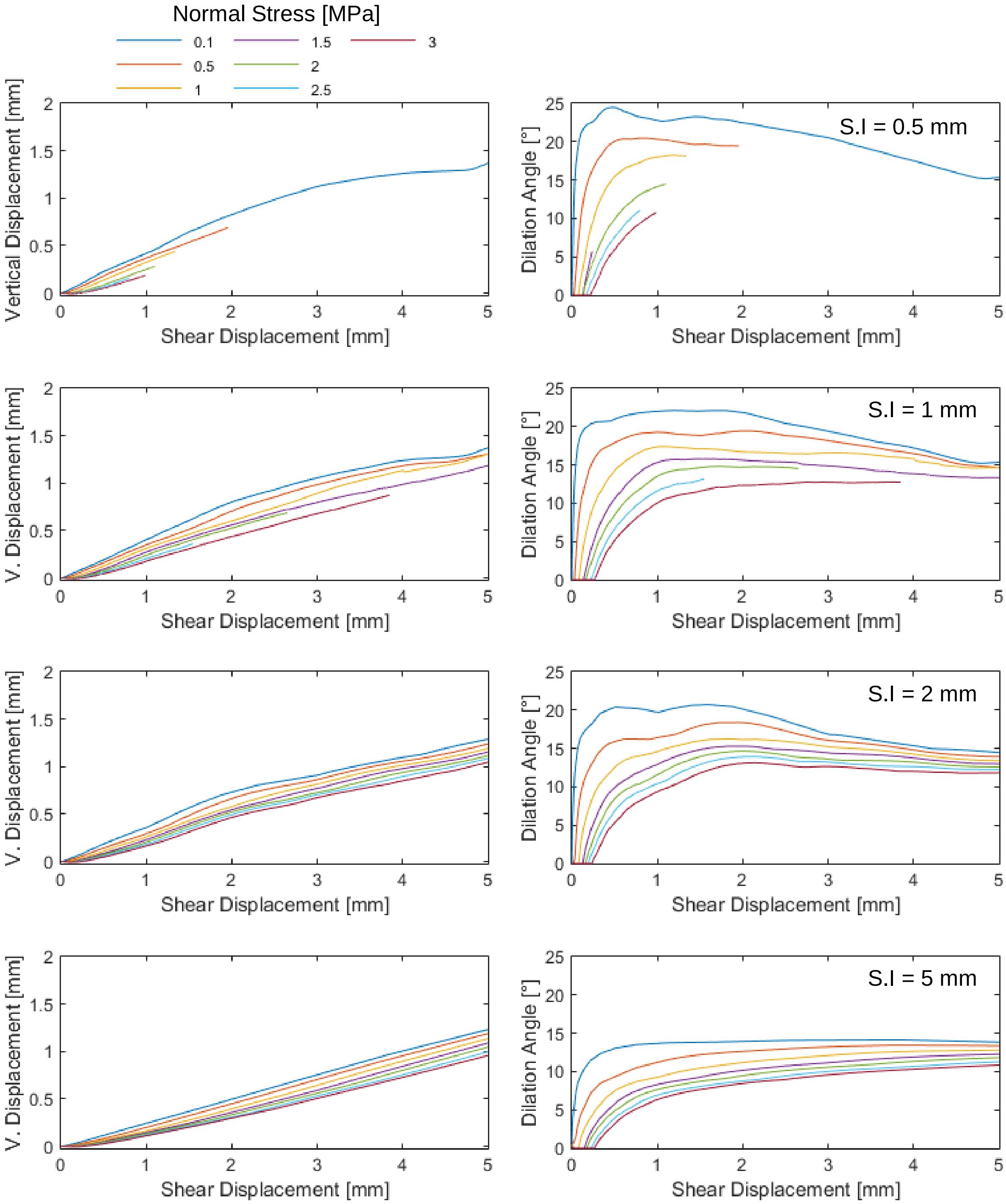

Figure 4.7. Vertical displacement - shear displacement curve and secant dilation angle (Equation (3.3) as a function of the shear displacement, Barton profile N°6, Profile Length = 99 mm, nominal JRC = 10.8.

### Back-calculation of JRC

Figure 4.8 shows the effective JRC obtained from the back analysis of the simulation results, using Bandis methodology (Section 2.6.1), each plot presents the back-calculated JRC, for different normal stresses, and includes the nominal JRC of the analyzed profile (Table 4.1)

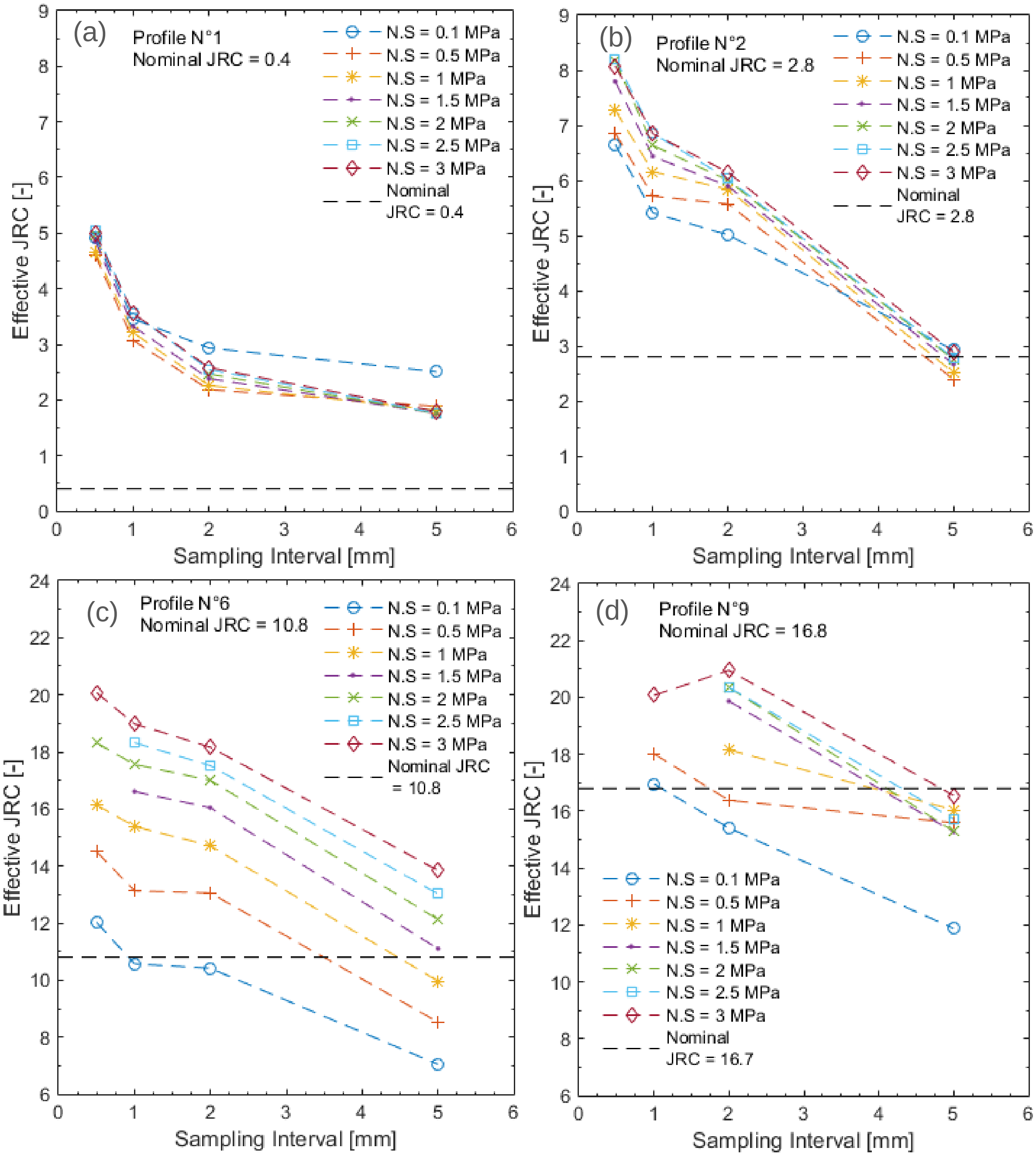

Figure 4.8. Effective JRC as a function of Sampling interval, estimated for each normal stress. Results for (a) profile N° 1, (b) profile N° 2, (c) profile N° 6, and (d) profile N° 9.

In Figure 4.9, the mean effective JRC of each Barton's profile, as a function of the sampling interval, is shown, the nominal JRC value of the profiles is included in the legend

Figure 4.10 shows the mean JRC normalized by the nominal JRC of each profile (Table 4.1), calculated using the same procedure that in Figure 4.8, but averaging all the normal stresses values.

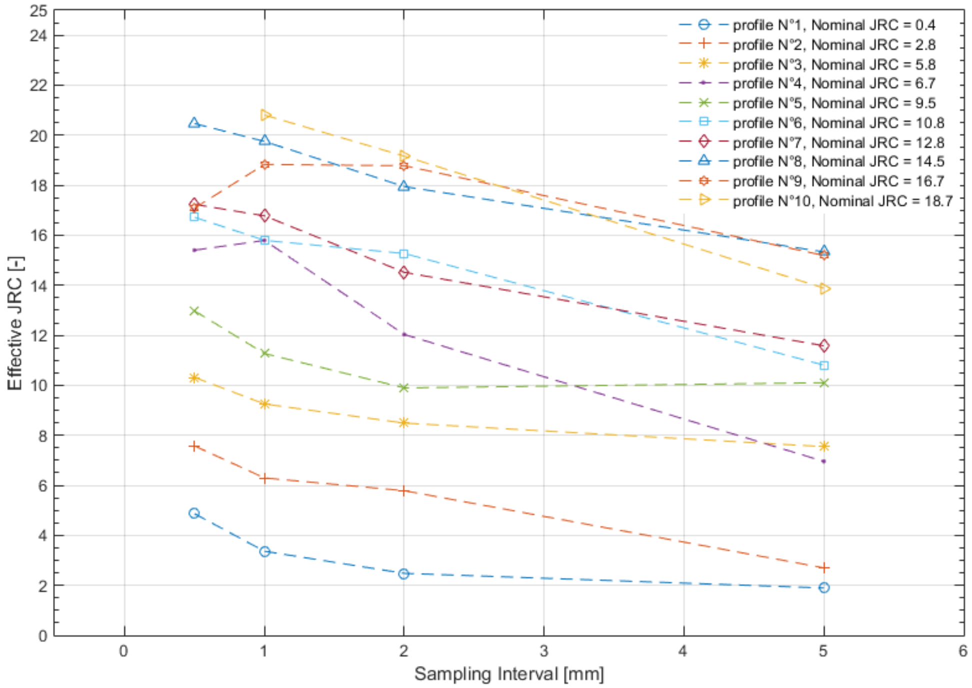

Figure 4.9. Mean effective JRC as a function of the Sampling Interval used on the profile.

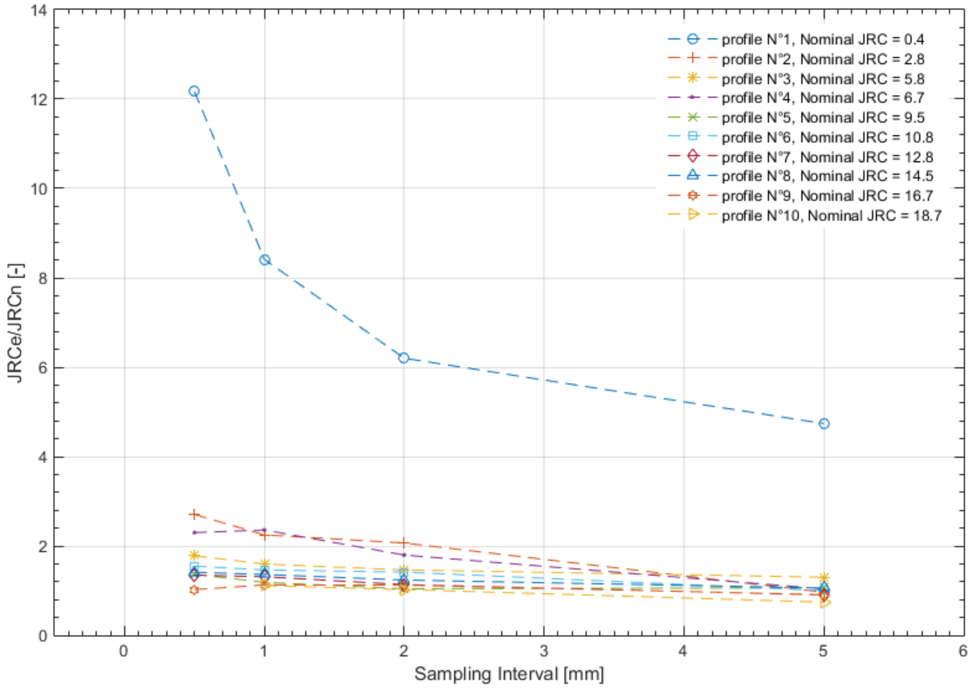

Figure 4.10. Mean effective JRC (JRCe) normalized by the nominal JRC of the profile (JRCn) as a function of the Sampling Interval.

## 4.2 Results from Abaqus/Explicit and Abaqus/Standard

To compare Abaqus/Explicit results with the results obtained from Abaqus/Standard, a sampling interval analysis was made for Barton profile N°6 (nominal JRC = 10.8). This analysis was performed with the shear stiffness parameter adjusted to match the simulations results with the Barton-Bandis criterion, for a sampling interval of 0.5 mm and 1 MPa of normal stress. Figure 4.11 summarizes the results for profile N°6.

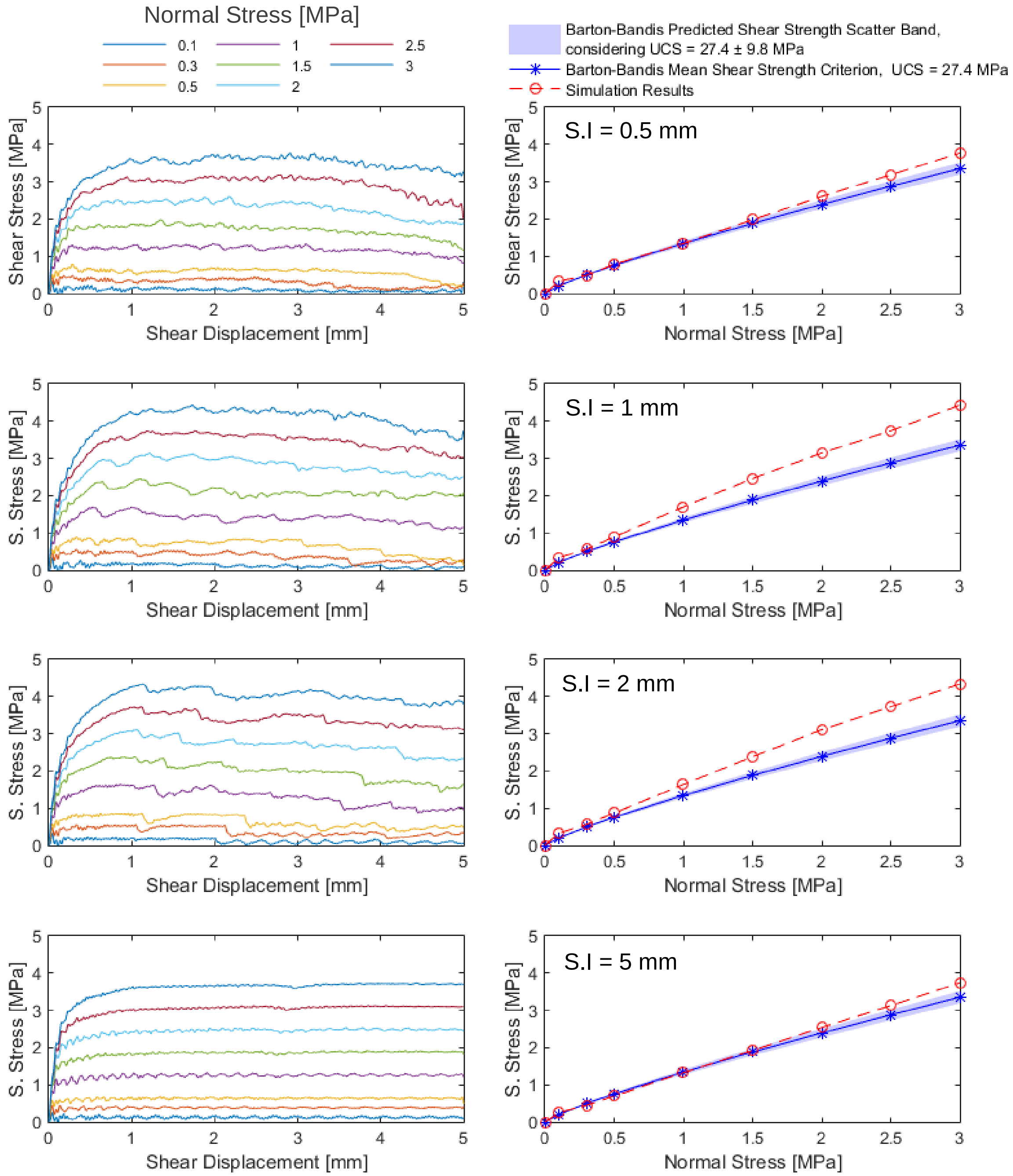

Figure 4.11. Abaqus/Explicit analysis results for Barton profile n°6, Shear stress - displacement curve and peak shear strength as a function of the normal stress.

To compare the results obtained from the Implicit and Explicit Analysis, Figure 4.12 shows the mean effective JRC back-calculated from the simulation results, in each case.

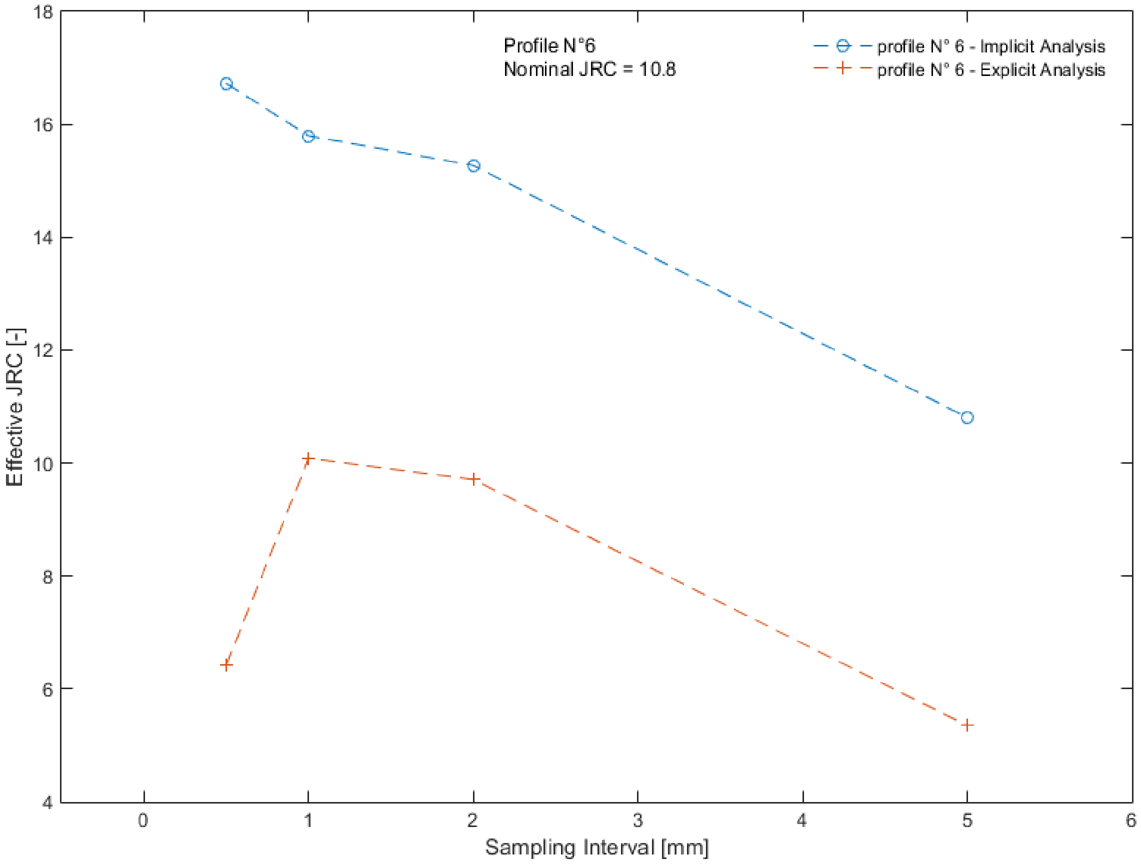

Figure 4.12. Comparison of the sampling interval effect on the effective JRC back-calculated from an explicit and implicit analysis, Profile n°6, Nominal JRC = 10.8.

## 4.3 Scale Effects on Shear Strength

As indicated in section 3.7, load-controlled tests were used to perform the scale effects on shear strength study. Small-scale models (~ 100 mm) direct shear test simulations were performed; then, the same models were enlarged by ten times the size (Figure 4.13), keeping all its material and joint properties intact, and direct shear tests were performed.

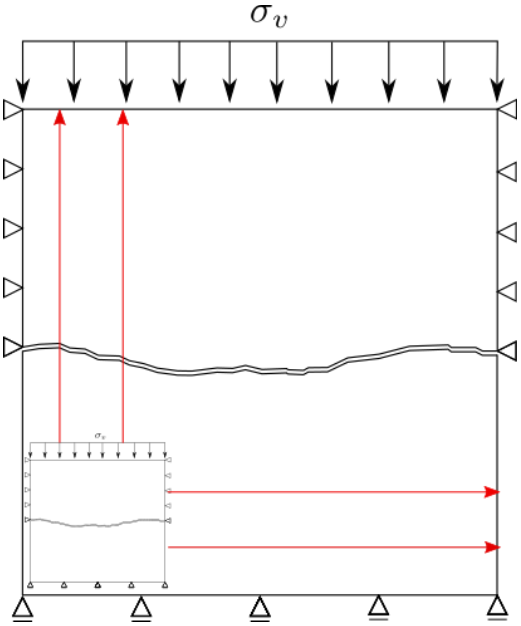

Figure 4.13. Different scales models.

Due to issues with the convergence of models under load-controlled conditions, high sampling interval was used (2 mm) for the study, to assure convergence of the models. The considered vertical stresses are shown in Table 4.4.

Table 4.4. Sampling intervals and normal stresses used for the Scale Effect Analysis.

| **Normal Stresses [MPa]** | 0.1 | 0.5 | 1 | 1.5 |
|---|---|---|---|---|
| **Sampling Interval [mm]** | 2 | | | |

### 4.3.1 Shear Test Simulation Results

Figure 4.14 shows the results for load-controlled and displacement-controlled tests, for small scale models (~100 mm) and varying normal stresses, for Barton profile n° 6. Figure 4.15, shows load-controlled tests results for both small-scale and big scale models. The nomenclature used is explained in Table 3.6. The results for the rest of the profiles is found in Appendix E.

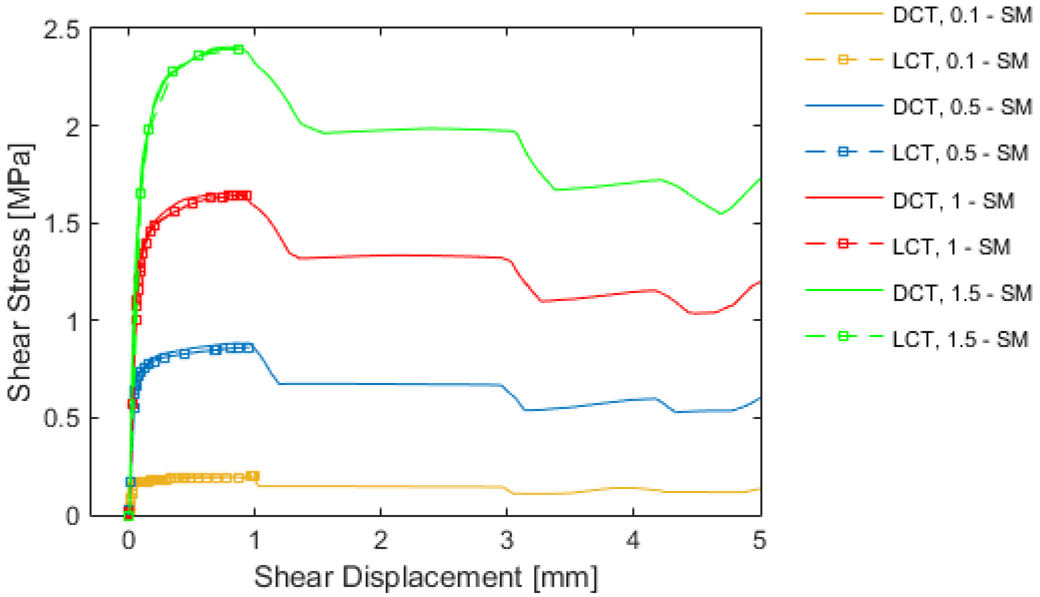

Figure 4.14. Shear stress v/s shear displacement test results for load-controlled (LCT) and displacement controlled (DCT) small-scale models (SM). Profile N°6, SI = 2 mm, nominal JRC = 10.8.

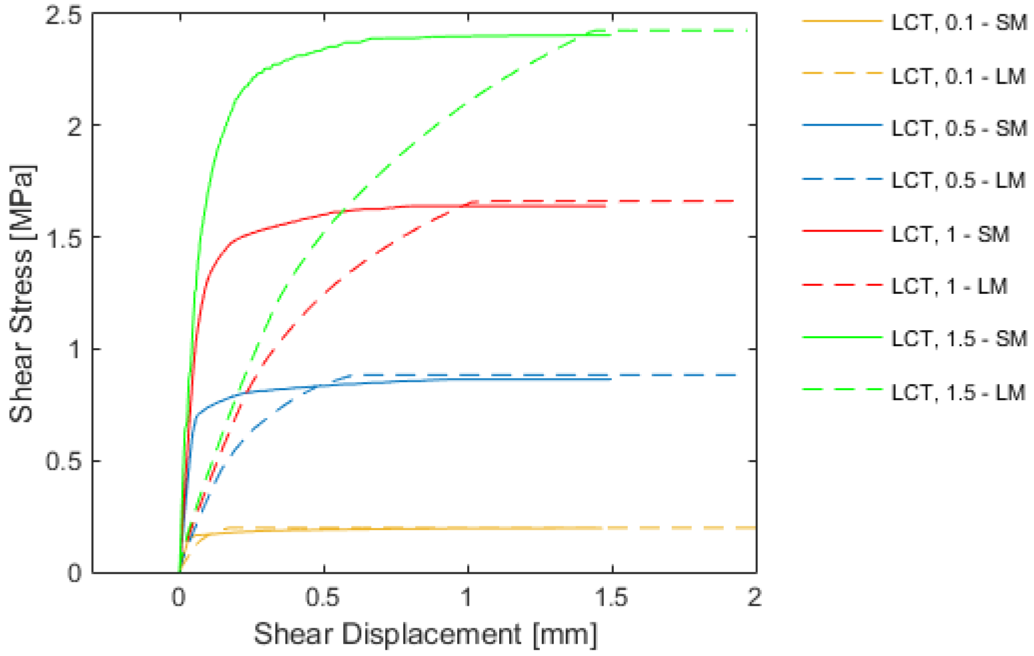

Figure 4.15.Shear stress v/s shear displacement test results for load-controlled (LCT) of small-scale (SM) and large-scale (LM) models. Profile N°6, SI = 2 mm, nominal JRC = 10.8.

To assess the stiffness of the joints, the results of the shear for both small-scale and large-scale models where normalized by their full length, as follows:

$$\epsilon_s = \frac{\delta_s}{L_x} \tag{4.1}$$

Where $\epsilon_s$ is the shear strain, $\delta_s$ is the shear displacement and $L_x$ is the length of the joint. Figure 4.16 shows the shear stress – shear strain curves, for Barton profile N°6.

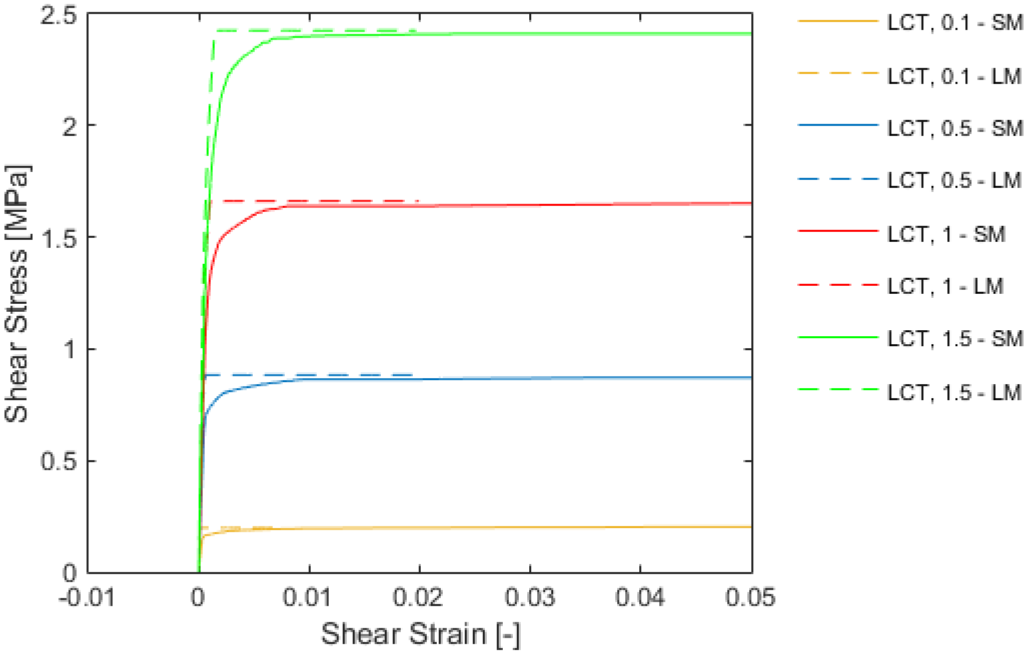

Figure 4.16. Shear stress v/s shear strain test results for load-controlled (LCT) small-scale models (SM) tests and large-scale models (LM), Profile N°6, SI = 2 mm, nominal JRC = 10.8.

Table 4.5 summarizes the execution time of the test, for large-scale and small-scale models, for profile N°6, at a sampling interval of 2 mm. Because the tests are load-controlled, there is no definite simulation end, so the final shear displacement reached for each test is included in the table.

Table 4.5. Execution time, for load-controlled tests, on small and large-scale model, profile N° 6, S.I. = 2 mm

| **Test normal stress** | **Small-scale model (99 mm)** | | **Large-scale model (990 mm)** | |
|---|---|---|---|---|
| | Execution Time [min] | Final Shear Displacement [mm] | Execution Time [min] | Final Shear Displacement [mm] |
| 0.1 [MPa] | 2 | 3 | 6 | 7.2 |
| 0.5 [MPa] | 6 | 2.4 | 8 | 73 |
| 1 [MPa] | 10 | 4.1 | 16 | 37.4 |
| 1.5 [MPa] | 18 | 2.4 | 27 | 35.5 |

# 5 Results Analysis and Discussion

## 5.1 Analysis of Results

The following section presents an analysis for the results shown in Chapter 4.

### 5.1.1 Sampling Interval Effects

**Peak Shear Strength**

Figure 4.1 shows the influence of the sampling interval in the mobilized peak shear strength, with the peak shear strength decreasing as the sampling interval increases. This behavior is seen in the results of every tested profile although it is less noticeable in the low JRC profiles, n°1 and n°2 (Figure 4.1a and Figure 4.1b respectively). The reduction in the peak shear strength when larger sampling intervals are used, is related to a shift in the mobilized asperities, from small steep asperities, to larger - smoother ones, the shift in asperities mobilization induces a change from a brittle to a more ductile behavior, requiring a larger shear displacement to mobilize the full strength of the joint. Although a peak shear strength is reached for lower sampling intervals in every case , only the smoother profiles, show a clear "residual" shear strength also, in both Profile n° 6 and n°9 (Figure 4.1c and Figure 4.1d respectively), there is no convergence to a residual value in the tests results. The predicted peak shear strength by the Barton-Bandis (1982) criterion is closer to the results for the test with a sampling interval equal to 5 mm. Lower sampling interval tests overestimate the joint shear strength. Finally, issues with the convergence of the rougher models, with smaller sampling intervals (0.1 and 0.5 mm), are detected, which will be discussed later.

The summary of the peak shear strength of each test as a function of the applied normal stress and the sampling interval, in Figure 4.2, shows a clear over estimation of the shear strength of the joints in the numerical simulation, when compared to the Barton-Bandis predicted value, for profiles n°1, 2 and 6 (Figures 4a, 4b, and 4c, respectively). The results of the simulations that agree the most with the shear strength predicted by the Barton-Bandis criterion are those with a sampling interval of 5 mm, in the case of profile n° 9 (Figure 4.2d), there is an underestimation in the shear strength of the joint, when a S.I. of 5 mm is used, compared to the Barton-Bandis predicted shear strength. In all cases, but especially in the rougher profiles, the results of the simulation show a more linear behavior, when compared to the Barton-Bandis criterion, where the non-linear component is given by the JCS/$\sigma_n$ ratio. The behavior on the profile n°9 results, for sampling intervals of 1 and 2 mm is erratic, with a higher shear strength in the cases of the lower sampling interval, at normal stresses higher than 1 MPa, although the peak for the 2 mm case is developed at a shear displacement that the 1 mm profile didn't reach due to convergence problems, which highlights the issues with convergences for rougher profiles, at lower sampling intervals.

The summary of each test performed, under varying loads and sampling intervals, for profile N°6 (Figure 4.3), agrees with the points commented above. It must be noted that convergence issues increase with higher applied normal stresses, as seen in the results for S.I. equal to 5 mm (Figure 4.3). This is related with the non-linearity of the interaction and will be discussed further in section 5.2. The impact of the sampling interval on the profile geometry is seen on Figure 4.4, smaller wavelength are not captured with higher sampling intervals, thus reducing the roughness of the profile and its impact on the shear strength, it is important to note that the "filtering" made by the sampling interval is not clean, not only removing smaller asperities but also modifying the geometry of asperities of larger wavelengths.

Figure 4.5 shows results presented on Figure 4.2 from another perspective, making easier to study the effect of the sampling interval on the peak shear strength, as a function of the normal load applied on the joint. In general, the peak shear strength mobilized by the joint is reduced for higher sampling intervals, as discussed before. It is important to note that there is no change in the sensibility to the sampling interval for varying normal stresses, which does not happen in reality, where smaller asperities are crushed at higher normal stresses, reducing its contribution to the shear strength greatly, as discussed later.

### Dilation

The results of the dilation of the joints agree with what was expected, with a reduction in the vertical displacement and secant dilation angle of the joints for higher normal stresses and larger sampling intervals.

There is a brief initial section with negative dilation, which later increases continuously. The length of the section is a function of the applied normal load. No correlation between the negative dilation amplitude with the profile roughness or the S.I. was found, as seen in the summary of the dilation on tests performed on profile N°6, for varying normal stresses and sampling intervals (Figure 4.7). When comparing the dilation between the results of profiles of different roughness, under the same applied normal stress (1 MPa), it was found that the dilation increases with increasing roughness (Figure 4.6).

### Back-calculation of JRC

The results of the JRC back calculation (Figure 4.8) for each profile, shows a reduction in the effective JRC with higher sampling interval values. A constant sensitivity to the sampling interval, for different normal stresses, is observed, an expected result given the behavior show by the peak shear strength for varying sampling intervals and loads (Figure 4.5). The results of the profiles N°1 and N°2 (Figure 4.8a and Figure 4.8b respectively), shows an overall significant difference between the back calculated JRC and its nominal value. In the case of rougher profiles, n°6 and n° 9, the nominal values agree with low sampling intervals, for the cases of low normal stress.

Figure 4.9 and Figure 4.10 summarize the sampling interval effect on the roughness of the model, by back-calculation of the mean effective JRC, using the parameters included in
Table 4.3. An overall decrease of the effective JRC with increased sampling interval is observed. Profiles n° 4 and n° 5 show a behavior that wasn't expected, as profile N°4 effective JRC surpasses N°5's at 3 of the 4 tested sampled intervals. In Figure 4.10 the normalized JRC of the profile n°1 is highlighted due to its large value. This is explained due low nominal JRC (0.4), which amplifies the normalized values.

### 5.1.2 Explicit and Implicit Analysis

Results obtained by the explicit analysis do not show an agreement between the peak shear strength and the sampling interval used, as seen in Figure 4.12, where the highest shear strength is obtained for the sampling interval equal to 2 mm and the lowest for the 0.5 mm, which isn't expected. On the other hand, implicit analysis results do follow the expected trend of reduction of the peak shear strength for larger sampling intervals, for the same profile and property conditions (Figure 4.3). Although using the explicit scheme analysis allows to complete the tests simulations, the implicit scheme analysis was preferred due to the good relationship shown by the models in the shear strength variation at different roughness and sampling intervals, with the expected results, as discussed earlier.

### 5.1.3 Scale Effects Analysis

Large-scale and small-scale models mobilize the same shear strength, as seen in Figure 4.15. Small-scale models appear more rigid than the large-scale ones, taking less shear displacement to mobilize its shear strength; however, when the shear displacement is normalized by the profile total length (Figure 4.16), large-scale models are more rigid.

When comparing the simulation time between different tests (Table 4.5), for a fixed sampling interval (2 mm), it is found that higher normal stresses require more computation time since higher normal stresses induce a high nonlinear behavior on the interacting joints, requiring smaller simulation time increments to solve the problem. The comparison between small-scale and large-scale models is not direct, even though the large-scale model takes more time for every normal stress, the reached shear displacement varies greatly, still, both model, small and large scale, stay on the same order of magnitude

## 5.2 Discussion

Based on the analyses shown on 5.1 the discussion of the results is presented below.

### 5.2.1 General Model Behavior

Although it is not apparent in the figures, due to the high sampling interval used in the models presented in this work (2 mm), load-controlled tests tend to non-convergence more easily than displacement-controlled ones, which does not allow the use lower sampling intervals or higher normal stresses. This is explained by two reasons; first, there is a rotational component imposed on the loaded side of the box, due to the unilateral loading, a phenomenon that is more relevant on rougher surfaces. This rotational component could not be completely solved due to conflicts with over-constrainment of the model. When no rotation is enforced, the over-constrainment induces a non-convergence by itself. Second, contact problems naturally have more issues with load-controlled conditions, as a large force increment may induce displacement that may not be solved in reasonable step time increments. An important result is that, at the same scale, both load-controlled and displacement-controlled models reached the same peak shear strength, at the same shear displacement before sliding, as seen in Figure 4.14, which validates the load-controlled method, even with all its issues.

A crucial point to discuss is the model lack of convergence for certain tests, usually at low sampling intervals, high nominal JRC and high vertical pressures, as seen for profiles n°9, n°10 (Figure D.17 and Figure D.19 respectively, Appendix D). Also, an erratic behavior was found for the results of profile n°9 tests, with results that do not follow the overall trend of the smoother profiles. An assessment of the model reliability for rougher profiles is required, ideally with more tests perform on the rough profiles. The implicit analysis is deemed not successful in performing the simulations for rougher profiles, a quasi-static, well calibrated and filtered explicit analysis is a possible solution for this issue.

### 5.2.2 Sampling Intervals Effect on Shear Strength

#### Peak Shear Strength

The shear stress/displacement curves of rougher profiles (Figure 4.1) show a more evident post-peak behavior than the smoother ones, this is an expected result in experimental tests, as the unevenness that allows a higher peak is sheared, resulting in lower resistance at large displacement. This is not an expected behavior for the models, as failure of the elements is not possible as a plastic constitutive law was considered, instead of a fragile one. A likely reason for this is that overriding small steep asperities is enough to decrease the shear strength, even if these asperities are not sheared in the process. Also, at higher stresses, rougher models showed a localization of the plastic strains in the interfaces, instead of continuing with the overriding. This limits the asperities overriding and may reduce the shear strength of the joint.

The overestimation of the shear strength of joint may have several reasons. First, the Barton-Bandis shear strength criterion considers the UCS as a representation of the material resistance, but this parameter is not a direct input in the model nor is used to calibrate it, which means that, even though the c, $\phi$ and the UCS were obtained from the same source, the correlation may not be direct, causing a possible over estimation of the strength of the rock in the input parameters used in the model. Also, an elastoplastic model was used, which means that “failed” elements still resist stresses, contrary to what happen to brittle materials, where failed asperities are sheared and no longer can resist shear stress. On the other hand, small steep asperities that may be easily sheared are not broken in the model and contribute to the shear strength of the whole test simulation time. The obtained results corroborate Grasselli et al. (2002) results, who found that a larger number of steeper and usually smaller asperities getting in contact with the opposing surfaces was positively correlated to a higher peak shear strength.

## Dilation

The dilation of the models is a function a roughness, sampling interval and normal stress, with the peak vertical displacement decreasing with larger sampling intervals and normal stresses. The small initial negative dilation was first thought to be an issue with rigid rotation of the of the top of sample since the rotation is not directly constraint, which was later discarded as there is no increase in the negative phase with normal stress or profile roughness. Bandis (1983) assumed zero dilation at the start of the test up to one third of the peak shear displacement, disregarding negative dilation. It has been found that published experimental results do have an initial negative phase in the dilation (Figure 5.1) and has been already suggested as a correction to the Bandis proposition (Figure 5.2) by Assadollahi et al. (2010).

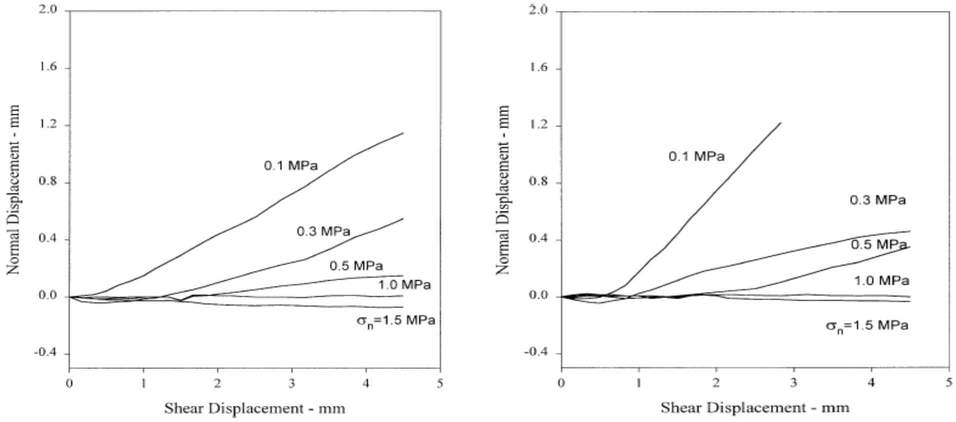

Figure 5.1. Normal Displacement v/s Shear displacement por saw-tooth profiles (a) asperities with a 15° of inclination (b) asperities with a 30° degree of inclination (Huang et al., 2002).

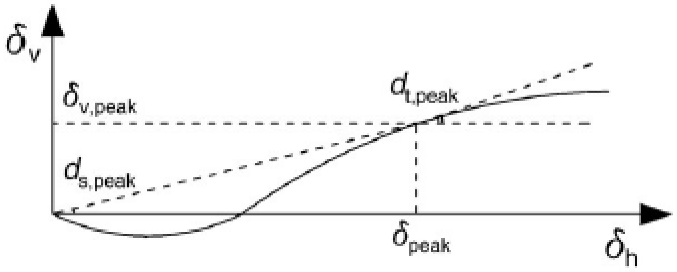

Figure 5.2. Suggested dilation model (Assadollahi, 2010)

When comparing the obtained results to the ISRM guidelines for laboratory characterization of rock joints (Muralha et al., 2014), shown on Figure 2.4d, only the first section of the test relates to the simulation results, with no decline in the vertical displacement in the post-peak behavior.

## JRC Back-calculation

The sensitivity of the effective JRC may be explain by the asperity plastification effect on the mobilized shear strength, which may be understood using the concept of energy, considering that at every increment of shear loading, there must be equilibrium between the external work and the internal energy. In reality, asperity will mobilize more internal energy as the loading increases, until the asperity is overridden, crushed or sheared. In the case of the last two, the brittle failure of the steeper asperities means that its contribution to the total energy becomes 0, generating a redistribution of stresses to smoother asperities, which are less likely to reach failure, but aren't capable of mobilizing the same energy (or strength). In the performed simulations, once the asperities reach failure, plastification occurs, a fully plasticized asperity won't be able to mobilize more strength, but will not reduce its reached contribution either, which means that the contribution of steeper asperities will be always present.

The effective JRC curves for the rest of the profiles fall under the expected behavior, besides the overall increase in the JRC of the profiles, when compared to the Barton and Choubey (1977) experimental results. The correlation is nonlinear and an increase in the sampling interval may result in a big drop in the JRC. This is explained since large sampling intervals may not capture key asperities in the joint interaction, and as such reduce the effective JRC

The JRC v/s sampling interval charts may not be used as a reference, as more profiles need to be tested to increase the chart robustness. In particular, it is important to assess the behavior of joints of similar nominal JRC but different geometry. This will allow to study JRC effectiveness as a roughness characterization parameter and not only as adjusting constant, as it was developed initially. Ideally, more roughness characterization parameters, such as $Z_2$, structure function (SF) and fractal dimension D (Appendix B) should be included in the analysis, to assess each method robustness and behavior.

Another way to explain the over estimation of the shear strength of the model, is that the steeper asperities seen in the profiles with lower sampling interval (Figure 4.4), which should increase the shear strength of the joint in the model, may not have an incidence in the peak shear strength measured in laboratory tests, as they are rapidly sheared on real experiments, before mobilizing a meaningful amount of strength, a phenomenon not reproduced by the model used in this work. This effect was already noted by the Tatone et al. (2013) for surface roughness measurements, who concluded that roughness characterization is heavily dependent on the sampling interval and window size, with profiles measured with higher sampling intervals always showing a larger roughness value, in all of roughness characterization methods used in his study.

### 5.2.3 Scale Effects on Shear Strength

Results found between small-scale and large-scale models do agree with those obtained by Ueng et al. (2010), who tested experimentally synthetic enlarged Barton profile models, and did not found that a scale effect (Figure 5.3).

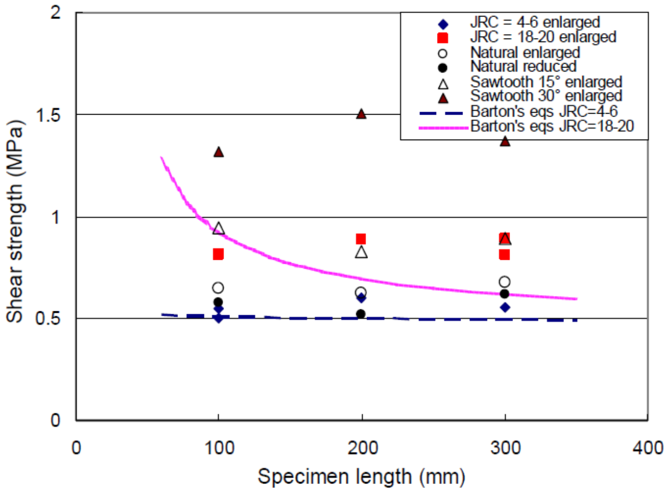

Figure 5.3. Shear strength as a function of scale for enlarged Barton profiles (Ueng et al., 2010)

Observing Figure 4.16, the large-scale model is clearly more rigid, a result that was not expected, since when comparing both models, the large scale does not require to override the asperities as much as the small-scale one. This should not be numerically related since the critical slip displacement was defined as an absolute value and not a function of element size. From this result, it may be proposed that the inclination angle is the defining parameter in joint peak shear strength, and not the degree of overriding of the asperities, but more studies are required to confirm.

An important consideration is that the results should not be extrapolated to real in-situ conditions, due to differences between the followed methodology and how rock joint properties scale in nature. In this work, it was assumed that the properties of the material are constant for all scales, something that has been proved wrong empirically for rock masses (Hudson & Harrison, 1997). Also, it was assumed that the surface geometry would scale in both roughness and asperity height, proportionally to the profile length dimension, which is not right either. In reality, roughness is not the same at different sampling windows, with larger joints having smoother surfaces when asperities height is compared to its length, as seen in Figure 5.4.

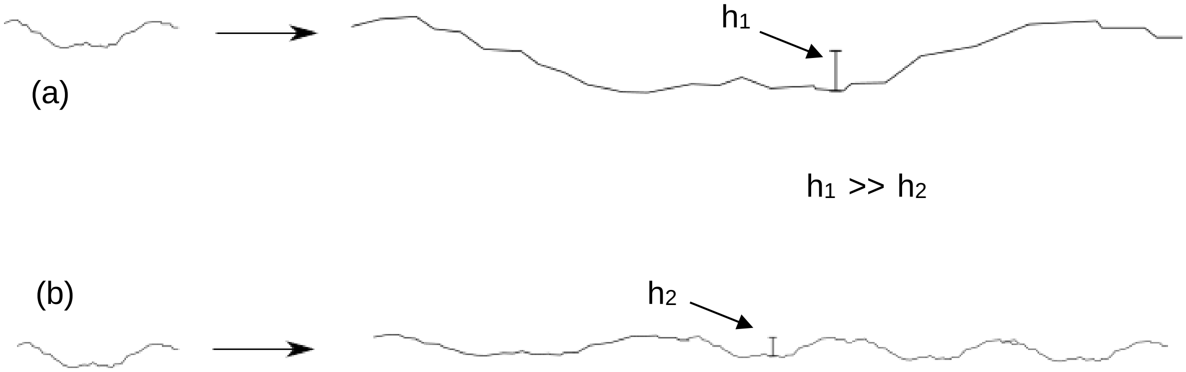

Figure 5.4. (a) followed methodology to study scale effects on this work (b) representation of geometry scaling in nature.

This work assumes the wrong idea of using the JRC directly to estimate the shear strength of joints, as a professional may try to measure the surface geometry of large-scale joints and characterize it directly by inspection and comparison or a correlation with the JRC. However, as the results found have shown, doing this considers that both small and large-scale joints would be able to mobilize shear strengths of the same order, which has been recognized as wrong empirically. It must be noted that the scale effects on shear strength are a topic that is still widely studied and a consensus in its behavior is far from being closed.

## 5.3 Practical Implications

Until this day, there is not a standard methodology to assign a JRC value to a joint in the field several orders magnitude larger than the laboratory scale. Although the complete joint surface topography may be measured and digitized (Oppikofer et al., 2011), using complete joint surfaces as input for numerical stability models would be computationally expensive, since potential rockslides are composed by several joints with different roughness properties (Oppikofer et al., 2008). Instead, joints are usually modeled as straight lines with a Barton-Bandis (1982) failure criterion, with the JCS, $\phi'$ and JRC as input parameters (García et al., 2018; Kveldsvik et al., 2008; Sepúlveda et al., 2012).

For clean rock joints, i.e. no gouge found in between the joint surfaces, the following approaches to determine the large scale JRC currently exist:

1. Determining the small scale JRC value through visual comparison or laboratory tests perform on specimens directly extracted from outcrops or drill cores (50 to 100 mm-length specimens). Then, scale the JRC using an scaling law, such as the Barton-Bandis scale law (Barton & Bandis, 1982).
2. Performing in-situ tilt-tests on specimens with a length equal to the block size, extracted directly from the joint of interests. According to Barton & Choubey (1977) experience, scale effects for lengths larger than the block size are negligible. In this case, the specimen length does not exceed a couple of meters.
3. Measuring the complete joint surface topography through contact or non-contact methods (Appendix A), assigning a JRC value through an analysis of the complete surface topography.

As noted on this work, scale effects on the shear strength occur due to differences in the geometry of the joint, for different scales, and differences in the rock mechanical properties, with both phenomena interacting together in the joint shearing process. Rock mechanical properties may be scaled based on literature or laboratory tests, although the scatter on the results is high and depends on the rock mineralogy (Darlington et al., 2011; Thuro & Plinninger, 2001; Thuro et al., 2001). The first method lacks a way to consider geometry scaling unless it is directly considered through an extra waviness component added to the shear strength of the joint:

$$\tau = \sigma_v * \tan(\phi_b + s_n + i) \tag{5.1}$$

Where $s_n$ corresponds to the small asperity component (roughness) and i to the large asperity component (waviness).

Since rock joints profiles and surfaces are better modeled as self-affine rather than self-similar fractals (Huang & Doong, 1990b; Kulatilake & Um, 1999; Mandelbrot, 1982; Odling, 1994; Yang et al., 2001) (Appendix B.2), small specimens need to be scaled by different factors in its height and length (Figure 5.4). Considering a self-affine fractal model, the scaling factor SF would be:

$$SF = \begin{cases} r \text{ for Length} \\ r^H \text{ for Height} \end{cases} \tag{5.2}$$

Where r is the scaling factor and H is the Hurst exponent, which is related to the fractal dimension D of the profile. Since H depends on the roughness of the profile, the sampling interval and the estimation method, it is hard to estimate it correctly, existing differences in the values for the Barton profiles, obtained by different authors (Yang et al., 2001).

In the case when the complete surface topography of the joint is obtained, several methods may be applied to correlate the surface roughness to a JRC value (Appendix B). Although attractive initially, two issues arise from using this methodology:

- It has been found that larger window sizes will give higher roughness parameters values (Tatone & Grasselli, 2013).
- It is not clear how the asperities across different length scales will behave under shear loading.

The asperities of a rock joint profile may be characterized by their wavelength and its inclination with asperity size being directly and partially related to the wavelength and inclination, respectively. In large rock joints, asperities of large wavelength always have an impact on the shear strength; on the other hand, small wavelength asperities are not always mobilized. The role of the small asperities in the shear strength depends on:

- Degree of alteration and weathering.
- Existence of filling material inside the joint.
- Matedness degree.
- Ratio between intact wall compressive strength and normal loading (JCS/$\sigma_n$).

In the case of fresh joints, the first two points do not apply. The impact of the matedness has been well documented (Johansson, 2016; Zhao, 1997), and depends on the degree of relative displacement between the surfaces (in case the rock joint is fresh). The degree of matedness complicates the analysis, since the assumption that the steeper asperities are the one mobilized under shear loading (Grasselli et al., 2002; Tatone & Grasselli, 2010), does not necessarily applies for mismatched surfaces.

Finally, the ratio between JCS/$\sigma_n$ measures, in a simplified way, if smaller wavelength asperities will be overridden, and thus increasing the mobilized shear strength, or be crushed in the shear process, having a negligible impact on the shear strength of the whole joint.
Yang (2001) studied the effect of the order of magnitude of the asperities, generating artificial specimens from joint profiles filtered computationally (Figure 5.5b & Figure 5.5c) and tested experimentally in direct shear using joints casted from the filtered profiles, using molds (Figure 5.6). Yang found that asperities of higher orders of magnitudes have an impact on the shear strength, under high JCS/$\sigma_n$ ratios, but its influence is negligible under lower ratios JCS/$\sigma_n$.

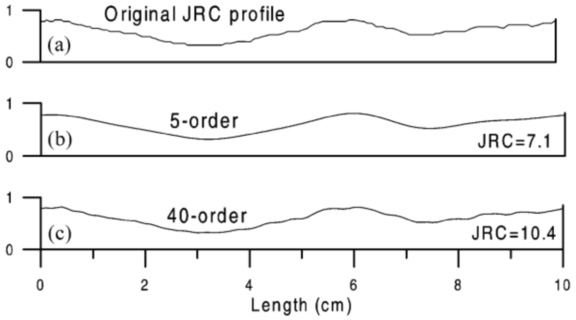

Figure 5.5. filtering of a joint profile (a) Original profile (b) 5th order harmonic profile (c) 40th order harmonic profile (Yang et al., 2001).

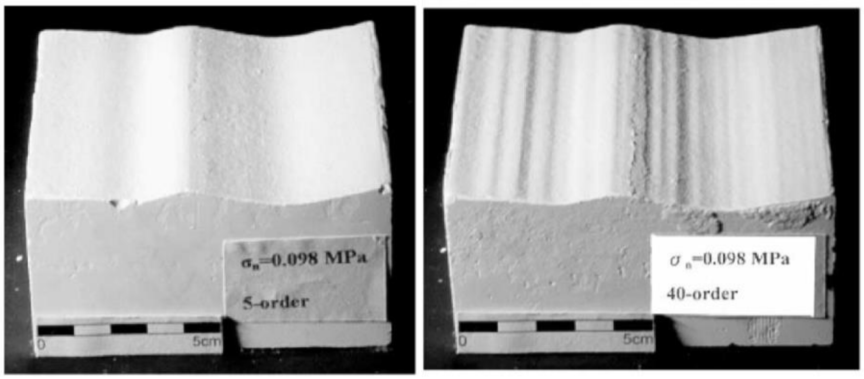

Figure 5.6. (a) 5th order filtered profile (b) 40th order filtered profile (Modified from Yang et al., 2001).

Finally, if it is not possible to characterize the roughness of the profile to the detail (available equipment is limited to a coarse sampling interval or some areas aren't accessible) the small scale asperities may be ignored, using only the large wavelength asperities (Waviness), if its favorable to the slip direction (Hencher & Richards, 2015). for the same case, the roughness characterization may be performed either using the measure of maximum asperity height relative to a mean plane method (Barton, 1982), making use of the chart displayed in Figure 5.7, measuring the inclination of the controlling asperities or with a visual comparison with the Barton profiles. It has to be considered that if a Barton-Bandis criterion is to be used, the compressive strength of the joint wall (JCS) should also be scaled.

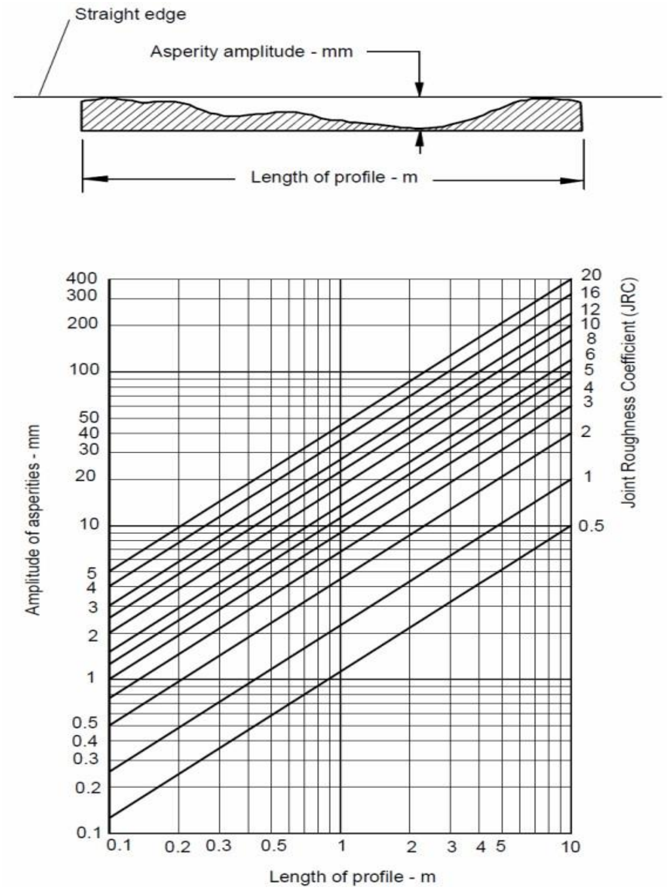

Figure 5.7. Joint roughness coefficient as a function of asperity amplitude and length of the profile (Barton, 1982).

About the asperity amplitude method indicated above, it is important to remember that, as various authors have noted (Patton, 1966; Tatone & Grasselli, 2010; Yang et al., 2001) and the results obtained in this work corroborates (Figure 4.15), the roughness impact on the shear strength is mostly related to the asperity angle, which is usually correlated to asperity height, but not necessarily, which means that, it may be incorrectly assumed that the measured asperity height is correlated to an apparent asperity inclination, which would overestimate the maximum joint asperity inclination.

Neglecting the small-scale roughness will always result in an underestimation of the shear strength, implying that characterizing the roughness with the methods described before, will be always on the safe side for stability assessments. Also, large-scale asperities are, on average, smoother than small scale roughness, which means that their impact on the shear strength should be less sensible to the JCS/$\sigma_n$ ratio.

# 6 Conclusions

The automatization of the numerical direct shear tests of bidimensional rock joint profiles is deemed successful as a highly independent process. Few input parameters are required to draw the shear box geometry, mesh the model, apply boundary conditions, execute the simulations, and post-process the results. Although three different computer programs are used in the process, it can be completely controlled in the Matlab interface, giving a smoother learning curve for any user. The compatibility among the software is enough for the analysis and has the potential for more complex two-dimensional analysis to be performed.

It was determined that the implicit analysis was the most appropriate scheme to perform this study, due to its accuracy, easiness of use, and available material properties. Issues were found with the model convergence and reliability of the results for rougher profiles (Barton profiles N°9 and N°10), at lower sampling intervals and higher normal stresses, which may be related to the issues of implicit scheme with non-linear problems (Dassault Systèmes Simulia Corp., 2013a). The explicit analysis must not be immediately discarded, as it offers strong contact modeling capabilities and the possibility to avoid the convergence issues existent on the implicit analyses, and its calibration should be possible with a complete focus on its performance.

There is an overestimation by the model in the peak shear strength of the tested joints, when compared to the Barton-Bandis predicted peak shear strength, for all cases, especially for smoother profiles (Barton profiles n° 1, 2, 3, and 4), and higher normal stresses. This phenomenon is observed in the linearity of the shear strength – normal stress curves of the test results, not showing the nonlinear component, related to the $\log_{10}\left(\frac{JCS}{\sigma_n}\right)$ in the Barton-Bandis model, which represents the degradation of the small asperities impact on the shear strength. The behavior of the model may be explained by the plastic failure of the mobilized small steeper asperities, instead of a brittle failure, which allows the joint to mobilize higher peak shear strength, even under higher normal loads, not representing the behavior of joints tested experimentally under laboratory conditions.

Results in this study related to the sampling interval are in partial agreement with the literature, the sampling interval was found to be a key parameter when surface roughness characterization, and/or joint numerical simulations are performed. The model was unable to replicate the reduction in sensibility of the sampling interval effect on the peak shear strength, at higher normal stresses; the reason being the model's lack of asperity damage, which overestimate the small asperity contribution to the mobilized shear strength at higher normal stresses. The sampling may induce errors if not accounted in joint roughness measurement and characterization. The parameter by itself may be one of the reasons for the contradicting results found in literature, for scale effects studies, as concluded by Tatone and Grasselli (2013).

The dilation of the model behaves as expected, with a reduction in the peak vertical displacement and secant dilation angle as the sampling interval and/or the normal stress increases, an increase in both peak vertical displacement and dilation angle is observed when profiles get rougher. An initial negative phase in the vertical displacement was found, with the width of the phase being a function of the normal stress, which agrees with the results of experimental tests found on the literature, and the model proposed by Assadollahi et al. (2010), which suggests corrections to the initial proposals made by Bandis (1983), who assumed zero negative dilatancy.

The charts of JRC as a function of sampling interval require a larger number of tested profiles, to understand how profiles of similar nominal JRC but different geometry behave at varying sampling intervals and across different scales. Although more work is required to increase the charts robustness, this work is deemed as a good introduction for more analyses and tests, with the objective to produce charts that may be useful in the engineering practice, and not only in theory, as profiles of larger sampling sizes require a significantly less computation time than smaller ones.

As expected, no difference was found between the peak shear strength achieved by a small profile and its enlarged counterpart. Although this does not follow the results found in the literature, the methodology may be extended to study the scale effects by other means, such as those suggested in Section 6.1. Load-controlled tests displayed no differences with displacement-controlled tests on small-scale models and show no variations in the peak shear strength mobilized by joints of different lengths, as opposed to the displacement-controlled tests. Larger samples were found to be more rigid than the smaller models, suggesting that the asperity inclination is the key geometrical parameter in the asperity overriding impact in the peak shear strength, and not the shear displacement or strain, since the same peak shear strength is mobilized for different values of displacement or strain.

The JRC should not be extended outside of the initial definition, which just proposes a curve fitting parameter developed to consider the roughness influence on peak shear strength of direct shear tests of small-scale models. Several authors have already determined its limitations for an accurate description of the surface roughness. If a precise large-scale representation is desired, one has to be open to consider the JRC and joint length/area insufficient to characterize the scale effect on the joint shear strength, as the small-scale asperity impact on the shear strength of fresh joints depends on the $\left(\frac{JCS}{\sigma_n}\right)$ ratio and the degree of matedness, which don’t have a parameter that characterize them reliably yet. For a stability assessment of a joint, neglecting the small-scale roughness and only using the characterization of the large-scale waviness will always be on the safe side, as waviness with a favorable dip angle will always be mobilized. Classic methods used for small scale roughness characterization may be used for larger-scale undulations, but a scaled JCS must be considered if the Barton-Bandis criterion is to be used.

## 6.1 Recommendations

General model recommendations:

1. Use a model able to consider the tensile strength of the material, as traction failure is a component of the shearing of rock joints, as some authors have noted (Bahaaddini, 2016; Johansson & Stille, 2014).
2. Do a better calibration work for the Abaqus/Explicit quasi-static analysis, to make use of its better contact formulation and assured competition of the analysis.
3. Consider a more complex model formulation (DEM, FEM/DEM) to study fracture propagation and asperity degradation, allowing a better representation of the material behavior under low confining stresses, although, to perform this on several tests, much more processing power is required.
4. Perform tests of three-dimensional surfaces, as joint shearing behavior is anisotropic ((Huang & Doong, 1990b; Kulatilake & Um, 1999; Tatone & Grasselli, 2009a), and as such cannot be simplified to two dimensions if the full phenomenon is to be characterized.

About sampling interval studies recommendations:

1. Perform direct shear simulations with varying sampling intervals, using a lag in the start of the sampling to capture different points. With this methodology, the captured roughness will vary, even with the same sampling interval, which will allow studying if the roughness value, characterized by the JRC, is robust within the profile geometry.
2. Perform the tests for more profiles, to capture a broader number of profiles, this will allow getting a better understanding of the correlation between the effective JRC and its degradation with higher sampling intervals.
3. Perform a characterization of the profile, using more complex roughness characterization parameters such as $Z_2$, $R_p$ or $\left(\frac{\theta^*}{C+1}\right)$, and analyze how these correlates to the change in the shear strength obtain on the simulation, for varying profiles and sampling intervals.

About scale effects studies:

1. Perform numerical simulations of large-scale sampled profiles from the field, so the behavior of natural profiles may be better understood. These simulations may be compared to profiles of similar JRC to measure the differences in the shear strength. Profiles of the same joint may also be numerically sheared independently and be compared to the larger ones.
2. Synthetic small and large-scale profiles may be generated under conditions that assure similar roughness of the profiles, as the methods performed in tribology using fractal geometry and random processes (Borri & Paggi, 2015; Vallet et al., 2009). The benefit is that theoretically, infinite profiles could be

generated and thanks to the random nature of the fractals, profiles generated under the same exact conditions would present different geometry, which would allow studying the roughness characterization method accuracy, and the parameters robustness.

3. A possible approach would be to perform numerical simulations on complete profiles and sections of it of varying length, scaled differently in its length and height, considering a power law relation like the one suggested in equation (5.1), as Figure 5.4 suggests. This approach would allow to study if a relationship between the geometry of a profile and its subsections exist, and how it relates to the shear strength.

To understand the role of the asperity wavelength in the shearing of rock joints, as a function of JCS/$\sigma_n$, a future work methodology is proposed, in which profiles with roughness with multiple scales are processed, filtering the asperities as a function of wavelength (Figure 6.1), these profiles may be tested under direct shear conditions numerically and/or characterizing in terms of its roughness. It is important that the constitutive model used can capture the damage in the asperities, to make the model as realistic as possible.

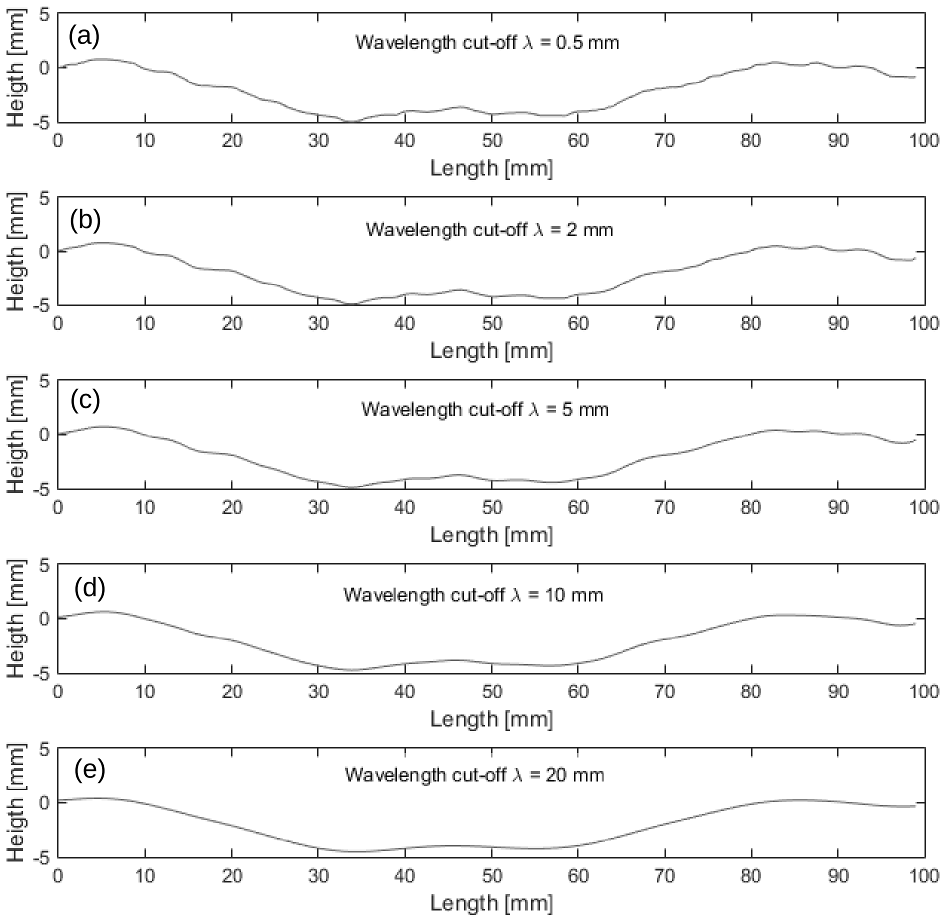

Figure 6.1. Barton profile N°6, Nominal JRC = 10.8, filtered for varying wavelength (a) $\lambda = 0.5\ \mathrm{mm}$ (b) $\lambda = 2\ \mathrm{mm}$ (c) $\lambda = 5\ \mathrm{mm}$ (d) $\lambda = 10\ \mathrm{mm}$ (e) $\lambda = 20\ \mathrm{mm}$.

# 7 Bibliography

Assadollahi. (2010). Constitutive Model for Rock Fracture Revisiting Barton's Empirical Model. *Engineering Geology*, *113*, 11–32.

Astm. (2008). Standard Test Method for Performing Laboratory Direct Shear Strength Tests of Rock Specimens Under Constant Normal Force. *Astm*, *4*(D5607-8), 1–8. https://doi.org/10.1520/D5607-08.

Bahaaddini, M. (2016). Experimental and numerical study of asperity degradation in the direct shear test. *Engineering Geology*, *204*, 41–52.

Bahaaddini, M., Hagan, P. C., Mitra, R., & Hebblewhite, B. K. (2014). Scale effect on the shear behaviour of rock joints based on a numerical study. *Engineering Geology*, *181*, 212–223. https://doi.org/10.1016/j.enggeo.2014.07.018

Bahaaddini, M., Sharrock, G., & Hebblewhite, B. K. (2013). Numerical direct shear tests to model the shear behaviour of rock joints. *Computers and Geotechnics*, *51*, 101–115. https://doi.org/10.1016/j.compgeo.2013.02.003

Bandis. (1980). Experimental Studies of Scale Effects on the Shear Behaviour of Rock Joints. *Terra*, *18*.

Barton. (1973). Range of normal stress The most important factor in the shear strength of a rock joint is the. *Small*, *7*, 287–332.

Barton, N. (1982). Modelling rock joint behavior from in situ block tests: implications for nuclear waste repository design. *Office of Nuclear Waste Isolation*, *ONWI-308*(March), 1–114. Retrieved from http://inis.iaea.org/search/search.aspx?orig_q=RN:14736771

Barton, N., & Bandis, S. C. (1982). Effect of block size on the shear behavior of jointed rock. *The 23rd U.S Symposium on Rock Mechanics (USRMS)*, 739–760.

Barton, N., & Choubey, V. (1977). The shear strength of rock joints in theory and practice. *Rock Mechanics*, *10*(1–2), 1–54. https://doi.org/10.1007/BF01261801

Barton, & Bandis. (1990). Review of predictive capability of JRC-JCS model in engineering practice. *International Symposium on Rock Joints*, (April), 603–610.

Beer, A. J., Stead, D., & Coggan, J. S. (2002). Estimation of the Joint Roughness Coefficient (JRC) by visual comparison. *Rock Mechanics and Rock Engineering*, *35*(1), 65–74. https://doi.org/10.1007/s006030200009

Birch, J., & ADAM Technology. (2006). Using 3DM Analyst Mine Mapping Suite for Rock Face Characterisation. *Laser and Photogrammetric Methods for Rock Face Characterization*, (June 17-18), 15.

Borri, C., & Paggi, M. (2015). Topological characterization of antireflective and hydrophobic rough surfaces: Are random process theory and fractal modeling applicable? *Journal of Physics D: Applied Physics*, *48*(4). https://doi.org/10.1088/0022-3727/48/4/045301

Brady, B., & Brown, E. (1971). *Rock Mechanics information service*. *Rock Mechanics Felsmechanik Mecanique des Roches* (Vol. 3). https://doi.org/10.1007/BF01238443

Brown, S. R., & Scholz, C. H. (1985). Broad bandwidth study of the topography of natural rock surfaces. *Journal of Geophysical Research*, *90*(B14), 12575. https://doi.org/10.1029/JB090iB14p12575

Chioreanu, A., Paul, N., Vlaicu, A., & Orza, B. (2014). 3D techniques used for conservation of museum patrimony 3D Techniques used for Conservation of Museum Patrimony, (January 2008).

Controls Group. (n.d.). Profilometers (Barton Comb). Retrieved February 1, 2018, from http://www.controls-group.com/eng/rock-mechanics-testing-equipment/profilometers-barton-comb.php

Darlington, W. J., Ranjith, P. G., & Choi, S. K. (2011). The effect of specimen size on strength and other properties in laboratory testing of rock and rock-like cementitious brittle materials. *Rock Mechanics and Rock Engineering*, *44*(5), 513–529. https://doi.org/10.1007/s00603-011-0161-6

Dassault Systèmes Simulia Corp. (2013a). Abaqus Analysis User's Manual.

Dassault Systèmes Simulia Corp. (2013b). Abaqus Theory Guide.

Deere, D., & Miller, R. (1966). Engineering Classification And Index Properties For Intact Rock. *Distribution*, *1*, 65–116.

Du, S., Hu, Y., & Hu, X. (2009). Measurement of joint roughness coefficient by using profilograph and roughness ruler. *Journal of Earth Science*, *20*(5), 890–896. https://doi.org/10.1007/s12583-009-0075-3

Fardin, N. (2008). *Influence of structural non-stationarity of surface roughness on morphological characterization and mechanical deformation of rock joints*. *Rock Mechanics and Rock Engineering* (Vol. 41). https://doi.org/10.1007/s00603-007-0144-9

Feng, Q., Fardin, N., Jing, L., & Stephansson, O. (2003). A New Method for In-situ Non-contact Roughness Measurement of Large Rock Fracture Surfaces. *Rock Mechanics and Rock Engineering*, *36*(1), 3–25. https://doi.org/10.1007/s00603-002-0033-1

García, M., Pastén, C., Sepúlveda, S. A., & Montalva, G. A. (2018). Dynamic numerical investigation of a stepped-planar rockslide in the Central Andes, Chile. *Engineering Geology*, *237*(February), 64–75. https://doi.org/10.1016/j.enggeo.2018.02.001

Ge, Y., Kulatilake, P. H. S. W., Tang, H., & Xiong, C. (2014). Investigation of natural rock joint roughness. *Computers and Geotechnics*, *55*, 290–305. https://doi.org/10.1016/j.compgeo.2013.09.015

Geuzaine, C., & Remacle, J.-F. (2017). Gmsh.

Giacomini, A., Buzzi, O., & Krabbenhoft, K. (2008). MODELLING THE ASPERITY DEGRADATION OF A SHEARED ROCK JOINT USING FEM. *Rock Mechanics and Rock Engineering*, *41*(2), 229–266. https://doi.org/10.1007/s00603-007-0139-6

Gischig, V., Preisig, G., & Eberhardt, E. (2016). Numerical investigation of seismically induced rock mass fatigue as a mechanism contributing to the progressive failure of deep-seated landslides. *Rock Mechanics and Rock Engineering*, *49*(6), 2457–2478. https://doi.org/10.1007/s00603-015-0821-z

Grasselli, G. (2001). *Shear Strength of Rock Joints Based on Quantified Surface Description*. https://doi.org/10.1007/s00603-006-0100-0

Grasselli, G., Wirth, J., & Egger, P. (2002). Quantitative three-dimensional description of a rough surface and parameter evolution with shearing. *International Journal of Rock Mechanics and Mining Sciences*, *39*(6), 789–800. https://doi.org/10.1016/S1365-1609(02)00070-9

Hencher, S. R., & Richards, L. R. (2015). Assessing the Shear Strength of Rock Discontinuities at Laboratory and Field Scales. *Rock Mechanics and Rock Engineering*, *48*(3), 883–905. https://doi.org/10.1007/s00603-014-0633-6

Hoek, E. (2006). Practical Rock Engineering.

Huang, T. H., Chang, C. S., & Chao, C. Y. (2002). Experimental and mathematical modeling for fracture of rock joint with regular asperities. *Engineering Fracture Mechanics*, *69*(17), 1977–1996. https://doi.org/10.1016/S0013-7944(02)00072-3

Huang, & Doong. (1990a). Anisotropic shear strength of rock joints.

Huang, & Doong. (1990b). Anisotropic Shear Strength of Rock Joints.

Hudson, J. A., & Harrison, J. P. (1997). *Engineering Rock Mechanics*. *Engineering Rock Mechanics*. https://doi.org/10.1016/B978-008043864-1/50021-5

ISRM. (1978). Suggested methods for the quantitative description of discontinuities in rock masses. *Int. J. Rock Mech. Min. Sci. Geomech. Abstr.,*. https://doi.org/10.1016/0148-9062(79)91476-1

Jaboyedoff, M., Oppikofer, T., Abellán, A., Derron, M. H., Loye, A., Metzger, R., & Pedrazzini, A. (2012). Use of LIDAR in landslide investigations: A review. *Natural Hazards*, *61*(1), 5–28. https://doi.org/10.1007/s11069-010-9634-2

Jang, H. S., Kang, S. S., & Jang, B. A. (2014). Determination of Joint Roughness Coefficients Using Roughness Parameters. *Rock Mechanics and Rock Engineering*, *47*(6), 2061–2073. https://doi.org/10.1007/s00603-013-0535-z

Johansson, F. (2016). Influence of scale and matedness on the peak shear strength of fresh, unweathered rock joints. *International Journal of Rock Mechanics and Mining Sciences*, *82*, 36–47. https://doi.org/10.1016/j.ijrmms.2015.11.010

Johansson, F., & Stille, H. (2014). International Journal of Rock Mechanics & Mining Sciences A conceptual model for the peak shear strength of fresh and unweathered rock joints. *International Journal of Rock Mechanics and Mining Sciences*, *69*, 31–38. https://doi.org/10.1016/j.ijrmms.2014.03.005

Kim, D. H., Gratchev, I., & Balasubramaniam, A. (2013). Determination of joint roughness coefficient (JRC) for slope stability analysis: A case study from the Gold Coast area, Australia. *Landslides*, *10*(5), 657–664. https://doi.org/10.1007/s10346-013-0410-8

King, S., & Richards, T. (2013). Solving Contact Problems with Abaqus. *DS Simulia Abaqus Seminar*, (March), 325. https://doi.org/10.1016/B978-008044637-0/50115-3

Kulatilake, P. H. S. W. (1995). New Peak Shear Strength Criteria for Anisotropic Rock Joints. *Rock Mechanics and Mining Sciences*, *32*(7), 673–697.

Kulatilake, P. H. S. W., & Um, J. (1999). Requirements for accurate quantification of self-affine roughness using the roughness-length method. *International Journal of Rock Mechanics and Mining Sciences*, *36*(1), 5–18. https://doi.org/10.1016/S1365-1609(98)00170-1

Kveldsvik, V., Nilsen, B., Einstein, H. H., & Nadim, F. (2008). Alternative approaches for analyses of a 100,000 m3rock slide based on Barton-Bandis shear strength criterion. *Landslides*, *5*(2), 161–176. https://doi.org/10.1007/s10346-007-0096-x

Lanaro, F. (2000). A random field model for surface roughness and aperture of rock fractures. *Rock Mechanics and Mining Sciences*, *37*, 1195–1210.

Leal Gomes, A. (2003). Some New Essential Questions about Scale Effects on the Mechanics of Rock Mass Joints. *Rock Mechanics*, 721–728.

Lee, D.-H., & Cho, N.-G. (2012). Assessment of surface profile data acquired by a stylus profilometer. *Measurement Science and Technology*, *23*(10), 105601. https://doi.org/10.1088/0957-0233/23/10/105601

Lee, Y. H., Carr, J. R., Barr, D. J., & Haas, C. J. (1990). The fractal dimension as a measure of the roughness of rock discontinuity profiles. *International Journal of Rock Mechanics and Mining Sciences and*, *27*(6), 453–464. https://doi.org/10.1016/0148-9062(90)90998-H

Maerz, N. H. (1990). Joint Roughness Measurement Using, *27*(5), 329–343.

Mahabadi, O. K., Lisjak, A., Munjiza, A., & Grasselli, G. (2012). Y-Geo : New Combined Finite-Discrete Element Numerical Code for Geomechanical Applications, (December), 676–688. https://doi.org/10.1061/(ASCE)GM.1943-5622.0000216.

Mandelbrot, B. (1982). *The Fractal Geometry of Nature*.

Menezes, P. L., & Kailas, S. V. (2016). Role of surface texture and roughness parameters on friction and transfer film formation when UHMWPE sliding against steel. *Biosurface and Biotribology*, *2*(1), 1–10. https://doi.org/10.1016/j.bsbt.2016.02.001

Muralha, J., Grasselli, G., Tatone, B., Blümel, M., Chryssanthakis, P., & Yujing, J. (2014). ISRM suggested method for laboratory determination of the shear strength of rock joints: Revised version. *Rock Mechanics and Rock Engineering*, *47*(1), 291–302. https://doi.org/10.1007/s00603-013-0519-z

Murata, S., & Saito, T. (1999). The variogram method for a fractal model of a rock joint surface. *Geotechnical and Geological Engineering*, *17*, 197–210. https://doi.org/10.1023/A:1008917503259

Odling, N. E. (1994). Natural fracture profiles, fractal dimension and joint roughness coefficients. *Rock Mechanics and Rock Engineering*, *27*(3), 135–153. https://doi.org/10.1007/BF01020307

Oppikofer, Jaboyedoff, M., Blikra, L. H., & Derron, M.-H. (2008). Characterization and monitoring of the Åknes landslide using terrestrial laser scanning. *4th Canadian Conference on Geohazards: From Causes to Management*, *3*, 211–218.

Oppikofer, Jaboyedoff, M., Pedrazzini, A., Derron, M. H., & Blikra, L. H. (2011). Detailed DEM analysis of a rockslide scar to characterize the basal sliding surface of active rockslides. *Journal of Geophysical Research: Earth Surface*, *116*(2), 1–22. https://doi.org/10.1029/2010JF001807

Palmström, A. (2001). Measurement and characterizations of rock mass jointing. *In-Situ Characterization of Rocks - Chapter 2*, 1–40.

Papaliangas, T., Hencher, S. R., & Lumsden, A. (1994). Scale independent shear strength of rock joints. *Integral Approach to Rock Mechanics*, (January).

Papazafeiropoulos, G., Muñiz-Calvente, M., & Martínez-Pañeda, E. (2017). Abaqus2Matlab: A suitable tool for finite element post-processing. *Advances in Engineering Software*, *105*, 9–16. https://doi.org/10.1016/j.advengsoft.2017.01.006

Patton, F. D. (1966). Multiple modes of shear failure in rock. *1st International Congress on Rock Mechanics*, 509–513.

Patton, F. D. (1971). Significant Geologic factor in rock slope stability.

Pells, P. J. N. (2004). Substance and mass properties for the design of engineering structures in the Hawkesbury Sandstone. *Australian Geomechanics*.

Persson, B. N. J., Bucher, F., & Chiaia, B. (2002). Elastic contact between randomly rough surfaces: Comparison of theory with numerical results. *Physical Review B*, *65*(18), 184106. https://doi.org/10.1103/PhysRevB.65.184106

Roshan, H., Masoumi, H., & Regenauer-Lieb, K. (2017). Frictional behaviour of sandstone: A sample-size dependent triaxial investigation. *Journal of Structural Geology*, *94*, 154–165. https://doi.org/10.1016/j.jsg.2016.11.014

Schmittbuhl, J., Gentier, S., & Roux, S. (1993). Field measurements of the roughness of fault surfaces. *Geophysical Research Letters*, *20*(8), 639–641. https://doi.org/10.1029/93GL00170

Selvadurai, A. P. S., & Yu, Q. (2005). Mechanics of a discontinuity in a geomaterial. *Computers and Geotechnics*, *32*(2), 92–106. https://doi.org/10.1016/j.compgeo.2004.11.007

Sepúlveda, S. A., Fuentes, J. P., Oppikofer, T., Hermanns, R. L., & Moreiras, S. M. (2012). Analysis of a large-scale, stepped planar failure in the Central Andes uplands, Chile, using roughness profiles from terrestrial laser scanning. *Landslides and Engineered Slopes: Protecting Society through Improved Understanding*, (August 2015), 1243–1247.

Sharrock, G., & Akram, M. (2009). Application of synthetic rock mass modeling to estimate the strength of jointed sandstone. *American Rock Mechanics Association*, (Figure 1), 1–8.

Standard, J. C. (1964). Stratigraphy, structure and petrology of the Hawkesbury Sandstone. Ph.D. Thesis.

Stimpson, B. (1982). A rapid field method for recording joint roughness profiles. *International Journal of Rock Mechanics and Mining Sciences and*, *19*(6), 345–346. https://doi.org/10.1016/0148-9062(82)91369-9

Sturzenegger, M., & Stead, D. (2009). Close-range terrestrial digital photogrammetry and terrestrial laser scanning for discontinuity characterization on rock cuts. *Engineering Geology*, *106*(3–4), 163–182. https://doi.org/10.1016/j.enggeo.2009.03.004

Swan, G. (1983). Determination of stiffness and other joint properties from roughness measurements. *Rock Mechanics and Rock Engineering*, *16*(1), 19–38. https://doi.org/10.1007/BF01030216

Tannant, D. (2015). Review of Photogrammetry-Based Techniques for Characterization and Hazard Assessment of Rock Faces. *International Journal of Geohazards and Environment*, *1*, 76–87. https://doi.org/10.15273/ijge.2015.02.009

Tatone. (2009). *Quantitative Characterization of Natural Rock Discontinuity Roughness In-situ and in the Laboratory*. University of Toronto.

Tatone, B., & Grasselli, G. (2010). A new 2D discontinuity roughness parameter and its correlation with JRC. *International Journal of Rock Mechanics and Mining Sciences*, *47*(8), 1391–1400. https://doi.org/10.1016/j.ijrmms.2010.06.006

Tatone, B., & Grasselli, G. (2013). An investigation of discontinuity roughness scale dependency using high-resolution surface measurements. *Rock Mechanics and Rock Engineering*, *46*(4), 657–681. https://doi.org/10.1007/s00603-012-0294-2

Tatone, & Grasselli. (2009a). A method to evaluate the three-dimensional roughness of fracture surfaces in brittle geomaterials. *Review of Scientific Instruments*, *80*(12). https://doi.org/10.1063/1.3266964

Tatone, & Grasselli. (2009b). Use of a stereotopometirc measurement system for the characterization of rock joint roughness in-situ and in the laboratory. *Rock Engineering in Difficult Ground Conditions*, *2009*(May), 1–14. Retrieved from http://www.geogroup.utoronto.ca/xe/geogroup/PDF/4145_Tatone_revised.pdf

Tatone, & Grasselli, G. (2012). Modeling direct shear tests with FEM/DEM: Investigation of discontinuity shear strength scale effect as an emergent characteristic. *46th US Rock Mechanics/Geomechanics Symposium*.

Thuro, K., & Plinninger, R. J. (2001). Scale effects in rock strength properties. Part 2. Point load test and point load strength index. *ISRM Regional Symposium Eurock 2001*, 175–180.

Thuro, K., Plinninger, R. J., Zäh, S., & Schütz, S. (2001). Scale effects in rock strength properties. Part 1: Unconfined compressive test and Brazilian test. *ISRM Regional Symposium, 3-7 June*, 169–174.

Tse, R., & Cruden, D. M. (1979). Estimating joint roughness coefficients. *International Journal of Rock Mechanics and Mining Sciences and*, *16*(5), 303–307. https://doi.org/10.1016/0148-9062(79)90241-9

Ueng, T. T.-S., Jou, Y.-J. Y., & Peng, I.-H. (2010). Scale Effect on Shear Strength of Computer-Aided-Manufactured Joints. *Journal of GeoEngineering*, *5*(2), 29–37. Retrieved from http://140.118.105.174/jge/files/articlefiles/v5i2201012071996878529.pdf

Vallet, C., Lasseux, D., Sainsot, P., & Zahouani, H. (2009). Real versus synthesized fractal surfaces: Contact mechanics and transport properties. *Tribology International*, *42*(2), 250–259. https://doi.org/10.1016/j.triboint.2008.06.005

Weissbach, G. (1978). A new method for the determination of the roughness of rock joints in the laboratory. *International Journal of Rock Mechanics and Mining Sciences and*. https://doi.org/10.1016/0148-9062(78)90007-4

Woo, I., Fleurisson, J. A., & Park, H. J. (2010). Influence of weathering on shear strength of joints in a porphyritic granite rock mass in Jechon area, South Korea. *Geosciences Journal*, *14*(3), 289–299. https://doi.org/10.1007/s12303-010-0026-0

Wyllie, D. C., & Mah, C. (2004). Rock Slope Engineering: Fourth Edition, 456. Retrieved from http://books.google.ca/books/about/Rock_Slope_Engineering.html?id=q-pJfpur27gC&pgis=1

Yang, Z. Y., Di, C. C., & Yen, K. C. (2001). The effect of asperity order on the roughness of rock joints. *International Journal of Rock Mechanics and Mining Sciences*, *38*(5), 745–752. https://doi.org/10.1016/S1365-1609(01)00032-6

Zhao, J. (1997). Joint surface matching and shear strength. Part A: joint matching coefficient (JMC). *International Journal of Rock Mechanics and Mining Sciences & Geomechanics Abstracts*, *34*(2), 173–178. https://doi.org/10.1016/S0148-9062(96)00062-9

# Appendix A Surface Roughness Measurement Methods

## Appendix A.1 Contact Methods

Contact methods were the first procedures used to characterize interfaces accurately. Basically, the instrument must be in contact with the joint surface to be able to measure it, this means that direct access to the joint is required, something that is frequently not allowed in usual field conditions.

Although characterization of the joint geometry through two-dimensional profiles is an easier way to describe the discontinuity, the use of profiles requires the shear direction to be known beforehand, If this is not possible, then a complete surface characterization is recommended (ISRM, 1978). Details of the most relevant contact methods are presented below.

### Appendix A.1.1 Linear Profiling

Linear profiling is the process of measuring the perpendicular distances from a straight reference line to the discontinuity surface at regular intervals. The resulting (x, y) coordinates, connected by straight line segments, are referred to as a 2D roughness profile (Tatone, 2009). This can be achieved used different methodologies and instruments such as:

- Mechanical profilometry through combs (Barton & Choubey, 1977; Stimpson, 1982)
- Stylus profilometry (Brown & Scholz, 1985)
- Shadow profilometry (Maerz, 1990).

Mechanical profilometry consists in the use of a comb to capture the profile roughness. The comb must be pressed perpendicular to the analyzed surface, then the profile is plotted on a piece of paper, using the geometry captured by the comb as a reference, as seen in Figure A.1. The comb may be used to characterize both first and second order asperities (unevenness and waviness respectively), although it is recommended to be used mainly for unevenness, due to the limited length of the instrument.

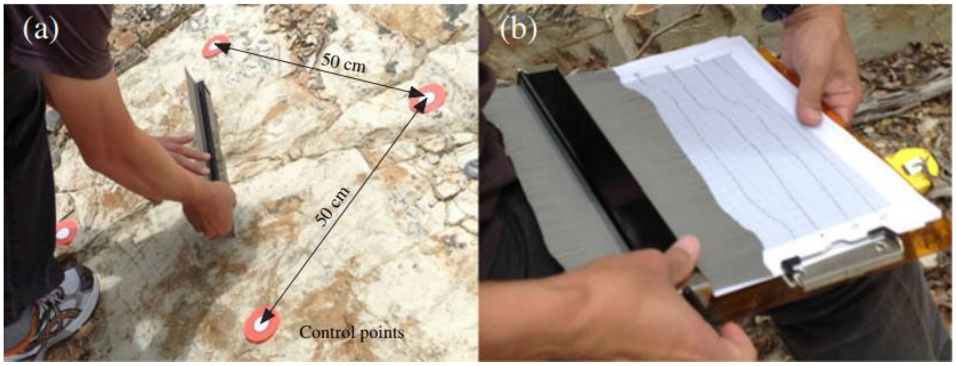

Figure A.1 (a) Barton comb used in situ (b) Obtained profiles (Kim et al., 2013) the precision of combs is limited, the sampling interval depends on the number of pins included in the comb (Tatone, 2009), it is light enough to carry around, 0.5 kg for a 150 mm and 1 kg for a 300 mm one (Controls Group, 2017), and of easy and quick use. These characteristics make it one of the preferred methods to characterize rock joints surface roughness, and the one suggested by the ISRM (ISRM, 1978). Over the years, more advanced version of the Barton Comb have been developed, such as the Du's prophilograph (Du et al., 2009), but the basic principle of the instrument has remained the same.

An option for more accurate results is the profilometer, which describes the studied surface using a stylus, a semi-spherical tip, relatively small compared with the analyzed profile, that moves horizontally in a parallel plane to profile (Figure A.2). Vertical displacements induced in the stylus due to the contact with the profile are measured and saved in a computer through an acquisition system.

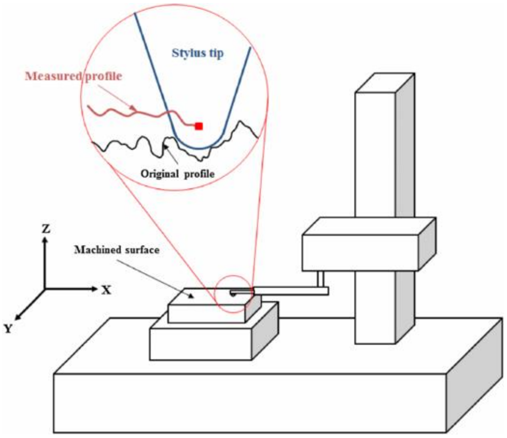

Figure A.2. Surface measurement using a stylus profilometer (D.-H. Lee & Cho, 2012).

In rock joints characterization, profilometers have been mainly used in laboratory setups (Kulatilake, 1995; Swan, 1983; Weissbach, 1978), although there are reports of their use in the field (Schmittbuhl et al., 1993) with success.

### Appendix A.1.2 Shadow Profilometry

In the method of shadow profilometry, a planar intersection is provided by the edge of a shadow cast onto the rock surface from a straight edge. The illumination angle must be kept at 45° to the surface, to ensure that the height of the shadow is the same as the height of the asperity (Maerz, 1990). A video camera is required to record the shadow, a ruler and an object of known height must be included in the setup for scale, as seen in Figure A.3.

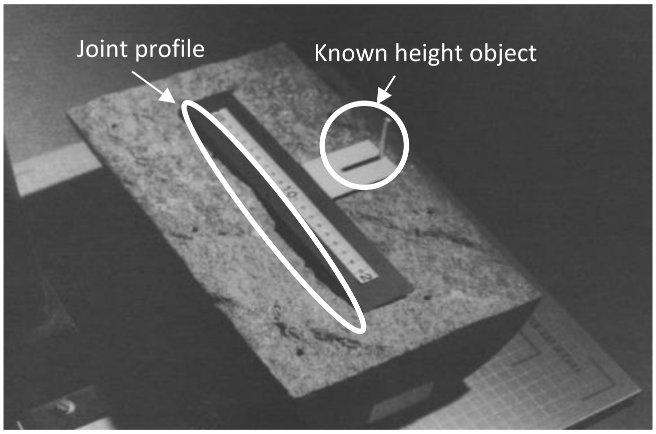

Figure A.3. Shadow profilometry setup (Modified from Maerz, 1990)

## Appendix A.2 Non-Contact Methods

Contact methods have some drawbacks, as they are time-consuming for capturing measurements and difficult to implement at dangerous and inaccessible locations (Feng et al., 2003), in such cases, non-contact methods are preferred, as they are able to measure surfaces in detail and from distances, for example, LIDAR (light detection and ranging) allows measurements up to distance of several hundreds of meters (Sturzenegger & Stead, 2009). Non-contact methods are preferred if the complete characterization of the joint surface geometry is required, if the direction of shear is unknown or if there is a strong anisotropy in the surfaces roughness (Kulatilake, 1995).

The following non-contact methods are the most used in geotechnical applications:

1. Photogrammetry
2. Range Cameras – Light Detection and Ranging (LIDAR)
3. Advanced Topometric Scanner

Although interferometry is a valid method to characterize the surface topography of a joint, it is not included in this review as bibliography about its use in measuring rock joint surfaces, in a rock mechanics context, was not found, Interferometry has several drawbacks, for example, reflective areas on the rough surfaces, like quartz crystals, introduce noise in the measurements, the laser-projection set-ups are difficult to calibrate, and the data is difficult to interpret (Grasselli, 2001). Details of these methods and some of the instrument used in them are presented below.

### Appendix A.2.1 Photogrammetry

Photogrammetry is a method used for determine 3D data from two or more 2D images of a scene. It functions under the principle of identifying the same point in each image and then projecting a ray into the scene from each point through the perspective center of each camera to find the location where they intersect, as seen in Figure A.4 (Birch, 2006).

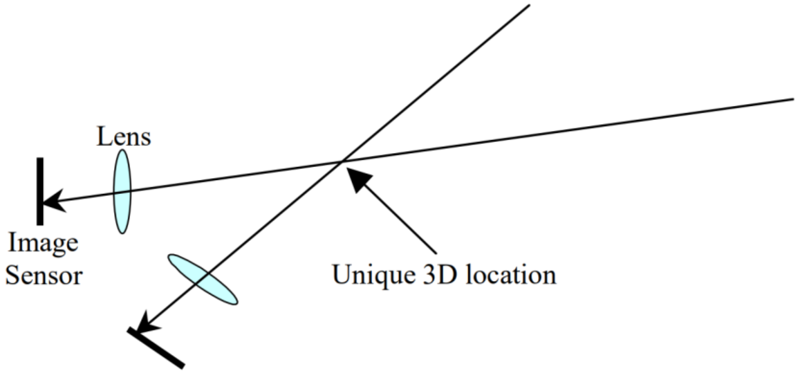

Figure A.4. Photogrammetry principle (Birch, 2006)

Photogrammetry methods date back to middle 19th century, it was suggested as a technique to characterize geotechnical systems by several rock mechanics academicians in the 70's, allowing its inclusion in the ISRM guidelines for joints quantitative description mapping in 1978 (Tatone, 2009). For several decades, the photogrammetry was not used due to several issues, the main one being difficulties with film-based cameras. This changed when CCD (charged coupled device) cameras were commercially available (digital cameras) making possible to study and analyze the images of the surface directly, using a personal computer, without any manual procedures (Grasselli et al., 2002).

Modern digital photogrammetry and image processing can be accomplished with commercial software that has been designed for geotechnical mapping purposes. Generally, the software uses a stereo pair of photos and automatically identifies and uses multiple corresponding points in each photograph to determine the camera location and orientation, and the 3D coordinates of common points in the photos by a complex bundle adjustment algorithm Figure A.5 (Tannant, 2015).

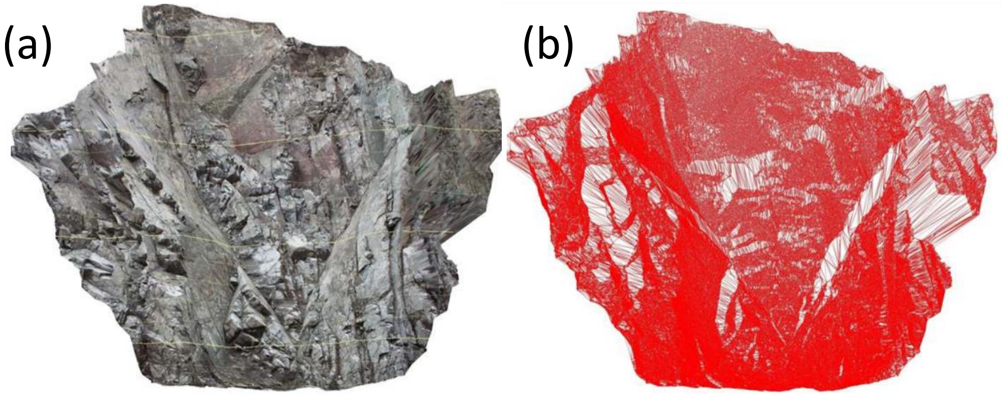

Figure A.5. (a) Oblique view of a digital terrain model of a small section of a rock slope (b) Point cloud created with photogrammetry (Modified from Tannant, 2015).

Several authors have use photogrammetry both in laboratory setups and mainly in situ, with satisfactory results, such as Baker (2008), Sturzenegger (2009), Tannant (2015), among others.

### Appendix A.2.2 Range Cameras – Light Detection and Ranging (LIDAR)

LIDAR systems are based on the principle of light time delay system, the instrument sends out laser pulses that get back-scattered by various objects (joint surface topography, in this case) and record the returning signal. The time of flight of the laser pulse $\Delta t$ is measured to compute distance d, using equation (A.1):

$$\mathrm{d} = \frac{c\Delta t}{2} \tag{A.1}$$

Where c is the velocity of the pulse of the laser beam. Knowing the line of sight (LOS) direction and the attitude, defined as the object orientation with respect to a local system coordinate (pitch, roll, and yaw), of the device allows determining the position $\Delta \mathrm{x}, \Delta \mathrm{y}, \Delta \mathrm{z}$ of a reflective surface relative to the device (Jaboyedoff et al., 2012).

What makes LIDAR the preferred type of laser scanning system for geomechanical characterization purposes is that, compared with other systems that rely on the time of flight concept, they are equipped with two mirrors mounted on orthogonal axes allowing the system to ‘progressively scan’ a 3D scene by automatically varying the azimuth and zenith of the emitted beam (Figure A.6). With the most recent equipment, high precision measurements may be achieved, as seen in Figure A.7, in the characterization made by Ge (2015).

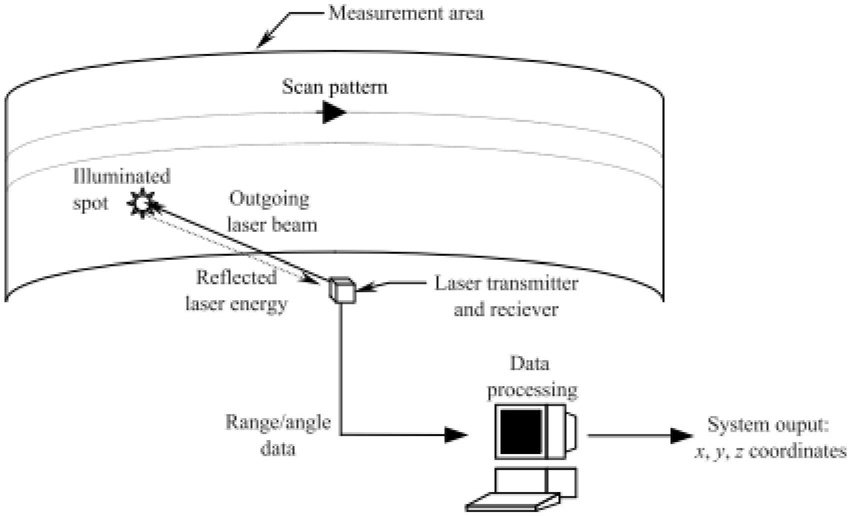

Figure A.6. Measurement principle using LIDAR (Tatone, 2009).

Figure A.7. LIDAR surface topography measurement process (Modified from Ge, 2015)

## Appendix A.3 Fringe Pattern Methods (Active triangulation)

Fringe pattern methods require a measuring head, a tripod, a controlling-box, two cameras, a projector and a PC. During the measurement, various white-light fringe patterns are projected onto the object surface and recorded by two digital cameras, from two different angles, as seen in Figure A.8 (Grasselli et al., 2002). The measurement process is based on the principle of optical triangulation, as the photogrammetry method, the idea is that the three-dimensional geometry of the surface will produce displacement in the stripe patterns projected on the surface, these displacements can be directly converted in 3D coordinates, if the distance of the cameras to the surface and the projector is known.

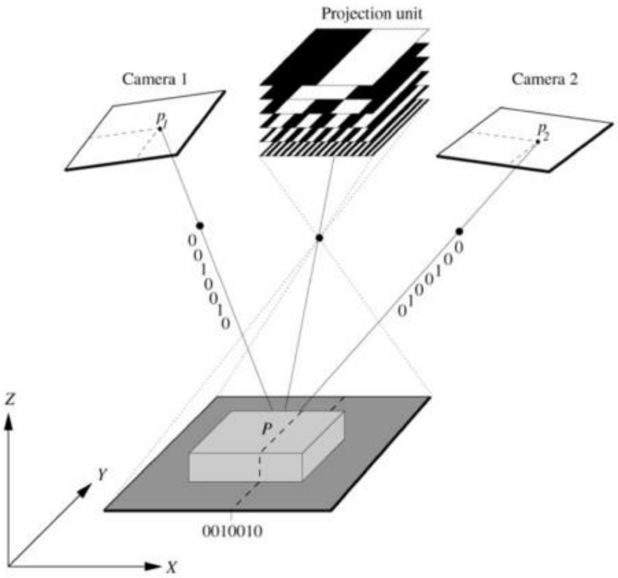

Figure A.8. Different fringe pattern projection (Grasselli et al., 2002).

The precision and range of the fringe projection method depend on the width of the stripes and their optical quality. The optical resolution of fringe projection methods depends on the width of the stripes used and their optical quality. An extreme reduction of stripe width proves inefficient due to limitations in depth of field, camera resolution and display resolution (Chioreanu et al., 2014).

The system is calibrated using a calibration panel with target points, which is placed in various positions. It is not necessary to know the positions of the panel and the target points distribution a priori. In the case of Advanced Topometric Sensor, the accuracy of the point cloud has been computed to be ± 50 µm at least (Grasselli et al., 2002), which means that a high data density of points is obtained, while it allows characterizing the roughness of a surface precisely. It requires a PC with good processing power.

Initially, this method was restricted to laboratory usage due to difficulties with the portability of the required equipment. With the development of stereo topometric measurement systems, the method has been validated both in the laboratory and in-situ conditions (Grasselli et al., 2002; Tatone & Grasselli, 2013, 2009a, 2009b).

# Appendix B Roughness Characterization Methods

## Appendix B.1 Statistical Methods

Mathematical statistical methods have been used by mechanical engineers to characterize surface roughness of metallic plates (Tse & Cruden, 1979), these methods allow characterizing rock discontinuities in an objective way. Statistical methods are available for characterization of both profiles and surfaces roughness.

### Appendix B.1.1 Classic Statistical Parameters

Tse and Cruden (1979) were the pioneers in using statistical methods to characterize rock joint profiles. They calculated the values of several statistical parameters of the Barton and Choubey's rock joint standard profiles (Figure 2.10). Then, they estimated the relationship between the statistical parameter value of each profile and its assigned JRC value. The relationships were assumed to be linear in a semi-log space.

The statistical parameters used by Tse and Cruden (1979) that showed the best correlation to the JRC parameter (R value near 1) were:

- Root Mean Square (RMS)
- The derivative of the Root Mean Square (Z2),
- The 2nd derivative of the Root Mean Square (Z3),
- The Structure Function (SF).

Considering a linear profile of length L, the amplitude height of the profile asperities defined as y(x), with x starting at 0 and ending at L, as seen in Figure B.1, the statistical parameters named above are given by equations:

$$\mathrm{RMS} = \frac{1}{\mathrm{M}}\left(\int_0^{\mathrm{M}} \mathrm{y}^2 \mathrm{dx}\right)^{1/2} \tag{B.1}$$

$$\mathrm{Z2} = \frac{1}{\mathrm{M}}\left(\int_0^{\mathrm{M}} \left(\frac{\mathrm{dy}}{\mathrm{dx}}\right)^2 \mathrm{dx}\right)^{1/2} \tag{B.2}$$

$$\mathrm{Z3} = \frac{1}{\mathrm{M}}\left(\int_0^{\mathrm{M}} \left(\frac{\mathrm{d^2y}}{\mathrm{dx^2}}\right)^2 \mathrm{dx}\right)^{1/2} \tag{B.3}$$

$$\mathrm{SF} = \frac{1}{\mathrm{L}}\int_0^{\mathrm{L}} \left(\mathrm{y(x)} - \mathrm{y(x+D)}\right)^2 \mathrm{dx} \tag{B.4}$$

Where M is the number of discrete measurements of the amplitude height, dx is the small constant distance between two adjacent readings, given by the sampling interval, and D is a fixed distance lag always smaller than L.

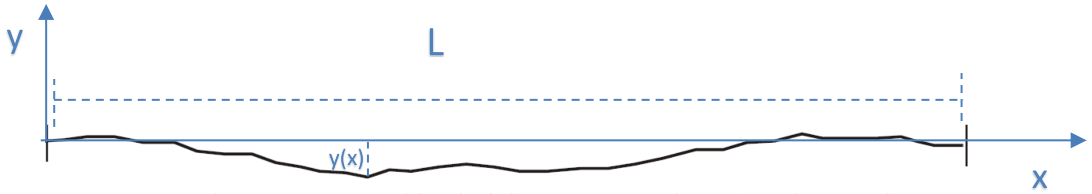

Figure B.1. Asperities height y as a function of profile length x.

From their analysis, Tse and Cruden (1979) concluded that the JRC was strongly correlated to the logarithm of the Z2 and SF parameters, as seen in

$$\mathrm{JRC} = 32.2 + 32.47\ \log_{10}(\mathrm{Z}_2) \tag{B.5}$$

$$\mathrm{JRC} = 37.28 + 16.58\ \log_{10}(\mathrm{SF}) \tag{B.6}$$

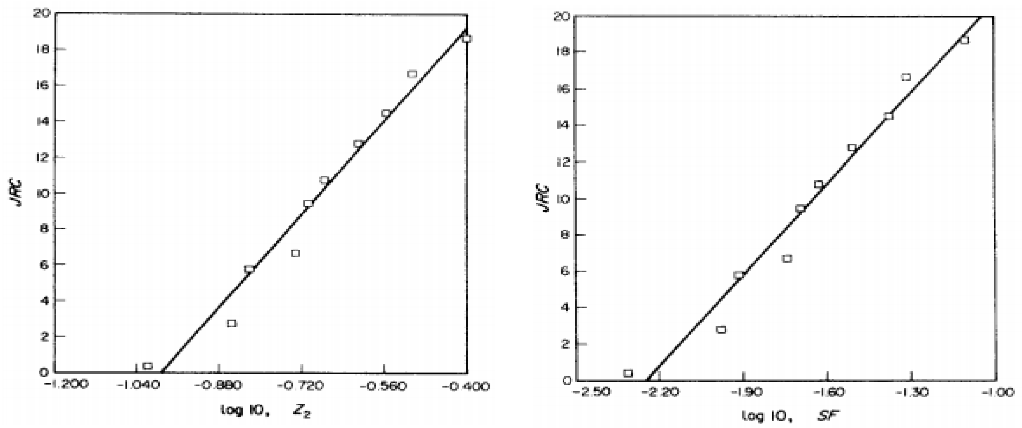

Figure B.2. Correlation between JRC and the $\log_{10}$ of the Z2 and SF parameters (Tse & Cruden, 1979)

Maerz (1990) used the same methodology that Tse and Cruden (1979), but with better digitization tools (computer photo analysis instead of manual digitization), to study the correlation between statistical parameters and the JRC of Barton's predefined profiles.

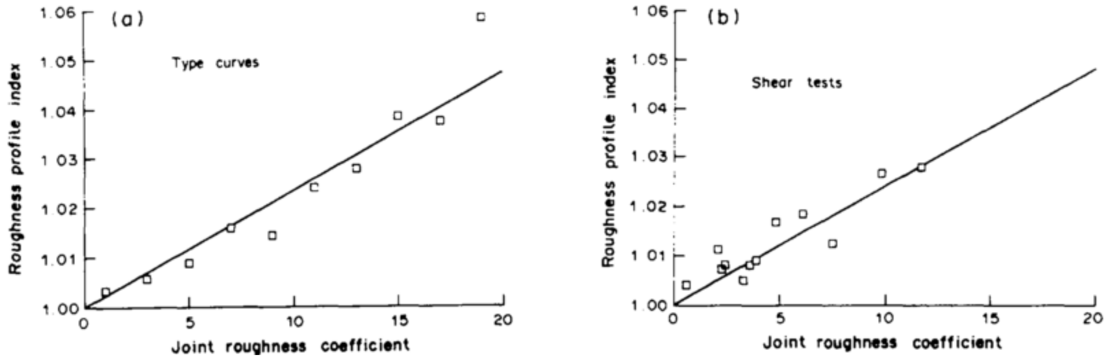

Figure B.3. (a) Correlation between the RP and JRC for Barton's profiles (b) Correlation between the RP and JRC for specimens tested (Maerz, 1990)

In this case, the best fit was given by the Roughness Profile Index (RP), as seen in Figure B.3, defined as the ratio between the true length of a profile $\mathrm{L_t}$ and its projected nominal length L, given by the equation:

$$\mathrm{RP} = \frac{\mathrm{L_t}}{\mathrm{L}} \tag{B.7}$$

Maerz (1990) also compared the measured RP of specimens tested in direct shear test in laboratory settings, performed by personnel of Noranda Mines in core and blocks of 50-300mm size, and analyzed the correlation with the JRC estimated by back analysis of the test results (Figure B.3b), although the scatter of the points is bigger than in Barton's profile case, the positive trend is still observed.

### Appendix B.1.2 The Maximum Apparent Dip Angle

Grasselli (2002) developed the method of estimation of surface roughness, by the measure of the effective surface contact area. In his method, both surfaces of the joint are reconstructed by triangulation of a point cloud. Based on the of the concept of threshold apparent dip angle $\theta^*$, the shearing mechanism may be simplified by assuming that only those zones of the surface facing the shear direction, and steeper than a threshold apparent inclination (defined as $\theta_c^*$), as seen in Figure B.4b, unique for each applied normal load, are involved in the shearing. Among these zones, the areas of the surface inclined exactly at $\theta_c^*$, will be just in contact, whereas the areas inclined more than $\theta_c^*$, will be deformed, sheared or crushed, depending on the redistribution of the normal load applied. In this way, it is possible to discriminate the surface that might be damaged during shearing as a function of a threshold value $\theta_c^*$. The sum of all areas in contact or damage during shearing is termed the total potential contact area, $\mathrm{A_0}$ (Grasselli, 2002).

To begin analyzing the triangulated surface, a specific analysis direction t must be selected. Afterward, the orientation of each individual triangle forming the rough surface can be uniquely identified by its dip and azimuth (Figure B.4a). Given the dip $\theta$ and azimuth $\alpha$, it is possible to define the apparent inclination of each triangle facing the specified analysis direction. This apparent inclination is termed the apparent dip angle $\theta^*$ and can be obtained by projecting the true dip vector d onto a vertical plane oriented along the analysis direction t. Based on the apparent dip angle of each triangle making up the surface, it is possible to distinguish the fraction of the surface that is more steeply inclined than progressively greater threshold values of apparent dip angle $\theta^*$. This fractional area is referred to as the normalized area, $\mathrm{A}_{\theta^*}$, defined by the area of the surface with an apparent dip greater than a selected threshold value normalized with respect to the total area of the surface, $\mathrm{A_t}$. (Tatone & Grasselli, 2009). Then $\mathrm{A}_{\theta^*}$ and $\theta^*$ may be related by the following expression:

$$A_{\theta^*} = A_0 \left( \frac{\theta^*_{\max} - \theta^*}{\theta^*_{\max}} \right)^{C} \tag{B.8}$$

Where C is a curve fitting parameter, calculated via a nonlinear least-squares regression analysis (Figure B.4c). Although C is a curve fitting parameter, studies by Grasselli et al. (2002) and Tatone & Grasselli (2009) determined that the relation $\left(\frac{\theta^*}{C+1}\right)$ on a joint surface, correlates well with surface shear strength, noting $\left(\frac{\theta^*}{C+1}\right)$ as a valid measure of surface roughness. Also, $A_0 \left(\frac{\theta^*}{C+1}\right)$ is the expression for the area below the curve of $A_{\theta^*}(\theta^*)$ between 0 and $\theta^*_{\max}$ (Figure B.4b). Large areas under the curve indicate that the surface contains a larger proportion of steeply dipping asperities and, thus, greater relative roughness (Tatone and Graselli, 2009).

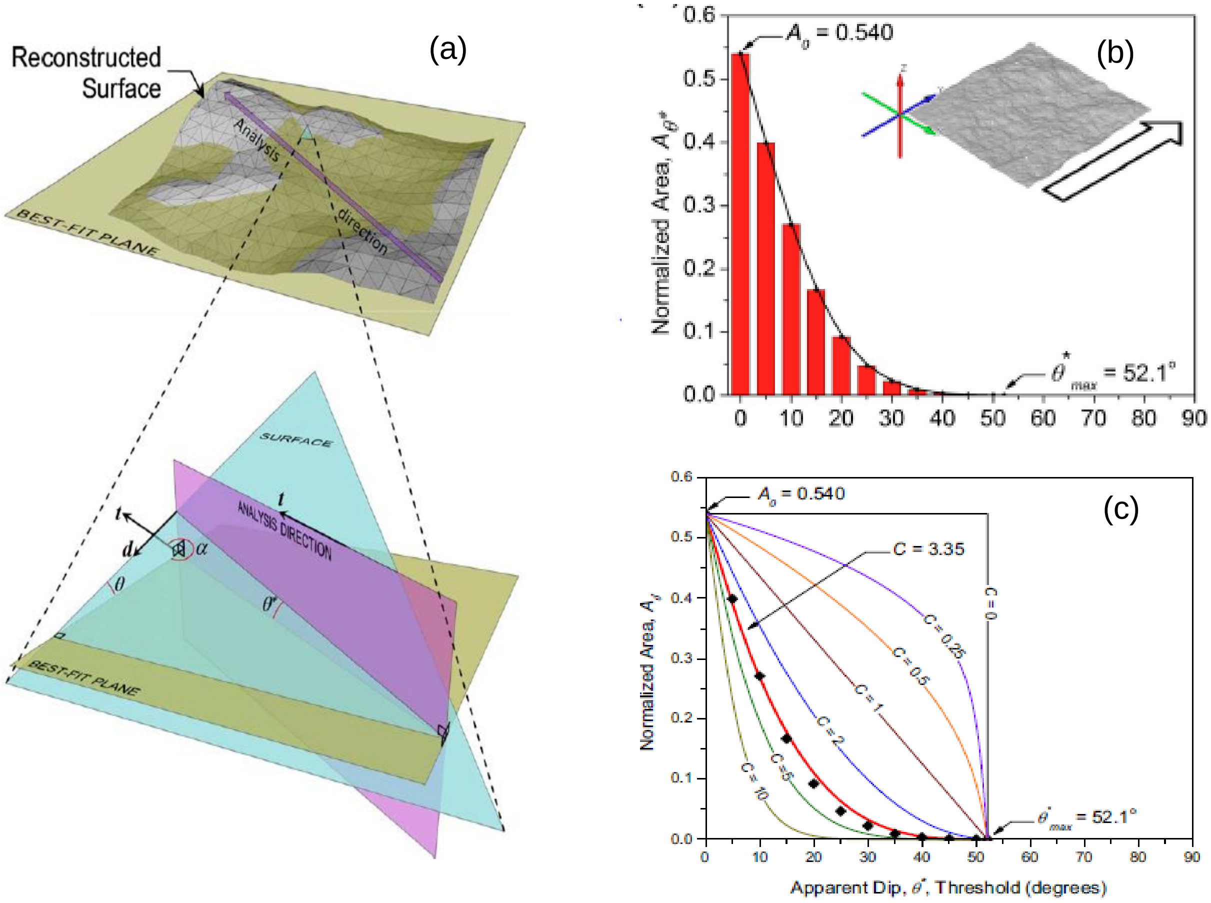

Figure B.4. (a) sheared surfaces as a function of shear direction and asperities dip angle (b) Effective area as a function of dip angle (c) estimation of coefficient C (Modified from Tatone & Grasselli, 2009).

## Appendix B.2 Fractal Methods

Fractal geometry is recurrently found on surfaces of natural origin (Mandelbrot, 1982), a fractal is an object having the property of self-similarity. Self-similarity is defined as a property of certain curves where each part of the curve is indistinguishable from the whole, or that the form of the curve is invariant with respect to scale (Y. H. Lee et al., 1990). In fractal geometry, two big types of fractals are defined, self-similar and self – affine.

A self-similar fractal is a geometric feature that retains its statistical properties through various magnifications of viewing. That means self-similar fractals provide scale invariant values. A self-affine fractal remains statistically similar only if it is scaled differently in different directions (Ge, 2014), as seen in Figure B.5. Rock joints are, on most of the cases, self-affine fractals, as pointed out by Kulatilake (2006) and Ge (2014), which implies that methods developed to obtain the fractal dimension of a self-similar fractal, won't give meaningful results when used to calculate the dimension of a rock joint profile.

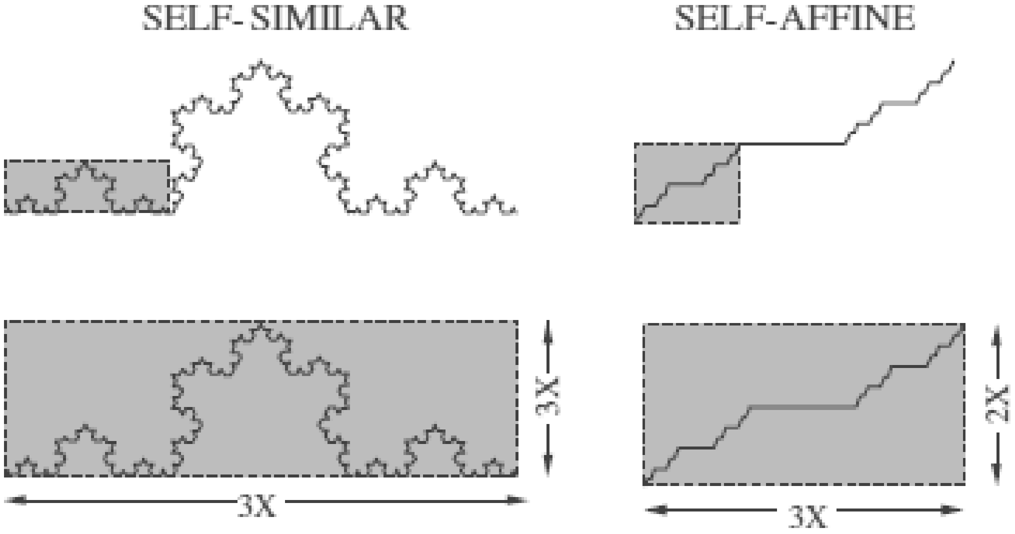

Figure B.5. Self-similar and self-affine fractal (Ge et al., 2014).

Fractals are troublesome to characterize in classical Euclidean geometry, as its topological dimension doesn't give enough information about the fractal. Mandelbrot (1982) developed the concept of Fractal dimension, which is defined as a ratio of the change in detail to the change in scale (Mandelbrot, 1982). According to the definition given by Mandelbrot (1982), the fractal dimension D of a self-similar figure is determined by the equation:

$$\mathrm{D} = \frac{\mathrm{Log\ N}}{\log\left(\frac{1}{\mathrm{r}}\right)} \tag{B.9}$$

Where N is Number of sides on the straight-line segment when a figure is superimposed, and r is the ratio of the figure edge length to the preceding segment length. Higher D values imply higher roughness of the profile, which allows it to use D as a roughness characterization parameter. In the paragraphs below, two of the most used methods to estimate the fractal dimension of rock joints are presented.

### Appendix B.2.1 Divider Method

In the Divider Method, a pair of dividers is set to a span, r, and then "walked" along the irregular line by starting each new step where the previous step leaves off (Figure B.6a). The number of divider steps N(r) needed to walk on the irregular line from one end to the other is counted. If the number of steps is multiplied by the divider, the approximate length of the line L(r) is obtained (Develi, 1998). A linear least-square regression analysis is used to estimate the fractal dimension in a Log-Log scale (Figure B.6b), given by the relationship:

$$\mathrm{Log}(\mathrm{N}) = \log(\mathrm{a}) + (1 - \mathrm{D})\ \log(\mathrm{r}) \tag{B.10}$$

Where Log(a) is the intercept of the log L – Log r plot (Figure A.1b).

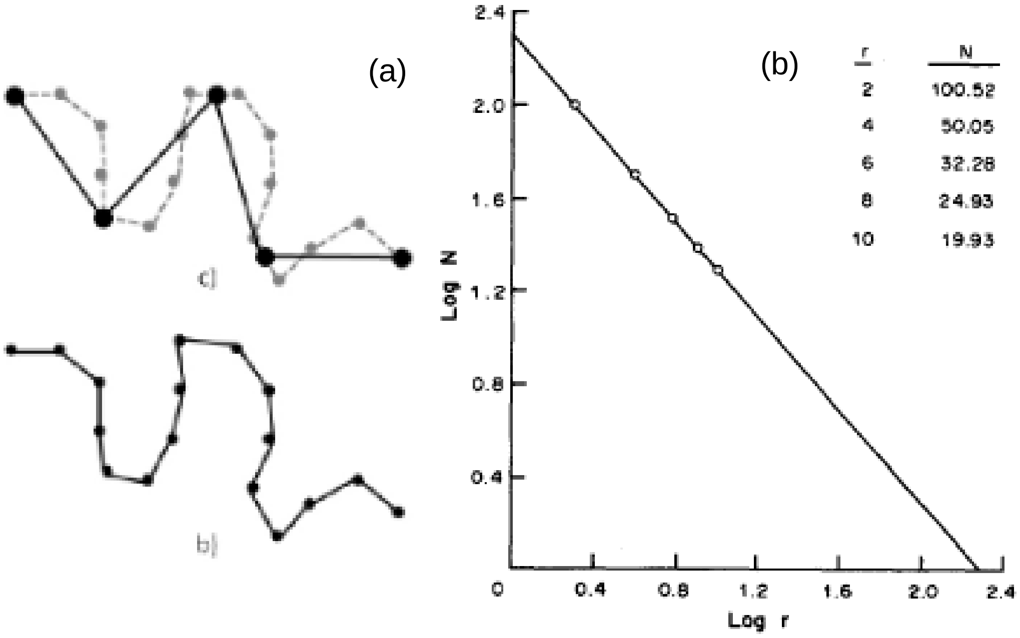

Figure B.6. (a) Divider's Method (Napolitano et al, 2012) (b) Log N – Log r plot (Y. H. Lee et al., 1990).

### Appendix B.2.2 Variogram Method

The variogram method has been used for spatial analysis in geo-statistics for a long time, being the calculation of the mineral’s grade on a certain site the typical use It has. It can also be used to estimate the fractal dimension of natural surfaces. The variogram is defined as the mean squared increment of points:

$$\gamma(\mathrm{h}) = \frac{1}{2\mathrm{n}} \sum[\mathrm{V}(\mathrm{x_i}) - \mathrm{V}(\mathrm{x_{i+h}})]\ \hat{}2 \quad \text{(B.11)}$$

Where, $\gamma(\mathrm{h})$ is the Variogram at lag distance h, $\mathrm{V}(\mathrm{x_i})$ and $\mathrm{V}(\mathrm{x_i} + \mathrm{h})$ are the roughness height at distances $\mathrm{x_i}$ and $\mathrm{x_{i+h}}$ respectively, and n is the number of pairs of roughness heights of the profile spaced at lag distance h. The dimension of the profile may be calculated using the following equation:

$$2\gamma(\mathrm{x}, \mathrm{h}) = \mathrm{K_v} \mathrm{h}^{2(2-\mathrm{D})} \quad \text{(B.12)}$$

Where, $\mathrm{K_v}$ is the intercept of the plot and D is the fractal dimension. $\mathrm{K_v}$ and D may be estimated from a log-log plot of the variogram v/s the lag (Figure B.7) using a least square regression analysis. While usually mono fractals tend to be characterized only by D, Kulatilake (1995) suggest that both Kv and D should be used to describe a rock joint surface topography accurately.

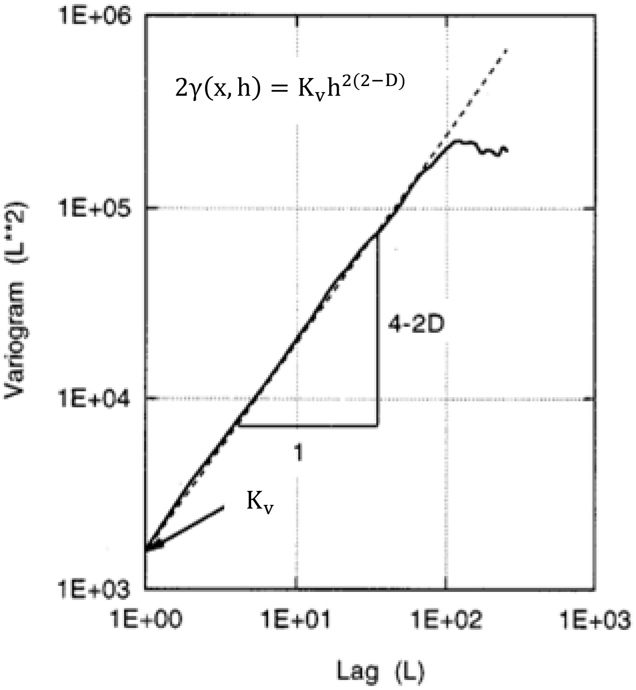

Figure B.7. Variogram v/s lag h plot in log-log scale (Murata & Saito, 1999).

# Appendix C Results processing and Calibration Work in Abaqus/Explicit

## Appendix C.1 Results Processing

For the results processing statistical (moving average) and signal analysis (low-pass filter) methods are available, the latter was chosen for the post-processing due to an induced perturbation on the quasi-static response with the moving average method.

The Low pass filter (Figure C.1) parameters were determined by inspection, while trying to keep the quasi-static response as undisturbed as possible. The filter used and its parameters are described in Table B.1. The filter effect may be seen in Figure C.2.

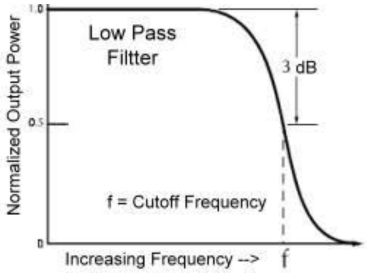

Figure C.1. Low Pass Filter.

Table B.1. Filter Properties.

| Filter | Type of Filter | Order | Frequency Cut-off [hz] | Sampling interval [-] |
|---|---|---|---|---|
| Butterworth | Low-Pass | 3 | 45 | 250 |

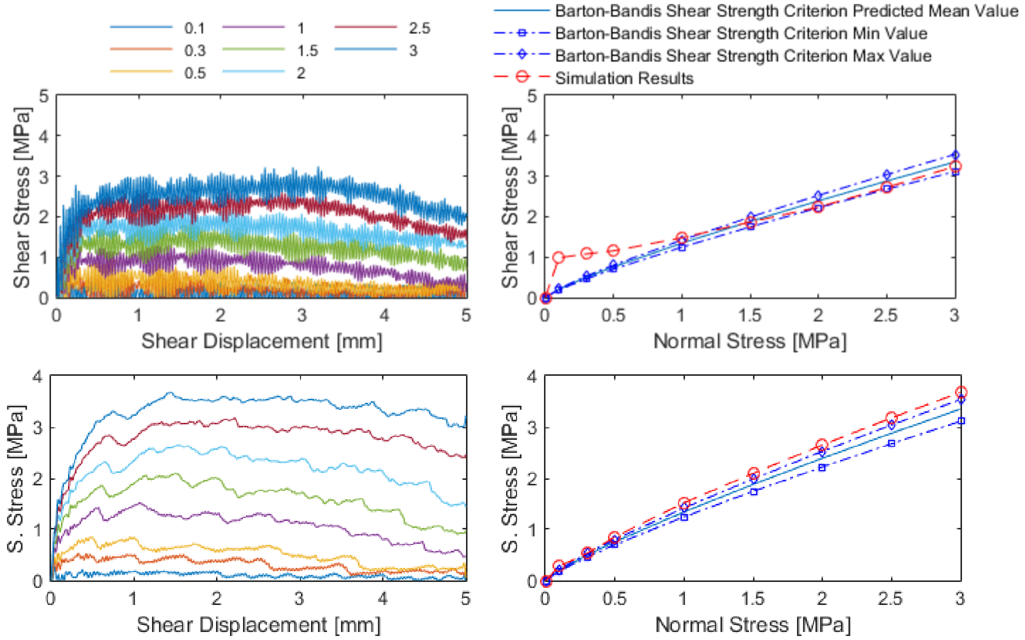

Figure C.2. Filter effect on the Abaqus Explicit results.

## Appendix C.2 Abaqus/Explicit Calibrations

Calibration for the Abaqus explicit analysis follows the same procedure than the Abaqus/Standard case. Keep in mind, that all the results were filtered, which means that there will some inherent bias. All of the models were small scale ( ~ 100 mm); Barton's profile n° 6 shear tests, with a sampling interval of 1 mm and vertical stress of 1 MPa.

### Appendix C.2.1 Shear Stiffness

In Abaqus/Explicit the friction model is controlled by the friction coefficient $\mu$ and the shear stiffness, instead of the $\gamma_{crit}$. Based on Figure 3.7, for a fixed friction coefficient, shear stiffness and $\gamma_{crit}$ are interdependent variables, which means that sensitivity analysis of both variables should have a similar outcome. Results of stress-displacement curves and peak shear strength for 18 different values of shear stiffness are displayed in Figure C.3. Barton profile n°6 was used, with a sampling interval equal to 0.5 [mm] and a normal stress of 1 MPa.

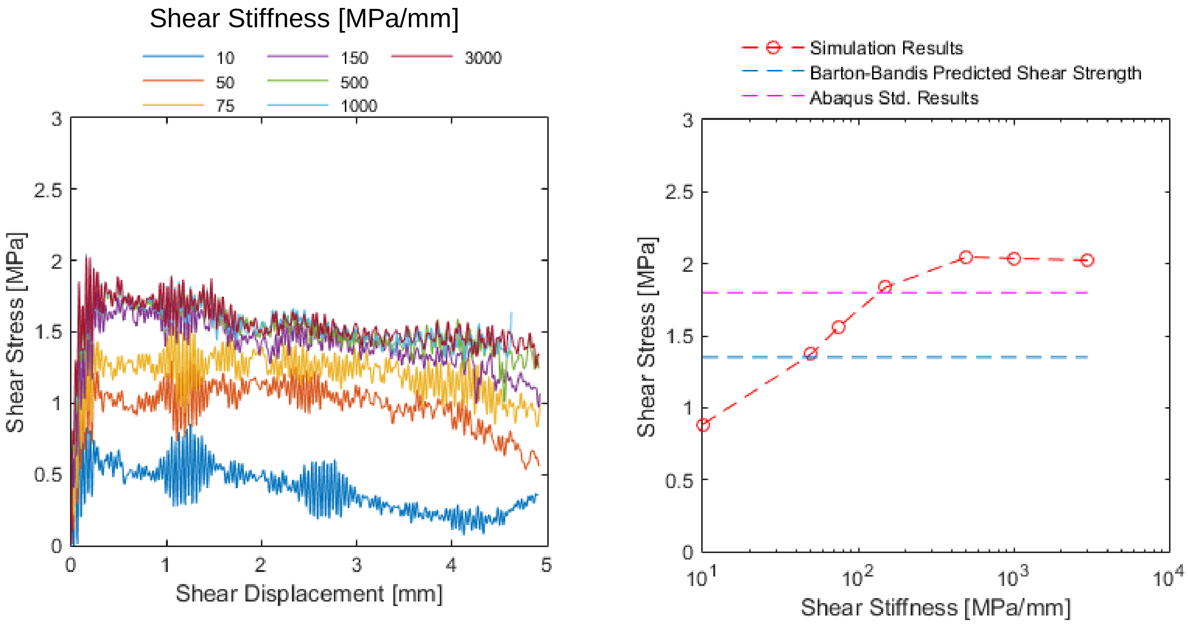

Figure C.3. Shear Stiffness sensitivity analysis results.

The shear stiffness has an influence on the peak shear strength. This may be partially explained if the $\gamma_{crit}$ is a fixed value on Abaqus/Explicit, but at 200 MPa the peak shear strength begins to converge asymptotically to a constant value, 2.1 MPa on this case, higher that both the predicted shear strength by the Barton-Bandis shear strength criterion and the Abaqus Standard results. Although this phenomenon allows the use of shear stiffness as a calibration parameter, it also makes the model less predictable, as the peak shear strength v/s shear stiffness curve may vary for different sampling intervals and scales, as will be seen in section 4.2. For the study, the shear stiffness was calibrated so Abaqus explicit results and the predicted Barton Bandis shear strength were the same.

### Appendix C.2.2 Mass Scaling

Mass scaling sensitivity analysis was not performed to calibrate the model, but to understand how it correlates with the stress/displacement curve behavior and the peak shear strength. Results were divided into two figures, to differentiate between orders of magnitude of the mass scaling value. A semi-log plot is included to visualize the mass scaling effect on the peak shear stress on all of the magnitudes (Figure C.4).

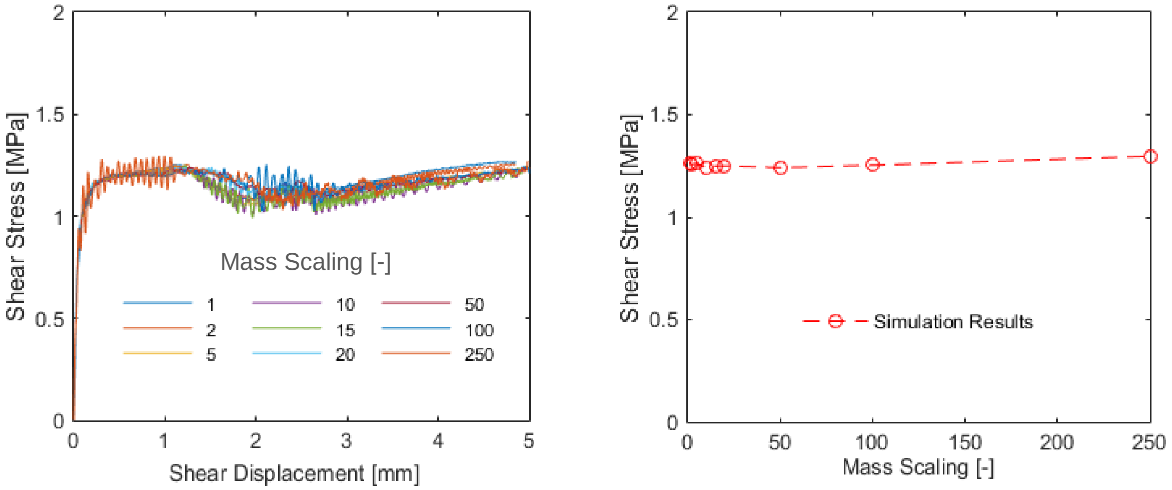

Figure C.4. Mass Scaling Sensitivity Analysis, values from 1 to 250.

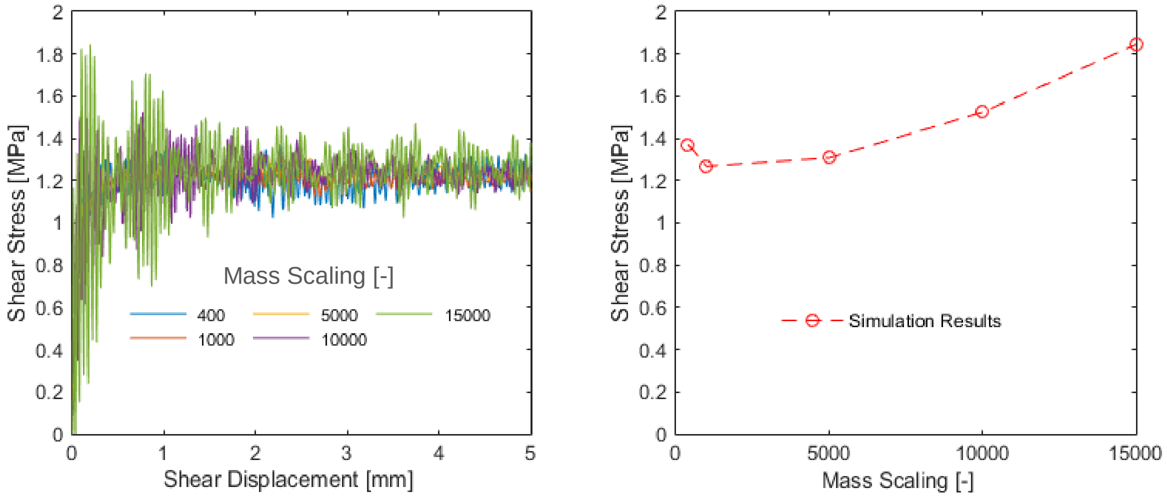

Figure C.5. Mass Scaling Sensitivity Analysis, values from 400 to 15000.

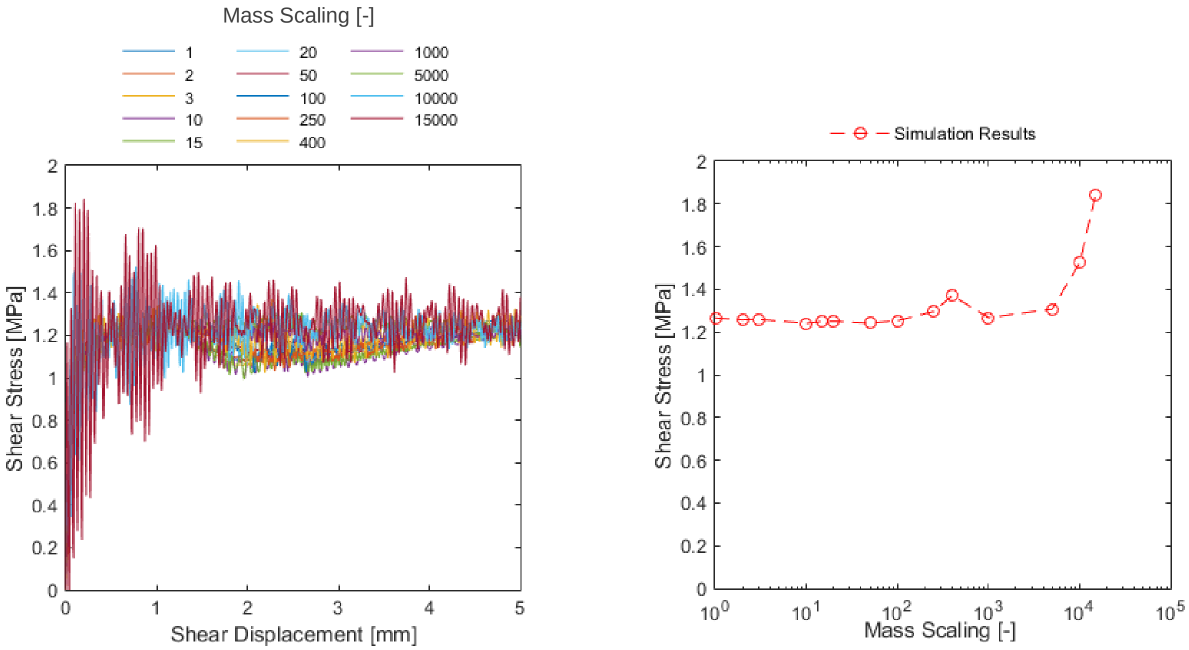

Figure C.6. Mass Scaling Sensitivity Analysis, Semi-log plot for the Shear Stress v/s Mass Scaling.

From Figure C.4, it is noted that variations in mass scaling increase the mid-frequency oscillations but doesn’t alter the stress-displacement curve or the peak shear strength of the joint. On the other side, Figure C.5 shows that mass scaling values of higher order of magnitude (10000 and above) indeed increase the peak shear strength by inducing a higher amplitude in the mid-frequency oscillations. The result pointed out above is important because if the stress-displacement curves are not checked, the performed explicit analysis may induce an overestimation of the peak shear strength, if the mass scaling is high enough. The overall behavior through different magnitudes is seen in Figure C.6, there is a relatively similar shear stress peak until a mass scale of ~$3*10^2$, for higher values the behavior changes.

# Appendix D Sampling Interval Analysis

## Appendix D.1 Shear Strength

### Appendix D.1.1 Profile N°1

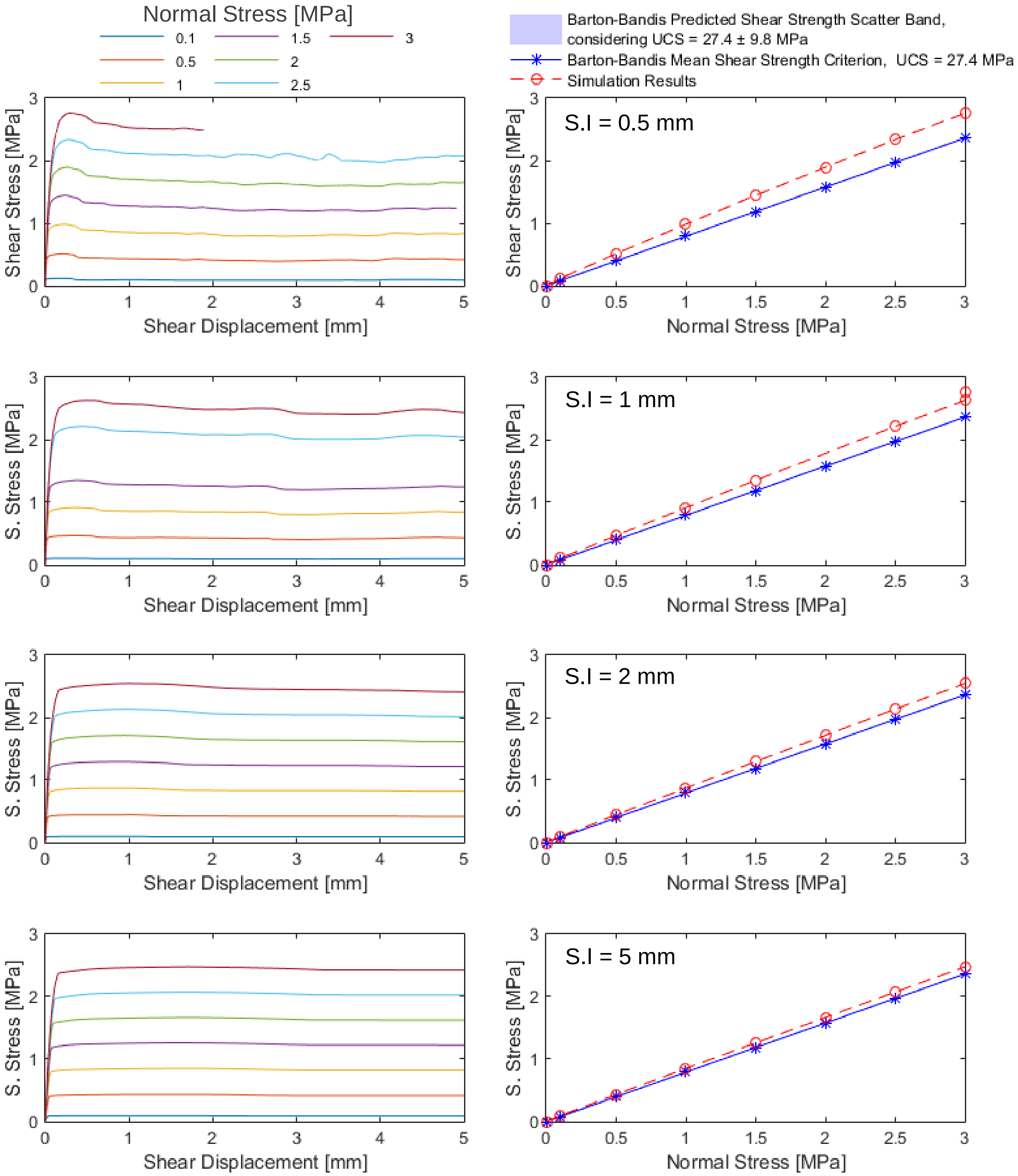

Figure D.1 Stress-strain curve and peak shear strength as a function of the normal stress, Barton profile N°1, profile length = 97.5 mm, nominal JRC = 0.4.

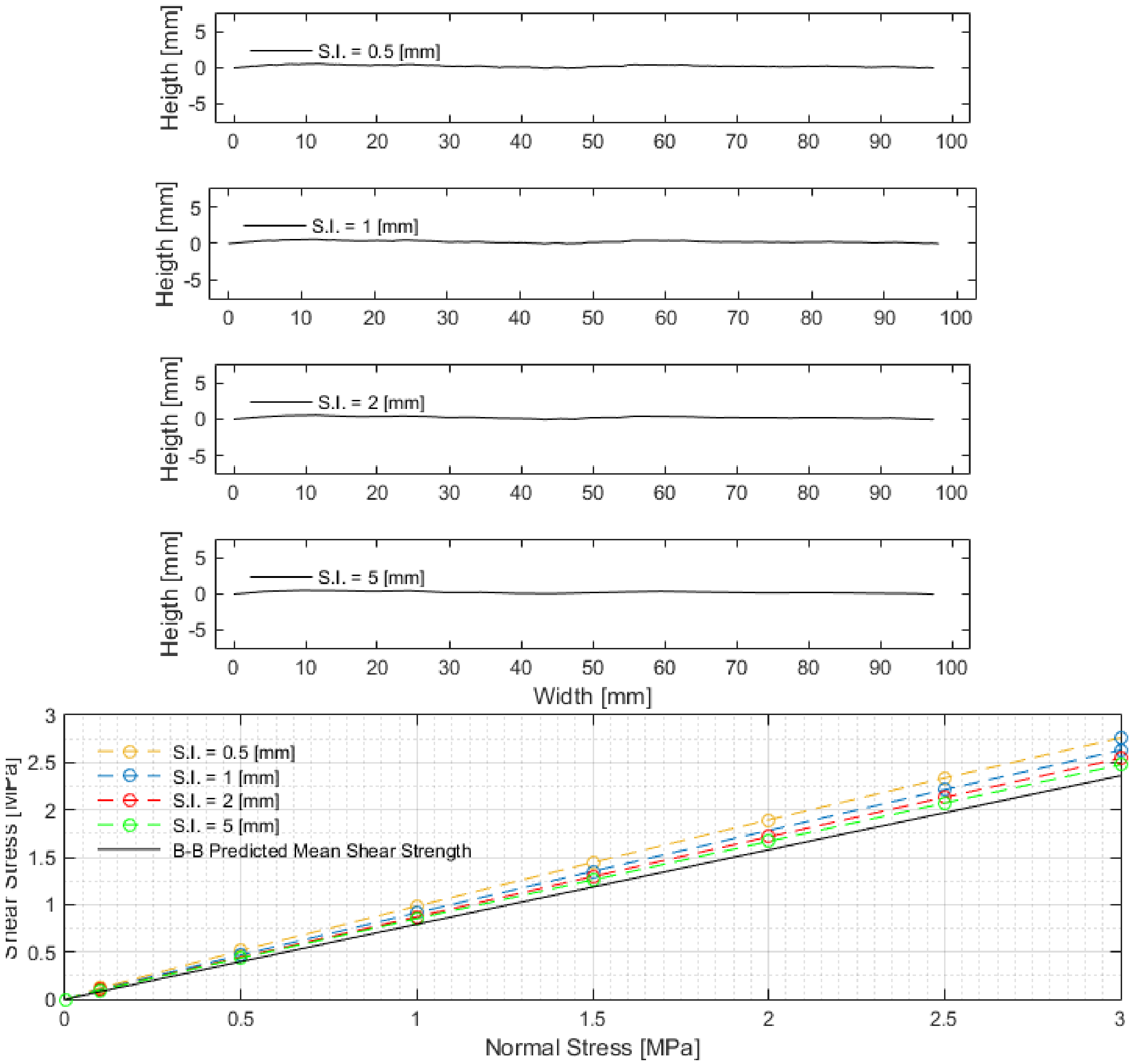

Figure D.2. Barton's profile n°1, sampled under different interval values and a summary of the simulation results for each sampling interval considered.

## Appendix D.1.2 Profile N°2

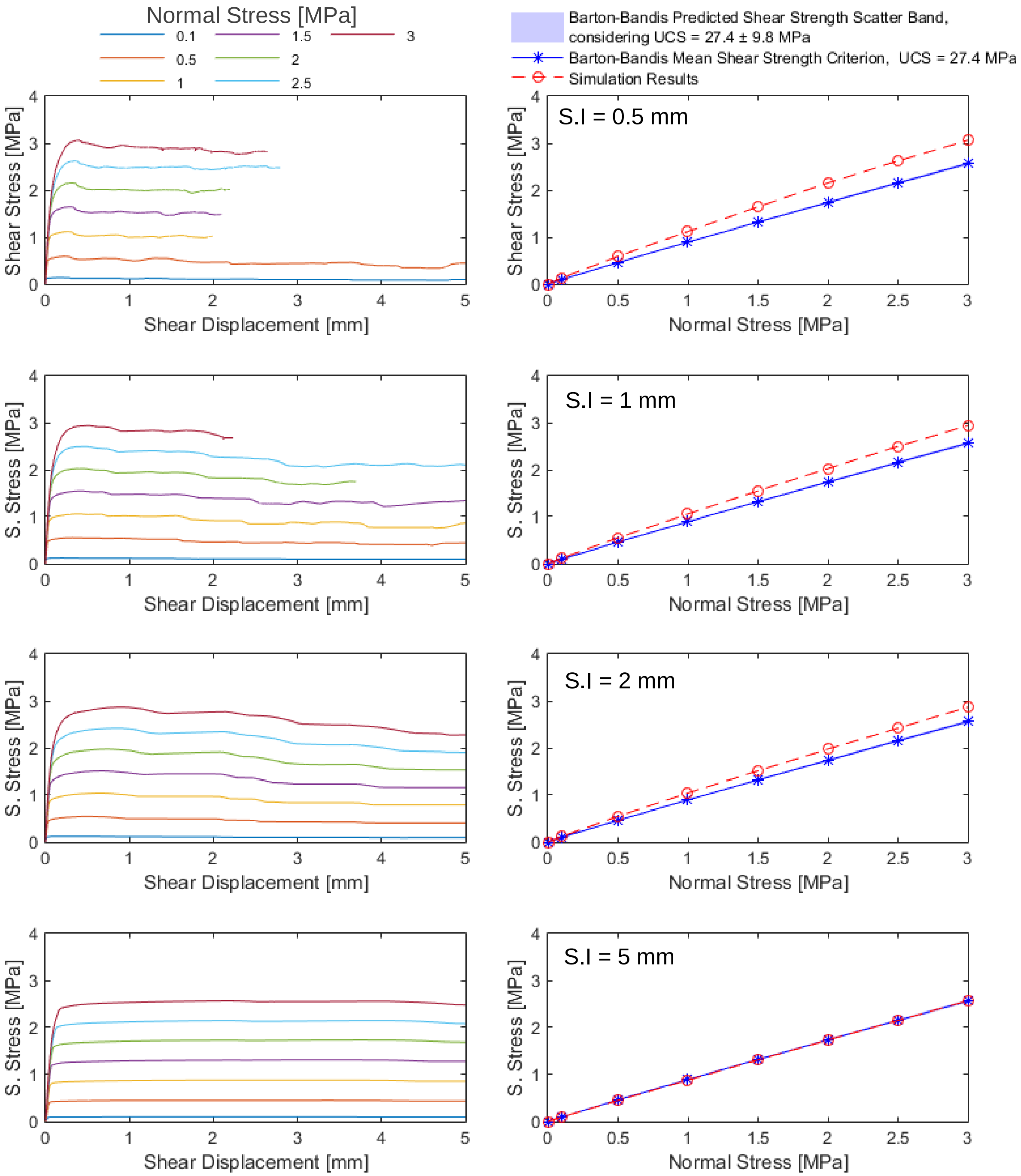

Figure D.3. Stress-displacement curve and peak shear strength as a function of the normal stress, Barton profile N°2, profile length = 100.5 mm, nominal JRC = 2.8.

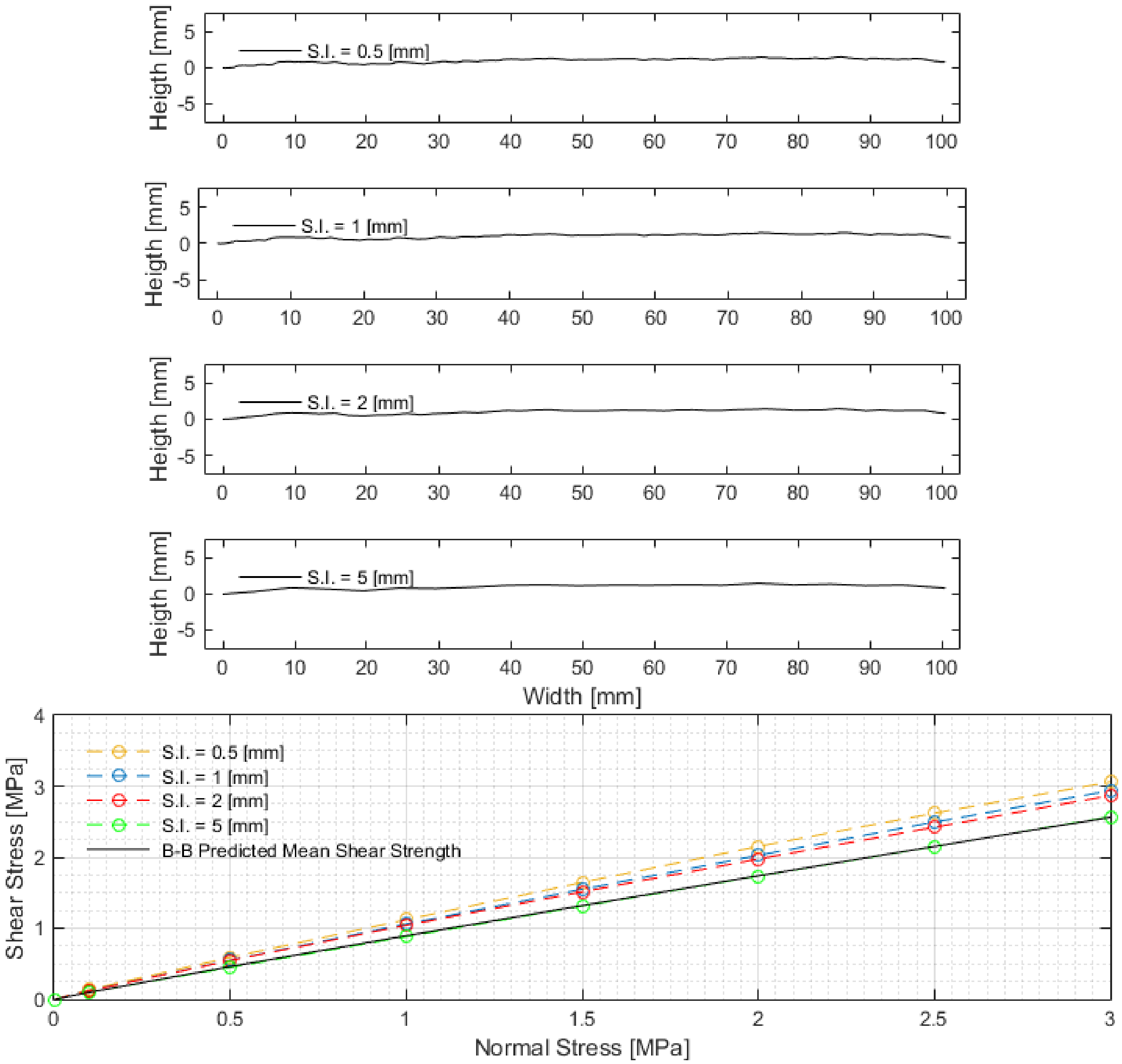

Figure D.4. Barton's profile n°2, sampled under different interval values and a summary of the simulation results for each sampling interval considered.

## Appendix D.1.3 Profile N°3

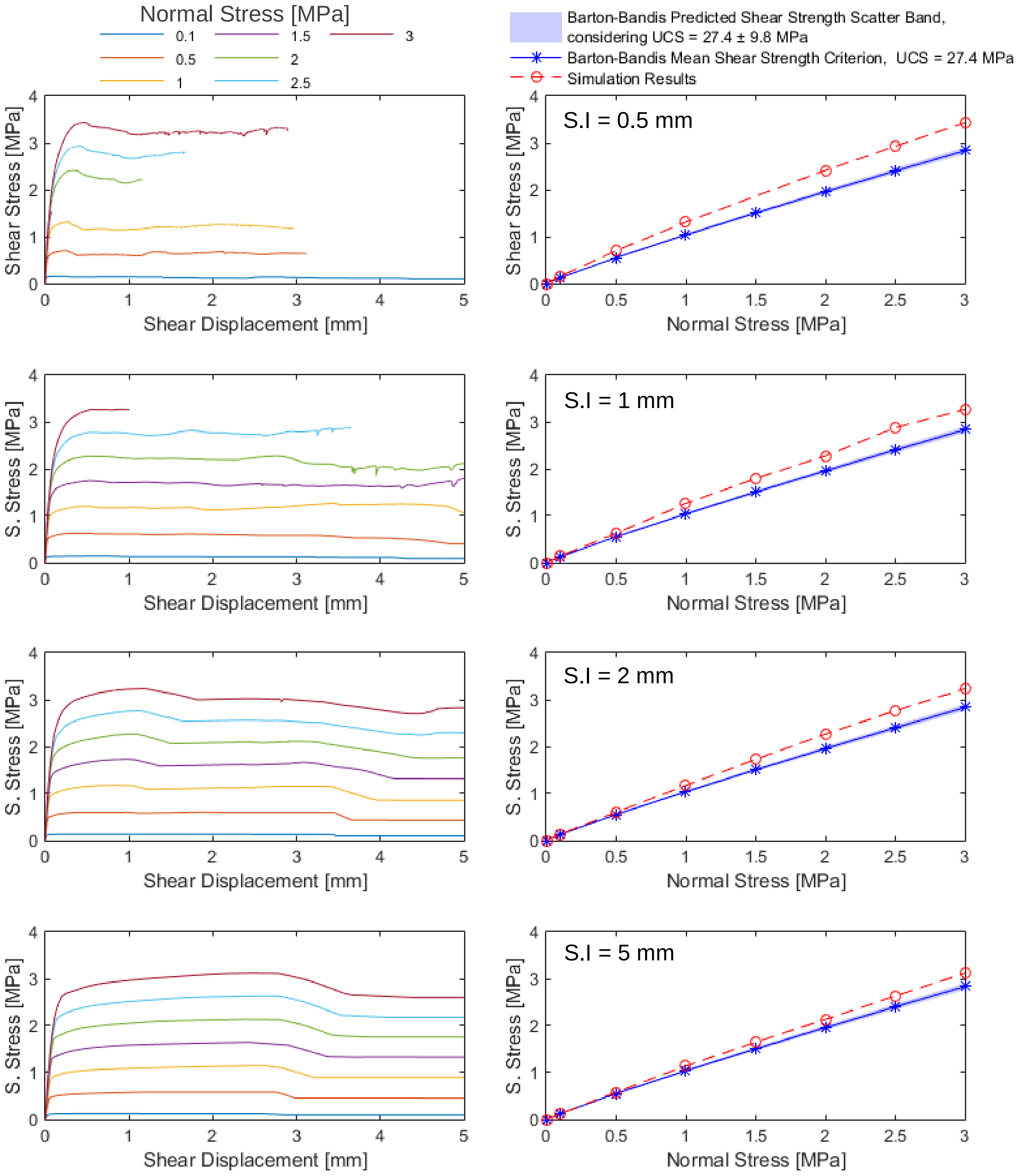

Figure D.5. Stress-displacement curve and peak shear strength as a function of the normal stress, Barton profile N°3, profile length = 100 mm , nominal JRC = 5.8.

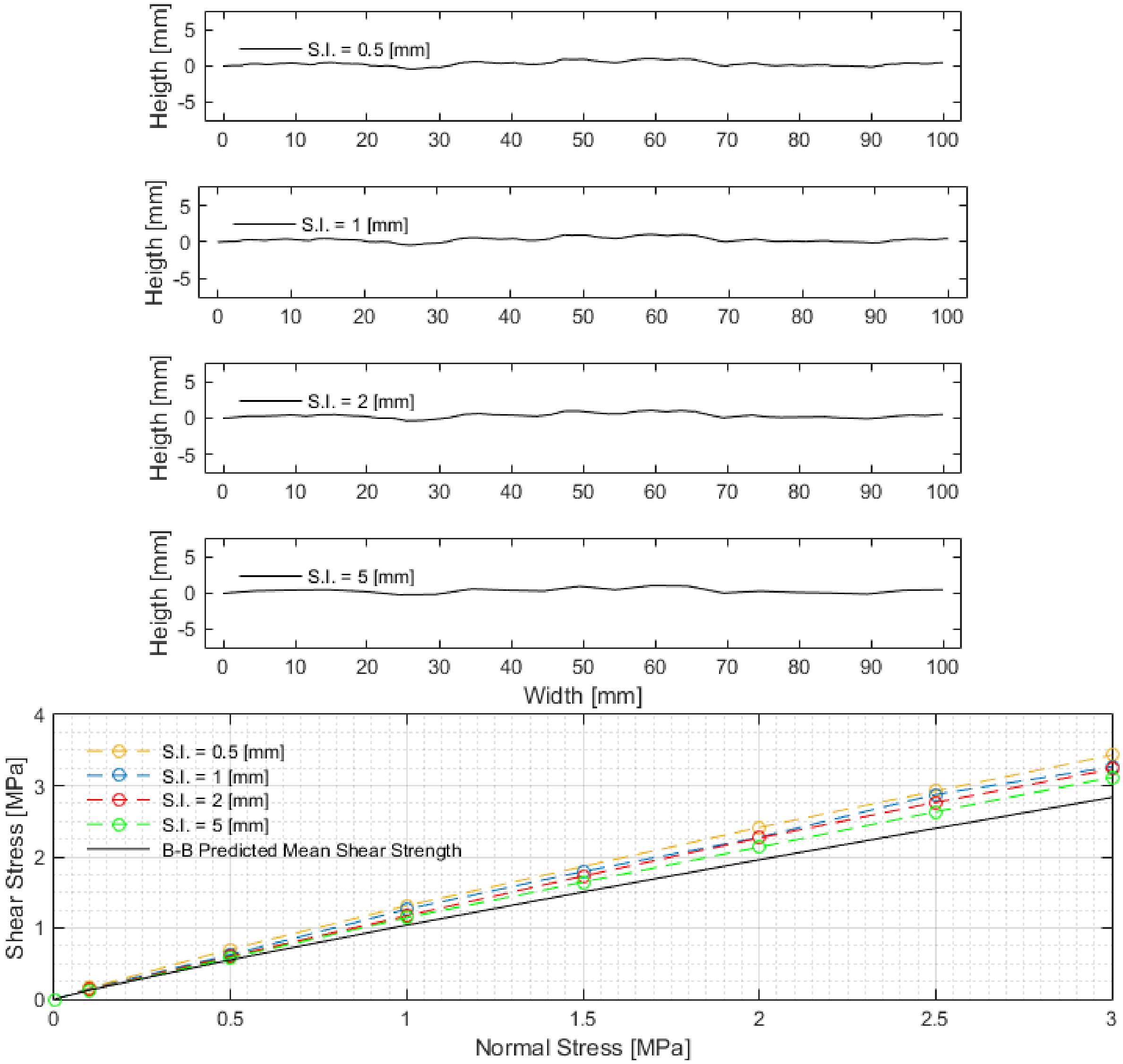

Figure D.6. Barton's profile n°3, sampled under different interval values and a summary of the simulation results for each sampling interval considered.

## Appendix D.1.4 Profile N°4

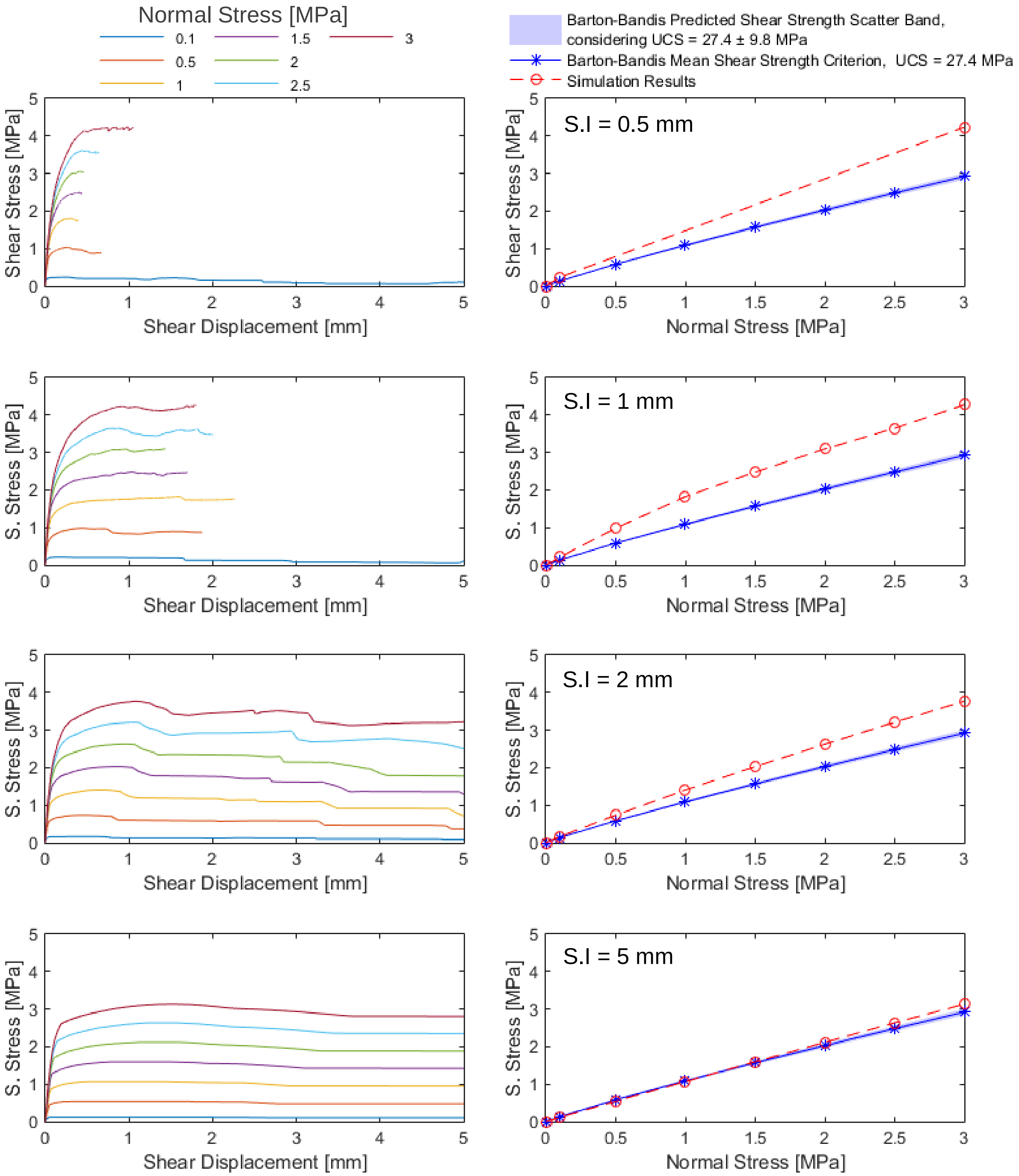

Figure D.7. Stress-displacement curve and peak shear strength as a function of the normal stress, Barton profile N°4, profile length = 99 mm, nominal JRC = 6.7.

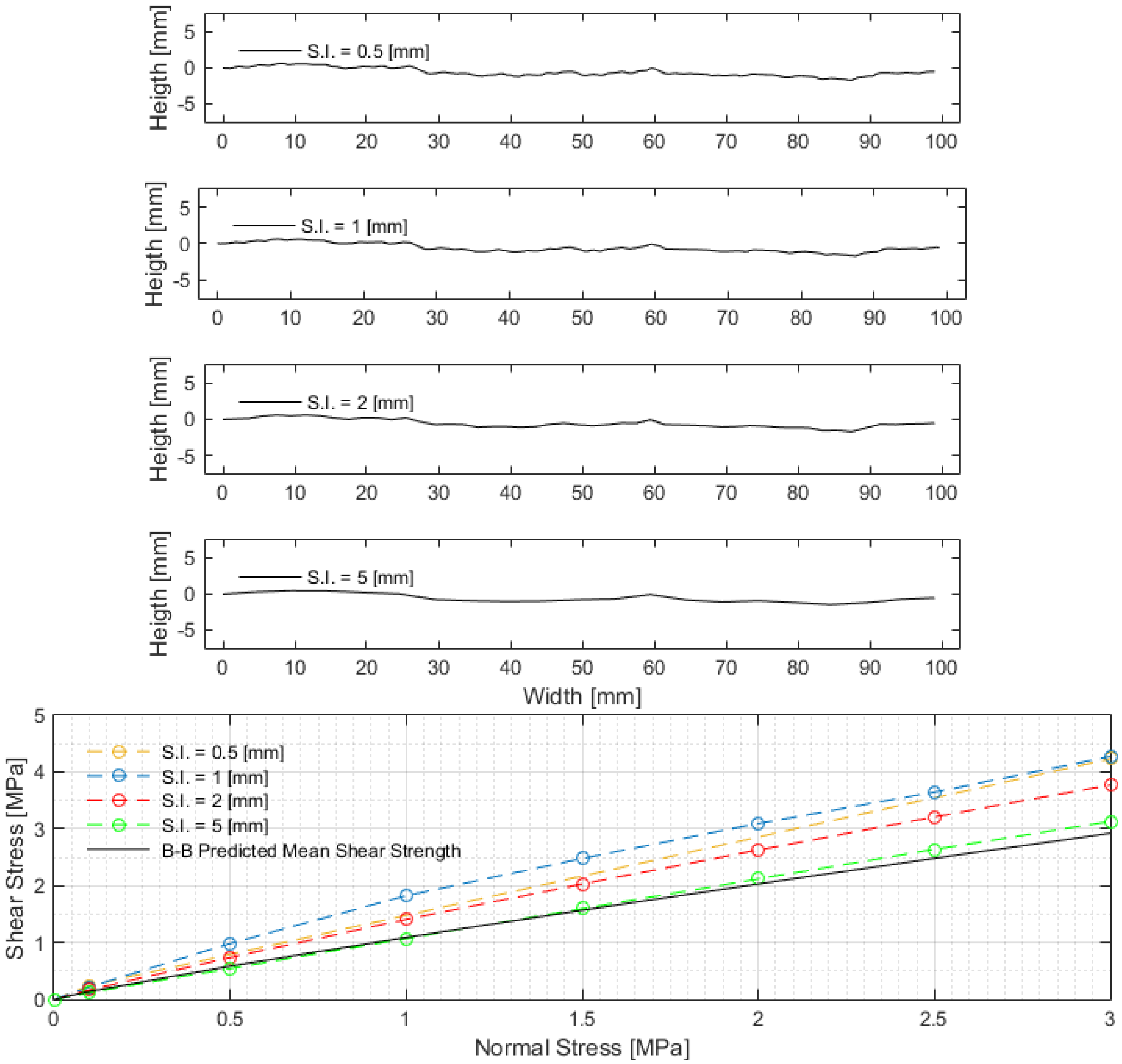

Figure D.8. Barton's profile n°4, sampled under different interval values and a summary of the simulation results for each sampling interval considered.

## Appendix D.1.5 Profile N°5

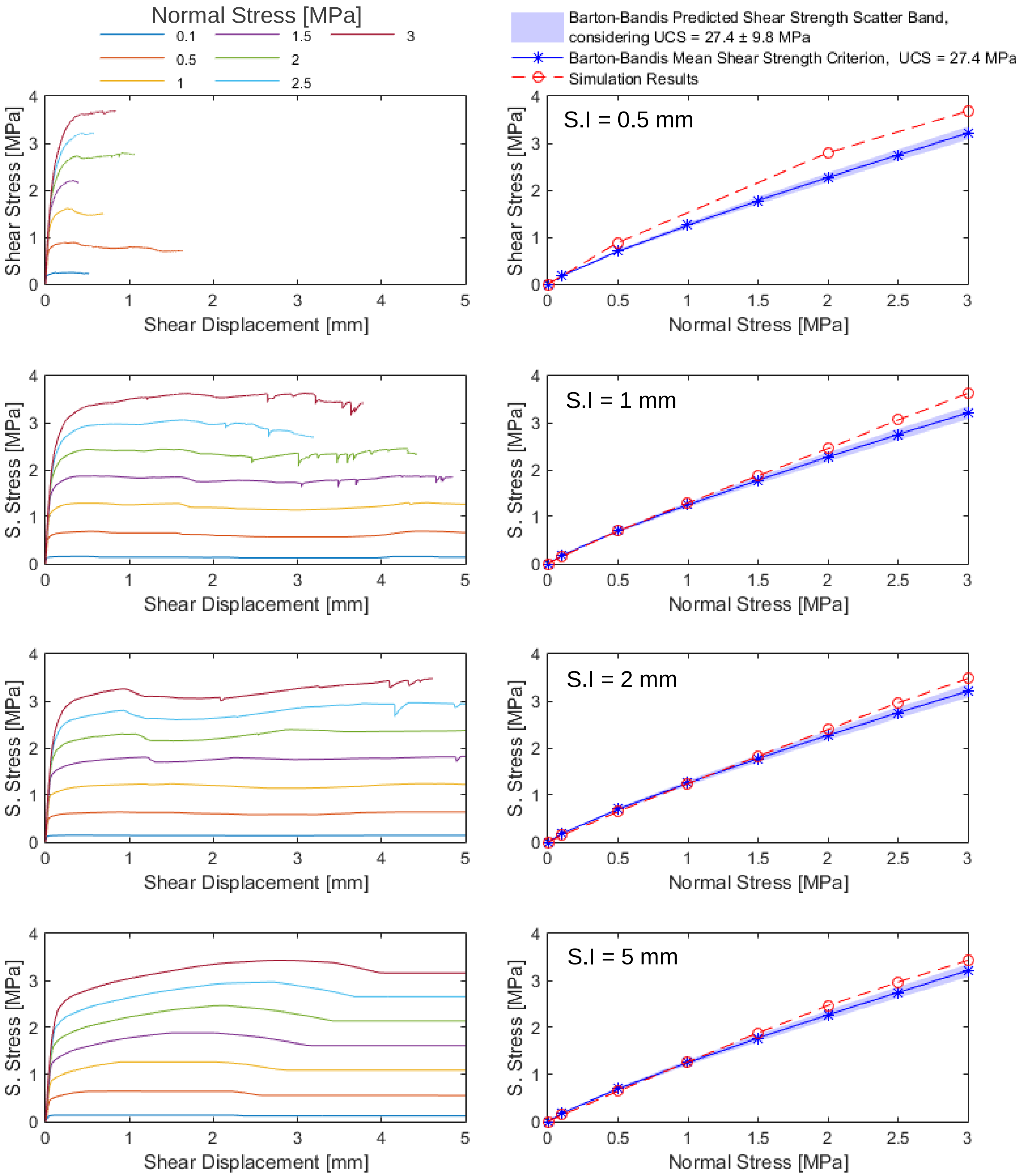

Figure D.9. Stress-displacement curve and peak shear strength as a function of the normal stress, Barton profile N°5, profile length = 98.5 mm, nominal JRC =9.5.

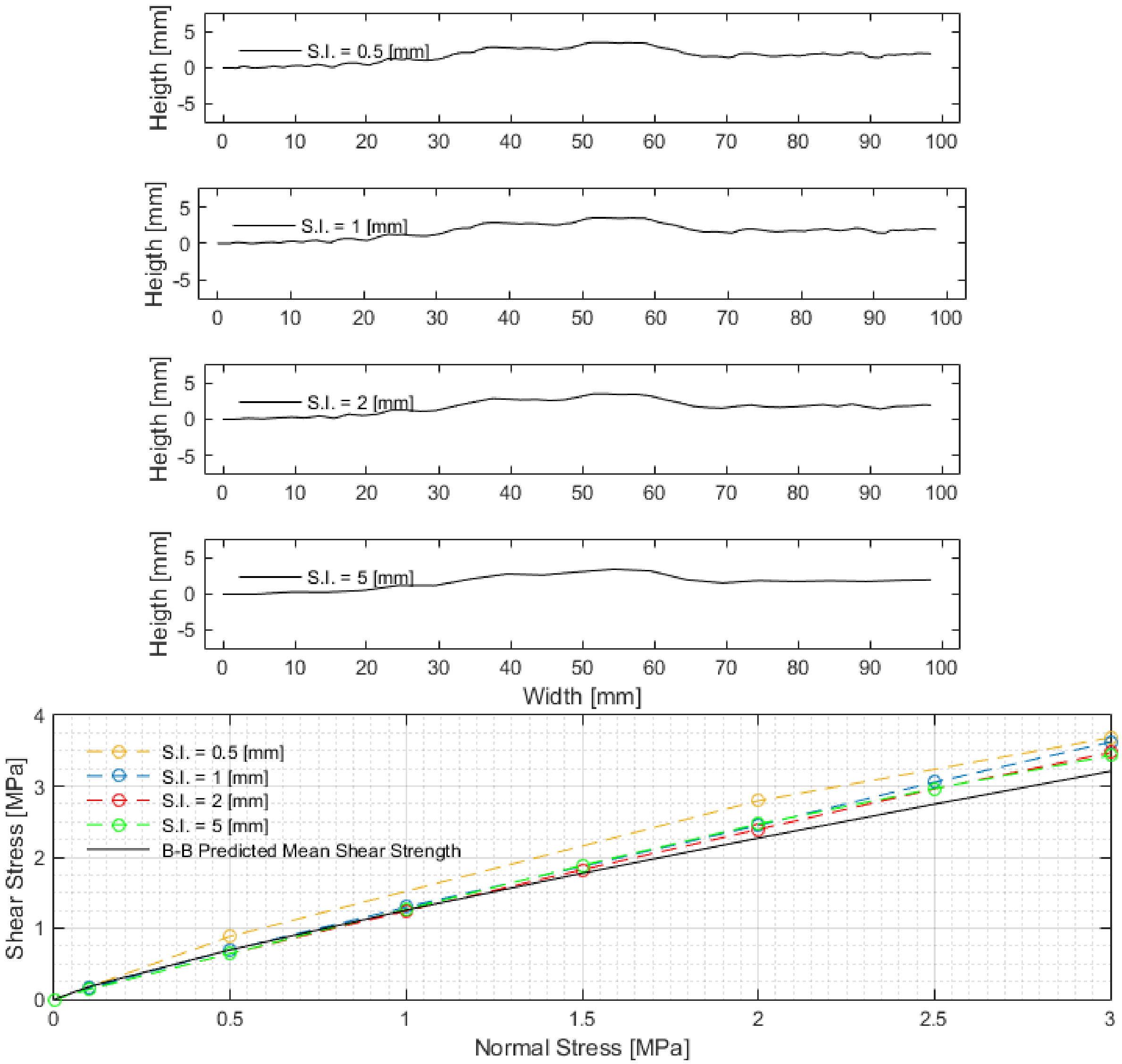

Figure D.10. Barton's profile n°5, sampled under different interval values and a summary of the simulation results for each sampling interval considered.

## Appendix D.1.6 Profile N°6

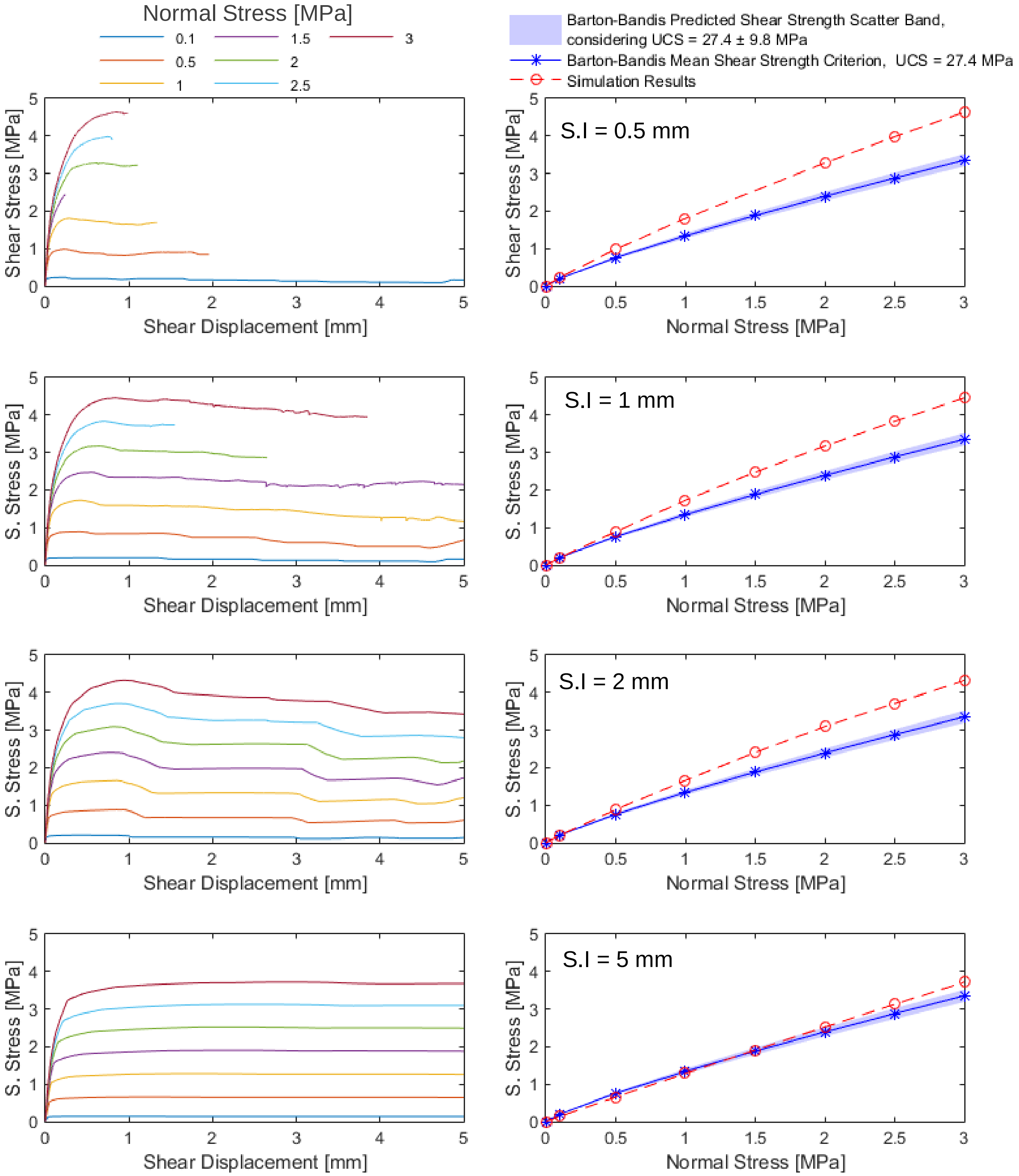

Figure D.11. Stress-displacement curve and peak shear strength as a function of the normal stress, Barton profile N°6, profile length = 99 mm, nominal JRC = 10.8.

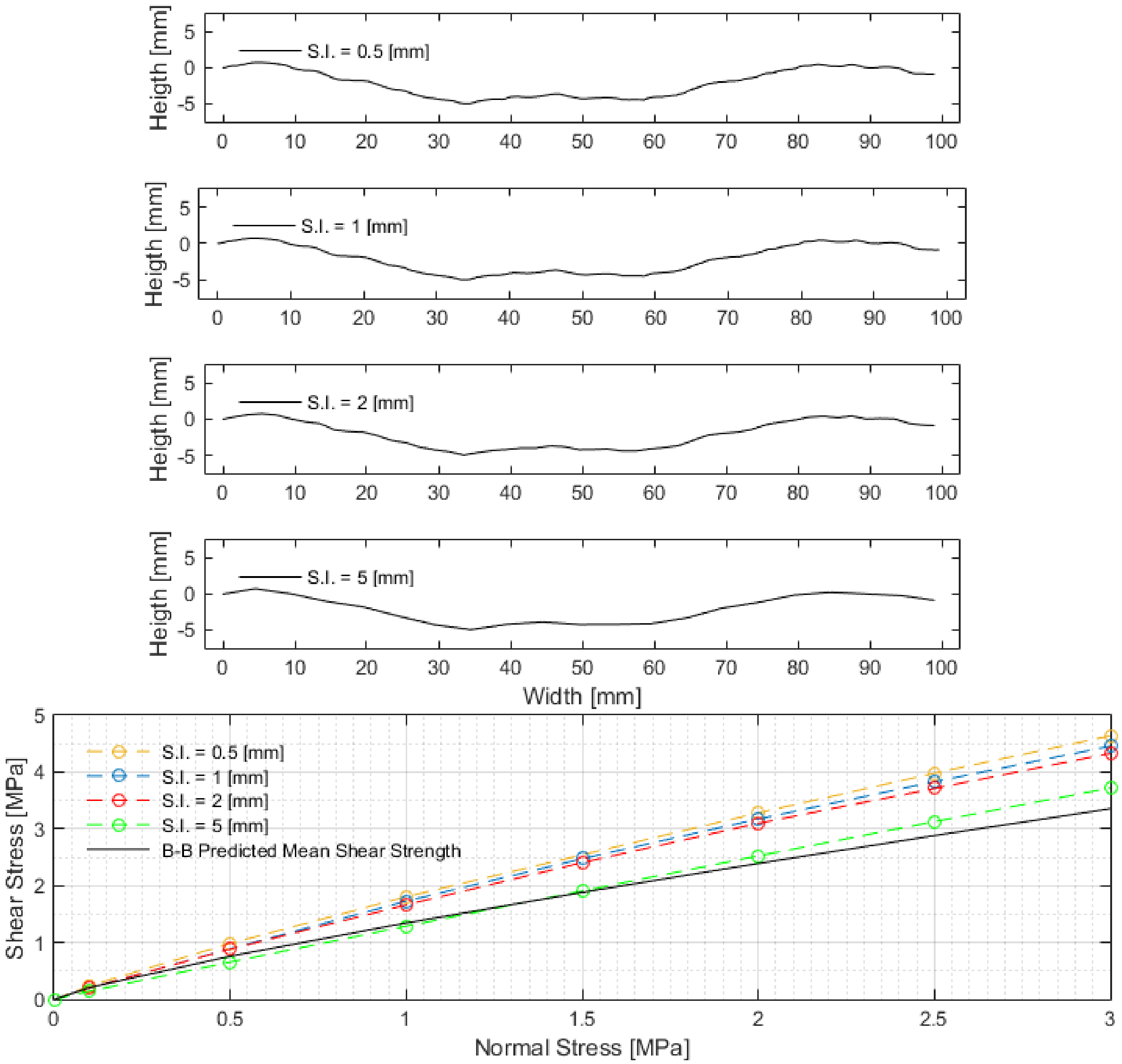

Figure D.12. Barton's profile n°6, sampled under different interval values and a summary of the simulation results for each sampling interval considered.

## Appendix D.1.7 Profile N°7

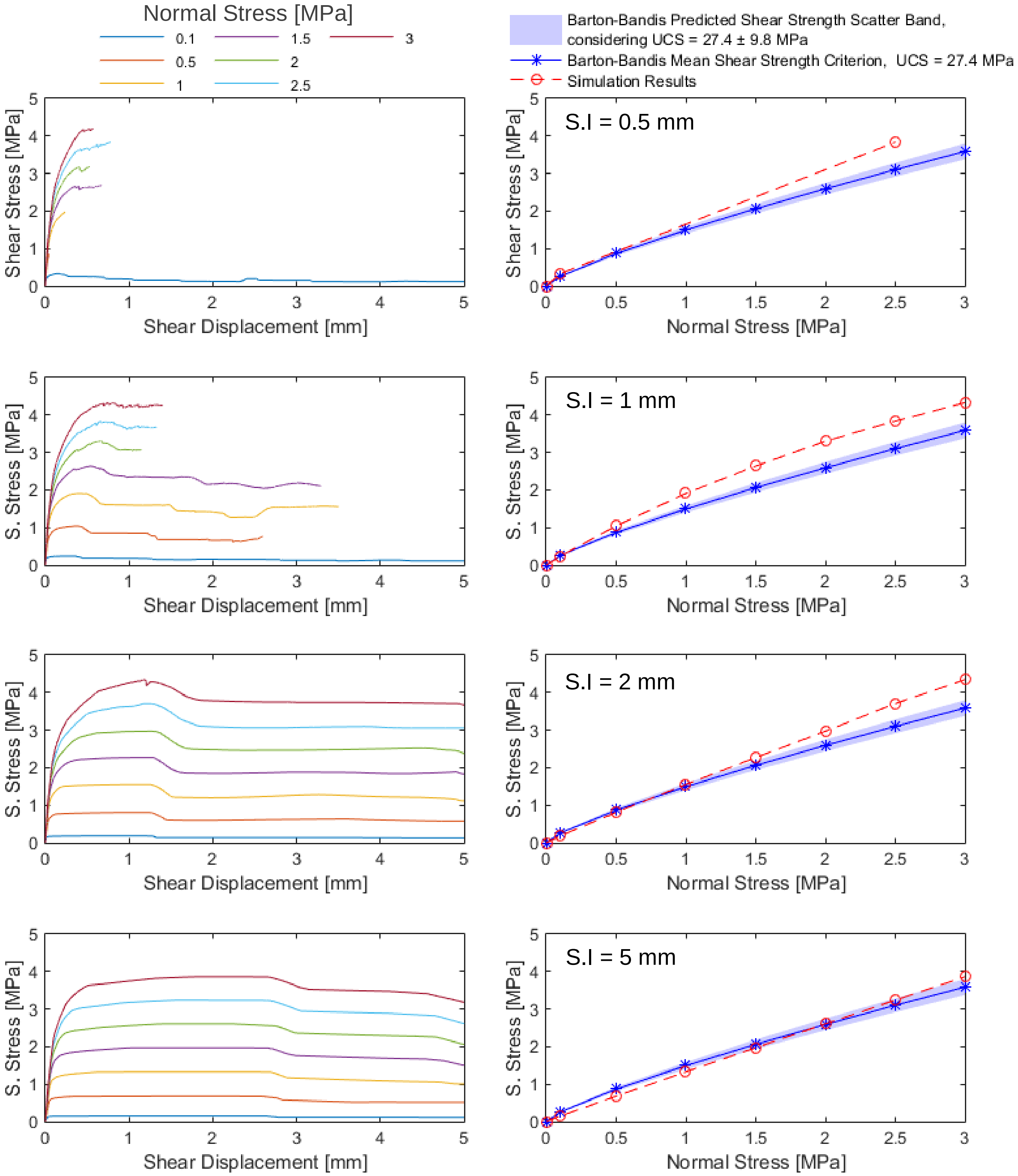

Figure D.13. Stress-displacement curve and peak shear strength as a function of the normal stress, Barton profile N°7, profile length = 96 mm, nominal JRC = 12.8.

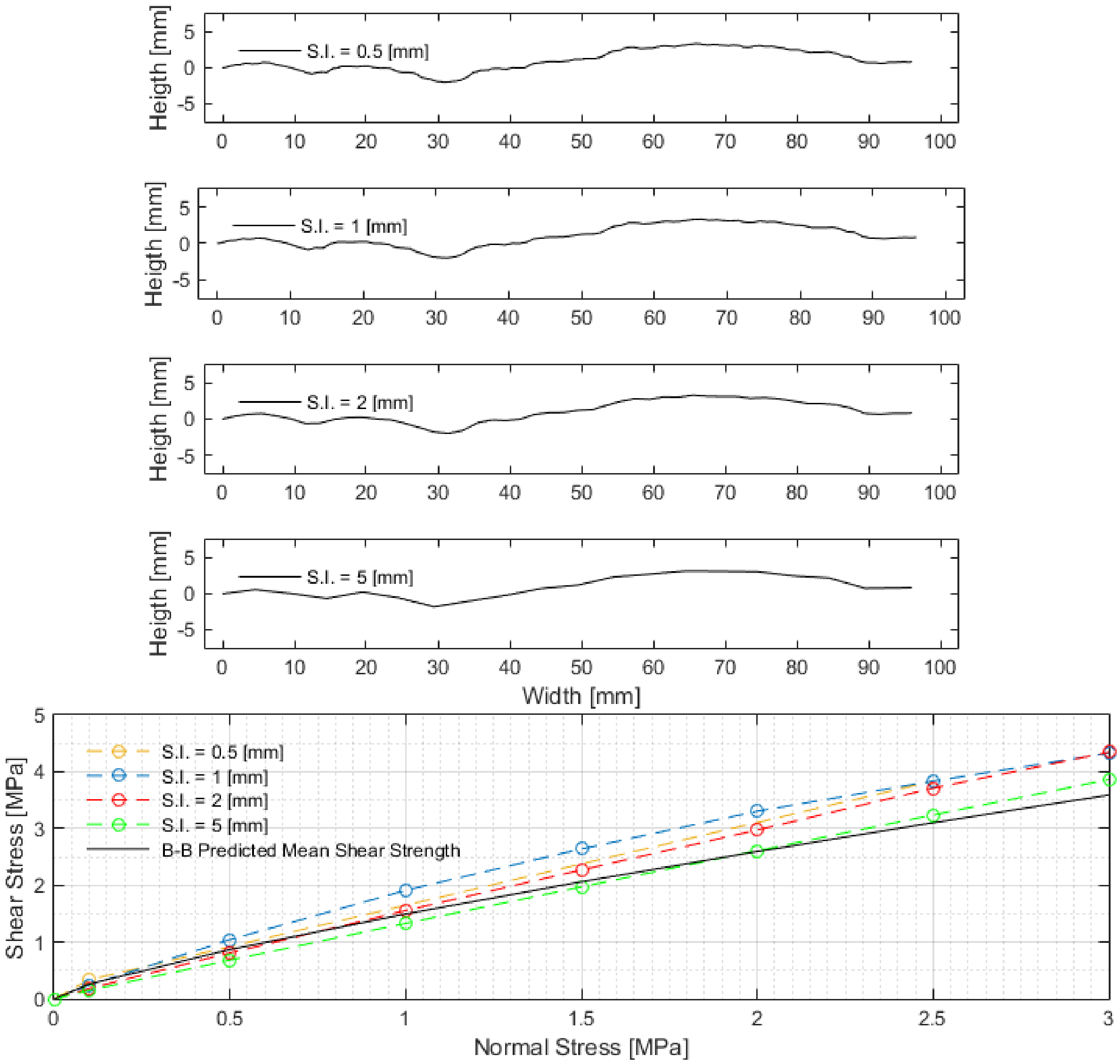

Figure D.14. Barton's profile n°7, sampled under different interval values and a summary of the simulation results for each sampling interval considered.

## Appendix D.1.8 Profile N°8

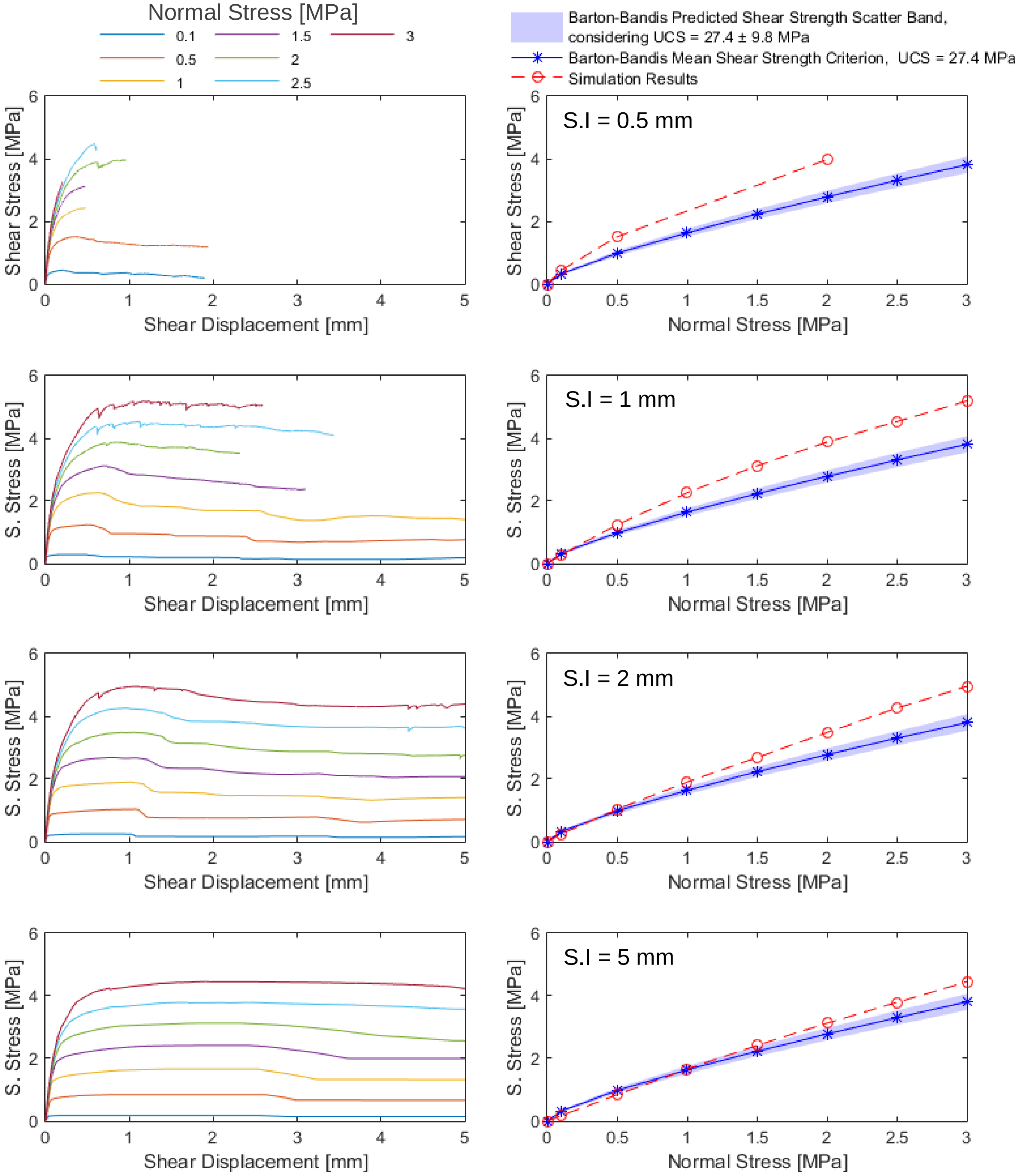

Figure D.15. Stress-displacement curve and peak shear strength as a function of the normal stress, Barton profile N°8, profile length = 100.5 mm, nominal JRC = 14.5.

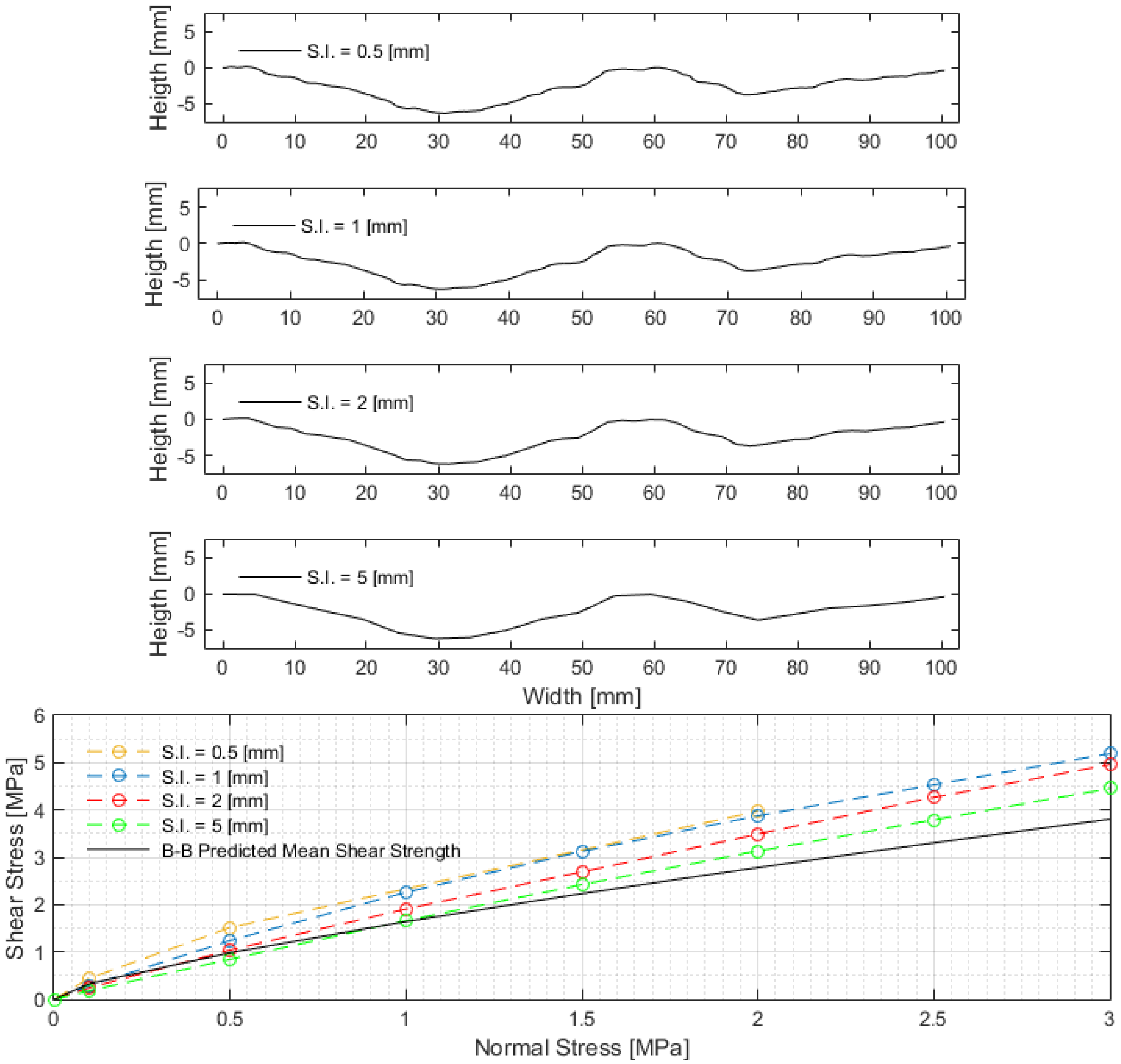

Figure D.16. Barton's profile n°8, sampled under different interval values and a summary of the simulation results for each sampling interval considered.

## Appendix D.1.9 Profile N°9

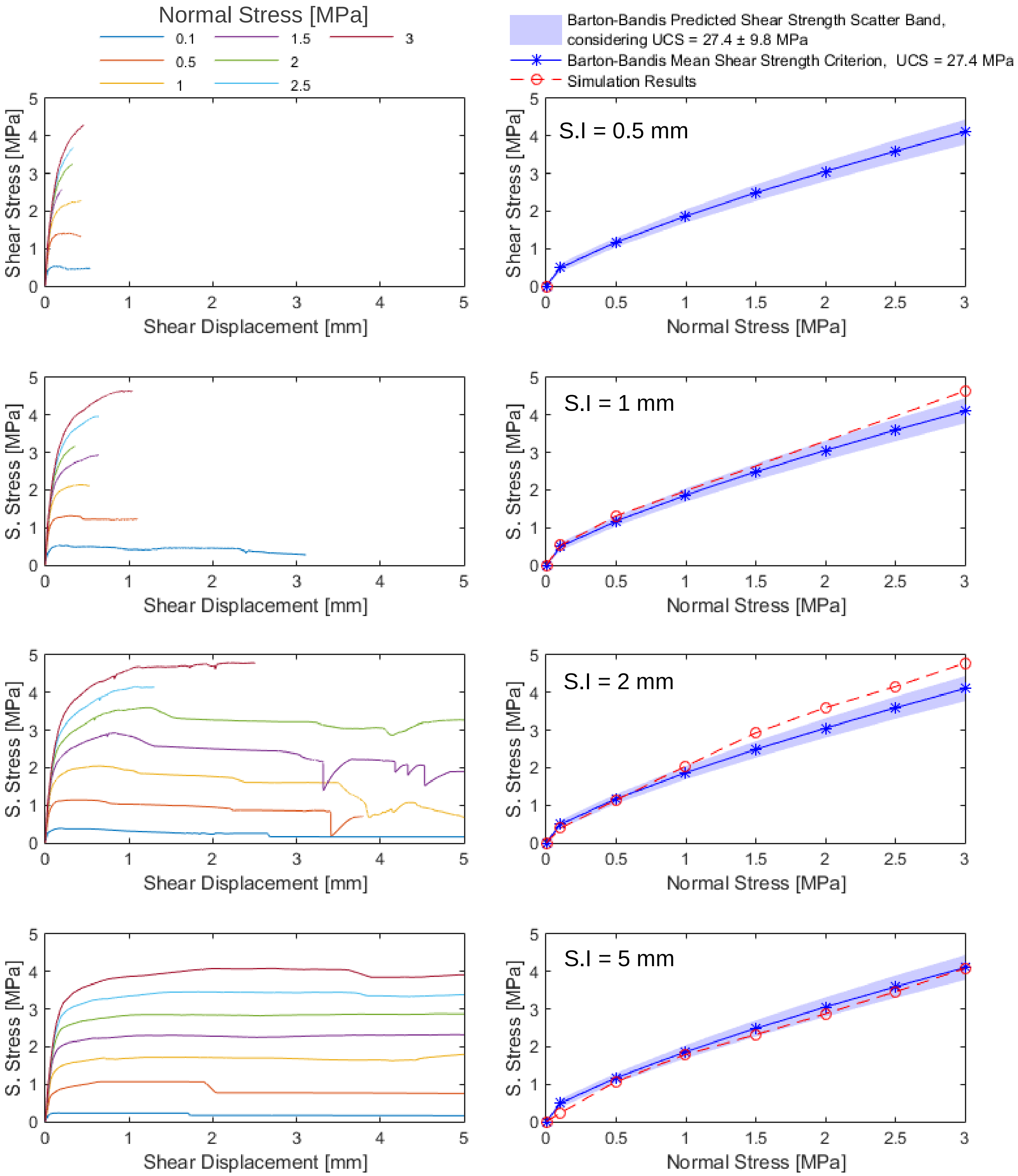

Figure D.17. Stress-displacement curve and peak shear strength as a function of the normal stress, Barton profile N°9, profile length = 99 mm, nominal JRC =16.7.

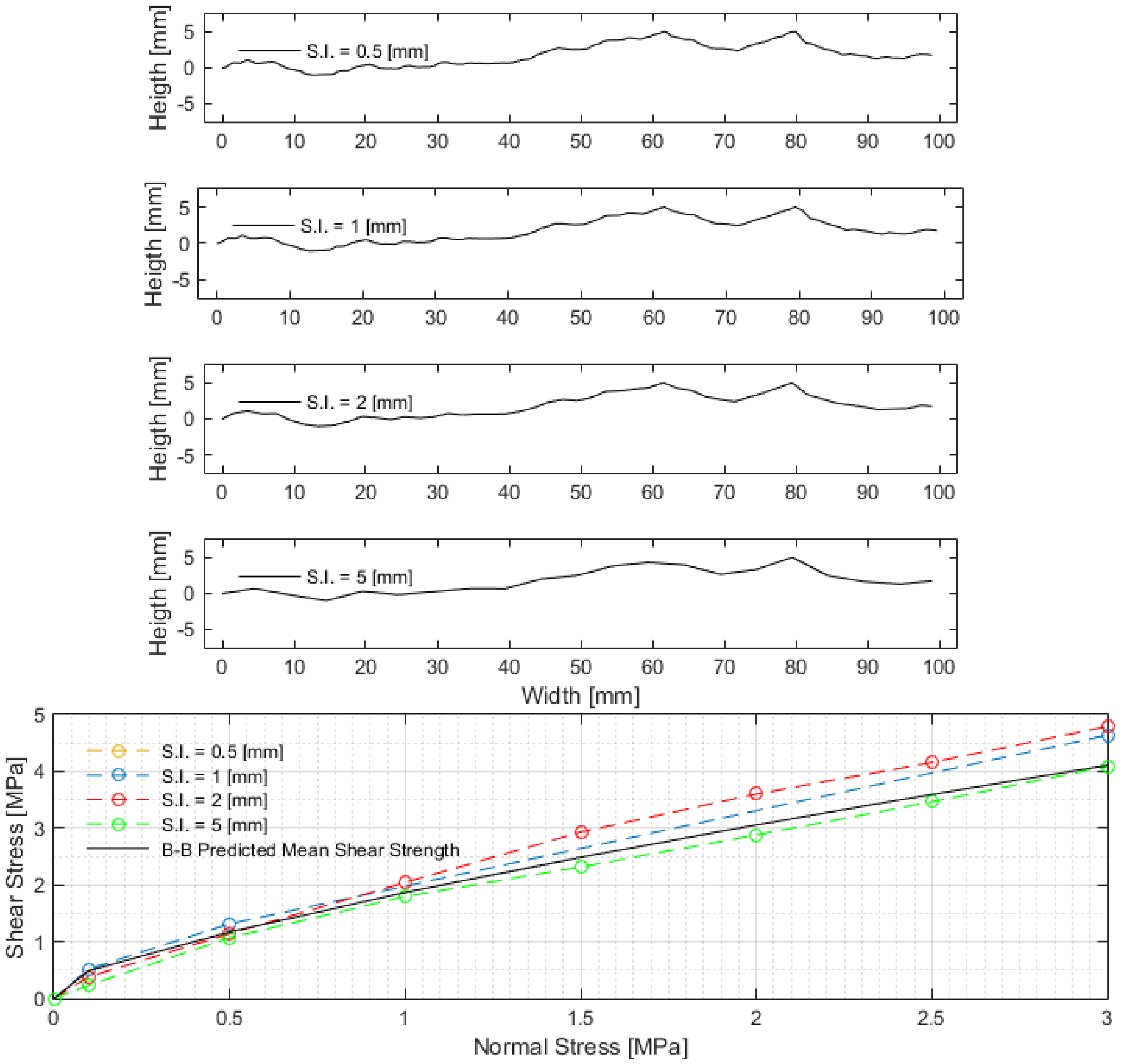

Figure D.18. Barton's profile n°9, sampled under different interval values and a summary of the simulation results for each sampling interval considered.

## Appendix D.1.10 Profile N°10

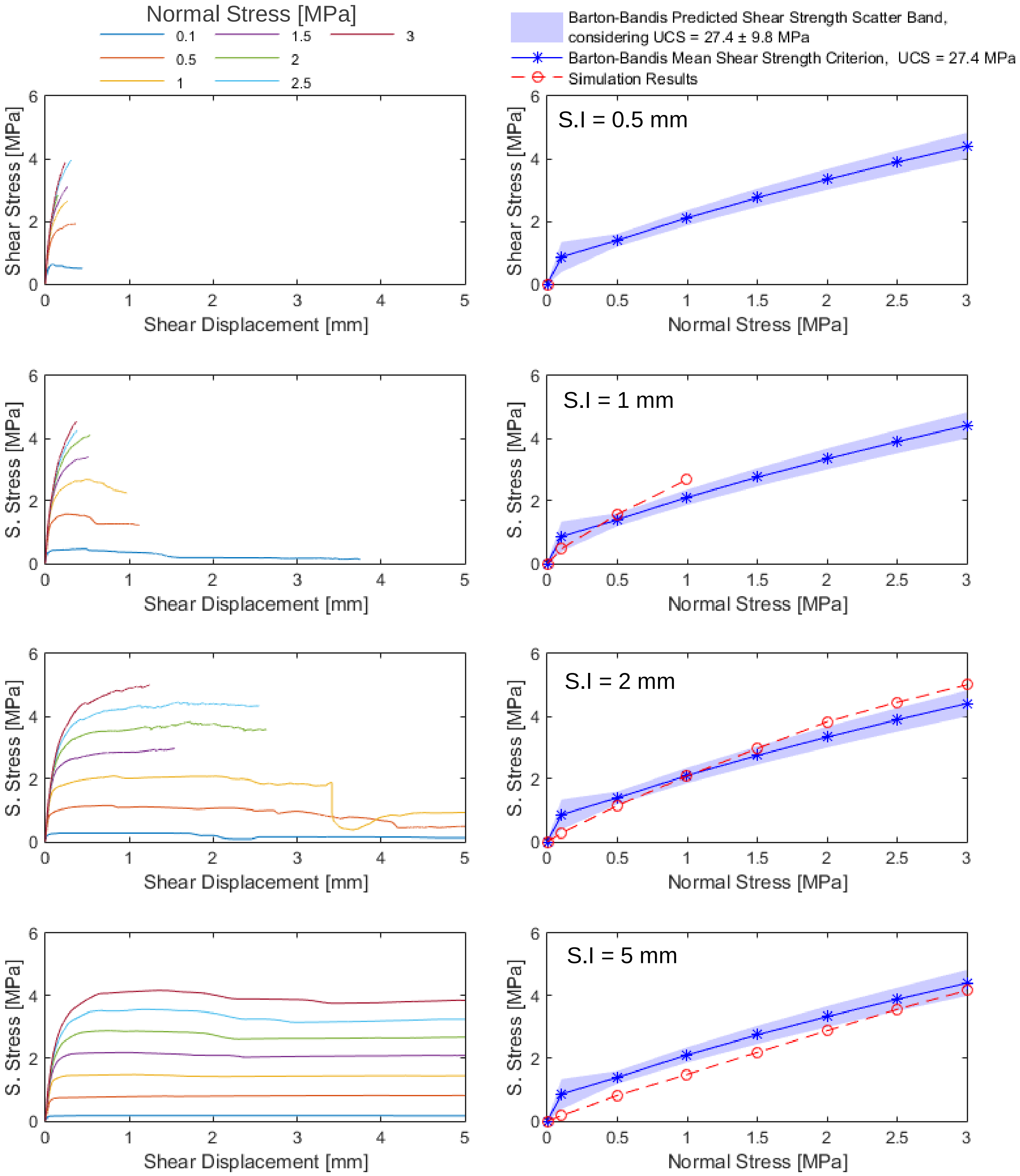

Figure D.19. Stress-displacement curve and peak shear strength as a function of the normal stress, Barton profile N°10, profile length = 99.48 mm, nominal JRC =18.7.

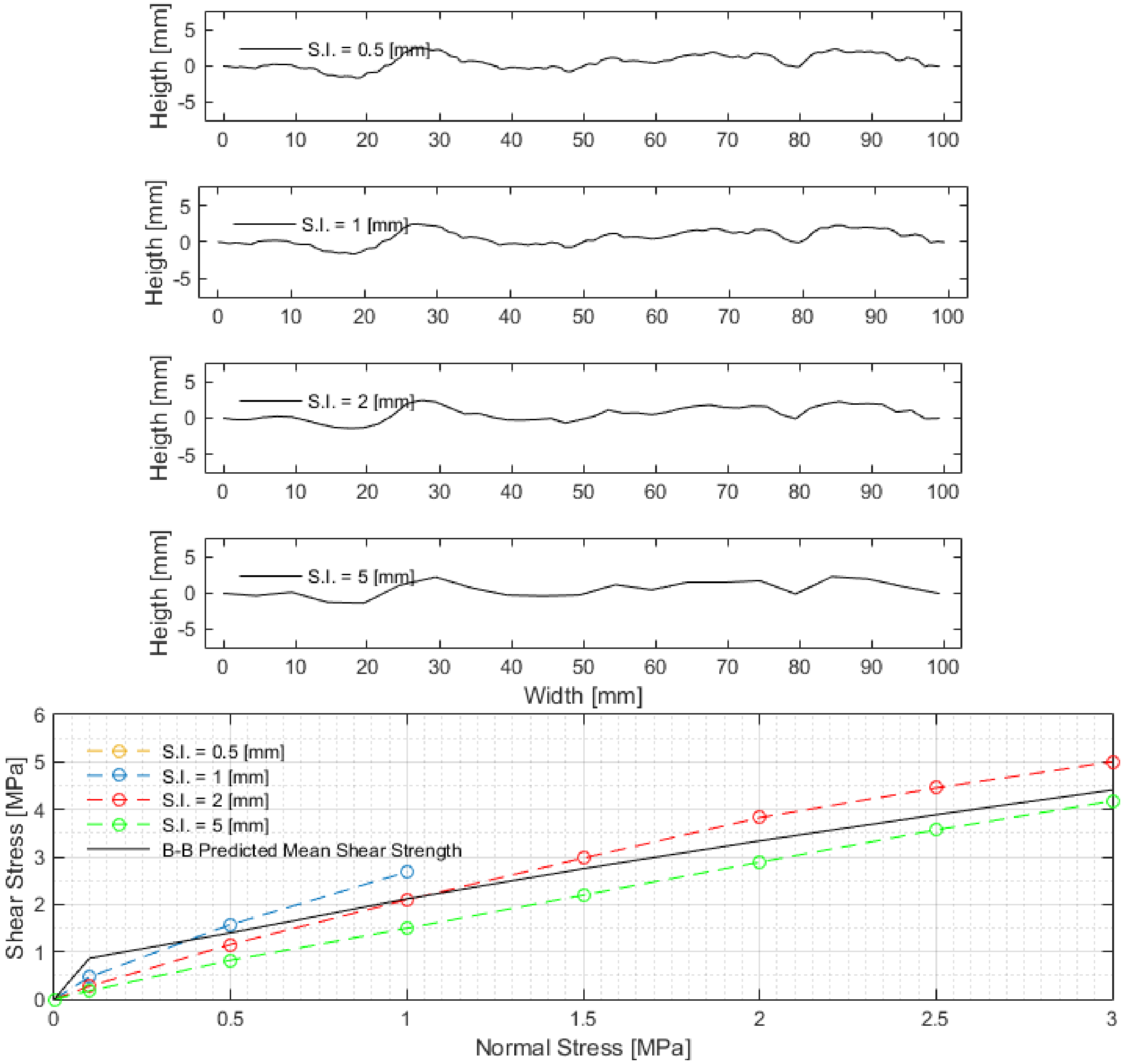

Figure D.20. Barton's profile n°10, sampled under different interval values and a summary of the simulation results for each sampling interval considered.

# Appendix D.2 Dilation Results

## Appendix D.2.1 Profile N°1

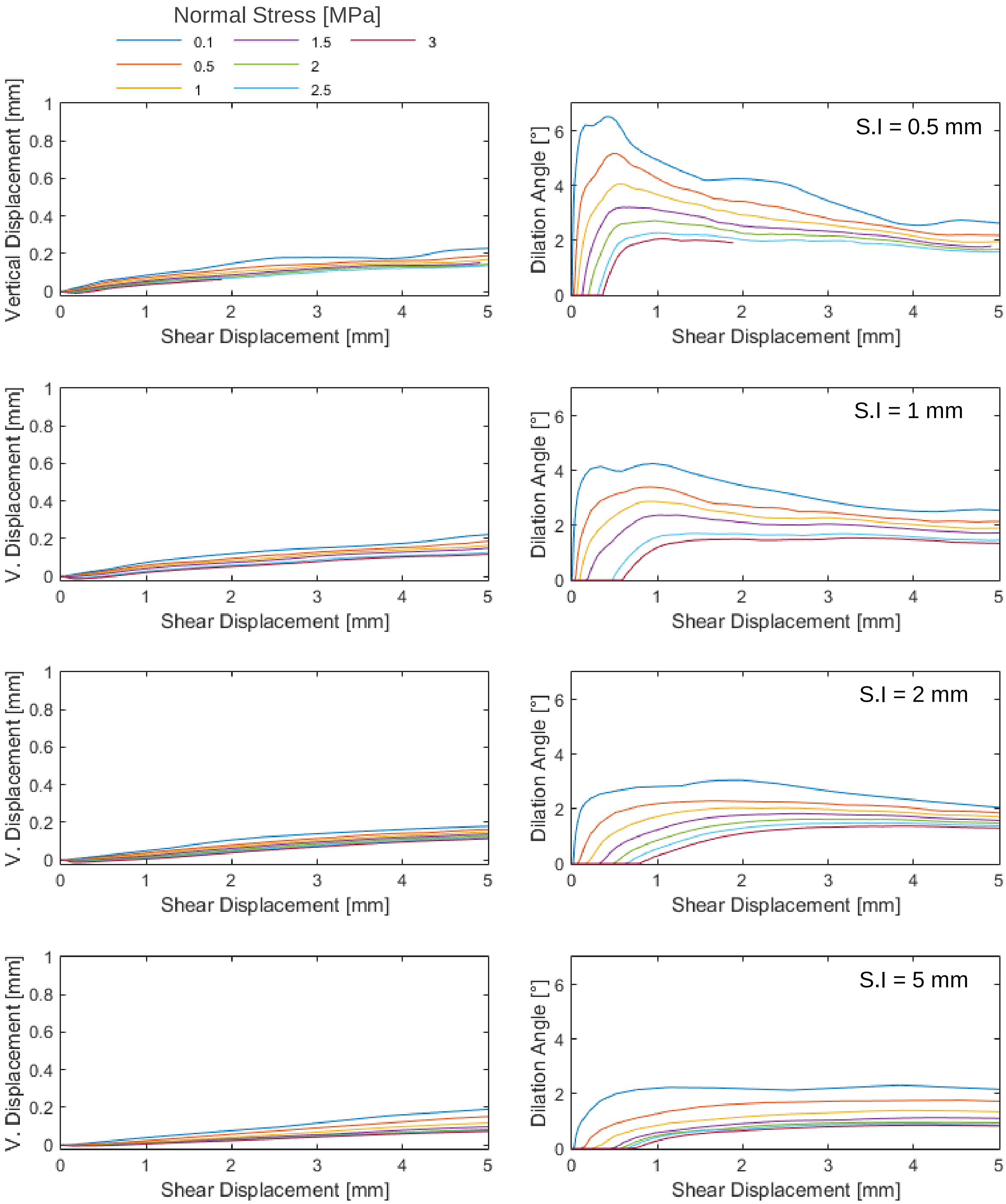

Figure D.21. Vertical displacement - shear displacement curve and secant dilation angle as a function of the shear displacement, Barton profile N° 1, nominal JRC = 0.4.

## Appendix D.2.2 Profile N°2

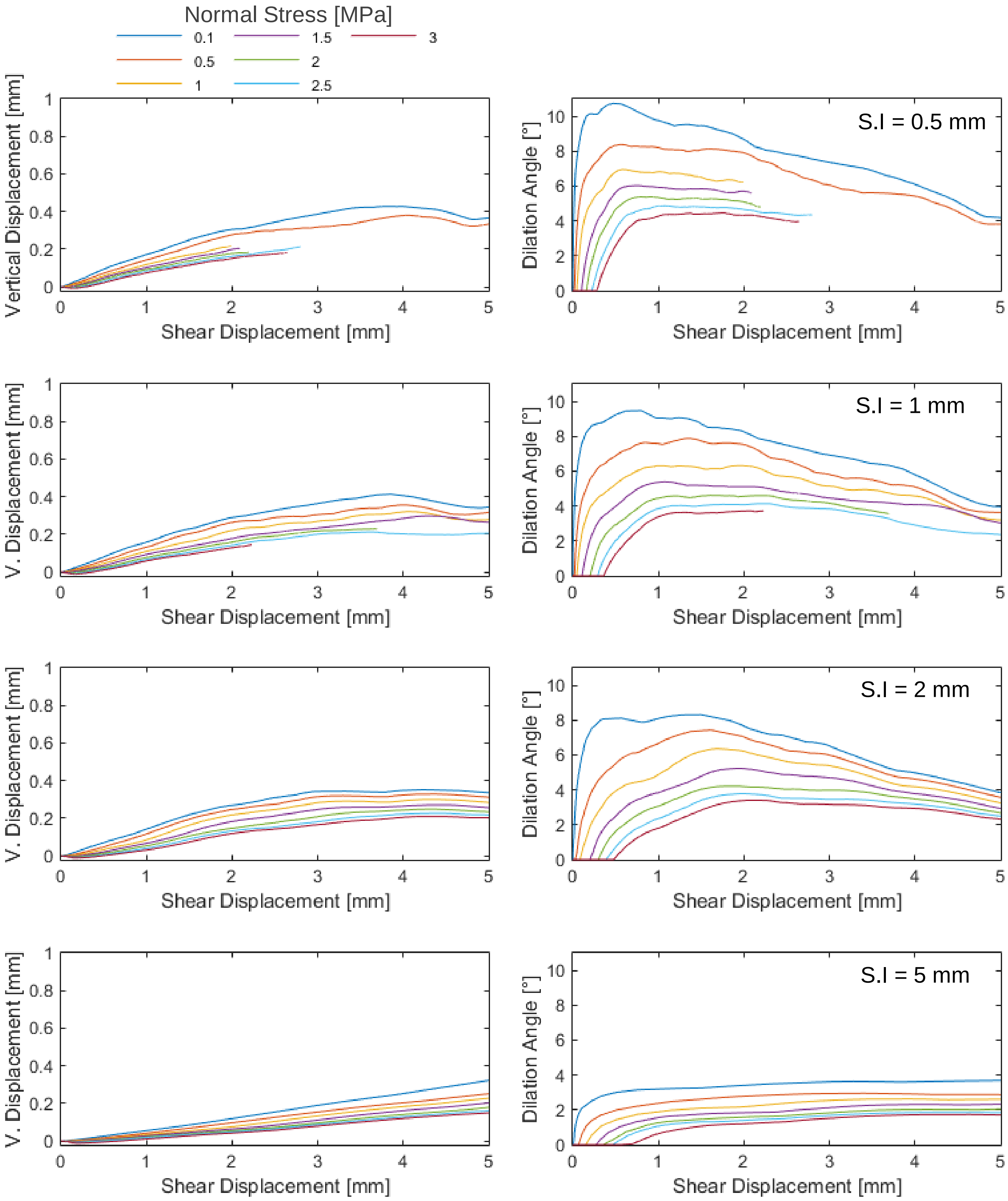

Figure D.22. Vertical displacement - shear displacement curve and secant dilation angle as a function of the shear displacement, Barton profile N°2, nominal JRC = 2.8.

## Appendix D.2.3 Profile N°3

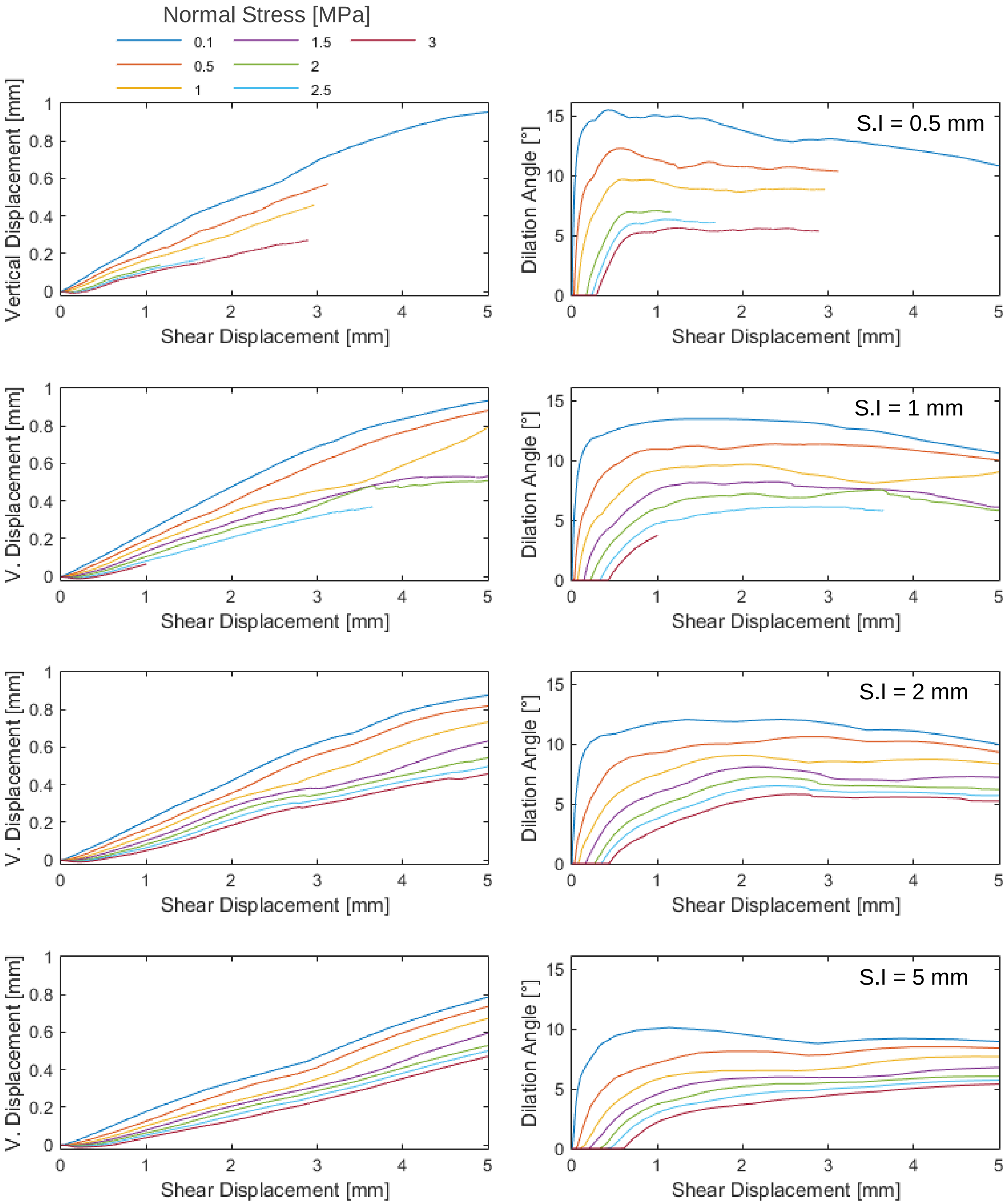

Figure D.23. Vertical displacement - shear displacement curve and secant dilation angle as a function of the shear displacement, Barton profile N°3, nominal JRC = 5.8.

## Appendix D.2.4 Profile N°4

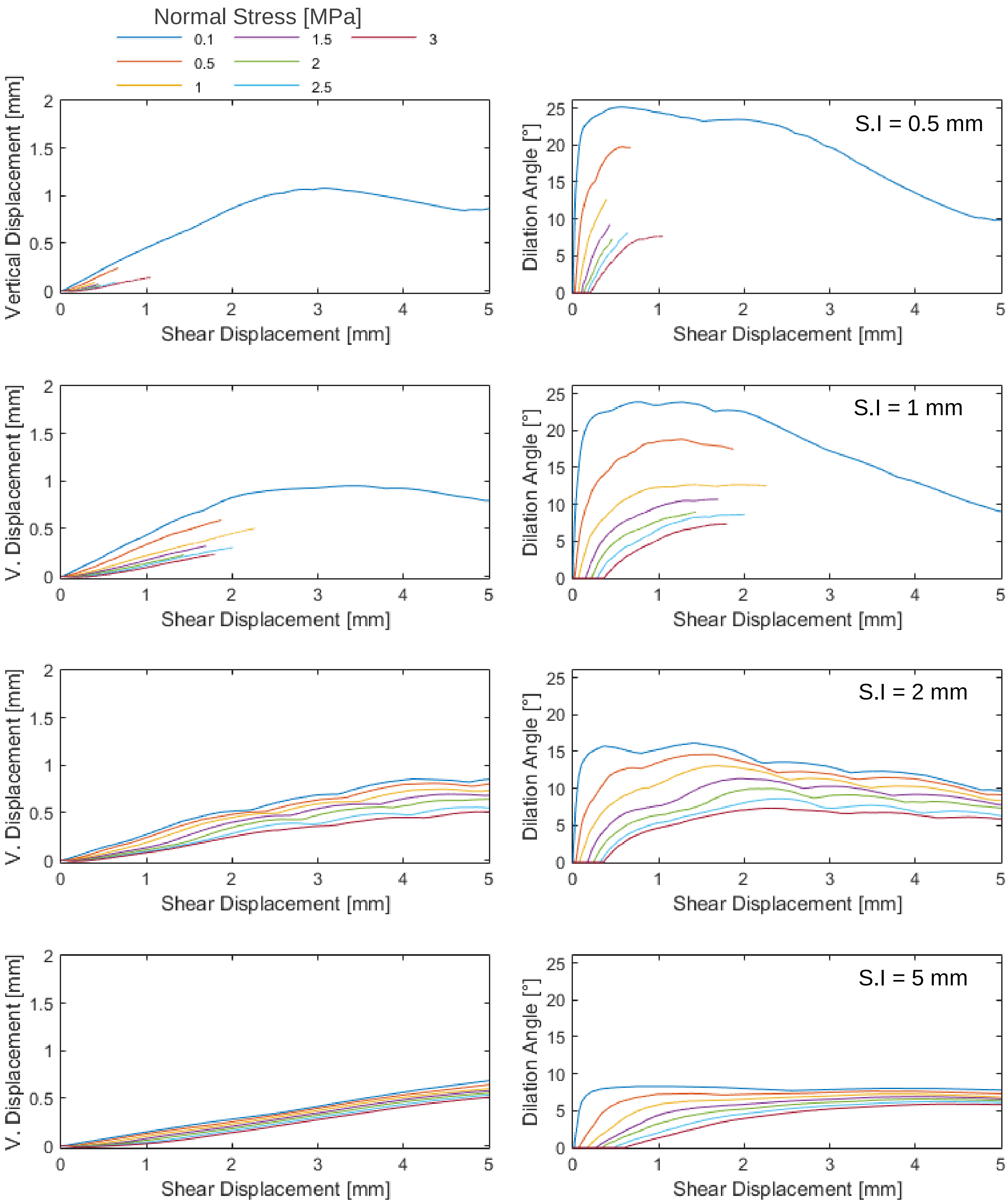

Figure D.24. Vertical displacement - shear displacement curve and secant dilation angle as a function of the shear displacement, Barton profile N° 4, nominal JRC = 6.7.

## Appendix D.2.5 Profile N°5

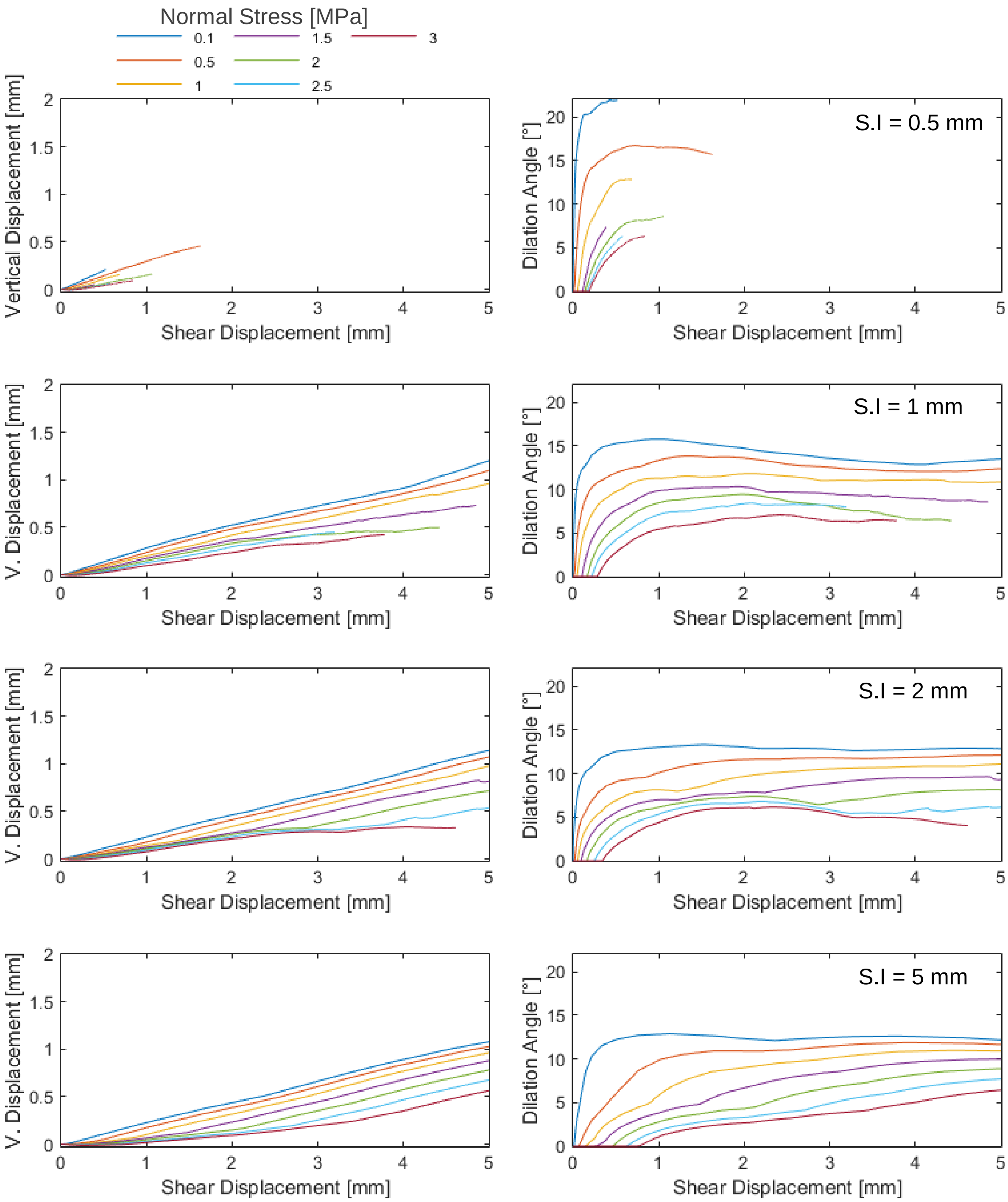

Figure D.25. Vertical displacement - shear displacement curve and secant dilation angle as a function of the shear displacement, Barton profile N°5, nominal JRC = 9.7.

## Appendix D.2.6 Profile N°6

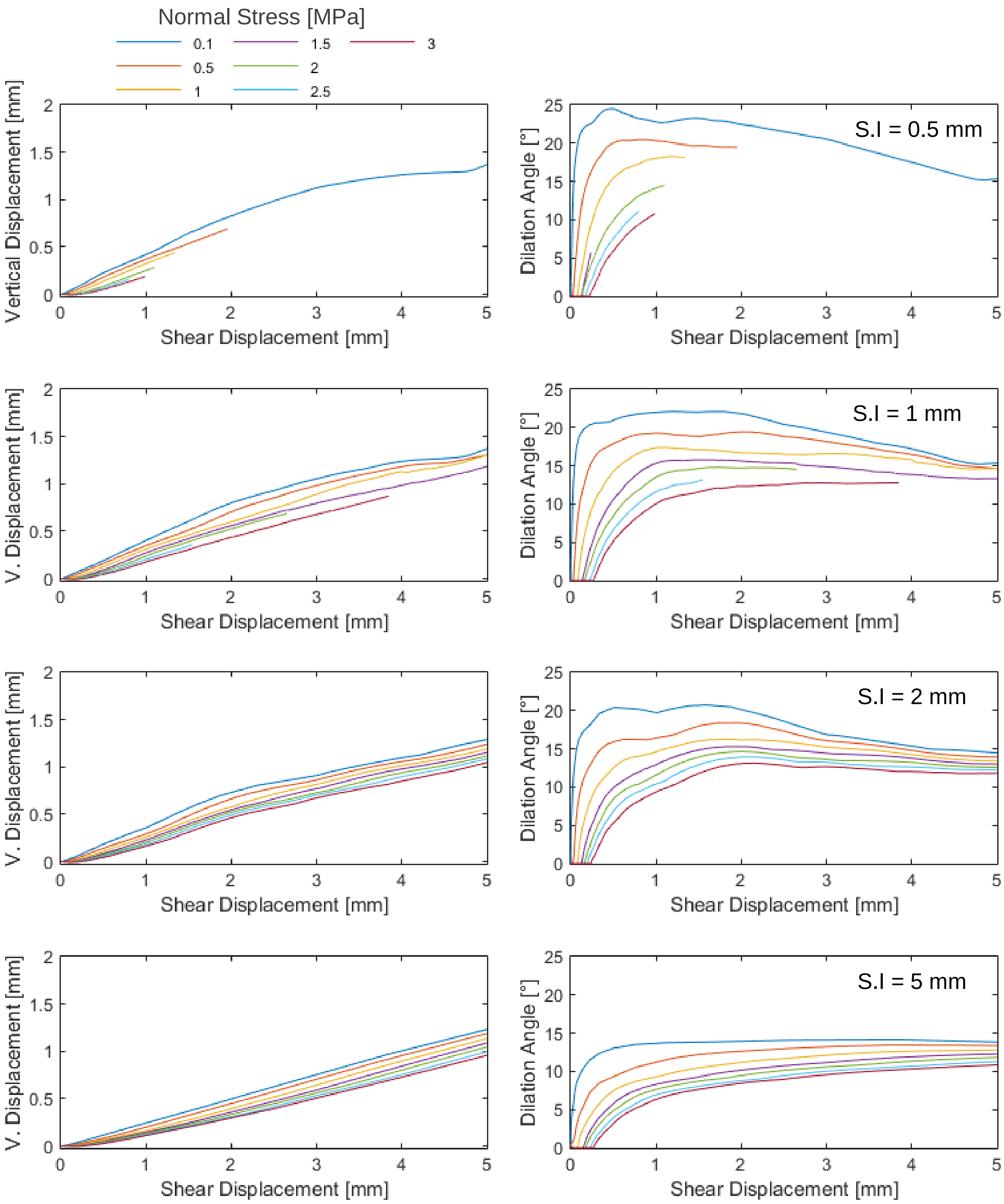

Figure D.26. Vertical displacement - shear displacement curve and secant dilation angle as a function of the shear displacement, Barton profile N°6, nominal JRC = 10.8.

## Appendix D.2.7 Profile N°7

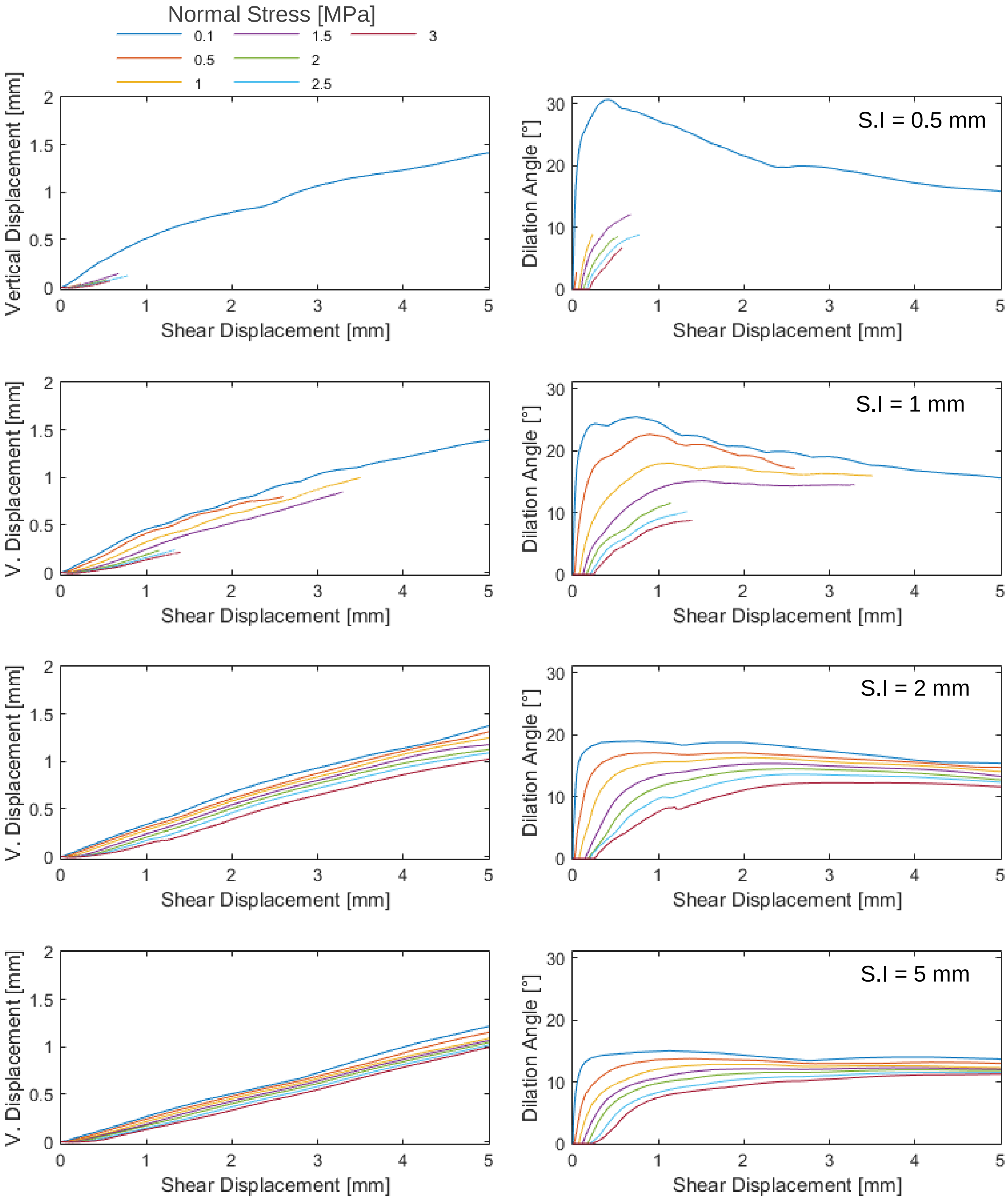

Figure D.27. Vertical displacement - shear displacement curve and secant dilation angle as a function of the shear displacement, Barton profile N°7, nominal JRC = 12.8.

## Appendix D.2.8 Profile N°8

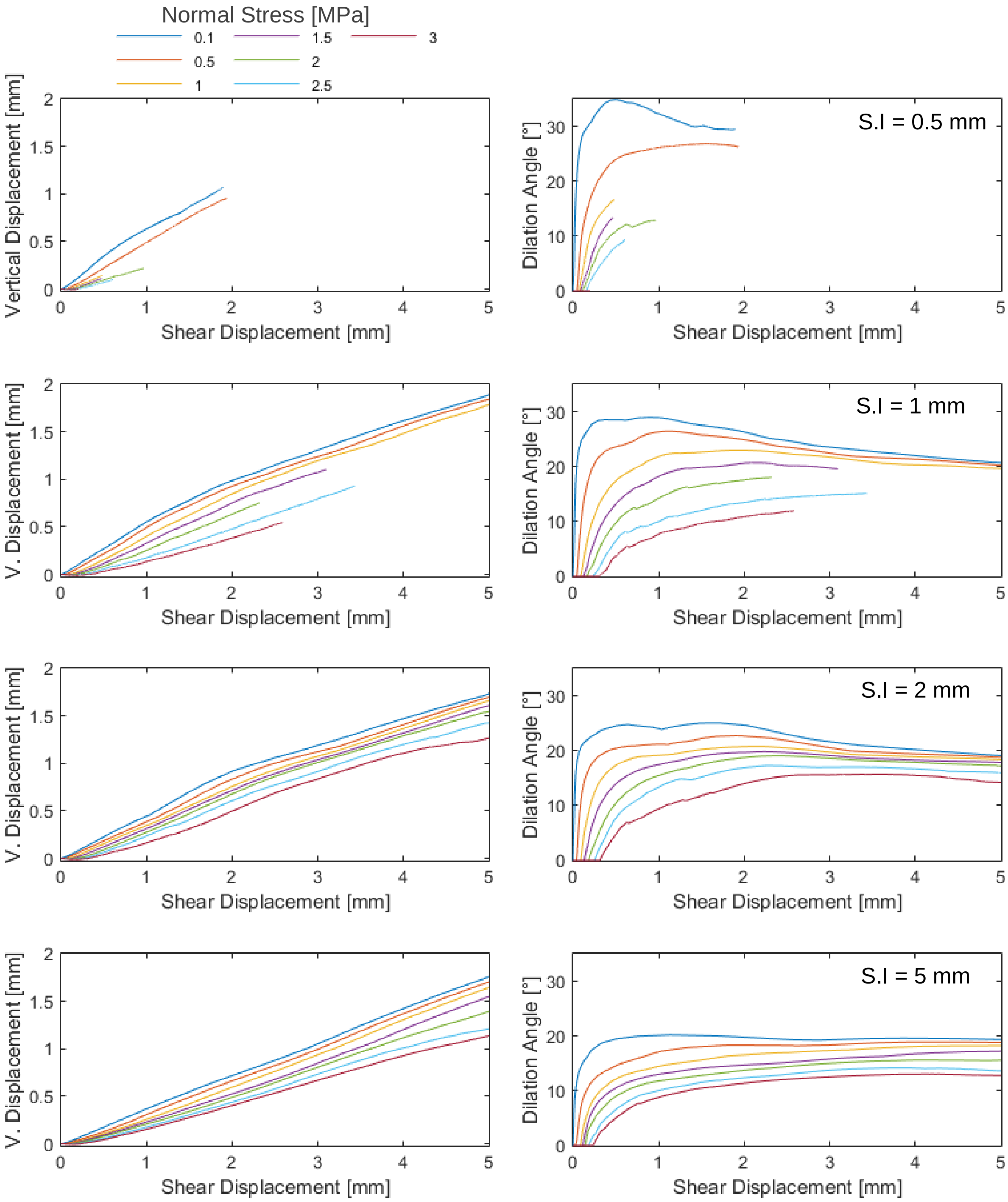

Figure D.28. Vertical displacement - shear displacement curve and secant dilation angle as a function of the shear displacement, Barton profile N°8, nominal JRC = 14.5.

## Appendix D.2.9 Profile N°9

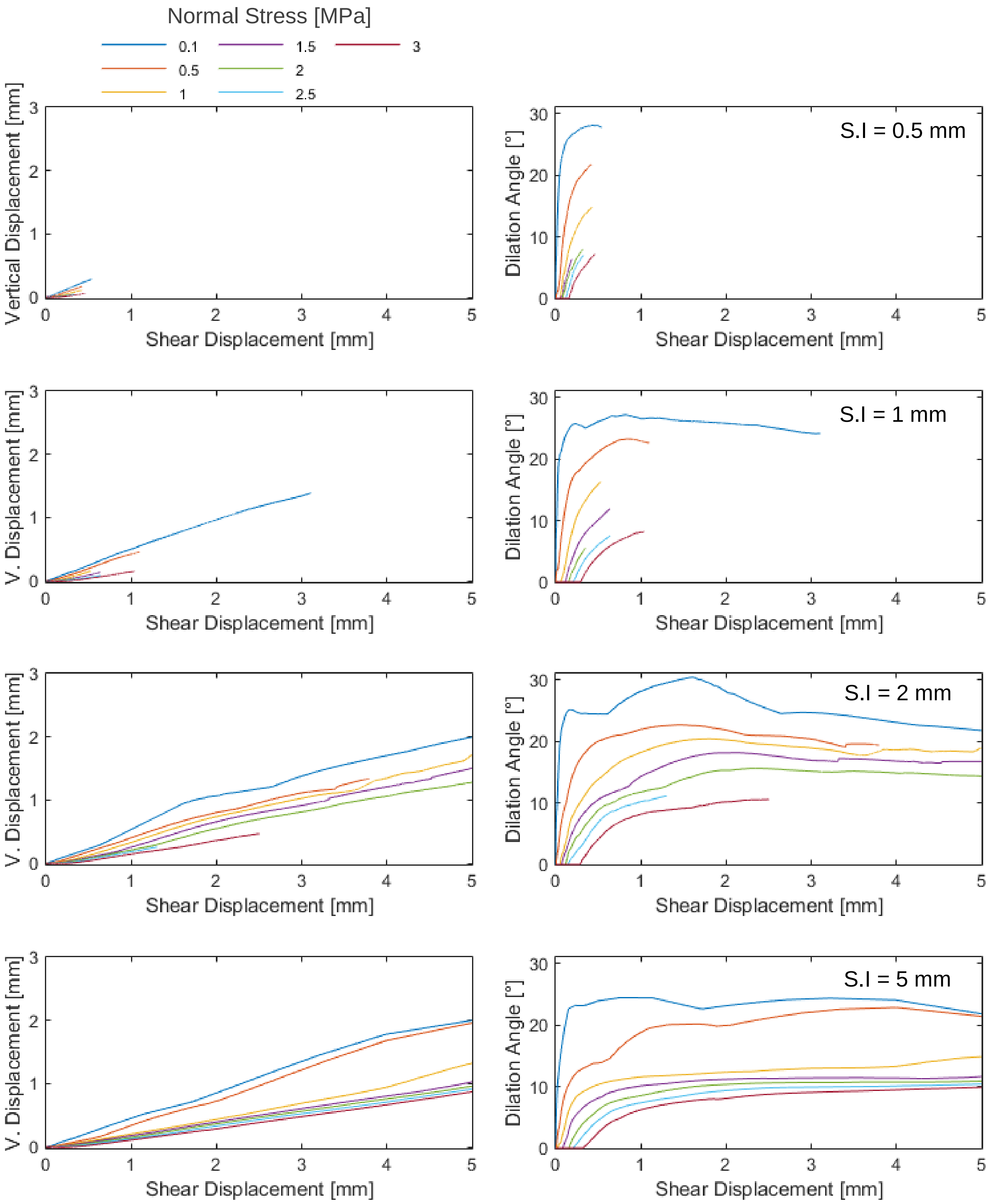

Figure D.29. Vertical displacement - shear displacement curve and secant dilation angle as a function of the shear displacement, Barton profile N°9, nominal JRC = 16.7.

## Appendix D.2.10 Profile N°10

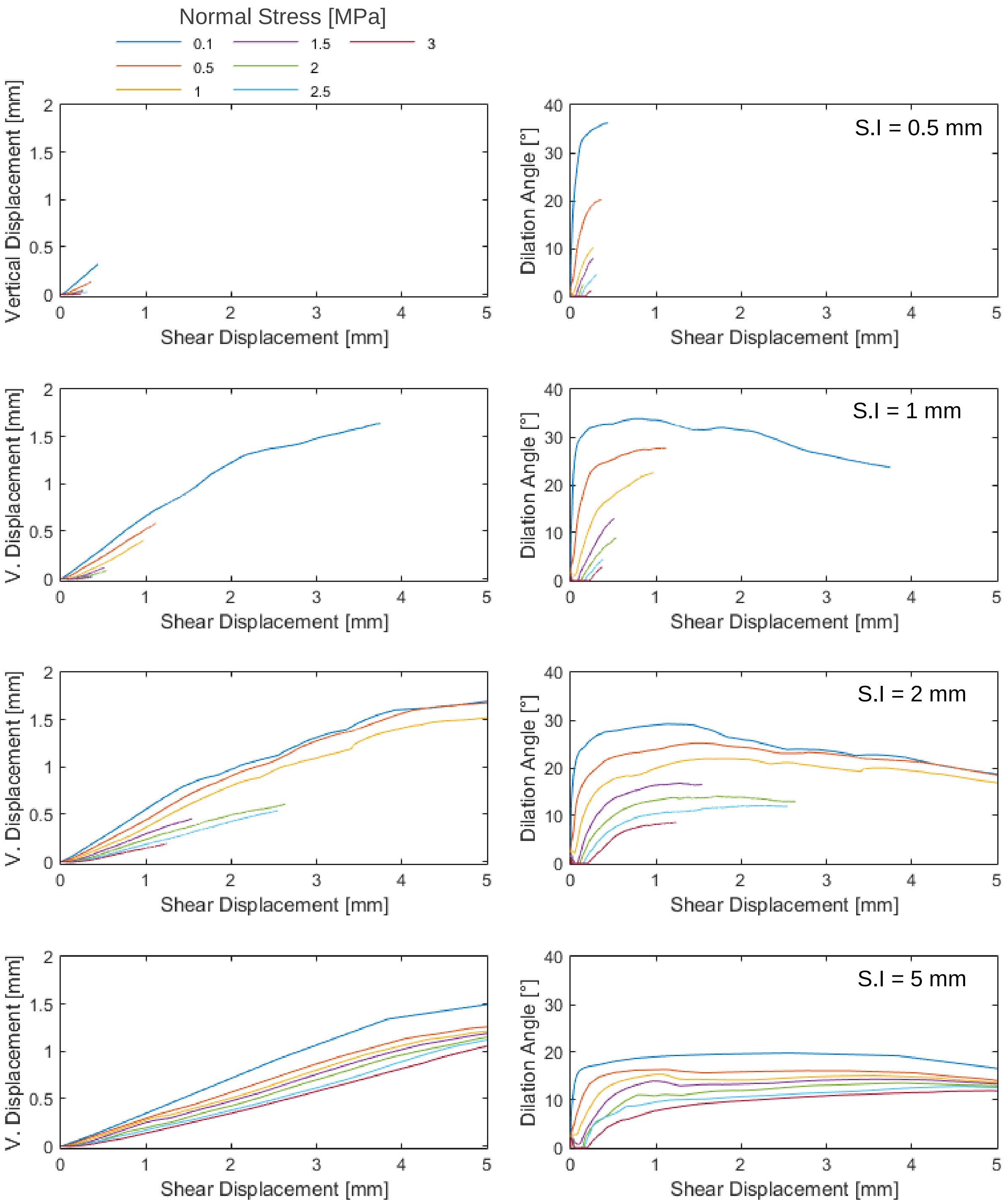

Figure D.30. Vertical displacement - shear displacement curve and secant dilation angle as a function of the shear displacement, Barton profile N°10, nominal JRC = 18.7.

# Appendix E Scale Effects Study

## Appendix E.1 Profile N°1

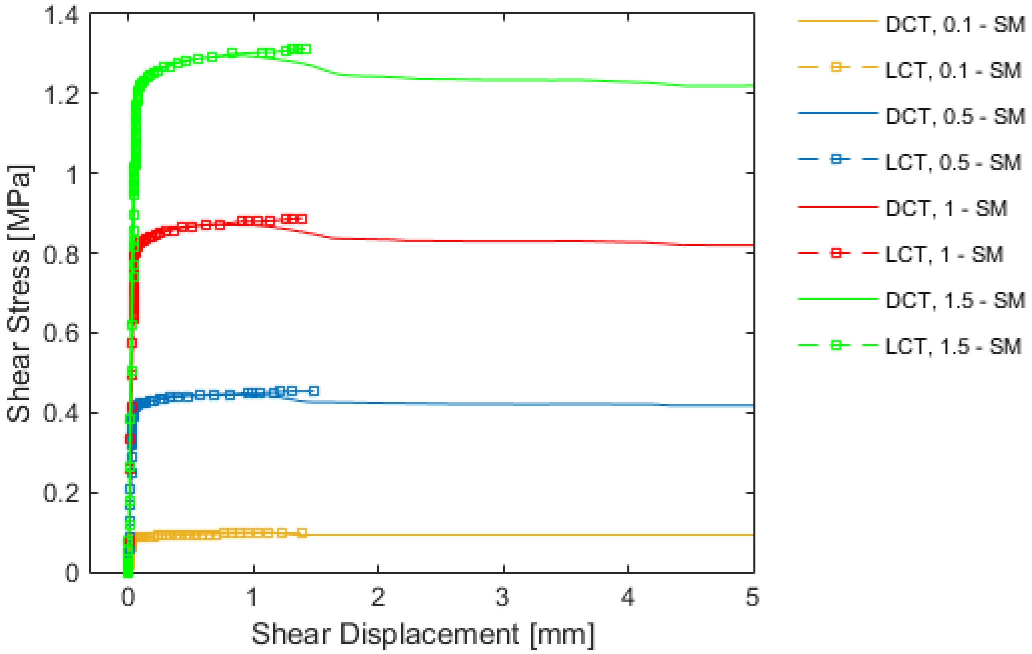

Figure E.1. Shear stress v/ shear displacement test results for load and displacement controlled small-scale tests, Profile N° 1, Nominal JRC = 0.4, SI = 2 mm.

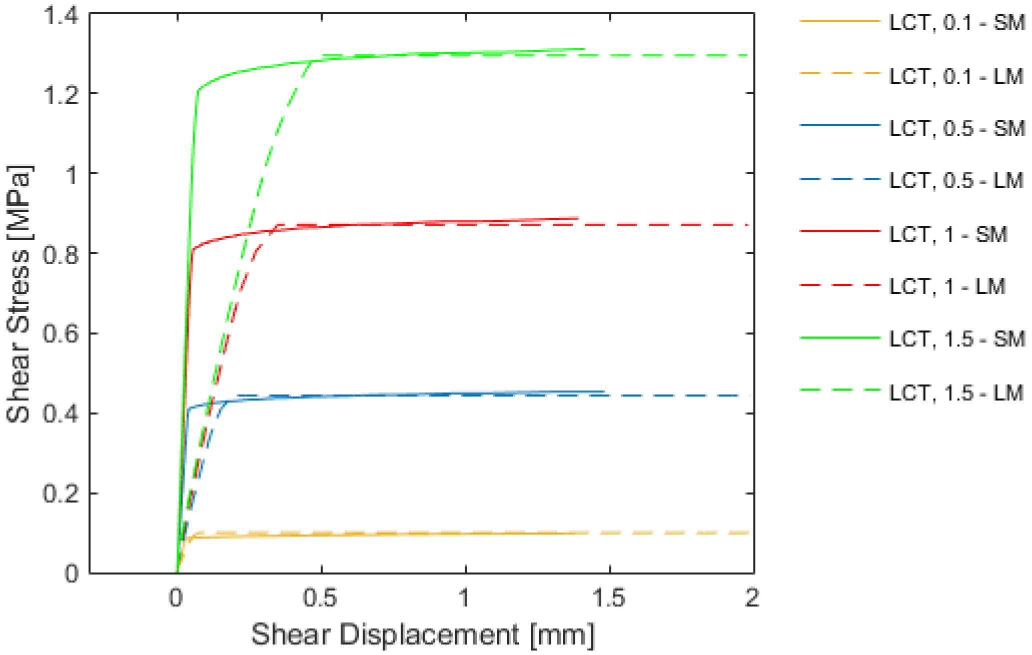

Figure E.2. Shear stress v/ shear displacement tests results for load-controlled small-scale and large-scale models, Profile N°6, nominal JRC = 0.4, SI = 2 mm.

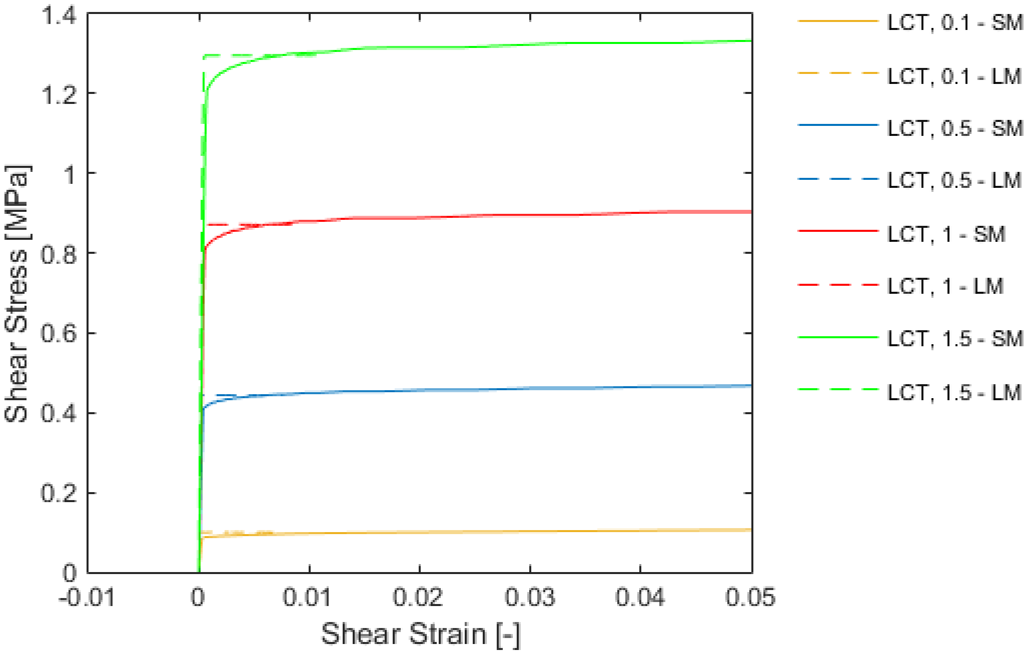

Figure E.3. Shear stress v/s shear strain test results for load-controlled small-scale and large-scale models, Profile N° 1, nominal JRC = 0.4, SI = 2 mm.

## Appendix E.2 Profile N°2

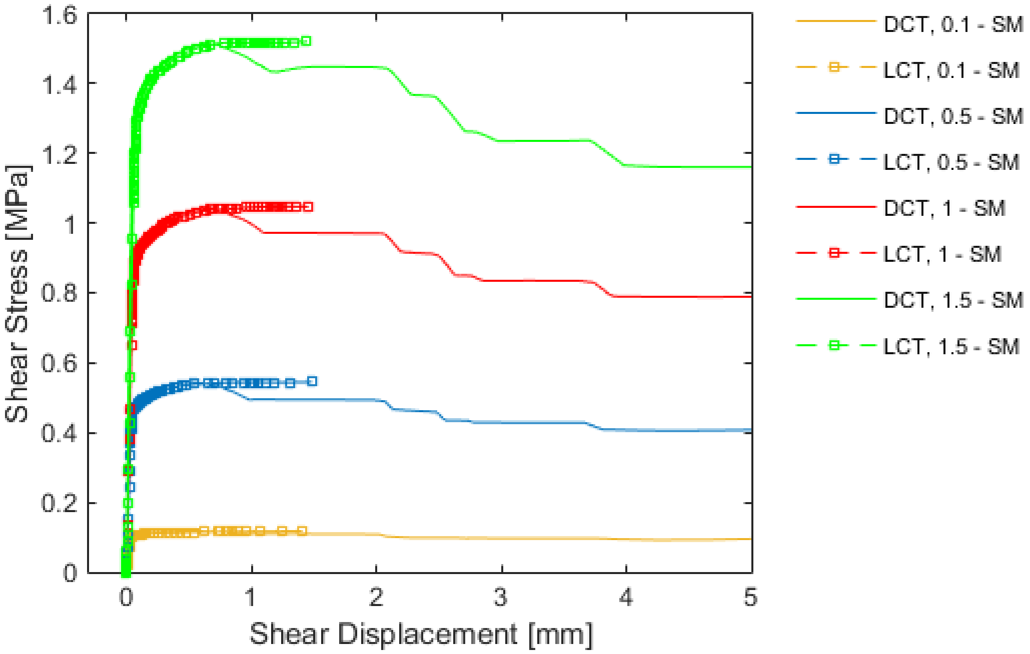

Figure E.4. Shear stress v/ shear displacement test results for load and displacement controlled small-scale tests, Profile N°2, Nominal JRC = 2.8, SI = 2 mm.

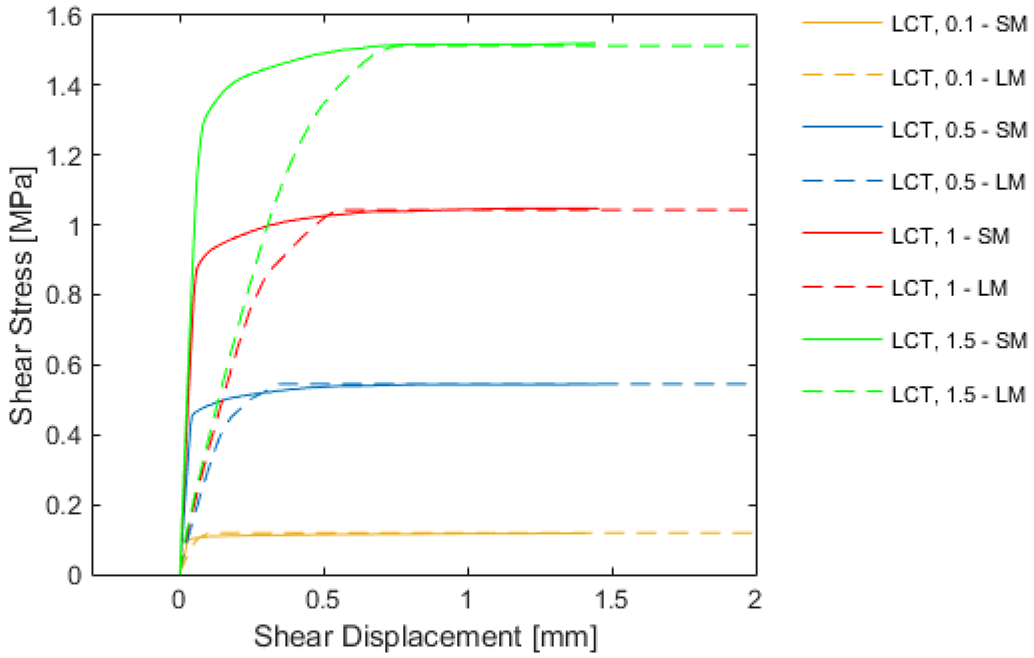

Figure E.5. Shear stress v/ shear displacement tests results for load-controlled small-scale and large-scale models, Profile N°2, nominal JRC = 2.8, SI = 2 mm.

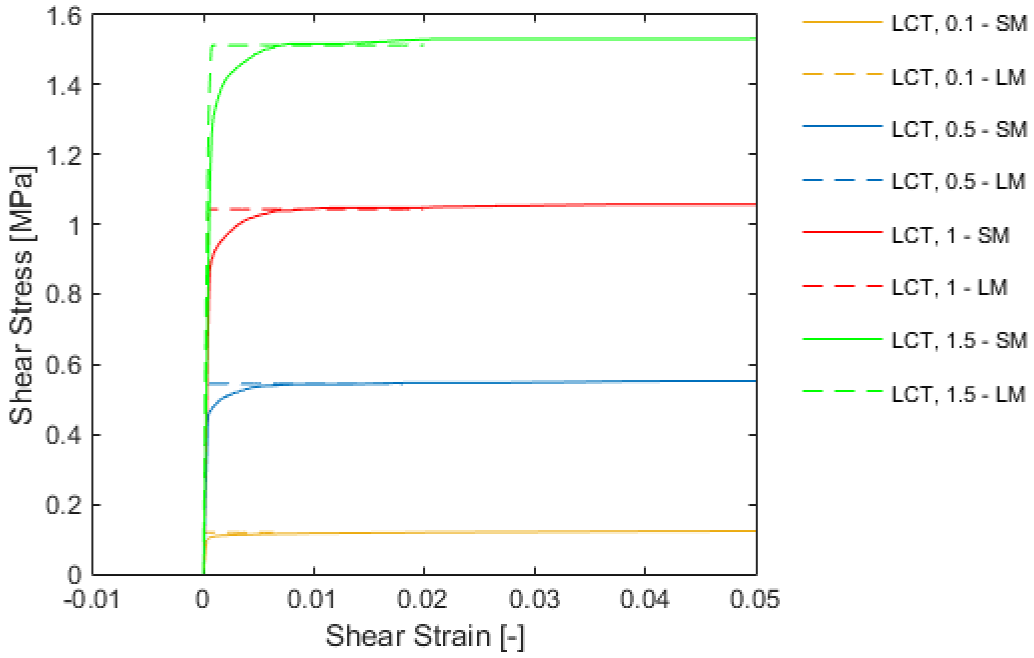

Figure E.6. Shear stress v/s shear strain test results for load-controlled small-scale and large-scale models, Profile N° 2, nominal JRC = 2.8, SI = 2 mm.

## Appendix E.3 Profile N°3

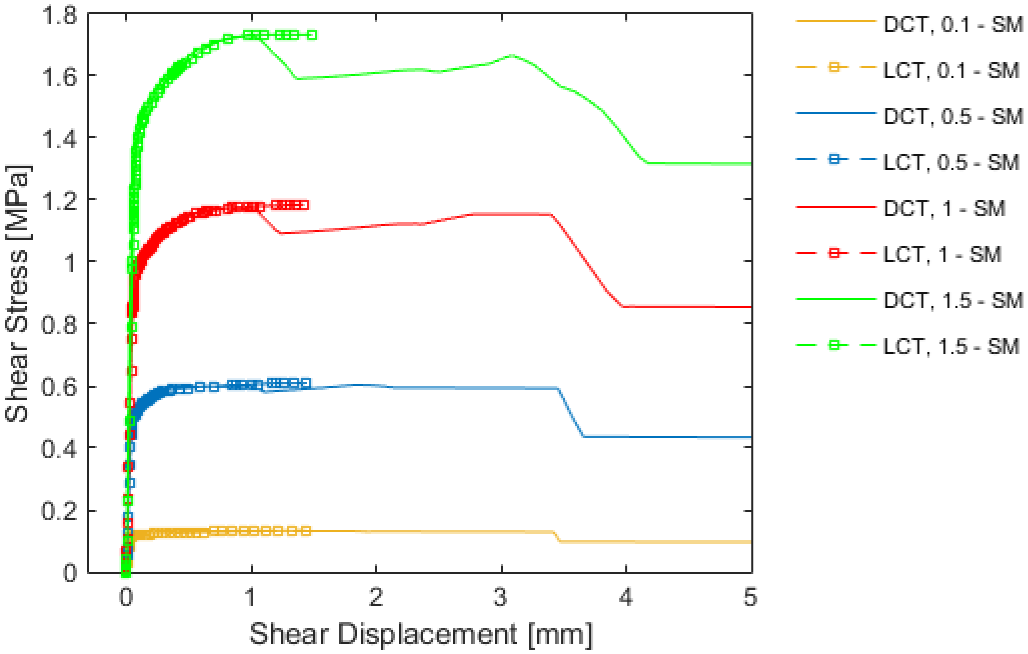

Figure E.7. Shear stress v/ shear displacement test results for load and displacement-controlled small-scale tests, Profile N° 3, nominal JRC = 5.8, SI = 2 mm.

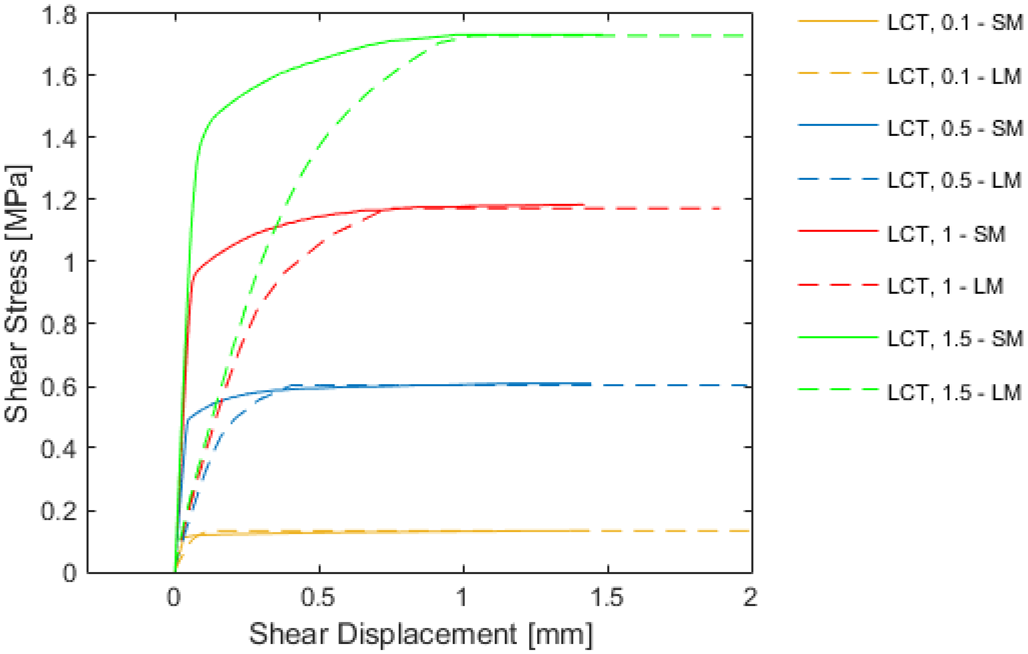

Figure E.8. Shear stress v/ shear displacement tests results for load-controlled small-scale and large-scale models, Profile N°6, nominal JRC = 5.8, SI = 2 mm.

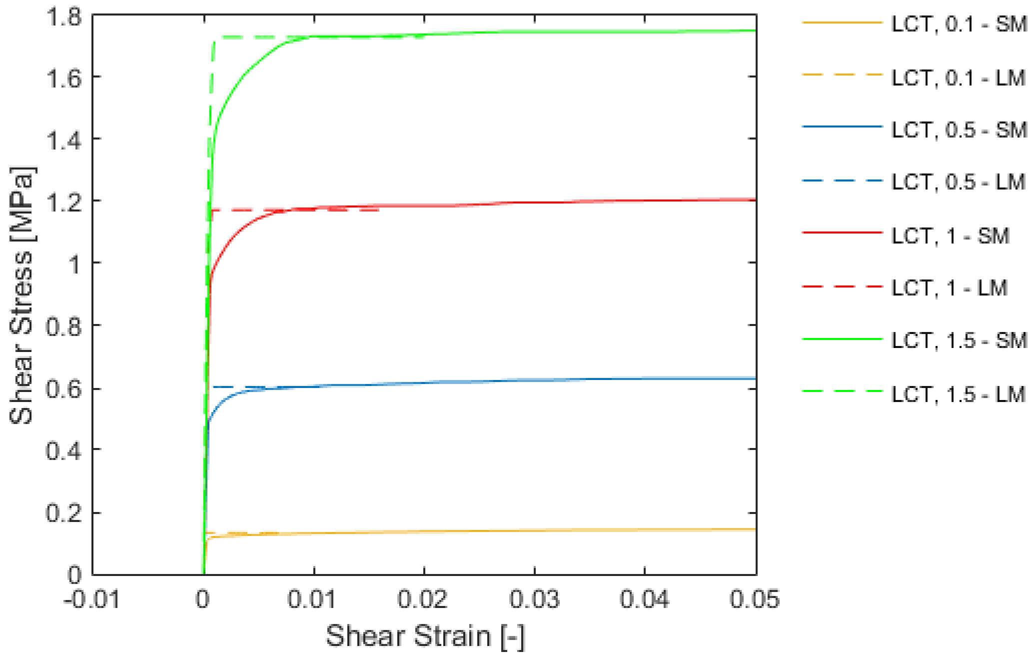

Figure E.9. Shear stress v/s shear strain test results for load-controlled small-scale and large-scale models, Profile N° 3, nominal JRC = 5.8, SI = 2 mm.

## Appendix E.4 Profile N°4

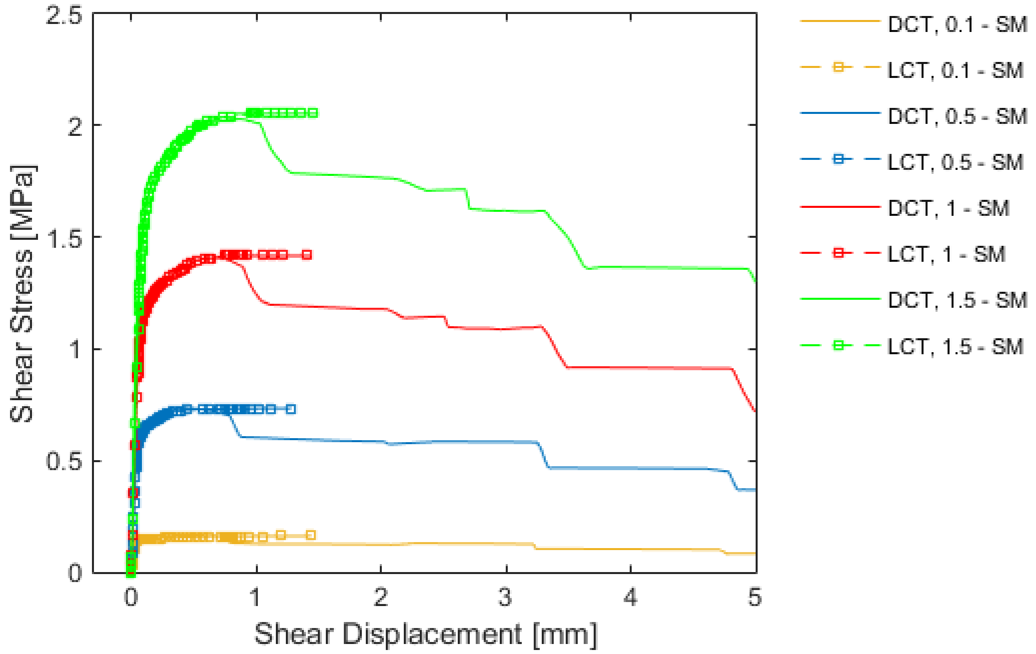

Figure E.10. Shear stress v/ shear displacement test results for load and displacement-controlled small-scale tests, Profile N° 4, nominal JRC = 6.7, SI = 2 mm.

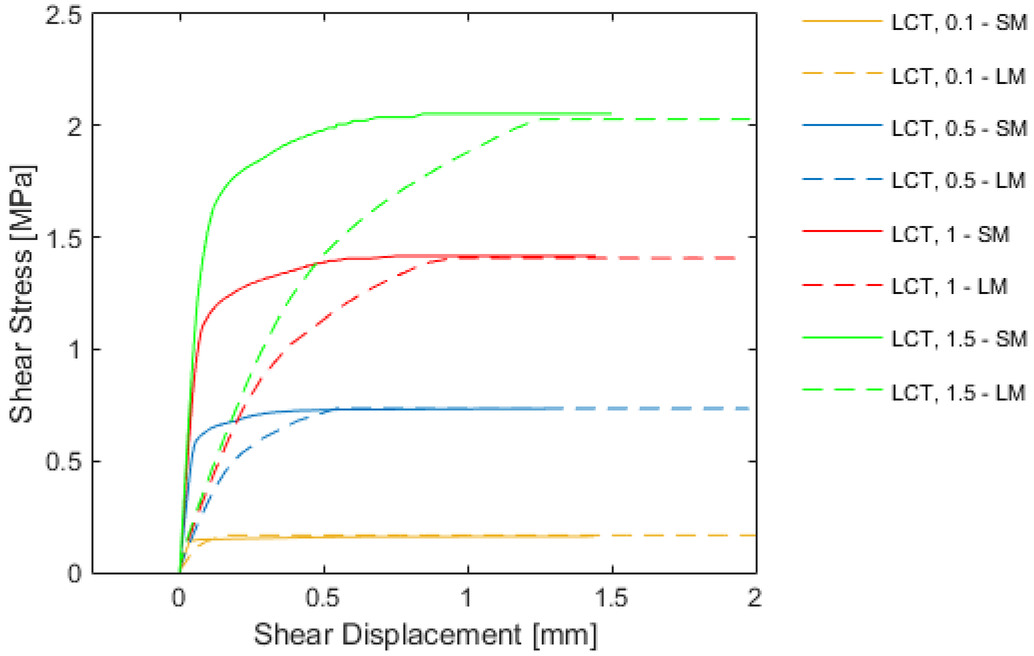

Figure E.11. Shear stress v/ shear displacement tests results for load-controlled small-scale and large-scale models, Profile N°4, nominal JRC = 6.7, SI = 2 mm.

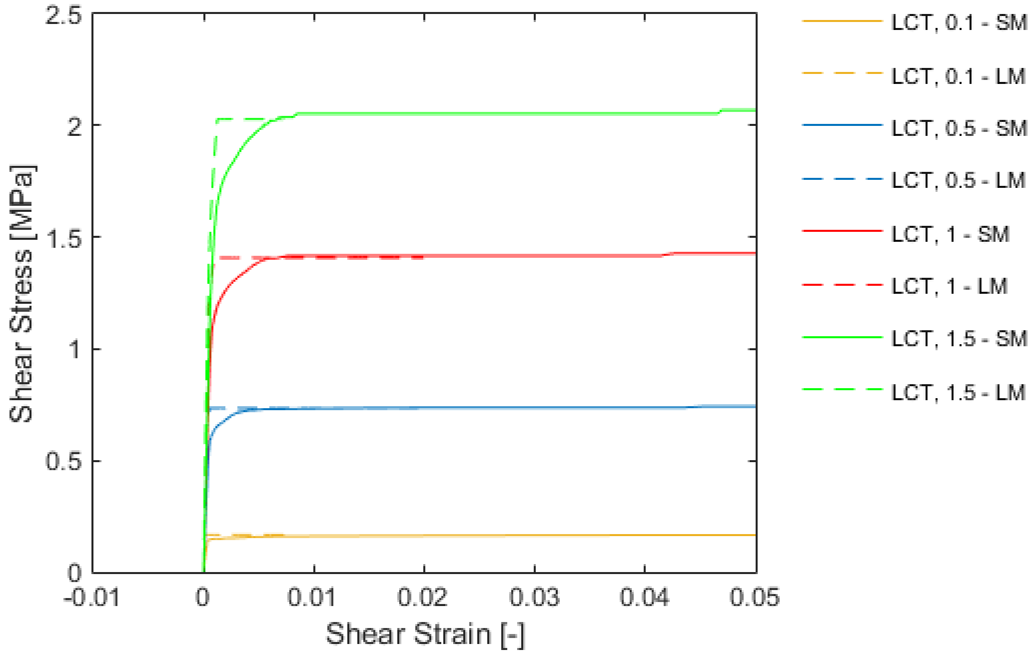

Figure E.12. Shear stress v/s shear strain test results for load-controlled small-scale and large-scale models, Profile N° 4, nominal JRC = 6.7, SI = 2 mm.

## Appendix E.5 Profile N°5

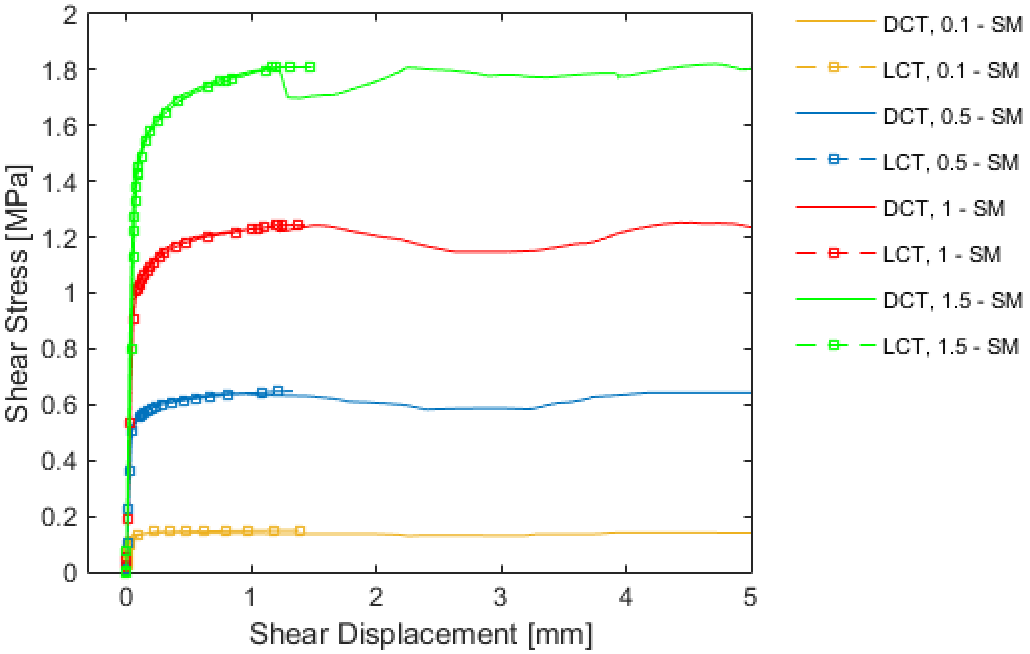

Figure E.13. Shear stress v/ shear displacement test results for load and displacement-controlled small-scale tests, Profile N° 5, nominal JRC = 9.5, SI = 2 mm.

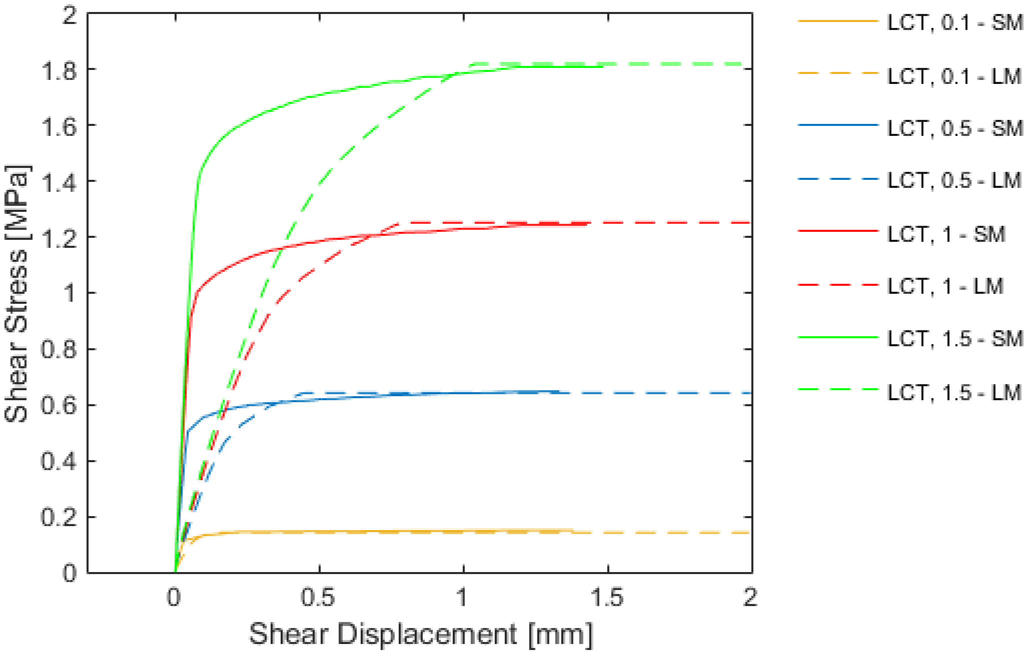

Figure E.14. Shear stress v/ shear displacement tests results for load-controlled small-scale and large-scale models, Profile N°5, nominal JRC = 9.5, SI = 2 mm.

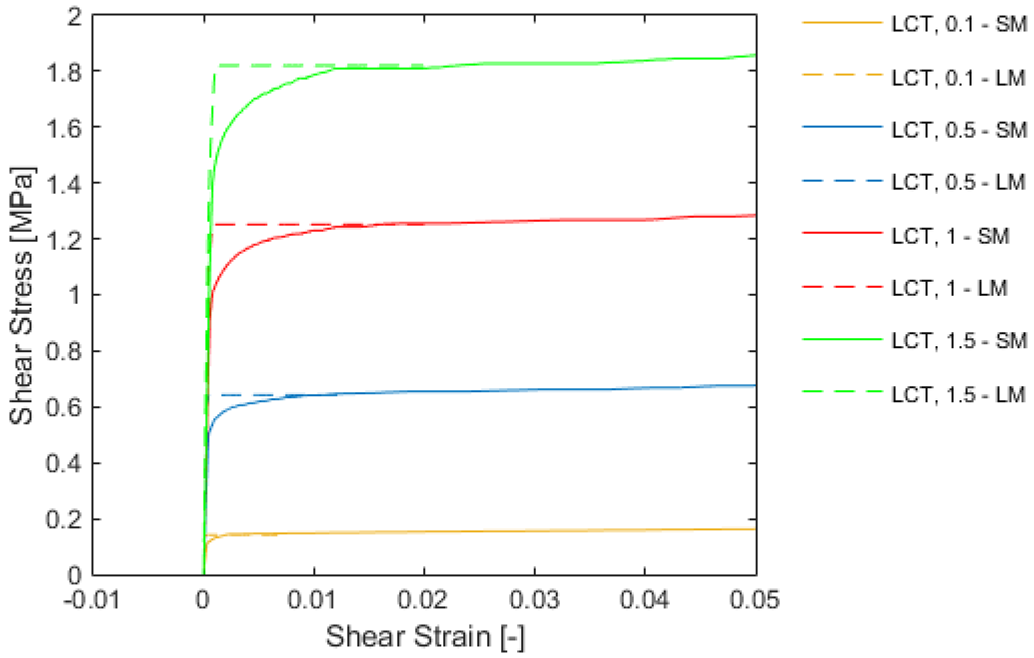

Figure E.15. Shear stress v/s shear strain test results for load-controlled small-scale and large-scale models, Profile N° 5, nominal JRC = 9.5, SI = 2 mm.

## Appendix E.6 Profile N°6

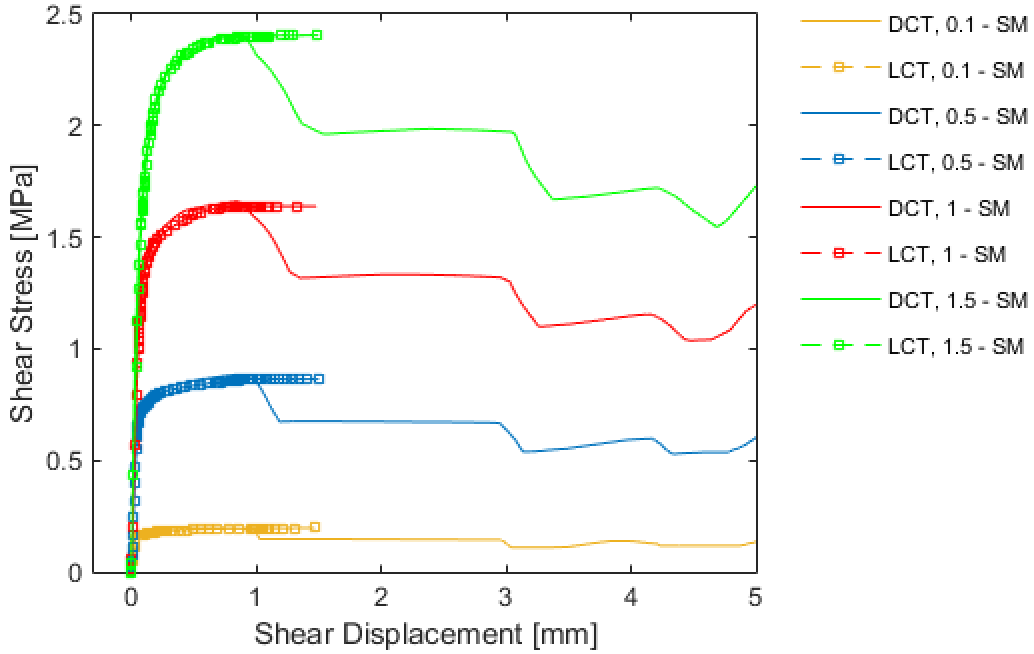

Figure E.16. Shear stress v/ shear displacement test results for load and displacement-controlled small-scale tests, Profile N° 6, nominal JRC = 10.8, SI = 2 mm.

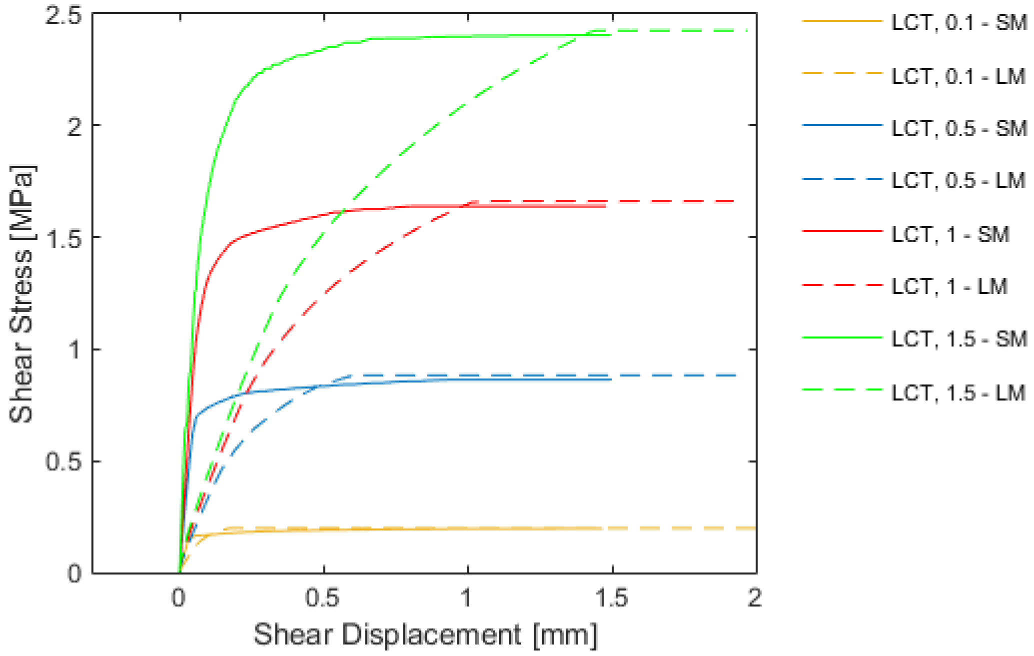

Figure E.17. Shear stress v/ shear displacement tests results for load-controlled small-scale and large-scale models, Profile N°6, nominal JRC = 10.8, SI = 2 mm.

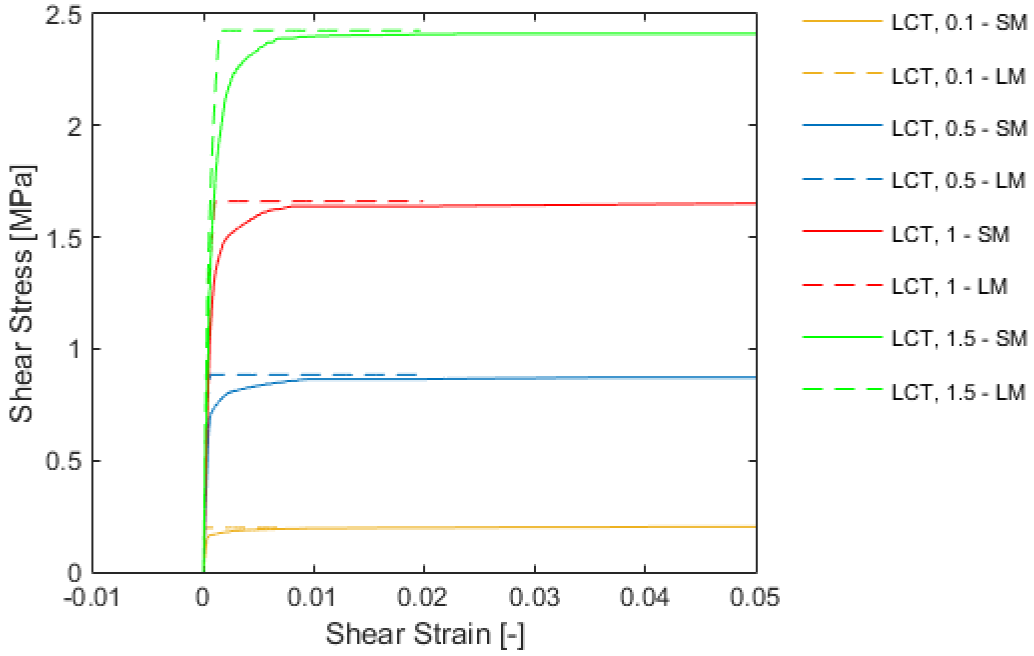

Figure E.18. Shear stress v/s shear strain test results for load-controlled small-scale and large-scale models, Profile N°6, nominal JRC = 10.8, SI = 2 mm.

## Appendix E.7 Profile N°7

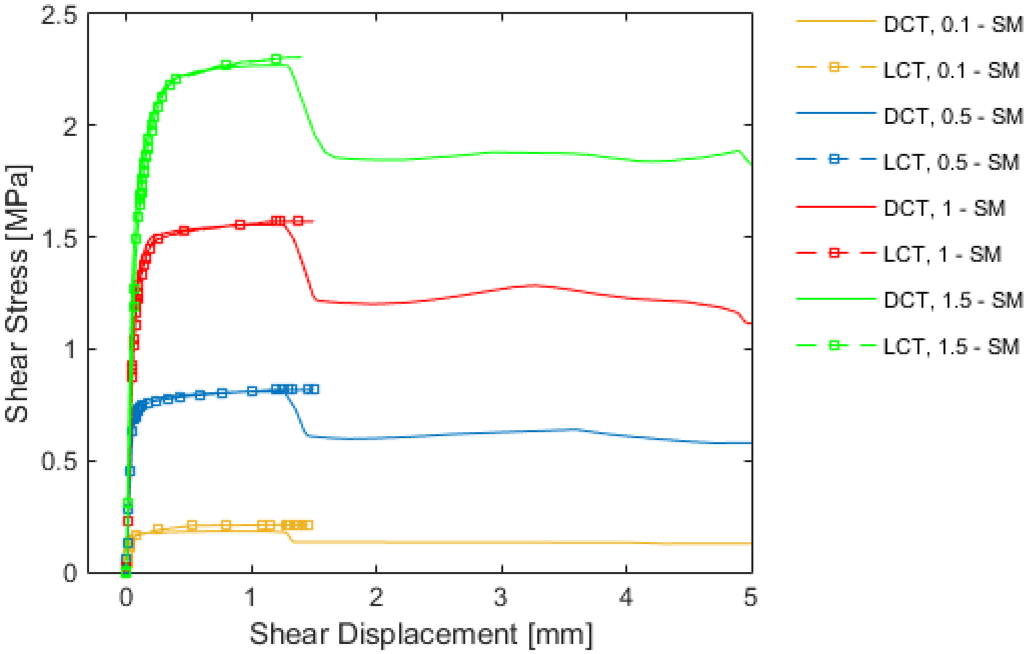

Figure E.19. Shear stress v/ shear displacement test results for load and displacement-controlled small-scale tests, Profile N° 7, nominal JRC = 12.8, SI = 2 mm.

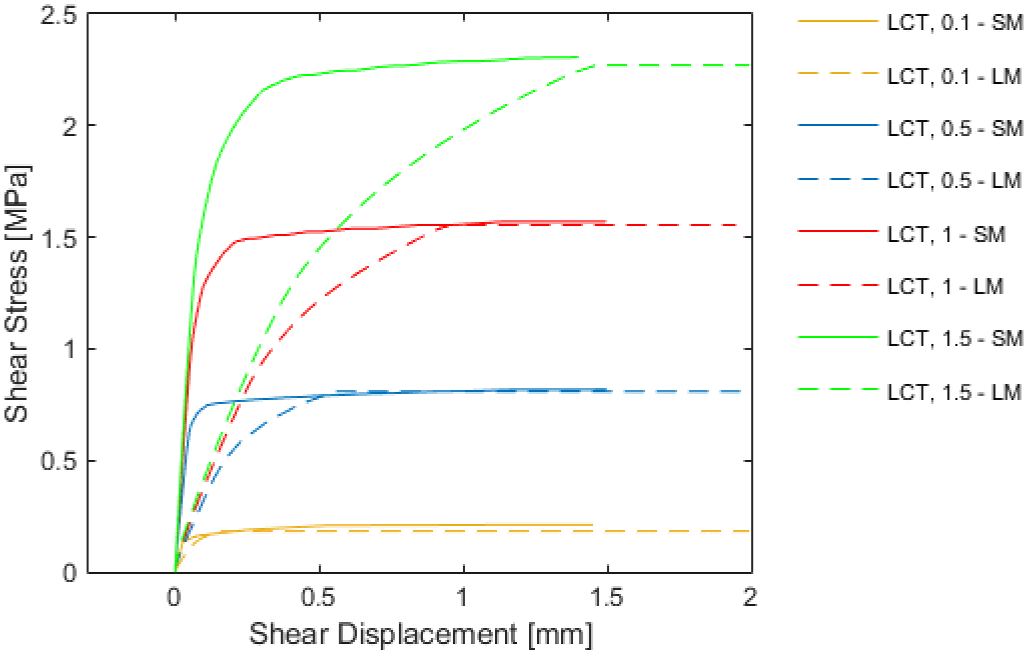

Figure E.20. Shear stress v/ shear displacement tests results for load-controlled small-scale and large-scale models, Profile N°7,nominal JRC = 12.8, SI = 2 mm.

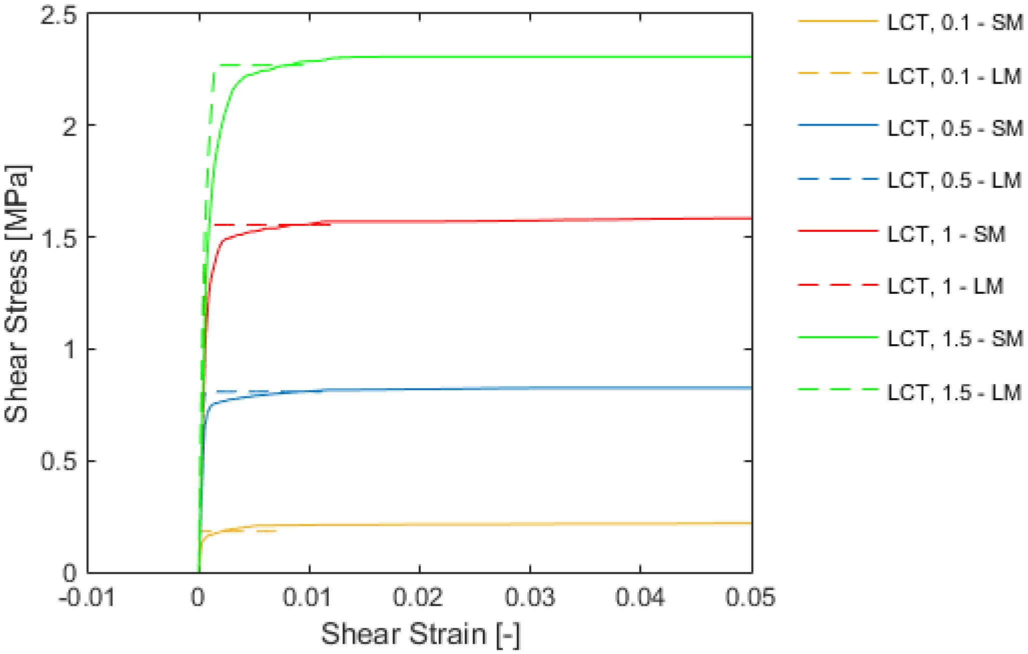

Figure E.21. Shear stress v/s shear strain test results for load-controlled small-scale and large-scale models, Profile N° 7, nominal JRC = 12.8, SI = 2 mm.

## Appendix E.8 Profile N°8

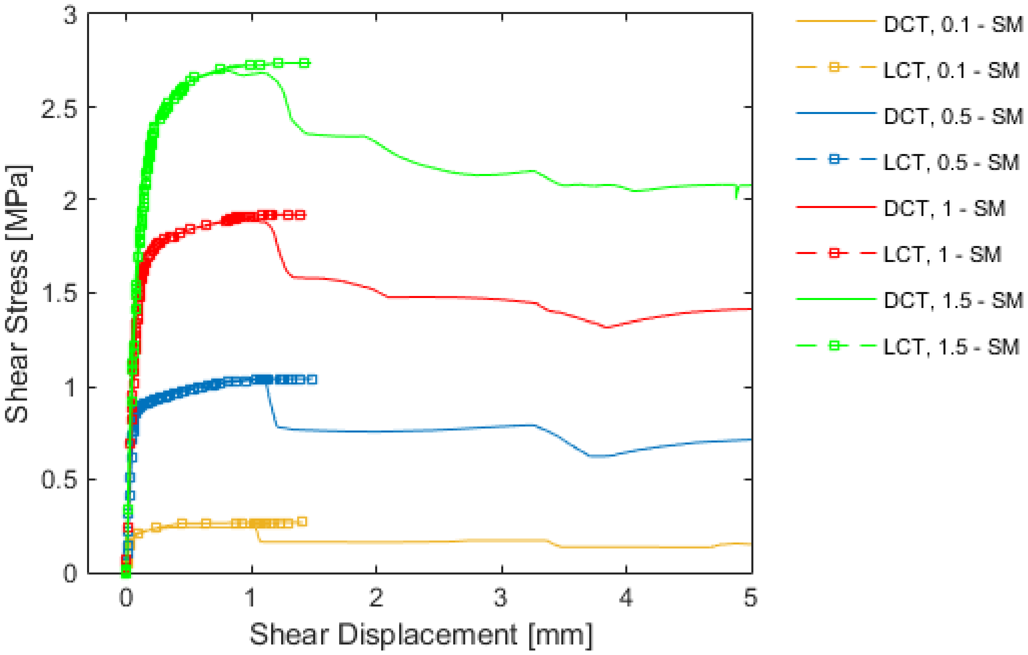

Figure E.22. Shear stress v/ shear displacement test results for load and displacement-controlled small-scale tests, Profile N° 8, nominal JRC = 14.5, SI = 2 mm.

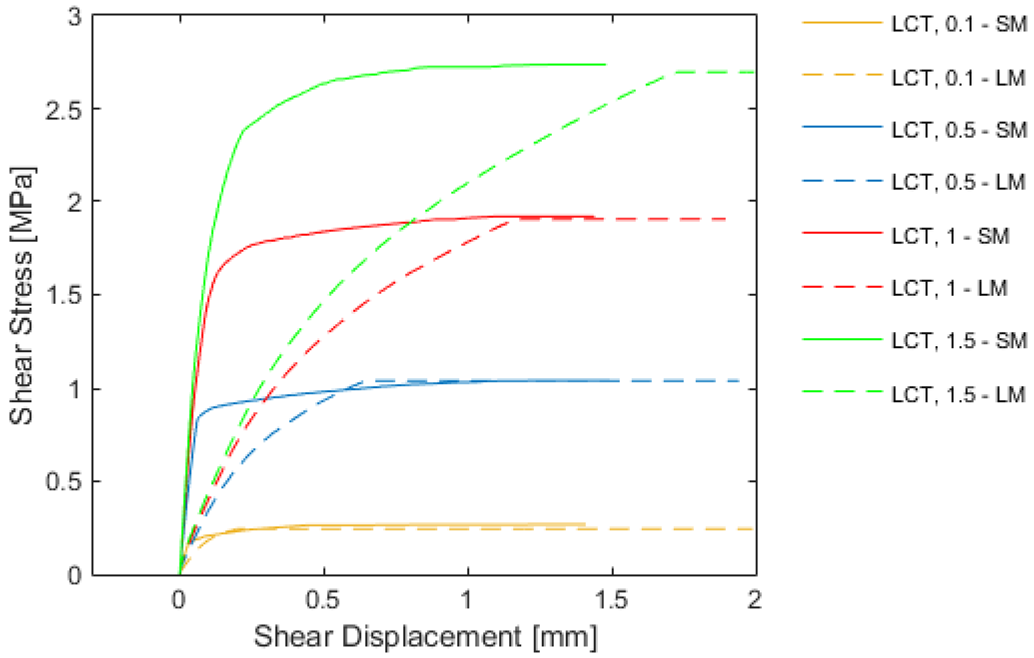

Figure E.23. Shear stress v/ shear displacement tests results for load-controlled small-scale and large-scale models, Profile N°8, nominal JRC = 14.5, SI = 2 mm.

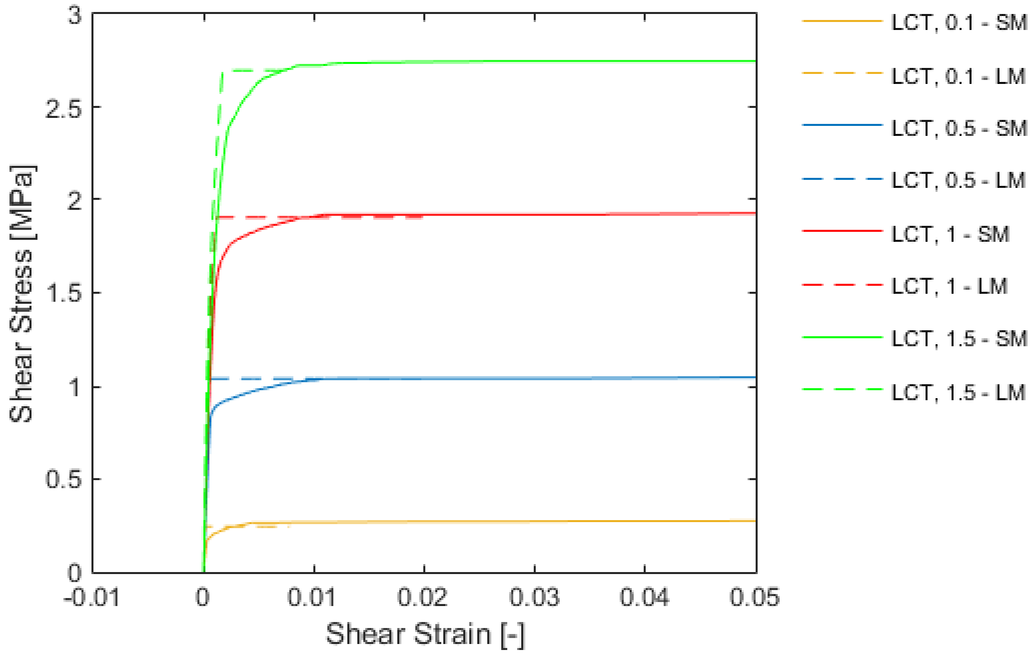

Figure E.24. Shear stress v/s shear strain test results for load-controlled small-scale and large-scale models, Profile N°8, nominal JRC = 14.5, SI = 2 mm.

## Appendix E.9 Profile N°9

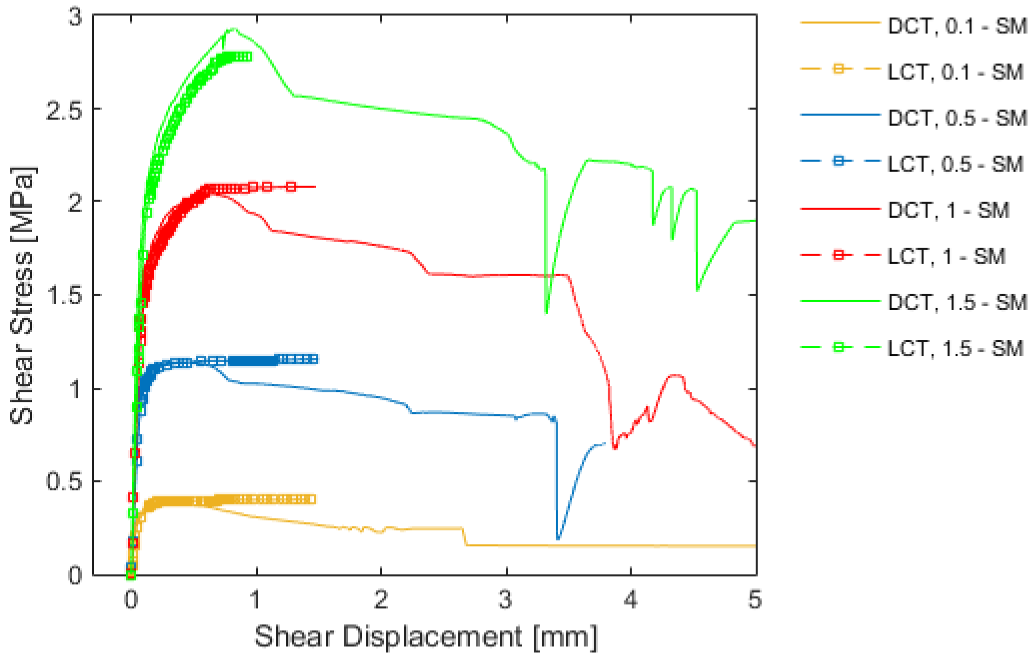

Figure E.25. Shear stress v/ shear displacement test results for load and displacement-controlled small-scale tests, Profile N° 9, nominal JRC = 16.7, SI = 2 mm.

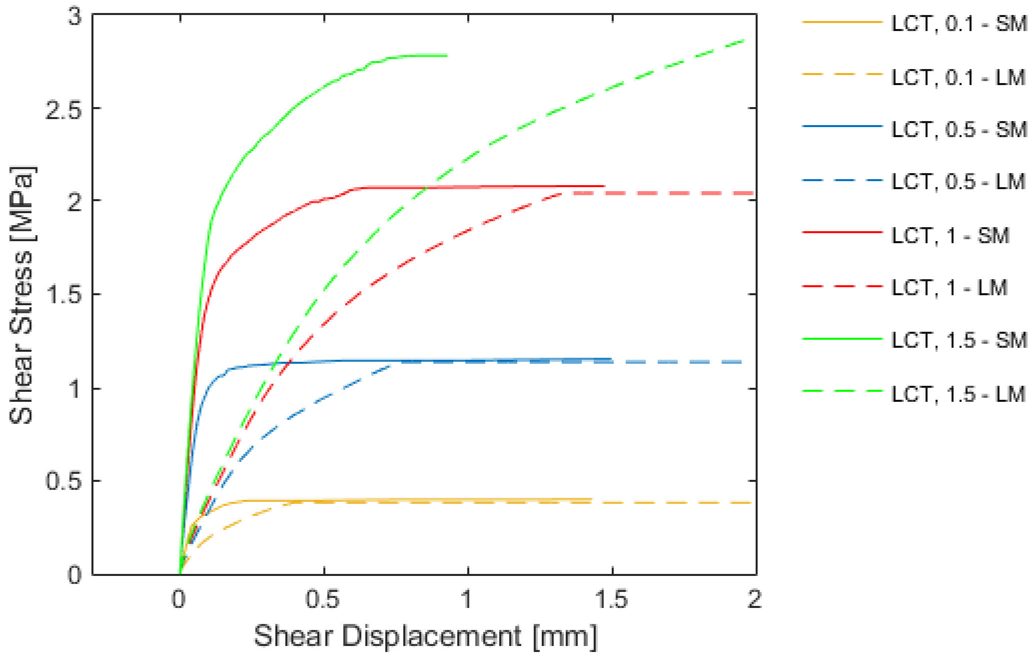

Figure E.26. Shear stress v/ shear displacement tests results for load-controlled small-scale and large-scale models, Profile N°9, nominal JRC = 16.7, SI = 2 mm.

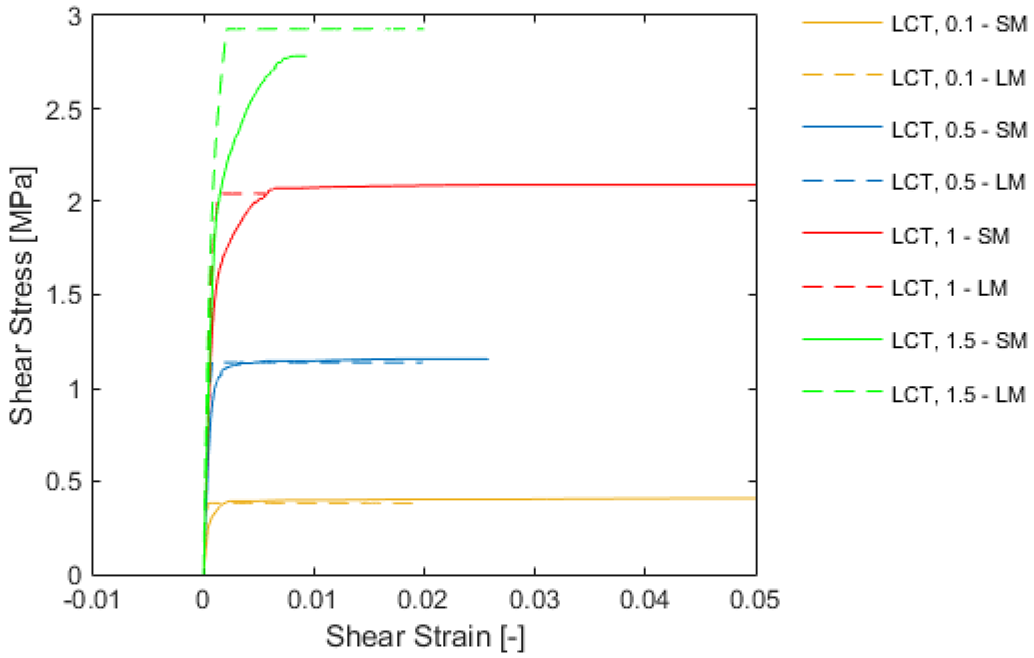

Figure E.27. Shear stress v/s shear strain test results for load-controlled small-scale and large-scale models, Profile N°9, nominal JRC = 16.7, SI = 2 mm.

## Appendix E.10 Profile N°10

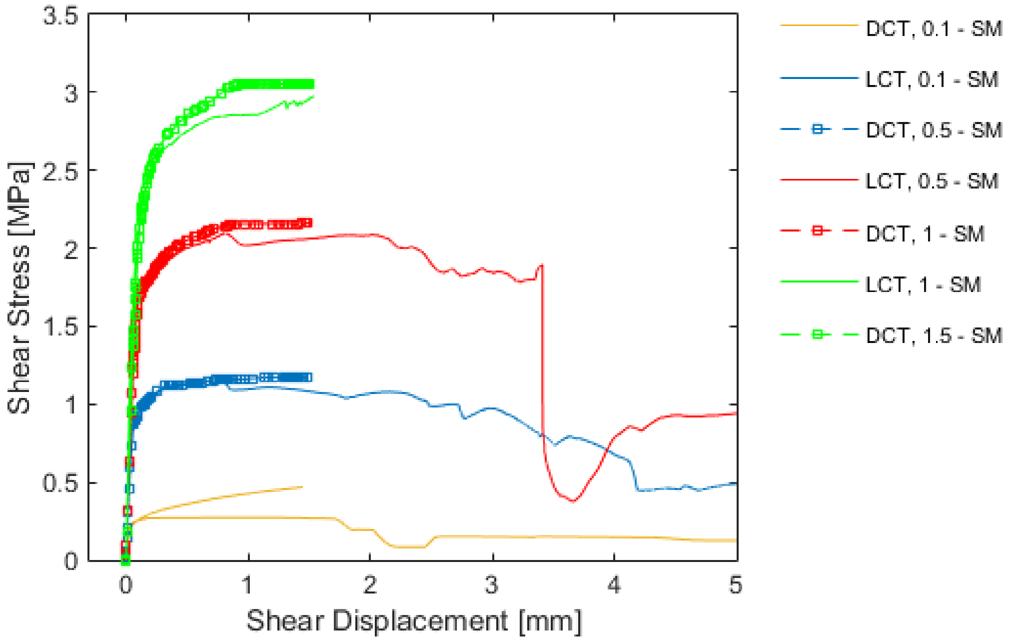

Figure E.28. Shear stress v/ shear displacement test results for load and displacement-controlled small-scale tests, Profile N° 10, nominal JRC = 16.7, SI = 2 mm.

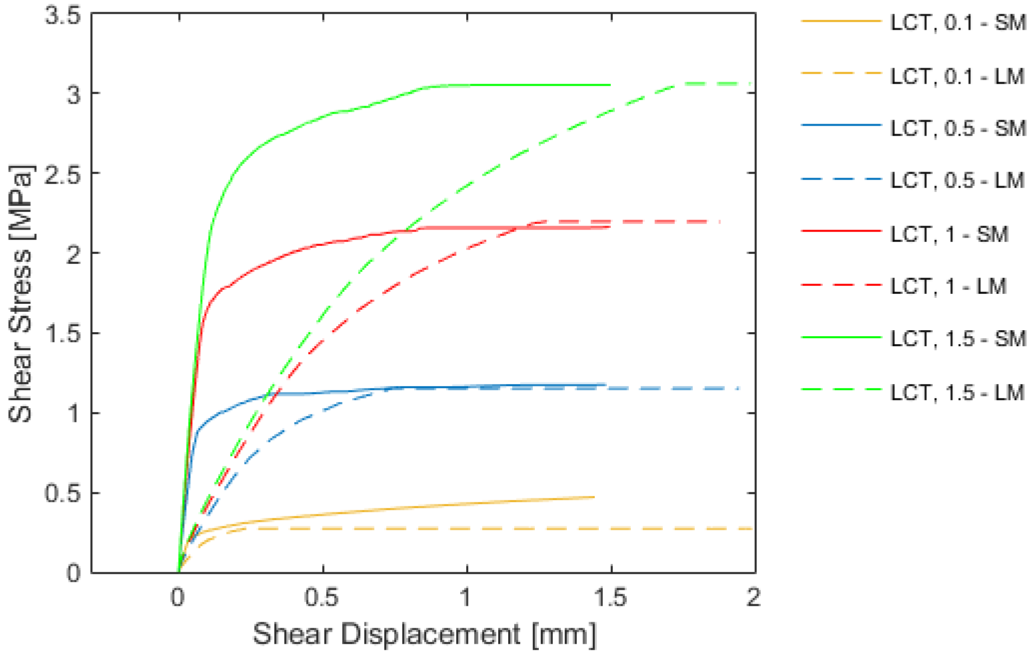

Figure E.29. Shear stress v/ shear displacement tests results for load-controlled small-scale and large-scale models, Profile N°10, nominal JRC = 18.7, SI = 2 mm.

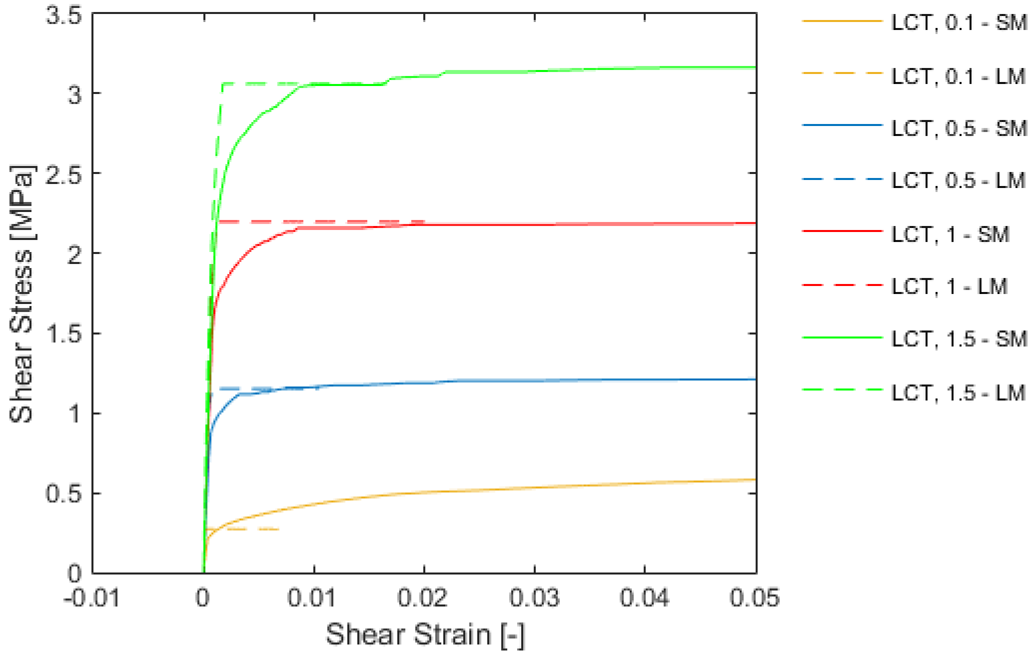

Figure E.30. Shear stress v/s shear strain test results for load-controlled small-scale and large-scale models, Profile N°10, nominal JRC = 18.7, SI = 2 mm.